Technical Report

TR-10-57

SR-Site: Oxygen ingress in the rock at Forsmark during a glacial cycle

Magnus Sidborn, Kemakta Konsult AB

Björn Sandström, WSP Sverige AB

Eva-Lena Tullborg, Terralogica AB

Joaquín Salas, Flávia Maia, Anne Delos, Jorge Molinero
Amphos21

Lotta Hallbeck, Karsten Pedersen
Microbial Analytics Sweden AB

November 2010

Svensk Kärnbränslehantering AB
Swedish Nuclear Fuel
and Waste Management Co

Box 250, SE-101 24 Stockholm
Phone +46 8 459 84 00

ISSN 1404-0344
SKB TR-10-57
ID 1271362
Updated 2015-05

SR-Site: Oxygen ingress in the rock at Forsmark during a glacial cycle

Magnus Sidborn, Kemakta Konsult AB

Björn Sandström, WSP Sverige AB

Eva-Lena Tullborg, Terralogica AB

Joaquín Salas, Flávia Maia, Anne Delos, Jorge Molinero
Amphos21

Lotta Hallbeck, Karsten Pedersen
Microbial Analytics Sweden AB

November 2010

Keywords: redox evolution, oxygen ingress, geochemical reactive-transport modelling, glaciation, Forsmark.

Update notice

The original report, dated November 2010, was found to contain editorial errors which have been corrected in this updated version.

Preface

This report consists of several parts for which different authors have contributed material in a collaborative effort. A short description of the main contributors and the relevant parts of this report that they have been involved with follows:

Magnus Sidborn (project coordinator), Kemakta Konsult AB
(Sections 1, 2.1, 2.2, 2.4, 4, 5, 6, 8, 9, Appendices B.2, C, and E)

Björn Sandström, WSP Sverige AB
(Sections 3, 5.4, 5.5, Appendices A, B, and C)

Eva-Lena Tullborg, Terralogica AB
(Sections 3, 5.4, 5.5, Appendices A, B, and C)

Joaquín Salas, Flávia Maia, Anne Delos, Jorge Molinero, Amphos21
(Section 7, Appendix D)

Lotta Hallbeck, Karsten Pedersen, Microbial Analytics Sweden AB
(Section 2.3)

The SR-Site reports listed below are referenced in the text in bold typeface. The full references are found at the top of the main list of references in Section 10.

Backfill production report

Buffer production report

Closure production report

Data report

Radionuclide transport report

Summary

The aim of this report is to assess the possibility for oxygen to be transported by glacial melt-water to canister positions in a final repository for spent nuclear fuel at the proposed location in Forsmark.

The approach for this assessment is to combine reactive transport modelling with geological observations of present and historical indications of oxygen ingress. For safety assessment purposes a cautious approach in the modelling is required when estimating the extent of oxygen ingress. In this report, a cautious approach has been applied both in the conceptualisation of the problem and in the choice of input parameters used in the models. Oxygen consuming processes are only neglected in the modelling if they are expected to further decrease the extent of oxygen ingress.

Several oxygen consuming processes have been identified, each of which may play an important role in the scavenging of oxygen along recharge flow paths in the rock. These processes include biological pathways with degradation of organic material of ground surface origin, and biotically mediated reactions with reduced rock minerals and with various materials expected to be present in the backfilled repository volume. In the absence of microbes most of these reactions may also follow abiotic pathways.

Present day observations show that degradation of organic material is the most powerful oxygen scavenging process. At Forsmark, oxygen is generally depleted within a few metres under present day temperate conditions. Although biological activity is likely to exist also during different phases of a glaciation, large uncertainties exist regarding e.g. the population growth dynamics, the biotic reaction rates and the availability of organic material under the highly varying conditions expected. Microbial activity and degradation of organic material is therefore pessimistically neglected in the calculations in this report.

In the absence of organic material, ferrous iron present in minerals in the rock matrix is the main source of reducing capacity. The ferrous iron occurs in different reduced minerals, of which biotite and chlorite are the most abundant. The release rate of ferrous iron from biotite is slower than for most of the ferrous minerals considered. Therefore, the ferrous iron is cautiously assumed to be comprised in biotite, as a model substance, and the release rate is calculated based on this assumption. Furthermore, the oxidation of ferrous iron by oxygen is assumed to occur in two consecutive steps; dissolution of ferrous iron from the mineral lattice into the pore solution followed by homogeneous oxidation of the dissolved ferrous ions. Direct oxidation of ferrous iron incorporated in the mineral lattice is hence also cautiously approximated by these two coupled processes.

At early times, reduced minerals in the undisturbed rock matrix, which are directly exposed to the flowing water, are easily accessible from the flow paths in the fractures. In this situation, the extent of oxygen ingress along the flow path is determined by the relative rates of oxygen recharge and oxygen consuming reactions. Eventually, the reducing capacity of the rock close to the fracture becomes depleted and the remaining ferrous minerals can only be reached by diffusion in the rock matrix. With time, this diffusion resistance increases as the reducing capacity is depleted further into the rock matrix. The oxygen consuming reaction is then limited by the diffusion resistance. The extent of oxygen ingress is in this situation determined by the relative rates of oxygen recharge and diffusion into the rock matrix. Both of these situations are represented by two different models that are solved analytically in this report. The case of kinetically controlled oxygen consumption for early times is furthermore evaluated with the geochemical numerical codes PHREEQC and PHAST.

Sensitivity analyses of important parameters such as the pH, availability of specific reactive mineral surfaces, oxygen content in the glacial melt water, and rock matrix transport resistance are presented for both the analytical and the numerical models. In the numerical calculations, the effect of O_2 consuming reactions with reducing fracture infillings is also evaluated.

The results from the oxygen ingress models in this report are presented, or can easily be expressed, as the oxygen concentration as a function of the flow-related transport resistance (F-factor) of the recharge flow paths. This allows for the coupling of the oxygen ingress models with available results from hydrogeological models that include calculated F-factors along recharge flow paths under different static conditions. In this report, recharge flow path F-factors are used for stationary "snap-shots" of unfavourable glacial situations at Forsmark, where the ice front is assumed to halt over the repository footprint. These situations were chosen to represent flow conditions that are realistic but unlikely to persist over long times. A halting ice front may remain stationary for up to 1,000 years, but the probability for this to occur in an unfavourable position over the repository footprint is very low.

The results show that the worst of the glacial situations (ice location III, without permafrost) would expose 25 canister positions for oxygen at a concentration of 3 μM or higher. Out of these 25 positions, 14 canister positions would be exposed to a concentration of 0.3 mM or higher.

With a small displacement of the ice front margin (ice location II, without permafrost), six canister positions would be exposed to an oxygen concentration exceeding 3 μM and none of these positions would be exposed to a concentration of 0.3 mM or higher. It is noted that the small ice front margin displacement changes the flow field considerably so that all of the affected canister positions differ between ice location II and III.

It should be emphasised that with an intact bentonite buffer in the deposition holes, the oxygen concentration reaching the surface of the copper canisters would be lower. Furthermore, these results are valid at pH 8, neglecting microbial O_2 consuming reactions as well as reactions with reducing minerals, and for an oxygen recharge concentration in the glacial melt water of 1.5 mM. This high recharge concentration is pessimistically chosen based on theoretical constraints and not on sampled oxygen content in present-day glaciers.

Assuming a lower melt water recharge oxygen concentration of 0.3 mM, 11 canister positions would be exposed to a concentration of 3 μM or higher for ice location III. None of the canister positions would be exposed to this concentration or higher for ice location II.

From the model results in this report, the possibility that oxygen may reach a few canister positions in the repository can not be excluded if the ice front margin would remain stationary in the most unfavourable position. This pessimistic situation is however deemed to be highly unlikely to persist over long times.

The absence of observations of a redox transition zone in the bedrock at Forsmark as well as the scarce indications of historical redox changes (a few possible mineralogical alterations in the upper 200 metres of the bedrock) strengthen the conclusion that the models developed are pessimistic with respect to the extent of oxygen ingress along flow paths at Forsmark.

Sammanfattning

Denna rapport avser att uppskatta förutsättningarna för att syre transporteras med glacialt smältvatten till kapselpositioner i ett slutförvar för använt kärnbränsle vid den föreslagna platsen i Forsmark.

Förutsättningarna uppskattas genom att kombinera modellering av reaktiva transportprocesser med geologiska observationer som kan antyda pågående eller tidigare perioder av syreinträngning. Med föresatsen att använda modellerade uppskattningar av omfattningen av syreinträngning i en säkerhetsanalys, är en pessimistisk hållning nödvändig. I denna rapport har försiktighet iakttagits både vid bedömningen av vilka processer som studeras och vid valet av de parametervärden som används i modelleringen. Syreförbrukande processer har undantagits från modelleringen enbart om dessa kan förväntas ytterligare reducera inträngningen av syre.

Ett flertal processer som förbrukar syre har identifierats, vilka alla kan spela en viktig roll i förbrukningen av syre längs flödesvägar i berget. Bland dessa processer finns biologisk nedbrytning av organiskt material från markytan samt mikrobiella reaktioner med reducerade mineral och diverse material som förväntas finnas tillgängligt i det återfyllda förvaret. De flesta av dessa processer kan också ske abiotiskt i frånvaro av mikrober.

Observationer som gjorts visar att nedbrytningen av organiskt material är den viktigaste syreförbrukande processen under nu rådande förhållanden. Syre förbrukas normalt inom några meters djup från markytan vid nutida tempererade förhållanden. Även om biologisk aktivitet är trolig också under olika glaciala faser så finns stora osäkerheter rörande exempelvis den dynamiska populationstillväxten, biotiska reaktionshastigheter och tillgängligheten av organiskt material under de kraftigt varierande förhållanden som kan förväntas. Mikrobiell aktivitet och nedbrytning av organiskt material försummas därför i beräkningarna i denna rapport av försiktighetsskäl.

I frånvaro av organiskt material utgör tvåvärt järn i bergmatrisens mineral den största källan till reduktionskapacitet. Tvåvärt järn ingår i olika reducerade mineral, där biotit och klorit är de vanligast förekommande. Upplösningshastigheten av tvåvärt järn från biotit är långsammare än från de flesta andra beaktade järnmineral. Av försiktighetsskäl antas därför allt tvåvärt järn i matrisen vara bundet i biotit, som modellsubstans, och upplösningshastigheten beräknas baserat på detta antagande. Oxidationen av det tvåvärda järnet i matrisen antas ske i två på varandra följande steg; upplösning av järnet från mineralgittret till porvattnet följt av oxidation av de upplösta järnjonerna med syre. Direkt oxidation av tvåvärt järn på plats i mineralgittret approximeras alltså pessimistiskt också av dessa två kopplade processer.

För korta tider är reducerade mineral i den del av den ostörda matrisen som är direkt exponerad för det flödande vattnet lätt tillgängligt från flödesvägar i sprickorna. Under dessa omständigheter bestäms syreinträngningen längs med flödesvägen av relationen mellan flödeshastigheten och reaktionshastigheten för den syreförbrukande reaktionen. Så småningom blir reduktionskapaciteten nära sprickan utarmad, och återstående tvåvärt järnmineral kan enbart nås genom diffusion i den porösa matrisen. Diffusionsmotståndet ökar med tiden allteftersom reduktionskapaciteten utarmas längre in i matrisen. Hastigheten för den syreförbrukande reaktionen begränsas då av diffusionsmotståndet och syreinträngningen längs med flödesvägen bestäms av relationen mellan flödeshastigheten och matrisdiffusionshastigheten. Dessa båda situationer representeras i denna rapport av två olika analytiska modeller. Fallet då reaktionskinetiken initialt begränsar syreförbrukningen analyseras dessutom numeriskt med de geokemiska simuleringsverktygen PHREEQC och PHAST.

Känslighetsanalyser för viktiga parametrar såsom pH, tillgängligheten av reaktiva mineralytor, syrehalt i det glaciala smältvattnet och transportmotståndet i matrisen redovisas både för de analytiska och de numeriska modellerna. I de numeriska beräkningarna utvärderas även effekten av syreförbrukande reaktioner med reducerade sprickfyllnadsmineral.

Resultaten från syreinträngningsmodellerna i denna rapport redovisas, eller kan enkelt uttryckas som syrehalt som funktion av det flödesrelaterade transportmotståndet (F-faktorn) för flödesvägarna. Detta möjliggör att resultaten från syreinträngningsmodellerna kan relateras till resultat från hydrogeologiska flödesmodeller som inkluderar F-faktorer längs med flödesvägar för olika statiska förhållanden. I denna rapport har beräknade F-faktorer för flödesvägar under stationära glaciala situationer använts där isfronten antas avstanna i ogynnsamma lägen rakt över förvarsvolymen i Forsmark. Dessa situationer representerar realistiska flödesförhållanden men förväntas inte fortgå under långa perioder. En avstannande glacial isfront kan förbli stationär upp till 1 000 år men sannolikheten för att detta skall ske i en ogynnsam position över förvarsvolymen är mycket liten.

Resultaten visar att 25 kapselpositioner skulle exponeras för syre med en koncentration som överstiger 3 μM för den mest ogynnsamma glaciala situationen (isläge III utan permafrost). Av dessa 25 positioner skulle 14 kapselpositioner exponeras för en syrekoncentration som överstiger 0.3 mM.

En liten förflyttning av isfronten (isläge II utan permafrost) resulterar i att sex positioner exponeras för en syrekoncentration som överstiger 3 μM och ingen av dessa positioner skulle exponeras för en koncentration som överstiger 3 mM. Värt att notera är att en liten förflyttning av isfrontens läge ändrar flödesfältet avsevärt så att alla påverkade kapselpositioner är olika för isläge II och III.

Det bör betonas att med en intakt bentonitbuffert i deponeringshålen skulle syrekoncentrationen som når kopparkapslarnas yta bli lägre. Dessutom gäller dessa resultat för pH 8 där både mikrobiella syreförbrukande reaktioner och reaktioner med reducerade sprickfyllnadsmineral har undantagits samt en syrehalt i det glaciala smältvattnet på 1.5 mM. Denna höga koncentration är pessimistisk och vald baserad på teoretiska begränsningar och inte på uppmätta halter i nutida glaciärer.

Med en lägre syrehalt i smältvattnet på 0.3 mM skulle 11 kapselpositioner exponeras för en koncentration som överstiger 3 μM för isläge III. Ingen av kapselpositionerna skulle exponeras för denna koncentration eller högre för isläge II.

Förutsättningen för att syre kan nå några kapselpositioner i förvaret kan inte uteslutas baserat på modellresultaten i denna rapport, under förutsättning att isfronten avstannar i den mest ofördelaktiga positionen. Att en sådan situation skall bestå under långa tidsperioder bedöms emellertid mycket osannolikt.

Det faktum att observationer av en redox övergångszon saknas i Forsmark och att endast sällsynta indikationer på tidigare förändringar i redox har observerats (några få möjliga mineralogiska förändringar i de övre 200 metrarna av berget) stärker slutsatsen att de utvecklade modellerna är pessimistiska vad gäller inträngning av syre längs flödesvägar i Forsmark.

Contents

1 Introduction

1.1 Background

Plans are advanced for the construction of a deep geological repository for high-level radioactive nuclear waste at Forsmark on the east coast of Sweden. According to the proposed method, the waste is encapsulated in copper canisters that are placed in excavated deposition holes surrounded by engineered barriers including low permeability bentonite clay at some 500 metres depth in granitic rock.

The redox evolution in the deep subsurface rock at Forsmark over the lifetime of the repository is an important issue in the safety assessment of this underground facility. The copper canisters corrode extremely slowly in the prevailing reducing ground waters at these depths. However, it is important to understand and quantify the processes that produce, scavenge and transport any oxidants to the repository, since the corrosion of the copper canisters is much faster in an oxidising environment compared to reducing conditions. Furthermore, a breached canister would expose the spent fuel, which consists of 95% uranium dioxide with embedded highly active radionuclides, to the oxidising water. Oxidising conditions strongly increases the solubility of the uranium oxide and many of the embedded nuclides. In addition, leached nuclides dissolved in the seeping water are less strongly retarded by sorption processes in an oxidising environment compared to reducing conditions.

The only important oxidant of concern in this context is molecular oxygen that dissolves in water exposed to the atmosphere at the ground surface and may be transported with the groundwater through fractures in the rock. The understanding of oxygen consuming processes, such as the oxidation of reducing minerals that occur in the rock, is therefore of main interest in this report.

Microbially mediated degradation of organic matter close to the ground surface is the most potent oxygen consuming process. At present day temperate conditions, traces of oxygen in Forsmark are rarely found deeper than a few metres from the surface. This can be attributed to microbial activity in the top soil and upper rock layers, as will be discussed in this report. Deeper in the rock, in the absence of easily degradable organic substances, other reductants such as reducing minerals present in the rock may become important for the consumption of oxygen.

The geochemical evolution of groundwaters is very complex, influenced by temporal and spatial variations in various geochemical parameters such as groundwater pH, redox condition, carbon dioxide concentration, ionic strength, colloid content, organic and inorganic ligands, groundwater speciation, mineralogical composition at the water-rock interface and structure of the groundwater flow paths /Savage et al. 1999/.

Although many of these parameters can be described and understood qualitatively, predicting the evolution over large temporal and spatial scales is very complex. Processes that would have to be considered in an “ideal” model capable of dealing with all relevant transport and reaction processes simultaneously have been suggested /MacQuarrie and Mayer 2005/. These include transient boundary conditions for recharge rates, hydraulic heads and composition of the recharge waters due to climate changes, a number of geochemical reactions including abiotic and microbially mediated redox reactions, mineral dissolution-precipitation reactions, aqueous complexation and hydrolysis, activity corrections and ion-exchange. The “ideal” model formulation also needs to be able to adequately describe reactive transport in a dual-porosity system, subject to fracture-matrix interactions, reaction-induced porosity and permeability changes in the fractures and in the matrix. In addition, the model should be able to simultaneously deal with extreme variations in temporal and spatial scales, with times more than 100,000 years and spatial scales along flow-paths of hundreds to thousands of metres and in the matrix of a few centimetres.

The “ideal” model as suggested in /MacQuarrie and Mayer 2005/ does not exist at present time, but efforts are being made to include many of the desired properties in existing models. It should be recognised however, that implications of uncertainties regarding input parameters increases with increasing complexity of the models. Furthermore, the results from models incorporating many complex interactions between different processes may be difficult to interpret. Justifiable simplifications in the conceptualisation are therefore desirable in order to limit the sensitivity of parameter uncertainties and to increase the transparency of the model results.

Some of the more widely used numerical codes for studying oxygen ingress in fractures in the rock are reviewed in Section 7.1 in the present report. It can be concluded that many of these numerical multi-component reactive transport codes share the limitation that they are computationally demanding.

Fractures in the rock often contain reducing mineral infill or coatings lining the fracture surfaces. These minerals are easily accessible for the flowing water in the fractures. Redox changes in recharge-discharge environments on the Canadian Shield were found to be largely related to this interaction /Gascoyne 1997/. The flowing water however, tends to be directed to fractures or parts of fractures with less infillings /Gascoyne 1999/. Furthermore, the interaction with reducing minerals lining the fracture surfaces is expected to cease with time when these minerals become depleted.

Deep in the bedrock, the main reservoir of reducing capacity occurs as minerals inside the rock matrix, adjacent to the fractures. These minerals are not as easily accessible as the fracture infilling minerals. However, micro-fractures and void spaces between mineral grains in the rock matrix are connected in a porous network that allows for diffusive transport of dissolved species. In the saturated zone, below the groundwater table, the reducing capacity in the matrix can thus be accessed from flow paths in the fractures by diffusion and considerably contribute to the scavenging of oxygen.

In addition to processes consuming oxygen, the transport of O_2 down to the repository must be considered. In areas with cyclic periods of glaciation, such as the Forsmark area in Sweden, great variations in hydraulic conditions are expected. When the ice front margin passes over the repository volume, increased hydraulic head gradients are likely to occur, resulting in higher groundwater recharge flow rates. The extent of such increased flow-rates under different glacial conditions is estimated with hydrogeological models.

1.2 Aim and scope

The aim of this report is to evaluate the potential for oxygen to reach the copper canisters in a repository at Forsmark during a glaciation cycle.

Observations made at the Forsmark site provide the means to evaluate the general extent of present day and historical oxygen ingress. However, the groundwater flow field in the sparsely fractured rocks in Forsmark is highly heterogeneous. It is therefore difficult to exclude the possibility of deeper ingress of oxygen along yet unnoticed fast flowing channels solely from observations.

Reactive transport modelling provides additional means to study the oxygen ingress along flow paths in the rock. It should be emphasised that the modelling efforts in this report aim at predicting the possible extent of oxygen ingress with a conservatively chosen set of parameters. The results from the models are generalised to allow a comparison with hydraulic modelling results that are available for the Forsmark site. The reactive transport modelling results combined with the hydraulic modelling results may then be used to evaluate the possible extent of oxygen ingress in recharge flow paths.

1.3 Structure of the report

In Section 2 in the report, the processes deemed to have major influence on the extent of oxygen intrusion are described. The section is divided in to four subsections.

In Section 3 important observations of the extent of oxygen intrusion are presented. This section includes observations made on a regional scale as well as on a mineral grain size scale.

The processes that are deemed to be of importance in Section 2, and the information obtained from the observations are compiled into a conceptualisation of the oxygen scavenging process presented in Section 4.

Section 5 is devoted to summarising the data available that may be used in the development of models that are able to predict the extent of oxygen intrusion.

In Section 6, two analytical models are developed that are based on the problem conceptualisation in Section 4 and the data available in Section 5. In the first approach, the extent of oxygen ingress is evaluated analytically assuming that diffusion in the pores of the matrix limits the oxidation of ferrous minerals in the rock matrix. In the second approach, reaction kinetics is included, some simplifying assumptions are introduced and the extent of oxygen ingress is calculated analytically. The generic solutions from these two approaches are valid at different time scales as the process transitions from initially being controlled by chemical reaction kinetics to being limited by matrix diffusion at longer times. This section also includes uncertainty analyses of sensitive parameters.

Section 7 includes a numerical evaluation of the extent of oxygen ingress when chemical reaction kinetics limits the scavenging of oxygen. The problem definition is identical to the one in Section 6 but without the simplifications underlying the analytical solution.

The generic solutions obtained in Sections 6 and 7 are applied to hydrogeological conditions at the Forsmark site for different glaciation situations as obtained from hydrogeological modelling. The applied results for oxygen ingress under these conditions are evaluated in Section 8.

The main findings are discussed and final conclusions are drawn in Section 9.

2 Description of relevant processes

2.1 Transport processes

2.1.1 Advective transport along flowpaths

Groundwater transport is dominated by advection in fast flowing channels in fractures and fracture zones in the rock. In this section some of the important hydraulic parameters and their relation to each other are discussed. In particular, the difference between single fracture and fracture network approaches is presented. Also, the effect of any fracture infill on the hydraulic properties is discussed. The relations given in this section are valuable tools for the interpretation of results for different rock types and domains. Also, they give insights in the development of preferential flow paths in channels in the rock.

Two distinct flow modes can be observed in groundwater transport through channels in the rock. In a heterogeneous rock domain, comprising one or a few highly transmissive fractures and several less transmissive ones, the flow tend to be directed to those with high transmissivities. In rock domains with such properties it is reasonable to model the single fracture carrying most of the flow. This is referred to in this report as the single fracture approach. In a homogeneous rock domain, with randomly distributed fractures with similar transmissivities, the flow tends to be distributed evenly between the channels. In such rock domains, with no specific preferential flow path, the system may be better described by a connected fracture network approach. These two distinct flow modes may be considered as end-members of different flow patterns in fractured rocks. In most cases a mix of the two is probably most likely.

The single fracture and fracture network approach are treated somewhat differently in hydraulic calculations. However, in both flow modes it is found that the magnitude of the surface in contact with the flowing water, A_Q, also referred to as the flow-wetted surface, has a dominating influence on the amount of minerals that can be accessed for reaction. The ratio between the flow-wetted surface and the water flow-rate, A_Q/Q_{flow}, sometimes referred to as the F-factor, determines the interaction with minerals on the fracture surface and in the matrix.

The relation between these two flow modes and the parameters used for each case are summarised in Eqns. 2-1 to 2-6.

In Eqns. 2-1 through 2-6, T is the fracture transmissivity, i is the hydraulic gradient, K is the mean hydraulic conductivity of the rock, and a_R is the specific surface area per volume of rock, Q_{flow} is the volumetric flow-rate, A_Q is the flow-wetted surface. The parameters L, W, and h are illustrated in Figure 2-1 and Figure 2-2.

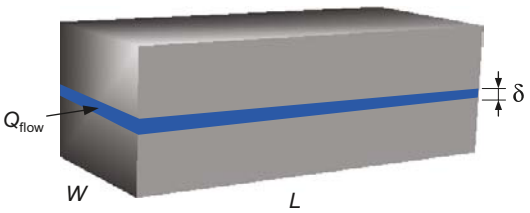

Figure 2-1. *Rock domain with a single conductive fracture.*

$$Q_{flow} = TiW \quad (2\text{-}1)$$

$$A_Q = 2LW \quad (2\text{-}2)$$

$$\frac{A_Q}{Q_{flow}} = \frac{2L}{Ti} \quad (2\text{-}3)$$

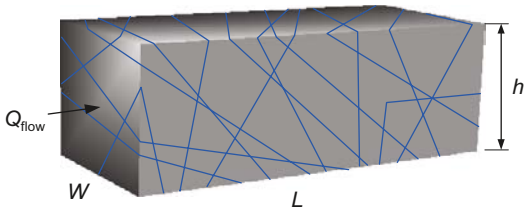

Figure 2-2. *Rock domain with a fracture network.*

$$Q_{flow} = KiWh \quad \text{2-4}$$

$$A_Q = LWha_R \quad \text{2-5}$$

$$\frac{A_Q}{Q_{flow}} = \frac{a_R L}{Ki} \quad \text{2-6}$$

The product of the fracture transmissivity and the hydraulic gradient equals that of the water velocity and fracture aperture, $Ti = v\delta$. The penetration distance downstream along the flow path, L, is equal for the two cases if the transmissivity equals the conductivity times two divided by the specific surface area of the rock, $T = 2K / a_R$.

The specific fracture surface area of the rock a_R, can be estimated from frequently measured entities in bore-core analyses; the flowing fracture frequency, f_f [m^{-1}], or the mean distance between fractures, S_f [m] /Gylling et al. 1998, SKB 2004/:

Parallel fractures: $$a_R\ [m^2\ m^{-3}] = 2f_f = \frac{2}{S_f} \quad \text{2-7}$$

Random fractures in network: $$a_R\ [m^2\ m^{-3}] = 4f_f = \frac{4}{S_f} \quad \text{2-8}$$

Dissolved species in the flowing water may interact with the surfaces in the adjacent rock matrix. This is the case for dissolved oxygen in the flowing water reacting with reducing minerals in the rock matrix, and also for e.g. sorption of dissolved radionuclides onto mineral surfaces. The flow-wetted surface to flowrate ratio (Eqn. 2-3 for a single flowpath and Eqn. 2-6 for a channel network) is an important parameter that is used to quantify the extent of interaction between dissolved species in the flowing water and the rock matrix. This parameter is often referred to as the flow-related transport resistance or F-factor.

Channeling effects

As mentioned previously, groundwater tends to flow through channels with a relatively low resistance resulting in a heterogeneous flow-field. This diversion of the flow into preferential flow paths is generally referred to as channelling. Six principal types of flow channelling were identified as having relevance for the bedrock transport evaluation within the Site Descriptive Modelling, SDM-Site /Crawford 2008/:

1. Network-scale flow channelling.
2. In-plane flow channelling.
3. Flow channelling at fracture intersections.
4. Flow channelling at geological interfaces.
5. Flow channelling within foliations.
6. Flow channelling within fault stepovers, shears and fracture jogs.

In the SDM-Site bedrock transport properties report /Crawford 2008/, these and other more exotic channelling phenomena are described in detail and how they may influence the flow properties at the Forsmark site.

The network-scale flow channelling effects refer to the diversion of the flow into e.g. conductive fractures and deformation zones. Depending on the presence of such preferential flow paths, either a single fracture or a fracture network approach may be best suited for describing the interaction between the groundwater and the minerals with which it comes into contact.

The in-plane flow channelling effects refers to diversion of the flow within a single fracture. This is due to the variability in fracture aperture referred to as constrictivity, resulting in a heterogeneous transmissivity field across the fracture plane. Thus, a few flow channels in the fracture plane carry most of the flow in that fracture. The remaining zones in the fracture plane are either completely closed, i.e. the upper and lower fracture surfaces are in contact, or open comprising stagnant water. This stagnant water is accessible from the main flow channels by diffusion.

Justified by appealing to arguments of conservatism, in-plane flow channelling effects were handled in SR-Can by reducing F-factors for the flow paths used in modelling by a factor of ten. This is illustrated in Figure 2-3a and b, where only 10% of the fracture plane carries the flow in that fracture. Since diffusion in the stagnant water is slow compared to the flowing water in the channel, the F-factor correction may be valid for very early breakthrough. With time, a concentration profile in the stagnant zone develops thus increasing the interaction surface between the dissolved species and the rock matrix. Therefore, the F-factor correction may be valid for very early breakthrough, but underestimates the interaction between dissolved species and minerals in the rock matrix for longer times. The time span for this early breakthrough depends on the interfacial area between the zones with flowing and stagnant water. As can be seen from Figure 2-3a and b, this area increases with increasing channelling.

In Appendix A in the **Radionuclide transport report**, a re-evaluation of the effect of in-plane flow channelling indicates that the F-factor correction used in SR-Can is over-conservative. This is argued for mainly based on the process of diffusion into stagnant water adjacent to flowing channels, which was not accounted for in SR-Can. The correction factor is therefore abandoned in the oxygen intrusion and radionuclide migration modelling for SR-Site.

Infill material in fractures may contribute to the reducing capacity of the fracture. However, the flow is restrained by the presence of such infill, due to in-plane channelling effects. This means that although infill particles contribute to the reducing capacity, their exposure to the flowing water in the fracture may be limited.

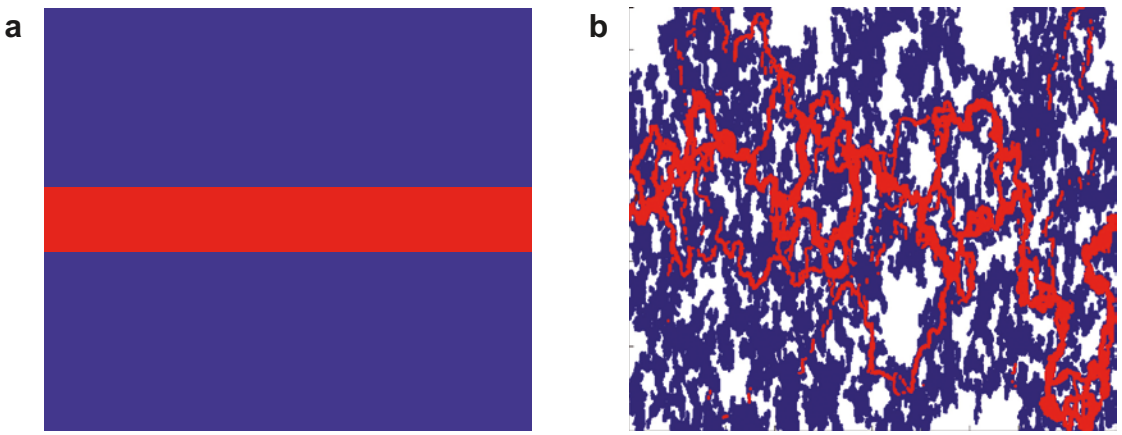

Figure 2-3. *Example of the effect of in-plane flow channelling for a fracture plane seen from above, (a) an idealised case with limited interfacial area between the main flow channel (red) and a zone with stagnant water (blue), (b) a more realistic case with a much larger interfacial area between the flowing (red) and stagnant (blue) water and areas where the fracture surfaces are in contact, i.e. no water (white). Picture in (b) is modified from Appendix A in the* ***Radionuclide transport report*** *for SR-Site.*

2.1.2 Diffusive transport in porous media

In a porous material, such as the rock matrix, solutes may be transported through a system of interconnected micro-pores. Transport in the pore system occurs mainly as molecular diffusion in the pore water. In a one-dimensional non-stationary system, where the diffusing solutes are accumulated or depleted, Fick's second law describes the accumulation and transport in a liquid in the x-direction according to:

$$\frac{\partial c}{\partial t} = D\frac{\partial^2 c}{\partial x^2} \qquad 2\text{-}9$$

If the system can be regarded as being stationary, i.e. the concentration profile in the medium does not change with time, Fick's first law of diffusion in a liquid applies describing the flux J in the x-direction according to:

$$J = -D\frac{dc}{dx} \qquad 2\text{-}10$$

In this report, matrix diffusion is frequently regarded as a pseudo-stationary process using Fick's first law of diffusion. The pseudo-stationary approximation implies that any change in solute concentrations in the pore water are assumed to be slow compared to the transport rate. Thus, a time dependent problem may be solved as a series of stationary-state problems. This approximation is applied in the analytical evaluation in Section 6.2.

Fick's first and second laws describe diffusion in a homogeneous medium, such as a liquid. In heterogeneous porous media, the diffusion path is longer than the free diffusion in a liquid, due to the tortuosity τ^2, of the pores. The diffusion is also affected by changes in pore size along the diffusion path, known as constrictivity δ_D. The pore diffusivity D_p, is therefore less than that in a pure liquid:

$$D_p = D\frac{\delta_D}{\tau^2} \qquad 2\text{-}11$$

The effective diffusivity, which is frequently used in the models in this report, also takes into account the transport porosity of the rock matrix $ø_m$, which refers to the pores where transport occurs and excludes pores with dead ends. The effective diffusivity is therefore less than the pore diffusivity and can be written:

$$D_e = D_p ø_m \qquad 2\text{-}12$$

The stationary diffusive flux of a solute in a porous medium can then be written as:

$$J = -D_e\frac{dc}{dx} \qquad 2\text{-}13$$

2.1.3 Summary

The relations in this section are important for the understanding of groundwater flow and transport of dissolved species in heterogeneous media such as fractured crystalline rocks. The principles described here form the basis for the development of the analytical and numerical codes that are described in Sections 6 and 7. The interaction between the flowing water in fractures and the stationary water in the porous rock matrix is quantified by the ratio between the flow-wetted surface and the flow-rate in the flow channel. This is an important entity and is also known as the flow related transport resistance or F-factor and is referred to frequently in the modelling sections in this report. Network scale flow channelling is included in the hydrogeochemical modelling, briefly described in Section 8.1. In-plane flow channelling is considered based on recent re-evaluation of the channelling effects when also diffusion into parts of fractures with stagnant water adjacent to the flow channels is included. This section also includes a brief description of fundamental principles of diffusion of dissolved species in porous media such as the rock matrix.

2.2 Abiotic processes

In this section chemical reactions between dissolved oxygen in the groundwater and some important reducing minerals in the rock are discussed. The minerals deemed most important for the topic of the report are chlorite, biotite and pyrite. These are the ones shown to contribute the most to the reducing capacity (ferrous iron) of the rock in the absence of organic material. Amounts and properties of these minerals are further discussed in Sections 5.4 and 5.5. Rate expressions are presented when found in the literature. For reactions not thoroughly studied in the open literature, derivations and approximations of rate expressions needed for the models are also presented and discussed. The rates of the reactions presented here have implications on the rate of depletion of reducing minerals and the extent of oxidant intrusion downstream in a flow path when transport resistance can be neglected. For cases when the chemical reactions are limited by transport of reactants or reaction products, the reaction rates presented here are of limited importance. The chemical reactions presented here may also proceed though biological pathways mediated by microbes when the growth of appropriate cultures is permitted. These biological pathways are further discussed in Section 2.3. The distinction between homogenous and heterogeneous reactions should also be noted. Heterogeneous reactions occur at the interface between two phases, such as pore water and solid mineral surfaces, whereas homogeneous reactions occur in one phase only, such as the reaction between two species dissolved in water.

2.2.1 Biotite/Chlorite

The chemical formulae of biotite and chlorite can be written:

Biotite $K(Mg,Fe)_3A1Si_3O_{10}(OH)_2$ 2-14

Chlorite $(Mg,Fe^{2+},Fe^{3+},A1)_3(Si,A1)_4O_{10}(OH)_2$ 2-15

The relative amounts of the framework ions Fe, Mg, etc varies, which is indicated by the comma separated species embraced by parentheses in the formulae above. Biotite has usually been hydrothermally transformed into chlorite in and adjacent to fractures, but essentially retained its ferrous iron content. Therefore, chlorite occurs mainly close to fractures whereas biotite is mainly found inside the rock matrix. These aspects are further discussed in Section 5.4.

The oxidation reaction of biotite and chlorite with oxygen is assumed to occur in two consecutive steps. Heterogeneous non-oxidative dissolution of the framework ions is followed by homogeneous oxidation of dissolved ferrous ions with oxygen in the water. Hence, also the reaction between oxygen and ferrous iron that may occur directly in the mineral grain lattice is approximated by these two coupled processes.

Different aspects of non-oxidative dissolution of biotite and chlorite have been studied in the literature. These aspects include time-dependence (e.g. /White and Brantley 2003/ and references therein), pH (e.g. /Malmström et al. 1996, Kalinowski and Schweda 1996, Malmström and Banwart 1997/). Uncertainties in specific dissolution rates appear to be strongly related to the evaluation of available reactive surface areas, although other time-dependent effects may also have some influence on weathering of the silicates, such as formation of secondary precipitates. The difference in lab and in situ weathering rates discussed in /White and Brantley 2003/ also appears to be related to chemical affinity, which in situ is close to equilibrium. A decreasing specific dissolution rate with time appears to be strongly related to the evaluation of the reactive surfaces. The influence of dissolved oxygen in the leaching solution has also been studied /Sugimori et al. 2009/, where a slightly lower biotite dissolution rate was found under oxic conditions compared to low oxygen concentrations at pH 6.86. The experiment using atmospheric oxygen content showed an apparent 1.5 orders of magnitude lower dissolution rate for ferrous iron, a decrease attributed to extensive amounts of ferric iron precipitates under oxic conditions during the experiment.

In most of the laboratory experiments listed in /White and Brantley 2003/, flow-through reactors were used to study the weathering rates for biotite. During these experiments the leachate is continuously carried away so that the obtained dissolution rates may be considered as near maximum at the given conditions. In /Malmström et al. 1996, Malmström and Banwart 1997/, modelling indicates that stoichiometric dissolution is reached after ~50 years of leaching, which in the time scales of interest in this report may be regarded as short. The maximum ferrous ion release rate (depending on pH at an ambient ferrous ion concentration $c_{Fe} = 0$) is taken to be /Malmström and Banwart 1997/:

$$k_{Fe,diss}[\text{mol m}^{-2}\ \text{s}^{-1}] = 10^{-8.66} c_{H^+}^{0.51} + 10^{-18.92} c_{H^+}^{-0.81} \qquad 2\text{-}16$$

which becomes:

$$k_{Fe,diss}[\text{mol m}^{-2}\ \text{s}^{-1}] = 6.5 \cdot 10^{-13} \quad \text{(at pH 7)} \qquad 2\text{-}17$$

$$k_{Fe,diss}[\text{mol m}^{-2}\ \text{s}^{-1}] = 5.5 \cdot 10^{-13} \quad \text{(at pH 8)} \qquad 2\text{-}18$$

There are indications in /Malmström et al. 1996/ that the initial release rate of ferrous ions from chlorite may be slightly higher than for biotite. This difference is however neglected in this report, and thus the ferrous ion release rate from biotite and chlorite is assumed to be equal.

Taking $k_{Fe,diss}$ defined in Eqn. 2-16 as the maximum release rate of ferrous ions to the solution, and assuming a first order dissolution rate with respect to dissolved ferrous ions, a rate-law accounting for chemical affinity can be approximated:

$$r_{diss}[\text{mol}_{Fe}\ \text{m}^{-2}\ \text{s}^{-1}] = k_{Fe,diss}\left(1 - \frac{c_{Fe}}{c_{Fe,sol}}\right) \qquad 2\text{-}19$$

According to the rate-law specified in Eqn. 2-19, the maximum release rate occurs when the ambient solution contains no dissolved ferrous ions ($c_{Fe} = 0$). The rate decreases linearly towards zero as the ambient dissolved ferrous ion concentration increases and approaches the solubility limit.

For a heterogeneous surface reaction, the amount of available specific reactive surface of the reducing minerals per volume of pore water A/V is needed for estimating the rate of oxygen consumption in a volume of rock. This parameter is difficult to assess and for this reason Section 5.5 is dedicated to the estimation of reactive surface areas for biotite based on samples from boreholes in Forsmark. The volumetric dissolution can then be written:

$$R_{diss}[\text{mol}_{Fe}\ \text{L}_{water}^{-1}\ \text{s}^{-1}] = k_{Fe,diss}\frac{A_{react}}{V_{water}}\left(1 - \frac{c_{Fe}}{c_{Fe,sol}}\right) \qquad 2\text{-}20$$

See Section 5.5 for the estimation of A_{react} / V_{water} for biotite at Forsmark.

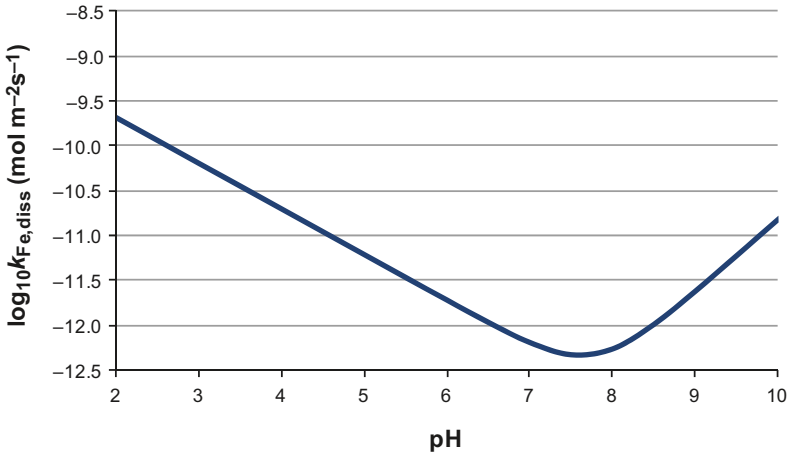

Figure 2-4. *Maximum release rate of ferrous ions by non-oxidative dissolution of biotite/chlorite as a function of pH.*

2.2.2 Pyrite

Non-oxidative dissolution of pyrite is sparingly reported in the literature. One reason could be that this process would require the formation of persulphide ions, S_2^{2-}, and the hydride, hydrogen persulphide, H_2S_2 /Lowson 1982/. These species, and also higher members of the polysulphide series, have a great tendency to decompose and release sulphur. For most practical purposes, the dissolution is therefore considered exclusively oxidative.

Oxidative dissolution of pyrite in the subsurface occurs by two different reaction paths, either with oxygen or ferric ions as the oxidant:

$$FeS_2 + H_2O + 3.5O_2 \rightarrow Fe^{2+} + 2SO_4^{2-} + 2H^+ \quad 2\text{-}21$$

$$FeS_2 + 8H_2O + 14Fe^{3+} \rightarrow 15Fe^{2+} + 2SO_4^{2-} + 16H^+ \quad 2\text{-}22$$

In the presence of oxygen the produced ferrous ions are oxidised by the oxygen (see Section 2.2.3). The resulting overall oxidation reaction is then:

$$FeS_2 + 3.75O_2 + 0.5H_2O \rightarrow Fe^{3+} + 2SO_4^{2-} + H^+ \quad 2\text{-}23$$

or with the consecutive precipitation of ferric hydroxide:

$$FeS_2 + 3.75O_2 + 3.5H_2O \rightarrow Fe(OH)_{3(a)} + 2SO_4^{2-} + 4H^+ \quad 2\text{-}24$$

A rate expression valid for pH 2–10 and widely used in the literature for oxidation of pyrite by oxygen is /Williamson and Rimstidt 1994/:

$$r_{Fe}[\mathrm{mol_{Fe}\ m^{-2}\ s^{-1}}] = 10^{-8.19} c_{O_2}^{0.5} c_{H^+}^{-0.11} \quad 2\text{-}25$$

where the concentrations are given in units of mol kg^{-1}.

2.2.3 Dissolved ferrous ions

The homogeneous oxidation of dissolved ferrous ions by oxygen is assumed to proceed according to:

$$4Fe^{2+} + O_2 + 4H^+ \rightleftharpoons 4Fe^{3+} + 2H_2O \quad 2\text{-}26$$

A widely used rate law for this reaction can be written for pH > 4.5 /Stumm and Lee 1961/:

$$R_{ox}[\mathrm{mol_{Fe}\ L^{-1}\ s^{-1}}] = k_r c_{Fe} P_{O_2} c_{OH}^2 - \quad 2\text{-}27$$

where $k_r = 1.3 \cdot 10^{12}$ [M^{-2} $atm^{-1}s^{-1}$] at 25°C.

The partial pressure for oxygen may be calculated using Henry's law with dissolved concentration given in units of mol L^{-1}:

$$P_{O_2} = c_{O_2}/k_H^\circ \quad 2\text{-}28$$

where the Henry's law constant for oxygen is taken as $1.3 \cdot 10^{-3}$ mol_{O_2} $L^{-1}atm^{-1}$ /Lide and Frederikse 1995/.

The homogeneous oxidation rate is obviously strongly dependent on pH. The produced ferric ions are hydrolysed forming amorphous ferric hydroxide along with production of protons so that the overall reaction becomes:

$$Fe^{2+} + 0.25O_2 + 2.5H_2O \rightarrow Fe(OH)_{3(a)} + 2H^+ \quad 2\text{-}29$$

The natural groundwaters in Forsmark are usually close to neutral buffered by carbonates and silicates present in large amounts in the rock matrix. It is assumed that the protons produced by reaction 2-2 are neutralised by reaction with those buffering minerals, and that the water is thereby maintained at near neutral pH.

2.2.4 Summary

In this section, important reducing minerals present in the rock matrix at Forsmark are described and rate expressions for abiotic dissolution and reaction kinetics in the literature are evaluated. The rate expressions for the dissolution of ferrous iron from biotite and homogeneous oxidation of ferrous ions by oxygen are used in the model development and implemented in the analytical and numerical codes described in Sections 6 and 7.

2.3 Biological oxygen reduction processes

Biological processes have been ongoing on the Earth for at least four billion years. O_2 started to accumulate in the atmosphere about three billion years ago when the first cyanobacteria appeared. The first aerobic respiring microorganisms evolved for about 2.5 billion years ago and the red banded iron-ore formations developed around two billion years ago.

Biological energy metabolism requires a reduced energy rich electron donor and an oxidized electron acceptor. For plants and animals and many microorganisms the energy and electron donor is organic carbon and O_2 is the electron acceptor. O_2 is the electron acceptor with the highest E_h that is used by the living organisms and thus gives the highest energy yield of all used electron acceptors. Its oxidative reactivity initiates many microbially induced degradation pathways of recalcitrant compounds such as aromatic hydrocarbons. Microorganisms can use other electron acceptors and these processes are called anaerobic respirations.

Prior to the description of biological oxygen reduction processes in the subsurface environment in association with a repository, the possible reductants, the energy and electron sources, that can be used in biological oxygen reducing processes are presented. The reductants can be divided in two groups, organic and inorganic reductants, and the groups have different origin as discussed below.

2.3.1 Reductants in biological oxygen reduction

Organic material and its production – autotrophy

On the surface of our planet, autotrophic processes reduce CO_2 to organic carbon compounds via photosynthesis and chemosynthesis. Photosynthesis with oxygen production is mediated via cyanobacteria, algae and plants (Eqn. 2-30). The term autotrophy refers to the use of CO_2 as carbon source. The opposite is heterotrophy, the use of organic compounds as carbon source.

$$6CO_2 + 6H_2O + \text{light energy} \rightarrow C_6H_{12}O_6 + 6O_2 \qquad 2\text{-}30$$

There are also bacteria with photosynthetic metabolism using reduced sulphur compounds as electron donor but they do not produce O_2. Examples are purple sulphur bacteria and green sulphur bacteria. These organisms are found in anaerobic shallow parts of the sea close to the sea shore. Photosynthesis is ongoing in all environments where the light intensity is sufficient and where there is enough water present. For example there is an intense photosynthesis ongoing on glaciers and ice sheets during the summer period.

There are other autotrophic microorganisms, not using light energy, that produce organic material. Autotrophic methanogens and acetogens are two groups that use energy and electrons from H_2 oxidation to reduce CO_2 into methane and acetate, respectively. The chemical reactions of the processes are found in Eqns. 2-31 and 2-32.

$$4H_2 + CO_2 \rightarrow CH_4 + 2H_2O \qquad 2\text{-}31$$

$$2H_2 + 2CO_2 \rightarrow CH_3COOH \qquad 2\text{-}32$$

These are anaerobic processes and both autotrophic methanogens and acetogens have repetitively been cultivated from groundwater in Sweden and Finland down to 978 metres depth /Hallbeck and Pedersen 2008a, Pedersen et al. 2008/. The CH_4 and acetate can be used as reductants in aerobic respiration.

Other autotrophic groups of microorganisms are found among the iron-, manganese- , ammonia and sulphur oxidising bacteria. This group uses reduced inorganic compounds such as Fe^{2+}, Mn^{2+} and S^0 as energy and electron donors and often O_2 as electron acceptor. This group is called lithotrophic organisms are discussed in below in this report.

Inorganic reductants

There are several reduced inorganic chemical species that can be used as electron- and energy donors by aerobic organisms present in groundwater. From the point of decreasing energy yield in the oxidation with O_2 these are H_2, H_2S, Fe^{2+}, Mn^{2+}, NH_4^+ but also U(IV) and Cr(III) can be used as energy and electron donors. The origin of these reducing compounds is discussed in the section describing the O_2-reducing processes with inorganic reductants.

Biological O_2 reduction by degradation of organic material – chemoorganotrophy

The use of organic material as energy and electron donor is widespread in all phylogentic groups of life. It is used by both aerobic and anaerobic organisms. The oxidation of organic material coupled to reduction of O_2 is usually written:

$$C_6H_{12}O_6 + 6O_2 \rightarrow 6CO_2 + 6H_2O \qquad 2\text{-}33$$

The organic material is composed of cell material and the main polymeric organic compounds are proteins, lipids, nucleic acids and polysaccharides. Microorganisms excrete enzymes that cut the polymers into oligo- and monomers (see Figure 2-5) before the monomers enter the cells for total mineralisation to CO_2, H_2O, NH_4^+ SO_4^{2-} and PO_4^{3-}.

The input of organic material from the ground surface is the most important factor in the reduction of O_2 in recharging groundwater. In the temperate vegetation zone this input varies with seasonal cycles. Carbon dioxide is fixed into organic material mainly in summer. The organic material is continuously degraded (oxidised), under consumption (reduction), of oxygen over the year with peak activity during autumn and winter. When oxygen is depleted, anaerobic respiring microorganisms continue the process of degradation. Examples of anaerobic microorganisms in groundwater are nitrate-, iron-, manganese- and sulphate-reducers. The reduced compounds from their respiration will then act in the O_2-reduction as discussed below.

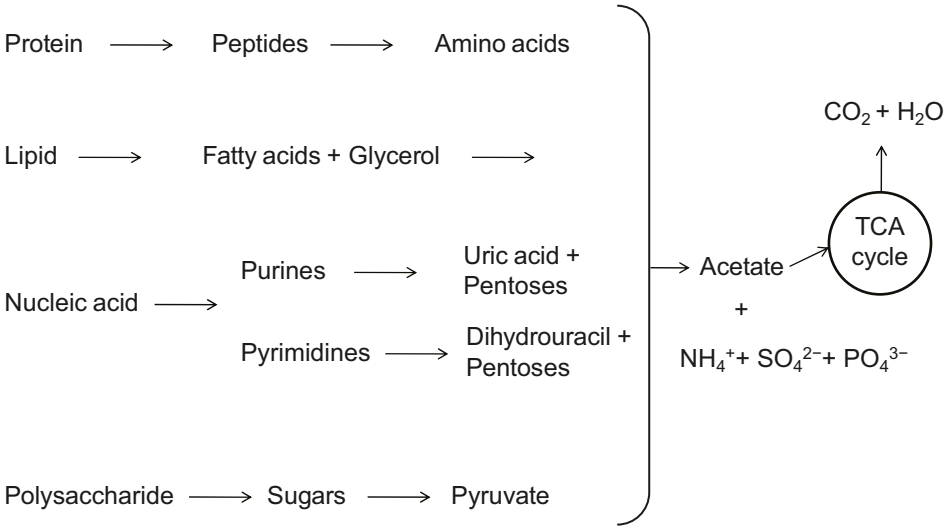

Figure 2-5. *Aerobic degradation of major cell components. The tricarboxylic acid (TCA) cycle is one of the key pathways in many degradation systems. From /Hallbeck 2010/.*

2.3.2 Description of the biological oxygen reducing processes

O_2 reduction by oxidation of organic matter – chemoorganotrophy

The degradation of organic material, produced by photosynthesis, starts as soon as the material has fallen to the soil surface. The main components of the organic matter are polymeric carbohydrates such as cellulose, lignin and starch. There are also cell constituents such as fat, protein and nucleic acids. The degradation starts with the degradation of the polymers into oligo-, di- and finally monomers; sugars, fatty acids, amino acids and nucleotides. The monomers are then degraded until mineralisation, to inorganic components, CO_2, NH_3, PO_4^{3-}, and SO_4^{2-}. The initial degradation process is performed by microorganisms such as fungi and bacteria. It is facilitated by fragmenting organisms such as worms and beetles but the actual mineralisation is done by microorganisms in the guts of these organisms. The term chemoorganotrophy refers to the chemical energy source, chemo-, and the organic source of electrons, organo-. Since the carbon source is organic the organisms are also heterotrophs.

Cellulose

Cellulose is the most abundant carbohydrate on Earth and it is composed of glucose molecules that are joined by a β-1,4-linkage. Decomposition of cellulose occurs by the concerted action of serveral enzymes: endo-β-1,4-glucanase, exo-β-1,4-glucanase and α,β-glucosidases. Many bacteria and fungi have these enzymes. The glucose molecules are then oxidised by almost all aerobic microorganisms via the glycolysis, the citric acid cycle with the final electron transport chain for ATP production.

Starch

Starch is composed of two distinct polymers, amylase and amylopectin. Enzymes involved in starch degradation are α- and β-amylase and amylo-1,6-glucosidase and the sugar monomers formed are maltose and glucose.

Other carbohydrates

Other carbohydrate polymers from plants are xylanes, glycogen, chitin and lignin. Of the polymers found in plants the lignin molecule is one of the most recalcitrant. It is also the most abundant renewable aromatic molecule on Earth. It is degraded by white rot fungi by random oxidative attack. It is thought that lignin is one of the original components in humus. The decomposition of lignin includes an oxidative attack by O_2. As there is a continuous supply of organic material to the surface, in the temperate areas during the productive months of the year, the oxygen is consumed by microorganisms degrading more easily degraded organic material. Due to this there will be a shortage of O_2 for the degradation of lignin. There are reports on anaerobic degradation of lignin in a sulphate-reducing environment /Dittmar and Lara 2001/.

Man made organic materials

In the repository there will be organic material during the construction phase and parts of those will be left at closure. Most of this material will be degraded by microorganisms such as fungi and bacteria especially as long as O_2 is available. Also after O_2 is consumed anaerobic degradation will continue and reduced electron acceptors be produced.

Reduction of O_2 by methane oxidation

CH_4 is a special organic compound since it is a gas. CH_4 can be oxidised with O_2 by certain micro-organisms called methanotrophs. They use CH_4 as sole energy and carbon source. These types of microorganisms are widespread in nature in soil and water. They live in narrow gradient zones where CH_4 meets O_2. The initial step in the methane oxidation is catalysed by the enzyme methane monooxygenase. The summarising oxidation-reduction reaction is written:

$$CH_4 + O_2 \rightarrow CO_2 + 2H_2O \qquad 2\text{-}34$$

If the production of organic material is taken into account the equation may be written:

$$5CH_4 + 8O_2 \rightarrow (CH_2O) + 3CO_2 + 8H_2O \qquad 2\text{-}35$$

Some of the CH_4 is partly oxidised to formaldehyde which is then incorporated into biomass via one of two types of carbon assimilation pathways. Some bacteria, called group II methylotrophs uses the serine pathway and one other group of organisms, called group I, uses a pathway named ribulose monophosphate pathway. In addition to CH_4 the methanotrophs can use a number of other one-carbon compounds. The organisms that use other one-carbon compounds than CH_4 are called methylotrophs. All methylotrophs are not methanotrophs. Methanotrophs are widespread in aquatic and terrestrial environments where stable sources of methane are present. CH_4 is produced in lake and sea sediments and diffuses toward the water column. Methanotrophs are often concentrated in a narrow band at the thermocline where CH_4 meets O_2. CH_4-oxidisers convert CH_4 from the anaerobic degradation into cell material and CO_2 /Madigan et al. 2003/.

Biological O_2 reduction with inorganic compounds – chemolithotrophy

Among the microorganisms, bacteria and archaea, there are groups that use inorganic energy and electron donors with oxygen as terminal electron acceptor, the chemolithotrophs. They use a chemical energy source (chemotrophy) and an inorganic electron source (lithotrophy). Examples of inorganic reductants found in Fennoscandian Shield groundwater are: Fe^{2+}, Mn^{2+}, NH_4^+, HS^-, S^0, H_2 and U(IV). Most of the chemolithotrophic organisms are able to obtain all their carbon from CO_2 fixation as discussed above. The organisms are totally self sufficient and do not need to assimilate organic carbon into their metabolism. The reduced inorganic compounds are generated both from metabolism of anaerobic microorganisms and from geological phenomena. H_2 are for example produced by several different processes deep down in the crust. There are at least six possible processes by which crustal H_2 is generated: (1) reaction between dissolved gases in the C-H-O-S system in magmas, especially in those with basaltic affinities; (2) decomposition of CH_4 to C (graphite) and H_2 at temperatures above 600°C; (3) reaction between CO_2, H_2O, and CH_4 at elevated temperatures in vapours; (4) radiolysis of water by radioactive isotopes of U and Th and their decay daughters and by radioactive isotopes of K; (5) cataclasis of silicates under stress in the presence of water; and (6) hydrolysis by ferrous minerals in mafic and ultramafic rocks /Apps and van De Kamp 1993/. The radiolysis of water has been proposed by /Lin et al. 2005/ as a possible H_2 generation process occurring in the granitic system in the Fennoscandian Shield. Fe^{2+}, Mn^{2+}, HS^- are produced via the anaerobic respiration by iron-, manganese- and sulphate reducing bacteria in anaerobic groundwater. S^0 is the product in H_2S oxidation. The source of NH_4^+ can be organic sediments in lakes and in the sea or from fertilizers. In Forsmark high values of NH_4^+ are found at depth down to 500 metres. The source of this is assumed to be remnants of Littorina sea water.

Reduction of O_2 by hydrogen oxidation

Bacteria that are able to grow with H_2 and O_2 are called knallgas bacteria. Most aerobic H_2 oxidising bacteria are also heterotrophic. When they grow on H_2 they often grow autotrophically and fix CO_2 using the reactions in the citric acid cycle. The equation for the reaction is as follows:

$$2H_2 + O_2 \rightarrow 2H_2O \qquad 2\text{-}36$$

The reaction is catalysed by the enzyme hydrogenase. Almost all H_2-oxidising bacteria have one or more hydrogenases. When the organisms use H_2 they often grow under micro-aerophilic conditions because the hydrogenase is O_2 sensitive. Concentrations of O_2 of about 5–10% in the gas phase, supports growth best. The ability to grow on H_2 is found in the genera Ralstonia, Pseudomonas, Paracoccus and Alcaligenes. Many of the H_2-oxidising bacteria can also grow on organic carbon compounds. H_2-oxidisers are found in most natural waters and soils /Madigan et al. 2003/.

Reduction of O_2 by iron and manganese oxidation

The reduced species of Fe and Mn, the dissolved ions Fe^{2+} and Mn^{2+}, are used as energy and electron donors by iron-oxidising and manganese-oxidising bacteria. The iron-oxidisers can be either acidophiles, living in low pH environments, or neutrophiles, living in environments with pH close to neutral.

There are several species in each of the groups. In the Leptothrix-group there are both iron- and manganese-oxidisers. Gallionella ferruginea is an iron-oxidiser that is found in large quantities in some areas in the Äspö tunnel /Anderson et al. 2006/. The enzymes of neutrophilic iron-oxidation are not yet studied but for the acidophilic iron-oxidiser Thiobacillus ferrooxidans, the first enzyme involved in the iron-oxidation is rusticyanin which is situated on the outside of the cell membrane. Fe^{2+} is oxidised and the electron is transported via cytochromes to O_2 inside the cell. The reaction can be written as follows:

$$4Fe^{2+} + O_2 + 4H^+ \rightarrow Fe^{3+} + H_2O \quad (2\text{-}37)$$

$$Mn^{2+} + O_2 \rightarrow MnO_2 \quad (2\text{-}38)$$

The manganese-oxidation process is still quite unknown even though some strains have been isolated /Ehrlich 1996/. The energy yield in the manganese-oxidation is even lower than in iron-oxidation. The manganese oxidising bacteria might be important in oxygen reduction since the Mn concentration in groundwater in Forsmark can be higher than the Fe^{2+} concentration. Iron-oxidisers, but also manganese-oxidisers, are clearly visible in the environment by the bulky orange-red or blackish-red masses of cells, extracellular structures and oxides of Fe and Mn. These organisms are gradient organisms living in narrow areas where they can compete with the chemical oxidation of Fe^{2+} and Mn^{2+}. These types of organisms are often found in areas where Fe^{2+} or Mn^{2+} rich out-flowing groundwater reach the atmosphere. Iron- and manganese-oxidisers are often autotrophic and live in groundwater with low organic carbon content /Madigan et al. 2003/.

Reduction of O_2 by sulphide and sulphur oxidation

Reduced sulphur species can be used as energy- and electron-donor by colourless sulphur bacteria. The most commonly sulphur compounds used by aerobic sulphur-oxidisers are H_2S, S^0 and $S_2O_3^{2-}$. The oxidation of H_2S occurs in stages and the first step results in S^0. Some sulphur-oxidisers store the S^0 inside the cell and it functions as energy storage. The chemical reactions for the oxidation of reduced sulphur compounds are written below:

$$H_2S + 2O_2 \rightarrow SO_4^{2-} + 2H^+ \quad (2\text{-}39)$$

$$2HS^- + O_2 + 2H^+ \rightarrow 2S^0 + 2H_2O \quad (2\text{-}40)$$

$$2S^0 + 2H_2O + 3O_2 \rightarrow 2SO_4^{2-} + 4H^+ \quad (2\text{-}41)$$

$$S_2O_3^{2-} + H_2O + 2O_2 \rightarrow 2SO_4^{2-} + 2H^+ \quad (2\text{-}42)$$

There are two different enzymatic pathways used, by different organisms, for the oxidation of reduced sulphur compounds. In the first step H_2S is oxidized to SO_3^{2-}. If $S_2O_3^{2-}$ is used this will also be oxidized to SO_3^{2-} but first it has to be reduced to H_2S. From SO_3^{2-} the oxidation can go either via sulphite oxidase to SO_4^{2-} or via a reversal activity of adenosine phosphosulphate, one of the key enzymes in sulphate-reduction. The sulphur-oxidising bacteria are often autotrophs and thus independent of any available organic carbon /Madigan et al. 2003/.

2.3.3 Biological oxygen reduction in the context of a repository

The geosphere

In the geosphere, the reductants can have different origins, the photosynthetically produced organic carbon coming from ground surface with recharge water and CH_4, H_2 and organic carbon autotrophically produced from CH_4 and H_2 coming from sources deep in the crust or with even deeper origin. There is measurable dissolved organic carbon (DOC) in granitic groundwater as can be seen in data from the site investigation in Laxemar/Oskarshamn /Hallbeck and Pedersen 2008b/ and Forsmark /Hallbeck and Pedersen 2008c/. The amount differs between the sampled sections and there is no significant relation to depth at either of the sites. Since there are active microorganisms in the groundwater, the pool of organic material is not static but should be regarded as a part of a steady state situation in a continuous culture system. The turn-over time of the organic material in these systems is unknown.

Measurable O_2 concentrations have never been observed in deep, below 100 metres depth, granitic groundwater in the Fennoscandian Shield. The O_2 from ground surface is consumed mainly by heterotrophic microorganisms in soil and water courses and thus depending on the amount of available organic material. Also, aerobic methanotrophic bacteria are present in granitic groundwater especially at depths above 20 metres from the ground surface, where O_2 is available /Chi Fru 2008/. In addition, lithotrophic organisms oxidising reduced inorganic compounds such as Fe^{2+}, Mn^{2+}, H_2 and S^{2-}, with O_2 are present in shallow groundwater. From an energetic point of view the H_2-oxidisers get most energy from the oxidation followed by HS^-, methane, sulfur, and iron oxidising organisms /Madigan et al. 2009/.

The open repository

During the open and operative period of the repository, the atmosphere will be air with its 21% of oxygen. During the construction phase large quantities of foreign material will be used /Hallbeck 2010/. There will be organic material such as wood, plastics, bitumen, emissions from diesel engines, wear of tires, detergents and degreasing agents, hydraulic and lubrication oils, diesel and organic material from human waste. The construction materials contain organic additions such as super plasticisers, accelerators and air-entraining agents. There will also be large amounts of metal structures such as rock bolts and other rock support. Anaerobic corrosion of iron will produce H_2 that support growth of different anaerobic microorganisms in the rock fractures. These organisms produce organic material that can function as reducers in oxygen reduction. Microbial degradation of organic material in contact with water will be ongoing during the open phase of the repository.

In open underground constructions such as mines and tunnels, i.e. Äspö HRL, there are large amounts of iron-, sulphur-, and manganese-oxidisers if there is an outflow of groundwater with reduced species of these elements, see Figure 2-6. By their respiration these organisms contribute to the oxygen consumption /Anderson et al. 2006/. The iron-, manganese-, and sulphur-oxidisers are easily recognised macroscopically because of their extracellular structures.

Figure 2-6. *Iron- and sulphur-oxidising bacteria in the Äspö HRL.*

The closed repository

The deposition tunnels in the repository will be closed gradually as they are filled. Cleaning of the tunnel surfaces is planned before the closure starts. Bentonite will be used both as buffer and backfill in the deposition tunnels /Hallbeck 2010/. The bentonite clay contain up to 0.4 wt% of organic material with an average content of 0.25 wt%. The organic material is assumed to be mostly humic and fulvic acids. To keep the backfill in place during the continued operation of the tunnel a plug consisting of iron and concrete will be placed in the openings of the filled deposition tunnels. The aerobic degradation of the available organic material has been ongoing in the tunnels during the operational phase and continues after closure until either the oxygen or the biodegradable organic material is depleted. If there is organic material left when the oxygen is gone, anaerobic processes will continue to degrade the material producing reduced species such as Fe^{2+}, Mn^{2+} and S^{2-}.

When the repository finally is filled with spent fuel, all constructions including roads are planned to be removed and the tunnel surfaces will be cleaned with pressure washing. The organics that are left will be material in buffer and backfill and minor remains of stray material. The estimated amount can be found in Table 2-1. There will also be about 400 tonnes of iron used as rock support during the construction. This iron can corrode anaerobically and produce H_2. The H_2 can be used in H_2S production if it is anaerobic in the area or by hydrogen-oxidising bacteria if O_2 is present. Presumable the O_2 left in the repository will be consumed before the organic material is consumed.

As the repository will be filled up with groundwater from the surrounding rock, there will be a transport of reduced chemical species with the water as discussed above. These reduced species will be oxidised by aerobic lithotrophic microorganisms probably until the oxygen is consumed. In addition, CH_4 and H_2 from deep origin can be consumed by aerobic methanotrophs and hydrogen-oxidising microorganisms with oxygen reduction. Any oxygen trapped in the bentonite will diffuse either towards the copper canister or towards the oxygen depleted groundwater. In both cases oxygen will be reduced either by copper oxidation or by oxidation of reduced species in the groundwater, Fe^{2+}, S^{2-}, H_2, CH_4 etc., because microbial O_2 consumption would be severely limited in the bulk of the highly compacted bentonite materials in the tunnels.

The time for complete oxygen depletion has been modelled /Wersin et al. 1994/. The result showed that the repository will be totally anoxic in between 7 and 290 years. In the modelling only abiotic reactions were considered. If biological oxygen reduction had been taken into account the time period would likely have been considerably shorter.

Table 2-1. Total amount of organic material in a repository, with and without the organic materials in bentonite (from /Hallbeck 2010/).

	Deposition holes		Deposition tunnels		Other areas	
	With bentonite organic materials (kg)	Without bentonite organic materials (kg)	With bentonite organic materials (kg)	Without bentonite organic materials (kg)	With bentonite organic materials (kg)	Without bentonite organic materials (kg)
Forsmark	$9.8 \cdot 10^5$	–	$5.1 \cdot 10^6$	$1.3 \cdot 10^4$	$8.5 \cdot 10^6$	$1.8 \cdot 10^4$
Laxemar	$9.8 \cdot 10^5$	–	$1.9 \cdot 10^7$	$2.0 \cdot 10^4$	$1.2 \cdot 10^7$	$2.3 \cdot 10^4$

Temperate periods

During temperate periods the vegetation on the ground surface will be close to what it is today with the most productive period during the summer and highest degradation rate of organic material during late summer and autumn. Chemical investigations in Äspö HRL and the site investigations in Forsmark and Oskarshamn/Laxemar have never shown any traces of oxygen at the depth for a repository. Comparison of data for O_2 and other redox sensitive chemical compounds from shallow groundwater sampled in soil pipes showed that at 9.6 metres depth, the highest O_2 concentration measured during a period of 22 months was about 2 mg L^{-1} which is 4% of fully oxygen saturated water, 50 mg L^{-1}, at 10°C, in an O_2 atmosphere /Hallbeck 2008/. Many samples showed values very close to 0 mg L^{-1}, also at the most shallow depth sampled, 1.6 metres, was the O_2 values close to 0 at several occasions. There are of course differences between different biotopes, how many organic material that are degraded and thereby consume oxygen but almost all sampled soil pipes discussed in /Hallbeck 2008/ showed O_2 values close to 0 mg L^{-1} at some sampling occasions during a period of about one and a half year.

The in situ experiment named the REX experiment (Redox experiment in detailed Scale) showed that microorganisms in groundwater and on fracture surfaces immediately consume the O_2 that is dissolved in discharging groundwater /Puigdomenech et al. 2001/. The conclusions from the experiment was that the O_2 reduction depended on microbial oxidation of DOC, Fe^{2+}, S^{2-} but also oxidation of H_2 and CH_4 diffusing from deeper groundwater. One conclusion from the experiment was that O_2-consumption by H_2 and CH_4 then is independent of the surface climate conditions, as discussed below.

Permafrost periods

By definition permafrost is ground that remains at or below 0°C for at least two years. The seasonal variation in temperature is limited to the upper ten metres of the ground in permafrost areas. In summer the air temperature exceeds 0°C thawing a thin layer of the ground surface. During summer photosynthesis with biomass growth is intensive in this area. The vegetation can be mosses, algae and small plants. The aerobic degradation is limited by the narrow depth range with thawed soil and liquid water. The limitation of possible anaerobic electron acceptors induces fermentation and methane production. Many investigations of the microbiology of permafrost areas have been performed (see /Hallbeck 2009/). There are data documenting presence of microorganisms and measurements of microbial activity in temperatures down to −17°C. The types of organisms found were aerobic heterotrophs, sulphate-reducers and methanogens. Measured Eh in permafrost and tundra soils in Arctic and Antarctic locations were reducing from +40 to −250 mV. Such low Eh values suggest that the inflow of oxygen is low and/or the consumption is high. O_2 consumption by aerobic methanotrophs, consume CH_4 with O_2 reduction, might be one explanation for the low Eh measured. Recent investigations in permafrost areas have shown presence of aerobic methanotrophs in the active layer of permafrost /Knoblauch et al. 2008, Liebner et al. 2009/. /Knoblauch et al. 2008/ showed that the CH_4 concentration increased from 4 µM at 4 centimetres depth to 30 µM at 10 centimetres depth in the active layer in the permafrost-affected tundra soil in northeast Siberia. The presence of aerobic methanotrophs showed a decrease in number in the same depth range. No oxygen measurements were made in this investigation.

Glacial periods

During the coldest period in glacial cycle, the temperature will be low and the inflow of surface water into the ground is limited. When the temperature increases and the ice start melting, also the biological activity increases. The amount of organic material on, in and under glacial ice is dependent on the type of glacier and the intensity of the solar radiation and thus also of season and the geographical location of the ice. There are considerable photosynthetic and heterotrophic populations on most of the studied glaciers and ice sheets in the world. In some cases the heterotrophic activity on the surface is so high that the inside of the ice surface blocks become anaerobic with anaerobic microbial activity /Hallbeck 2009/ and references therein. The photosynthetic activity increases with rising temperature which is a prerequisite for melting of glaciers and ice sheets. Studies of the environment beneath glaciers have shown that below many glaciers there were anaerobic processes ongoing. This must also depend on the status and type of the glacier.

2.3.4 Summary

This section provides important information of biological oxygen reducing processes over a glaciation cycle. Qualitative descriptions of the processes that are expected to occur both in the natural environment and in the engineered repository are included. It may be concluded that biological processes are responsible for the rapid scavenging of oxygen in shallow groundwaters under temperate conditions. An important observation is also the ongoing microbial activity during phases of a glaciation. This may reduce the amount of oxygen that is frozen into the ice under glacial conditions and to some extent reduce the amount of oxygen in the glacial melt water under the ice. This supports the conclusion in Section 5.7 that the theoretically maximum oxygen concentration in glacial melt water is conservative. Several microbiological pathways for the scavenging of oxygen are described in this section. The rate of oxygen depletion through these pathways is difficult to estimate conservatively in modelling for safety assessment purposes due to the dynamic growth and activity of the microbes. Furthermore, estimating the rate of supply of dissolved reducing species over large distances in the rock would involve additional uncertainties. Therefore, the biological pathways are conservatively neglected in the long term modelling efforts in this report, although they may have a large influence on the scavenging of oxygen in parts of the recharge flow-paths under favourable conditions mediating the growth of the microbial populations.

2.4 Relative importance between transport and reaction kinetics

Sections 2.2 and 2.3 aimed at describing some of the chemical and microbially mediated reactions that may have influence on oxygen ingress in the rock. Most rate-laws for these reactions are dependent on the concentration of one or more reactants or reaction products. One example is the affinity for the release of ferrous ions from biotite to water, which decreases towards zero as the ambient dissolved concentration of ferrous ions approaches the solubility limit (Eqn. 2-19). Another example is the affinity for the homogeneous oxidation of ferrous ions by oxygen, which decreases towards zero as either of the dissolved oxygen or ferrous ions approaches zero concentration (Eqn. 2-27).

In Section 2.1.2, the free diffusion of dissolved species was briefly described as well as the diffusion in a porous medium.

The rate of a chemical reaction, such as the ones mentioned above, is to some extent dependent on the rate at which reactants or reaction products are transported to or away from the reaction sites. In this section the relative influence of these processes (diffusion and reaction) is explored. We start by looking at characteristic times for the rate of non-oxidative release of ferrous ions from biotite limited by chemical kinetics (Eqn. 2-19) and limited by diffusion in the porous matrix.

2.4.1 Characteristic times

Oxidation of ferrous iron in minerals limited by dissolution kinetics

In this case we consider a porous rock matrix comprising reduced biotite but we neglect any diffusion resistance in the pores. The maximum release rate of ferrous ions from biotite is obtained when the ambient dissolved ferrous ion concentration c_2 is zero. Assuming that oxygen is available, instantly oxidising any released ferrous ions, this condition is fulfilled. The volumetric release rate can then be written (based on the rate-law in Eqn. 2-19):

$$R_3[\text{mol m}^{-3}\ \text{s}^{-1}] = k_{\text{Fe,diss}} \frac{A_{\text{biotite}}}{V} \qquad \text{2-43}$$

where A_{biotite}/V is the specific reaction surface area of biotite, derived in Section 5.5.1 to:

$$\frac{A_{\text{biotite}}}{V} = \left(\frac{A_{\text{biotite}}}{V}\right)_0 \left(\frac{c_3}{c_{30}}\right)^{2/3}$$

Rewriting the rate-law in Eqn. 2-20:

$$-\frac{dc_3}{dt} = \underbrace{k_{\mathrm{Fe,diss}}\left(\frac{A}{V}\right)_0}_{k_1}\left(\frac{c_3}{c_{30}}\right)^{2/3} \qquad 2\text{-}44$$

where $k_1 = (A/V)_0\, k_{\mathrm{diss}}$. This is a reaction of order 2/3 with respect to the solid concentration of ferrous iron. Separation and integration gives:

$$c_{30}\left(1-\left(\frac{c_3}{c_{30}}\right)^{1/3}\right) = \frac{1}{3}k_1 t \qquad 2\text{-}45$$

The decrease in solid ferrous iron concentration is described for times $t \le 3c_{30}/k_1$ by:

$$c_3 = -\frac{(k_1 t)^3}{27c_{30}^2} + \frac{(k_1 t)^2}{3c_{30}} - (k_1 t) + c_{30} \qquad 2\text{-}46$$

The initial specific external grain surface is estimated in Section 5.5.1 to $(A_{\mathrm{biotite}} / V) = 6{,}141$ [$\mathrm{m^2\, L_{water}^{-1}}$], which is based on an initial solid concentration of ferrous iron in the rock of $c_{30} = f_{\mathrm{Fe,r}}\rho_{\mathrm{r}} / (1{,}000\, ø_{\mathrm{m}}\, M_{\mathrm{Fe}}) = 380$ [$\mathrm{mol_{Fe}\, L_{water}^{-1}}$]. The mineral dissolution rate is taken from Eqn. 2-16 for pH 7.5 to 8.5. For pH 8 this is $k_{\mathrm{Fe,diss}} = 5.5\cdot10^{-13}$ [$\mathrm{mol\ m^{-2}s^{-1}}$], and the volumetric reaction rate constant in Equation 2-44 is then calculated to $k_1 = 3.4\cdot10^{-9}$ [$\mathrm{mol_{Fe}\, L_w^{-1}\, s^{-1}}$]. The concentration drop as a function of time is shown in Figure 2-7 for a pH range 7.5 to 8.5.

It is seen from the figure that it takes approximately 10,000 years to deplete the ferrous iron comprised in the matrix minerals for pH 7.5 to 8.0. This time decreases to approximately 5,000 years for pH 8.5 as a result of the pH dependence of $k_{\mathrm{Fe,diss}}$. As expected the dissolution rate decreases with time as the ferrous iron concentration drops and thereby the specific reactive surface area diminishes. The half-life of the reaction, which may be interpreted as the time required reaching half of the initial solid concentration, may be obtained from Eqn. 2-45 with $c_3 = 0.5c_{30}$. At pH 8 this time is approximately 2,200 years:

$$t_{1/2} = \frac{3c_{30}}{k_1}\left(1-\frac{1}{2^{1/3}}\right) = 7\cdot10^{10}\ [\mathrm{s}] \qquad 2\text{-}47$$

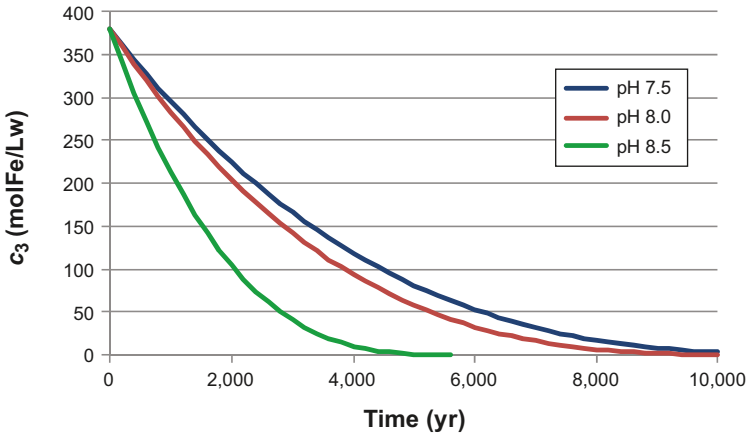

Figure 2-7. *Ferrous iron concentration in mineral per volume of water as a function of time when the release rate of ferrous ions is limited by dissolution kinetics.*

Oxidation limited by diffusion

In this case, we consider the same system as in the previous section, but the release rate of ferrous ions to the pore water as well as the oxidation rate is assumed to be fast. Instead the oxidation rate is limited by the diffusive transport of oxygen from a fracture adjacent to the matrix and into the matrix. Initially, the reducing minerals are directly exposed to the oxygen in the fracture, and there is no diffusion distance. This implies an infinite oxidation rate. As the minerals adjacent to the fracture are depleted, the diffusion distance increases. Thus the oxidation rate decreases with time due to the increasing diffusion resistance. The reaction front is in this case sharp, and moves further into the matrix with time. At the reaction front, the oxygen concentration is always zero, as a consequence of the assumed fast reaction rate.

A simple mass balance (see Section 6.2 for the derivation) for this system gives the distance d, to the redox front as a function of time t, oxidising capacity in the fracture and reducing capacity in the matrix:

$$d = \sqrt{\frac{2D_e c_{10} t}{f \phi_m c_{30}}} \qquad 2\text{-}48$$

where D_e is the effective diffusivity in the matrix and f is the stoichiometric factor between oxygen and ferrous ions in this case when c_{10} is the ambient oxygen concentration, ϕ_m is the matrix porosity and c_{30} is the ferrous iron concentration in the rock matrix per volume of pore water.

In Figure 2-8 the distance to the redox front is plotted as a function of time (blue line) for an ambient oxygen concentration of $c_0 = 1.5 \cdot 10^{-3}$ [$mol_{O_2}\ L_w^{-1}$], a ferrous iron solid concentration of $c_{30} = f_{Fe,r}\rho_r / (1{,}000\ \phi_m\ M_{Fe}) = 380.5$ [$mol_{Fe}\ L_w^{-1}$], a matrix porosity $\phi_m = 0.0018$, an effective diffusivity in the rock matrix $D_e = 2.1 \cdot 10^{-14}$ [$m^2 s^{-1}$] and a stoichiometric factor for the reaction $f = 0.25$ [$mol_{O_2}\ mol_{Fe}^{-1}$].

This result can now be compared with the half-life of the reaction at pH 8.0 (dashed line), indicating that these rates are equal at a diffusion distance of approximately five millimetres into the matrix. At pH 8.5 this distance would be approximately three millimetres (not shown in the figure). For shorter distances, the oxidation may be limited by reaction kinetics, and for longer distances the oxidation rate may be limited by matrix diffusion.

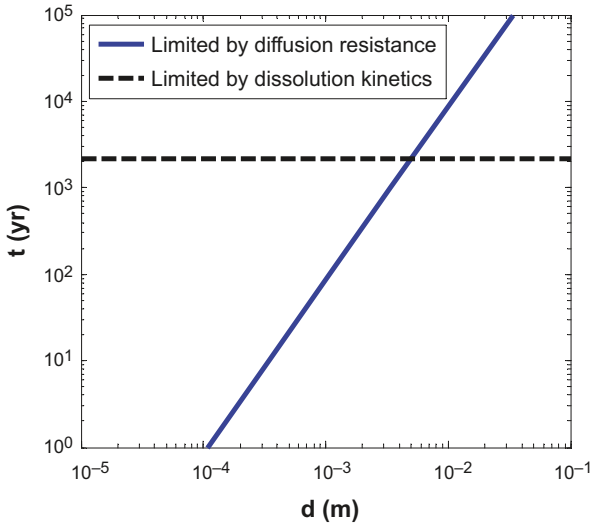

Figure 2-8. *Redox front distance as a function of time compared with the half-life of the reaction.*

3 Observations

3.1 Observations of the redox front and the redox transition zone

The normally oxidising condition prevailing in surface waters will change due to organic and inorganic processes and become reducing when intruding into the bedrock fracture network and rock matrix. This transition may take place at quite different depths depending on the content of oxidants in the recharge water but also on flow velocity, thickness of soil cover and bedrock properties. Two kinds of boundaries between mainly oxidising to reducing conditions are often present within the bedrock and they can be described as:

1. A redox front, here defined as a spatially steep gradient of redox conditions within the rock matrix. This type of redox front is generally sharp and can often be seen as a change in colour of the rock due to redox reactions (Figure 3-1 and 3-2).
2. A redox transition zone, here defined as where oxidising conditions in the fracture system close to the surface gradually changes into reducing conditions at depth (Figure 3-3). In the oxidised zone above the transition zone, all parts of the fracture system are under oxidising conditions whereas in the redox transition zone, oxidising and reducing conditions may occur contemporaneously at the same depth but in different channels within the fracture system. Below the lower limit of the transition zone, all parts of the fracture system are under reducing conditions. The position of the transition zone may vary in time, e.g. seasonally.

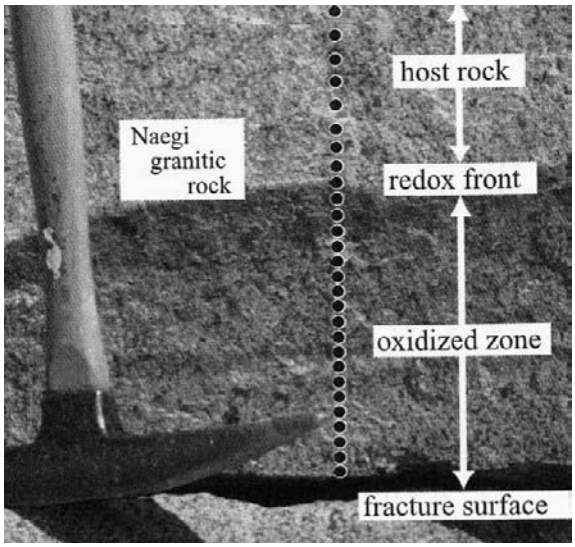

Figure 3-1. *Example of a sharp redox front in granitic rock. Modified after /Akagawa et al. 2006/.*

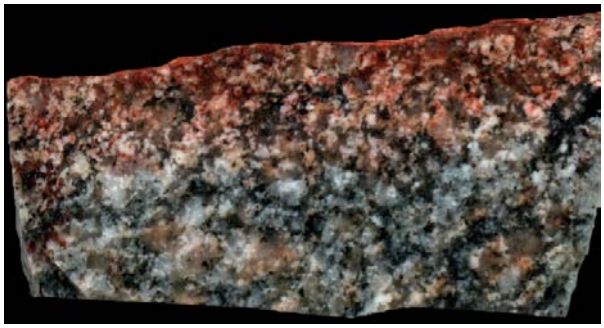

Figure 3-2. *Redox front in granodioritic rock adjacent to a laumontite-sealed fracture. Modified after /Sandström et al. 2010/. The base of the figure is approximately 6 cm.*

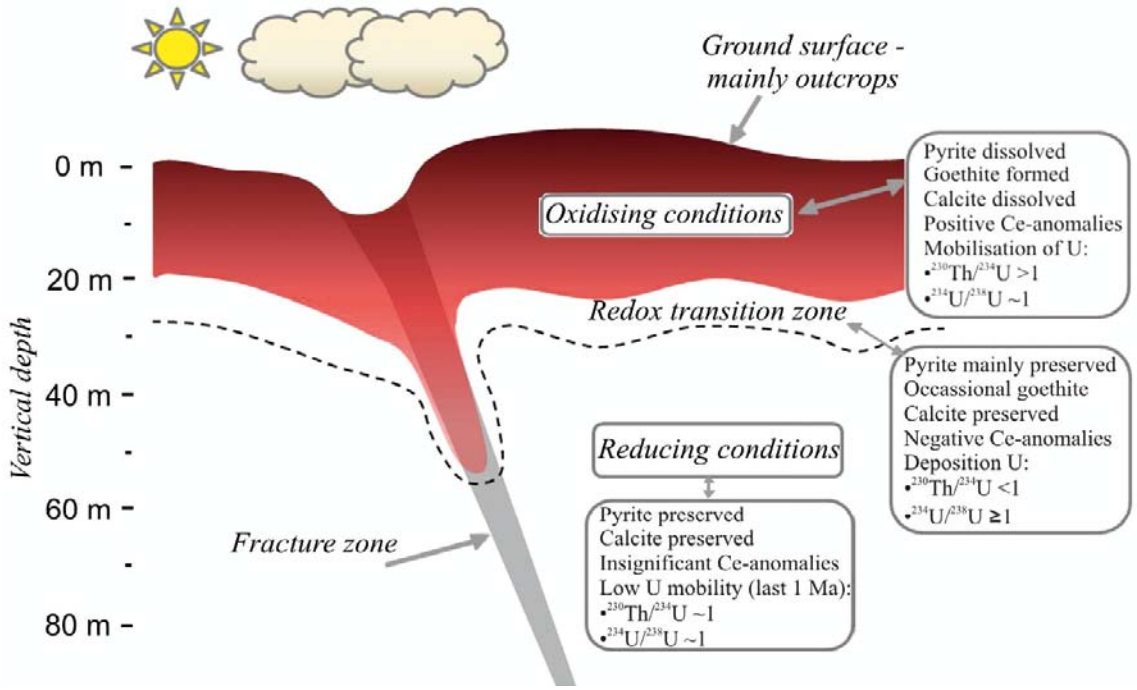

Figure 3-3. *Schematic figure of a redox transition zone and mineralogical and geochemical indicators. Adopted from /Drake et al. 2009/.*

Direct measurements of Eh (potentiometric) in the near surface groundwater may appear as the most straightforward way to locate the position of the present redox transition zone. However, Eh measurements are very complex and associated with several technical and conceptual problems /Auqué et al. 2008, Lindberg and Runnells 1984, SKB 2006a/. Furthermore, mixing of different waters is difficult to avoid in near surface environments and stable conditions are therefore seldom achieved. Instead, secondary evidence such as the spatial distribution of redox sensitive elements (e.g. Fe, Mn, U, S, Ce), fracture minerals (e.g. sulphides, Fe-oxides, Fe-oxyhydroxides) and Uranium-Series Disequilibrium analyses (USD) (e.g. /Akagawa et al. 2006, Tullborg et al. 2008, Drake et al. 2009/) can be used to detect the depth to which oxidising waters penetrate. Dissolution of fracture-coating calcite, which *senso stricto* is not a redox sensitive mineral, has also shown a close spatial relationship with the redox transition zone in crystalline rocks due to the often higher acidity of penetrating oxidising waters /Drake et al. 2009, Tullborg 1989/.

An observed redox transition zone or redox front can be representative for the present situation, i.e. it is reflected in the groundwater/porewater geochemistry and redox reactions are ongoing, or it can be fossil and represent where redox reactions occurred at some period in the hydrogeochemical evolution of the area. At a fossil redox transition zone/redox front, a redox gradient is not discernible in the groundwater/porewater. Hence, a fossil redox transition zone/redox front can only be observed by studies of solid phases (e.g. /Drake et al. 2009, Hofmann 1999/). The location of a fossil redox transition zone indicates how far oxidising fluids have penetrated the bedrock fracture system at *some time* during the hydrogeological evolution; the same is valid for the location of a fossil redox front in the rock matrix. Analysis of disequilibrium between the radionuclides in the U-series decay chain may show if oxidising events have occurred during the last 1 Ma /Ivanovich and Harmon 1992/. Oxidising conditions do not imply that the minerals have been completely oxidised; the degree of mineral oxidation depends on factors such as time, mineral properties and the potential of the oxidising fluid.

Observations of the position of a redox transition zone are generally based on studies of fracture minerals with data obtained from drill cores. An uncertainty with this approach is that the area sampled by the drill core only represents a very small part of the actual fracture system. Furthermore, oxidation of exposed fracture filling minerals may occur during circulation of drilling fluids or during subsequent drill core handling which could be difficult to distinguish from oxidation from natural processes in the bedrock.

3.1.1 International redox studies

Studies of natural analogues have been carried out at several locations in various geological settings in order to understand the migration and retardation of radionuclides /Smellie and Karlsson 1999/. Many of these studies have focused on uranium deposits. Since uranium is a redox sensitive element and can be used to give time constraints to redox process by applying U-series analysis, these sites have also provided opportunities for studies of redox processes in bedrock fracture systems, e.g. at the Cigar Lake uranium deposit in Canada /Cramer and Smellie 1994/, the Poços de Caldas project in Brazil /Chapman et al. 1991, Romero et al. 1992/, the Oklo natural analogue project in Gabon /Gauthier-Lafaye et al. 2000/, the El Berrocal and Mina Fe uranium deposits in Spain /Pérez del Villar et al. 2002, 1997/, and the Palmottu uranium deposit in Finland /Cera et al. 1999/.

Other studies have focused on the more small-scaled redox front propagation into granitic wall rock adjacent to fractures, e.g. in the Lac du Bonnet granite in Manitoba, Canada /Gascoyne and Cramer 1987/, the Carnmenellis granite in UK /Savage et al. 1987/, and the Naegi-Agematsu granite in Japan /Akagawa et al. 2006, Nishimoto and Yoshida 2010/.

At the Cigar Lake deposit, pyrite and marcasite provide the redox buffering capacity in the rock and are oxidised during penetration of meteoric oxygenated waters forming limonite and sulphate. The redox transition zone has penetrated to a depth of approximately 100 metres along fractures and through the permeable sandstone. It is inferred that oxidising waters have penetrated to these depth since the last glaciation (< 10,000 years ago) /Cramer and Smellie 1994, Smellie and Karlsson 1996/. Hydraulic conductivities of all hydraulic units within the Cigar Lake deposit range between $4 \cdot 10^{-9}$ and $3 \cdot 10^{-5}$ m s^{-1}. The connected porosity in the area is high, with values ranging between 2 and 20% /Cramer and Smellie 1994/. Very little data of the fracture network geometry are available from the site.

At the Osamu Utsumi mine at Poços de Caldas, infiltrating meteoric oxygenated waters cause pyrite oxidation with associated formation of Fe-oxyhydroxides. The upper 10–15 metres of the rock is characterised by a high hydraulic conductivity around 10^{-4} m s^{-1}. Below 30 metres, the rock is highly fractured and has a hydraulic conductivity in the range 10^{-8} to 10^{-6} m s^{-1}, and the flow is concentrated in the more conductive regions with closely spaced fractures (less than a few metres apart) and along larger fractures /Holmes et al. 1990, 1992/. The unfractured rock has a porosity ranging between 4 and 20% and a hydraulic conductivity in the order of 10^{-8} m s^{-1} /Romero et al. 1992/. At present, upward flow of reducing water occurs through the rock due to disturbance of the groundwater flow associated with excavation of the mine. Originally the bedrock received downward infiltration of oxidising waters. The geometry of the redox transition zone is controlled by fractures and shear zones and forms wedges or fingers of oxygenated rock penetrating the reduced rock (Figure 3-4 and Figure 3-5). The maximum depth of penetration of oxidising water along these fingers has been approximately 200 metres from the present surface. Three individual redox transition zones have been studied in detail, showing that one has been static (on a centimetre scale) for at least 700 ka whereas the two others have migrated in the range of 2–20 metres in 1 Ma, the latter is in agreement with the estimated regional erosion rate in the area /Chapman et al. 1991, Cross et al. 1991/.

The distribution of redox sensitive fracture filling minerals at Oklo uranium deposits in Gabon indicates that oxidation due to recent weathering has reached 11 metres down into the bedrock. However, locally along some fractures, oxidation is inferred down to a depth of ca 25 metres. The average hydraulic conductivity in the rock formation is 10^{-9} to 10^{-7} m s^{-1} /Gauthier-Lafaye et al. 2000/.

The intensity and depth of recent weathering and oxidation at the El Berrocal site in Spain are mainly related to the degree of fracturing and hydrothermal alteration of the granite. Weathered granite is found down to at least 140 metres below the present surface. The weathering, especially at depth, is spatially closely related to a uranium quartz vein and the age of the weathering is difficult to estimate /Pérez del Villar et al. 2003/. However, U-series analysis indicates that variable oxidising conditions during the last 1 Ma are restricted to the upper 100 metres /Pérez del Villar et al. 1997/. Measured transmissivities in boreholes in the area gave values ranging from 10^{-6} to 10^{-9} m^2 s^{-1}, and a strong downwards gradient was observed with values between 0.1 and 0.3 /Gutiérrez et al. 1997/.

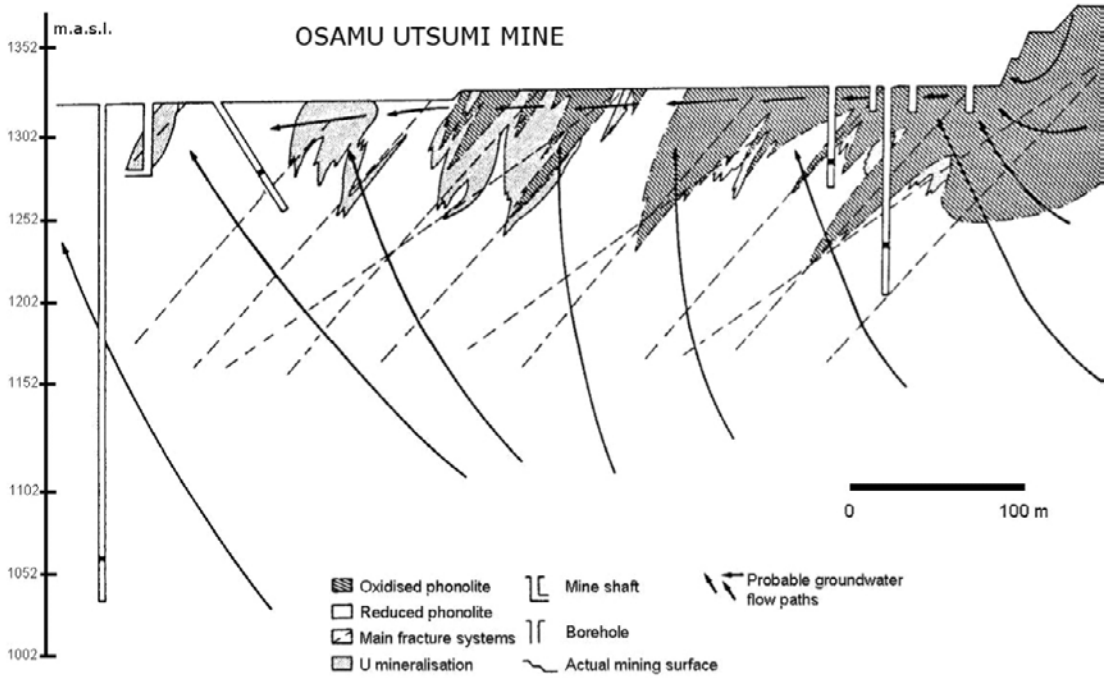

Figure 3-4. *Cross section of the Osamu Utsumi mine at Poços de Caldas, Brazil, showing the location of the redox fronts. Modified after /Cross et al. 1991/.*

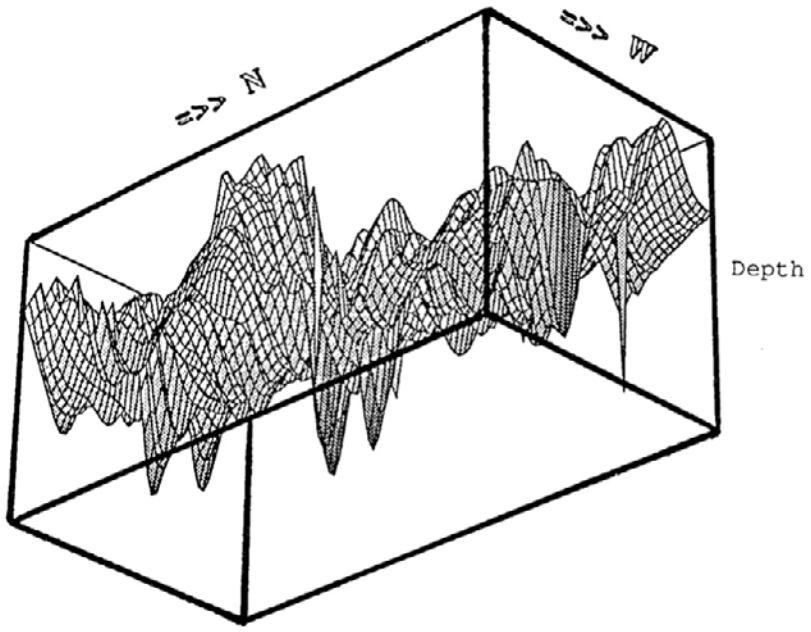

Figure 3-5. *A 3D-view of oxidised fingers at the Osamu Utsumi mine at Poços de Caldas, Brazil, seen from below. The box represent 600·360 m and the depth of the fingers varies between 0 and 200 m. Adopted from /Romero et al. 1992/.*

At the Mina Fe uranium deposit in Spain, a transition zone is found between oxidising and reducing conditions between 18 and 50 metres depth /Arcos et al. 2008/. The redox buffer capacity is mainly made up of sulphides, pitchblende and Fe(II)-carbonates, the main mineral formed in the upper oxidised zone is goethite. The original hydrogeological properties have not been possible to determine in the area due to disturbances from the mining activities. However, it is concluded that the hydraulics of the fracture system are quite uneven, depending on e.g. the size of the zones and fracture fillings, and that near-surface flow velocities are around 10^{-7} m s^{-1} /Pérez del Villar et al. 2002/. Four major fracture sets have been identified at Mina Fe and the spacing distribution among the fractures is lognormal with spacing varying between 0.35 and 0.53 metres /Crespo et al. 2003, Pérez del Villar et al. 2002/. Uranium mobility during the last 100 ka is indicated in several fractures, but the spatial distribution of U-series disequilibrium shows no defined trend with depth. Instead, the spatial differences in uranium mobility are inferred to different hydraulic behaviour in different parts of the fracture system /Crespo et al. 2003/.

Alteration (and various degrees of oxidation) of granitic rock matrix adjacent to fractures normally extends between a few millimetres to tens of centimetres into the rock matrix. However, in highly fractured zones, oxidation has been observed several metres into the wall rock. General characteristics of this alteration halo adjacent to fractures are complete or partial alteration of plagioclase and K-feldspar (saussuritisation and sericitisation), chloritisation of biotite and partial oxidation of magnetite and pyrite. The redox fronts described in most of the published studies of wall rock alteration in granitic rocks (e.g. /Gascoyne and Cramer 1987, Savage et al. 1987, Akagawa et al. 2006, Nishimoto and Yoshida 2010/) have developed under hydrothermal conditions at temperatures above 150°C and the processes are thus not comparable to those expected to occur under conditions at Forsmark during the lifespan of a repository. Nevertheless, these reactions may decrease the available reducing capacity of the rock.

Mineral reactions at these high temperatures mainly occur by dissolution-reprecipitation processes along a moving reaction front /Putnis 2002/, which may explain the frequently observed sharp redox fronts.

The age of the hydrothermal alteration seen in the Lac du Bonnet granite is, at least, older than 450 Ma. However, recent (< 1 Ma) overprinting by low-temperature water-rock interaction associated with uranium leaching from the wall rock under oxidising conditions has been indicated in the upper 260 metres by Uranium-Series Disequilibrium (USD) analysis /Gascoyne and Cramer 1987/. Intrusion of groundwaters to depths of at least 400 metres has been showed in this recharge area along near-vertical fractures and a few sub-horizontal fracture zones /Gascoyne 1997/.

The conditions at many of the natural analogue sites are difficult to compare with the conditions at Forsmark due to differences in rock and fracture porosity, hydraulic conductivity, thermal and hydrogeochemical evolution, uplift history etc. There are also often uncertainties in the interpretations of redox transition zone indicators such as the distinction between recently formed Fe-oxyhydroxides, rust from drilling activities and older, possibly hydrothermal Fe-oxides. Moreover, high-quality water chemistry analyses are often not available. The age of the observed redox transition zone is also often difficult to determine and several overprinting events of alteration make interpretations difficult. U-series analysis provides a useful tool for constraining the age of oxidising events, but the obtained results are often not straightforward due to complex processes during leaching and deposition of uranium and good control on the mineralogy and hydrogeology at the sites is important for the interpretations.

Most natural analogue sites are uranium deposits associated with abundant mineralisations of sulphides which at these sites function as the main redox buffering minerals. The high abundance of sulphides implies that the reducing capacity of the bedrock is higher at many of the natural analogue sites than in Forsmark. However, no quantitative values of the reducing capacity of the bedrock or fracture systems at the natural analogue sites are available. Little is also known of the distribution of sulphides along the conductive pathways and few observations of recent oxidation of sulphides have been described. At most locations in non-ore mineralised areas, such as the Forsmark site, mafic minerals such as biotite and chlorite are the most important redox buffering minerals. Although sulphides are very effective reducing agents, the abundance of sulphides in granitic rocks is commonly very low compared to the abundance of e.g. biotite. Therefore, in crystalline granitic bedrock, biotite and chlorite are the most important minerals available as a redox buffer.

Nevertheless, some general conclusions can be drawn based on the international natural analogue studies:

- The depth and geometry of the redox transition zone in fractured crystalline rock are controlled by fractures and shear zones and forms fingers or wedges of oxygenated rock penetrating the reduced rock (Figure 3-4 and Figure 3-5).
- The depth of oxidative leaching of uranium during recent time (< 1 Ma) due to infiltration of oxidising meteoric waters rarely exceeds 100 metres. Where the redox transition zone is found deeper, hydraulic conductivities of at least 10^{-6} m s^{-1} have been measured in the more conductive zones and the hydraulic gradient has been high.
- The extent of the alteration/oxidation is highly dependent on the porosity, including both matrix porosity and fracture porosity. A higher porosity implies a higher availability to reaction surfaces as well as pathways for transport of oxidants.
- The studies confirm that oxidising fluids are transported into the rock by matrix diffusion where they are buffered by mineral-water reactions.

3.1.2 Observations in the Fennoscandian Shield

Several studies aiming at detecting the location and describing the characteristics of the redox transition zone in fracture systems and the redox front in rock matrix adjacent to fractures have been carried out in crystalline rocks within the Fennoscandian Shield. Most studies have been carried out within SKB's research programmes and site investigations in Sweden. The studied sites include Kamlunge /Smellie 1985/, Klipperås /Tullborg 1989/, Lansjärv /Landström et al. 1989/, Stripa /Eliasson 1993/, Äspö /Banwart et al. 1994, Eliasson 1993, Landström et al. 2001/, Laxemar-Simpevarp /Drake et al. 2008, 2009/, and Forsmark /Sandström et al. 2010, 2008b/.

Studies carried out at Fjällbacka in the Bohus granite, Sweden, within the Hot Dry Rock research programme /Eliasson et al. 1989/ and the Palmottu natural analogue project in Finland /Cera et al. 1999/ have also contributed to the understanding of redox transition zone characteristics.

In a drill core from the Lansjärv area in northern Sweden, positive Ce-anomalies in fracture fillings suggest deposition under oxidising conditions in the upper 150 metres of the bedrock. However, it has been inferred that the deposition of Ce was related to circulation of fluids under hydrothermal conditions. Uranium removal under oxidising conditions during the last 1 Ma has been suggested by Uranium-Series Disequilibrium (USD) analysis in one fracture at a depth of 86 metres, all other 13 fractures analysed from the drill core indicate insignificant water-rock interaction or deposition of uranium during the last 1 Ma, the latter suggesting reducing conditions /Landström et al. 1989/. The hydraulic conductivity has been measured in one borehole and is around 10^{-6} m s^{-1} in the upper 200 metres of the bedrock with a few zones with up to 10^{-5} m s^{-1}. Below 200 metres, the hydraulic conductivity is in the range of 10^{-9} to 10^{-8} m s^{-1} except for in one zone where a conductivity of 10^{-7} m s^{-1} was measured /Larsson 1989/.

At Kamlunge in northern Sweden, the location of the redox transition zone is indicated at a depth of 50–60 metres based on increased precipitation of Fe-oxyhydroxides and lack of calcite above this depth /Smellie J 1989, pers. comm./. However, along major water conductive fracture zones, recent (< 0.5 Ma) removal of uranium under mildly oxidising conditions has been indicated by USD analysis even at depths of 375 metres /Smellie 1985/. A fossil, hydrothermal redox front is also evident in the rock matrix, extending 2 to 3 centimetres into the wall rock adjacent to fractures. Recent (< 1 Ma) overprinting of this alteration under low-temperature water-rock interaction is indicated within a narrow zone of ca 1 centimetre from the fractures based on USD analysis. The Kamlunge site is part of a groundwater recharge area and the most transmissive zones below 50 metres have a hydraulic conductivity of about 10^{-7} m s^{-1}. The steep topography in the region indicates a large hydraulic gradient.

At Fjällbacka in western Sweden, the distribution of Fe-oxyhydroxides suggests that oxidising waters have penetrated down to about 250 metres below the present bedrock surface. The deepest goethite occurrences are related to zones with elevated fracture frequencies /Eliasson et al. 1989/. However, no USD analyses or data of the water geochemistry are available from the site and the age of this oxidation cannot be determined. The topography in the area is steep which often is associated with high hydraulic gradients and the rock surface is often exposed due to an extremely thin Quaternary cover in the area, this could explain the deep penetration of oxygenated waters, if it is of recent origin.

At the Klipperås site in south-eastern Sweden, a redox transition zone interpreted to have developed due to infiltration of present-day surface water is located at a depth of a few tens of metres. Fractures above the redox transition zone are characterised by precipitation of Fe-oxyhydroxides and calcite dissolution. In a few fracture zones, oxygenated waters have been transported down to 150 to 200 metres /Tullborg 1989/. The hydraulic conductivity in these zones is in the order of 10^{-7} m s^{-1} /Gentzschein 1986/.

At Laxemar, south-eastern Sweden, a redox transition zone is observed in the bedrock fractures at a depth of about 15 to 20 metres. However, along highly transmissive fracture zones (> 10^{-6} m^2 s^{-1}), scattered occurrences of goethite indicate that oxygenated groundwater, at some time, has penetrated down to around 80 metres /Drake et al. 2009/. Furthermore, oxidising conditions in the upper 50 metres during the recent past has been indicated by the presence of nanometre scale Fe-oxides. No evidence of low-temperature formation of Fe-oxides has been found below 110 metres /Dideriksen et al. 2010/. The location of the redox transition zone at Laxemar is interpreted as the maximal depth to which oxygenated groundwater associated with varying Quaternary hydrogeological conditions has been able to penetrate before oxygen was consumed by mineral reactions and organic redox buffering. Above the observed transition zone, the wall rock is affected by oxygenated water as indicated by replacement of pyrite by goethite and alteration of biotite. Recent mineral alteration in the rock matrix is interpreted to have occurred during the Quaternary at temperatures close to present or lower during glaciations. The alteration is most common within one millimetre from the fracture but is locally observed up to two centimetres into the wall rock /Drake and Tullborg 2009, Drake et al. 2009/.

Post-glacial weathering of an exposed bedrock surface at Äspö, south-eastern Sweden, has resulted in a 0.2 to 0.5 centimetres thick weathered rim associated with e.g. dissolution of chlorite and plagioclase and leaching of uranium. Oxidation of pyrite, and formation of Fe-oxyhydroxide, has only been observed within the upper millimetres of the surface. The weathering process involves both chemical alteration and mechanical erosion caused by e.g. freeze and thaw reactions /Landström et al. 2001/.

Studies of the infiltration of oxygenated water into a vertical fracture zone after the construction of an entrance tunnel to the Äspö Hard Rock Laboratory have shown that all traces of molecular oxygen are removed within the shallow reaches of the fracture zone. The reducing capacity in the fracture zone includes dissolved organic carbon, Fe(II) and Mn(II) species as well as Fe(II)-bearing fracture minerals such as chlorite /Banwart et al. 1994/.

Fossil hydrothermal redox fronts in the rock matrix are common in the wall rock adjacent to fractures in the Laxemar and Äspö areas and can be seen as reddening of the granite. The altered zone is characterised by saussuritisation of plagioclase, sericitisation of K-feldspar, chloritisation of biotite and partial hematitisation of magnetite /Drake et al. 2008, Eliasson 1993/. This redox front formed at temperatures of about 250 to 400°C during the Proterozoic /Drake et al. 2008/. Similar reddening of rock adjacent to fractures caused by hydrothermal alteration has been described in the Bohus granite in western Sweden and the Stripa granite in central Sweden /Eliasson 1993/.

At the Palmottu natural analogue site in southern Finland, recent uranium leaching from fracture filling material under oxidising condition has been indicated down to a depth of about 60 metres. Removal of uranium during the last 100 ka has been seen up to 50 millimetres into the rock matrix adjacent to fractures in altered rock with a high porosity (mineral porosity 1 to 5%) and conductive structures /Suksi et al. 2001/. The upper 130 metres of the bedrock at Palmottu is characterised by a relatively high hydraulic conductivity with zones with values in the order of 10^{-9} to 10^{-6} m s^{-1} /Rouhiainen and Heikkinen 1998/.

The observations made of redox transition zones in bedrock fractures and redox fronts within the rock matrix in the Fennoscandian Shield confirm and strengthen the observations made globally:

- The geometry of the redox transition zone is mainly controlled by fracture zones and the depth rarely exceeds 100 metres. However, along major water conductive fracture zones (hydraulic conductivity > 10^{-7} m s^{-1}), indications of infiltration of oxidising waters have been found at greater depths.
- Hydraulic gradient, fracture frequency, the presence of major fracture zones and thickness of sedimentary cover are also factors influencing the depth of infiltration of oxygenated waters.
- The depth of infiltration is, as expected, generally greater in areas with groundwater recharge than in areas with groundwater discharge.
- Fossil hydrothermal redox fronts are common in the rock matrix adjacent to fractures within the Fennoscandian Shield and were generally formed during the Proterozoic.

3.1.3 Observations in Forsmark

At Forsmark, no evident redox transition zone has been detected within the bedrock fracture system based on the data available from the boreholes /Sandström et al. 2008b/. Instead, the preservation of well-developed cubic crystals of Palaeozoic pyrite /Sandström and Tullborg 2009/ and Palaeozoic carbonaceous material (asphaltite) in fractures and fracture zones within the upper 150 metres of the bedrock /Sandström et al. 2006/ indicates that reducing conditions has prevailed in most parts of the fracture system since, at least, the Palaeozoic (> 250 Ma). However, goethite occurrences in water conductive zones suggest that channelled flow of oxygenated fluids has occurred. The age of this goethite is not known and it is likely that at least some of the occurrences do not represent recent (< 1 Ma) recharge of oxygenated waters. Most of the observed goethite is found in the near-surface extensions of the gently dipping deformation zones ZFMA2 and ZFMA8 and the steeply dipping deformation zone ZFMENE1208B. The presence of pyrite in the same zones as goethite indicates complex redox evolution along these zones with e.g. development of micro-environments and channelled flow /Sandström et al. 2008b/.

No logging of drill core material from the upper five metres of the bedrock has been carried out at Forsmark; therefore, it is possible that a redox transition zone could be present in the uppermost part of the bedrock. If individual gently dipping fracture zones could be sufficiently sampled, it is also likely that a redox transition zone would be detected along these highly transmissive zones /Sandström et al. 2008b/.

No signs of calcite dissolution in the upper part of the bedrock covered by the drillcores have been found at Forsmark, indicating a stable hydrogeochemical evolution /Sandström et al. 2008b/. The Quaternary overburden at Forsmark is carbonate-rich /Bergman and Hedenström 2006/ and may function as a buffer increasing the pH of infiltrating waters. During the Quaternary glaciations, the conditions may have been quite different and the sedimentary cover is expected to have been significantly thinner. During these periods it is possible that waters undersaturated in calcite migrated along the fracture zones. Nevertheless, no typical dissolution textures of calcite have been observed /Sandström et al. 2008b/.

The absence of an evident redox transition zone in the bedrock could partly be due to that the transition zone is situated in the Quaternary cover (see Section 2.3.3) or that an earlier developed transition zone may have been overprinted by later reducing conditions. The uppermost hundred metres of the bedrock at Forsmark are characterised by sub-horizontal to gently dipping, highly transmissive fracture zones, which creates a strong horizontal component in the groundwater flow /Follin 2008/ and vertical migration and formation of a redox transition zone is not likely to occur at present conditions.

Uranium-Series Disequilibrium (USD) analysis of fracture filling material from Forsmark indicates mobilisation, as well as re-deposition of uranium in fractures in the upper 150 metres of the bedrock during the last 1 Ma /Sandström et al. 2008b/. This is ascribed to the transition from near-surface oxidising conditions to more stable reducing conditions at depth. However, some of the deeper samples show similar behaviour which may be explained by the presence of easily dissolvable and partly

oxidised uranium-phases (e.g. pitchblende). The observed mobilisation and re-deposition of this phase does not indicate that oxygenated waters have penetrated to this depth. Instead, it suggests that mildly reducing groundwaters with sufficient concentration of HCO_3^- (> 30 mg/L) are capable of keeping U(VI) mobile, resulting in variable accumulations occurring within the fracture zones to maximum depths of around 600 metres /Laaksoharju et al. 2008/.

Hematite occurs in many fractures in Forsmark /Sandström et al. 2008b, Stephens et al. 2007/. However, this hematite precipitation occurred during hydrothermal conditions at temperatures above 200°C, inferred from e.g. the characteristic high-temperature hydrothermal minerals cogenetic with hematite, e.g. epidote, adularia, prehnite and laumontite. Radiometric dating of adularia associated with hematite has constrained the age of hematite precipitation to > 1,000 Ma /Sandström et al. 2009/. A hydrothermal origin of the hematite is also indicated by studies of structure, crystal form and chemical composition of fracture coating Fe-oxides /Dideriksen et al. 2007/. Moreover, hematite is mainly found in fractures which are not hydraulically conductive at present. Most water conductive fractures contain minerals associated with a Palaeozoic generation of fracture minerals dominated by calcite, quartz and pyrite /Byegård et al. 2008, Sandström et al. 2008b/. Although reducing conditions have prevailed in the major part of the bedrock at Forsmark for, at least, 277 Ma /Sandström et al. 2009/, hematite which precipitated more than 1,000 Ma ago has been preserved in the fracture system. This indicates that the kinetics of hematite reduction under these low temperatures is very slow and that the presence of hematite says nothing about the present redox conditions.

A zone of reddened altered rock is found adjacent to many fractures in Forsmark. This alteration is most common adjacent to sealed fractures (Figure 3-6) but is also found adjacent to open fractures. The extent of this zone is normally from a few millimetres up to a few centimetres. Along deformation zones, the altered zone can be several metres wide. The reddening is due to hematite disseminations associated with hydrothermal alteration of the rock during several events during the Proterozoic /Sandström et al. 2010, Sandström and Tullborg 2006a/. Similar hydrothermal alteration of the rock matrix has been described at Laxemar and Äspö /Drake et al. 2008, Eliasson 1993/. Associated with this hydrothermal alteration is also chloritisation of biotite, saussuritisation of plagioclase and partial hematitisation of magnetite /Sandström et al. 2010/ (Figure 3-7). During the drill core mapping, this reddening has been called “oxidised rock” (e.g. /Stephens et al. 2007/). However, the change in degree of oxidation between the fresh granitic rock and the altered, reddened rock is statistically insignificant. Oxidation is instead seen mineralogically as partial hematitisation of magnetite (Figure 3-7) and as hematite dissemination. It should also be emphasised that alteration of the rock occurred as part of the chemical re-equilibrium reactions caused by circulation of hydrothermal fluids at temperatures above 200°C /Sandström et al. 2010/, not comparable with the conditions expected during the life-span of the repository.

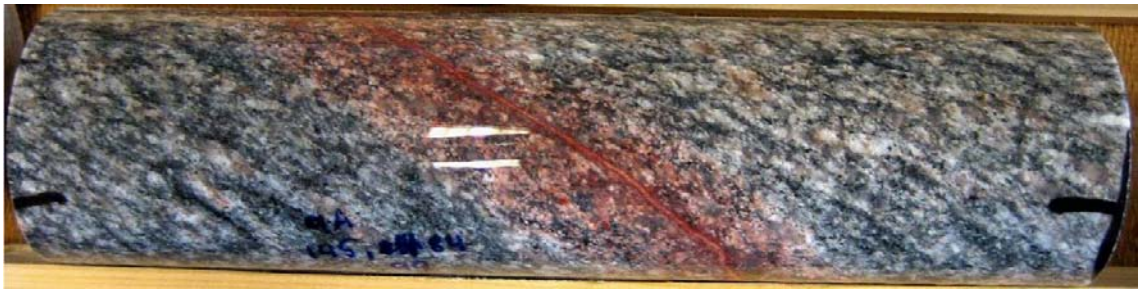

Figure 3-6. *Reddened, hydrothermally altered rock adjacent to a laumontite-sealed fracture. Adopted from /Sandström et al. 2008a/.*

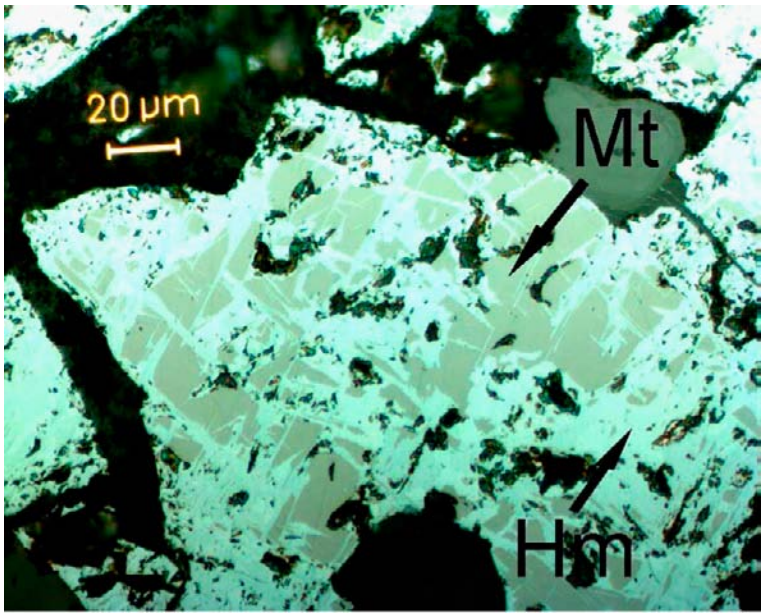

Figure 3-7. *Partial oxidation of magnetite (Mt) and formation of hematite (Hm) in hydrothermally altered rock. Adopted from /Sandström and Tullborg 2006a/.*

It could be argued that evidence of previous intrusions of oxidising waters and evidences of a deeper redox transition zone have been overprinted by later reactions under reducing conditions, although it is not certain if such events can be recognised. Observations of recent oxidation of old Palaeozoic pyrite in fractures show that oxidation occurs irregularly on the pyrite surfaces, destroying its often almost perfect cubic crystal habit /Drake et al. 2009/. Thus, it is unlikely that the abundant cubic Palaeozoic pyrite crystals observed in Forsmark fractures have suffered any events of oxidation and subsequent reprecipitation under reducing conditions without leaving any visible traces of these processes on the pyrite surface.

In a similar manner, it could be argued that previous development of a redox front in the wall rock could be overprinted by later reactions under reducing conditions. However, this scenario can be excluded since the mineral paragenesis in the wall rock is metamorphic (amphibolite facies) /Stephens et al. 2007/ and could not have formed during low-temperature conditions.

3.2 Observations on a mineral grain scale

Observations in shallow drill cores from Laxemar show evidence of recent (< 1 Ma) oxidation of pyrite and formation of Fe-oxyhydroxide in the rock matrix due to infiltration of oxygenated waters. The oxidation has occurred along sharp reaction fronts within the pyrite crystals (Figure 3-8) /Drake et al. 2009/. Similar sharp reaction fronts have been observed in pyrite oxidised during weathering close to the exposed bedrock surface at Äspö, Sweden (Figure 3-9) /Landström et al. 2001/. Similar studies of the near-surface bedrock have not been carried out at Forsmark due to lack of drill-core material from the uppermost five metres and the relatively few drillcores covering the upper 100 metres.

Partial chloritisation of biotite associated with infiltration of low-temperature oxygenated fluids at Laxemar and precipitation of Fe-oxyhydroxide can be seen occurring from the mineral edge inward (Figure 3-10). The resulting chlorite is most likely interlayered with corrensite as indicated by the presence of Ca in the crystal lattice /Drake et al. 2009/. The observation that the reaction occurs from the edge inward is in agreement with observations by /Murakami et al. 2003/, who showed that alteration/dissolution of biotite mainly proceeds from the edge inward, whereas reactions on the basal surfaces are much slower. The degree of oxidation of the altered biotite in Laxemar is not known. However, evidence of complete oxidation of biotite due to weathering of granitic rocks in South Korea have been published by /Jeong and Kim 2003/ (Figure 3-11). This indicates that all internal surfaces of biotite grains are available for oxidation.

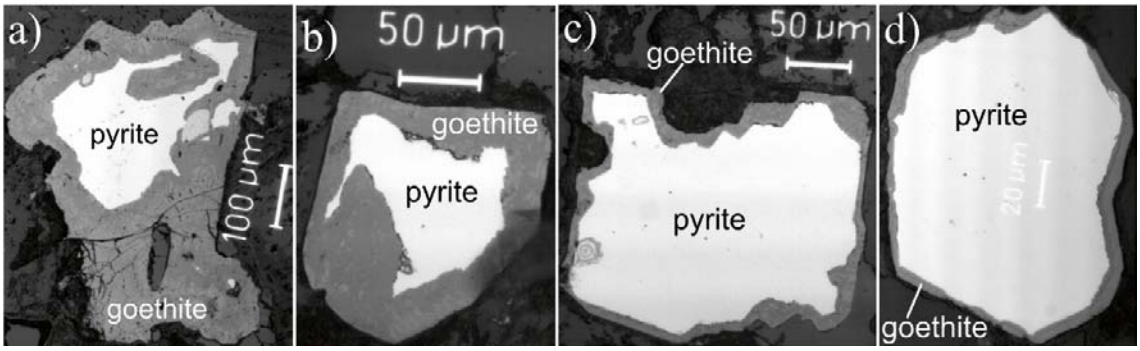

Figure 3-8. *Microphotographs (reflective light) of pyrite increasingly replaced by goethite with decreased distance from a fracture surface (a) 0.4 mm from the fracture, (b) 4 mm, (c) 10 mm, and (d) 17 mm. The sample is from Laxemar, Sweden, 2 m below the bedrock surface. Modified after /Drake et al. 2009/.*

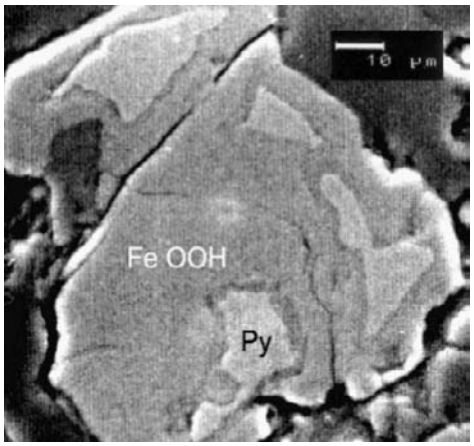

Figure 3-9. *Backscattered scanning electron image of pyrite in the rock matrix replaced by Fe-oxyhydroxide due to weathering 0.5 mm from the bedrock surface. The sample is from Äspö, Sweden, modified after /Landström et al. 2001/.*

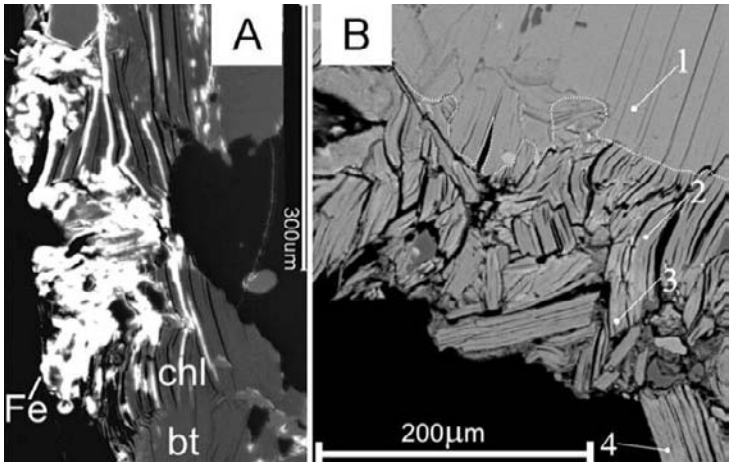

Figure 3-10. *(A) Backscattered scanning electron image of biotite in rock matrix (bt) replaced by chlorite (chl) adjacent to an open fracture. Fe-oxyhydroxide (Fe) has precipitated on the chlorite. (B) Scanning electron image of biotite in rock matrix (1) replaced by chlorite (2-4) along an open fracture. The approximate alteration front is marked with a thin dashed line. The sample is from 0.15 m below the bedrock surface. Modified after /Drake et al. 2009/.*

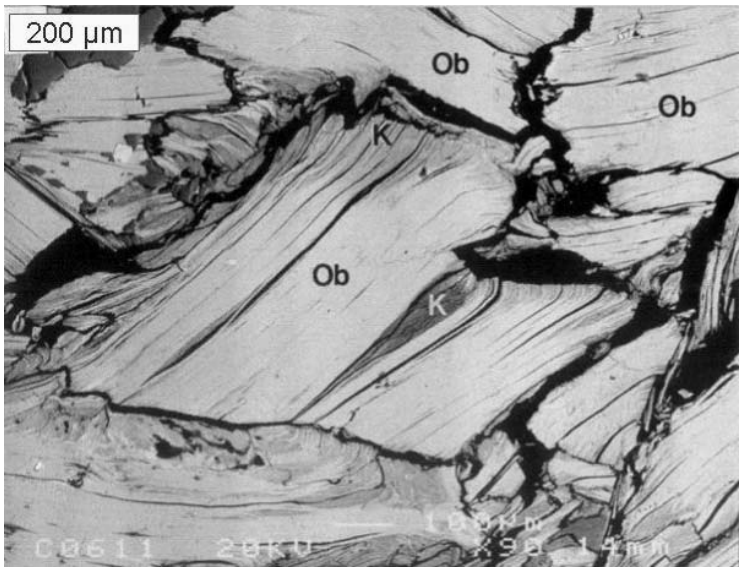

Figure 3-11. *Completely oxidised biotite (Ob) and partial kaolinisation (K) in weathered granitic rock from South Korea. Backscattered electron image modified after /Jeong and Kim 2003/.*

4 Model conceptualisation

In the previous sections, the relevant processes involved in the depletion of oxygen as well as the transport of oxygen along flowpaths in the rock and in the porous matrix have been explored and described. Also, observations of historical or ongoing redox processes have been summarised and described, on a macroscopic fracture network scale from various natural analogue sites as well as on a mineral grain scale.

In this section, a conceptualisation of an oxygen intrusion model is presented that is based on the main findings in these previous sections. A mathematical formulation of the conceptual model is developed and described in Section 6.

At the ground surface, biological processes are of utmost importance for the depletion of oxygen. Under present day temperate conditions, these processes dominate the oxygen scavenging and oxygen is seldom found below a few metres beneath a soil cover. Furthermore, the organic cover is increasing, indicating that the sedimentation of organic matter is faster than the degradation. However, the spatial variation is large: in some areas outcrops are exposed to the atmosphere and in other areas the bedrock is covered with tens of metres of reducing soils. In Sweden, the biological processes are also, to a large extent, dependent on seasonal variations, with much more organic sedimentation and more rapid oxygen consuming processes during the summer than during the winter. Obviously there are also large variations between different phases of a glaciation cycle, with much less organic degradation activity during the glacial period and no sedimentation except for organic material frozen into the ice.

Due to the large uncertainties in amounts and availability of organic material and spatial and time variations, the reducing capacity of the organic top layer is neglected in the model. This is obviously a conservative simplification, in particular during temperate conditions when biological degradation of organic material in the top soil consumes virtually all of the intruding oxygen.

In the absence of easily degradable organic substances, the main reducing capacity is ferrous infill minerals in fracture and fracture coatings, and ferrous minerals comprised in the rock matrix. Several parallel paths for oxygen depletion are then expected to have some influence on the redox conditions in the groundwater. Some of these are illustrated in Figure 4-1.

The fastest of the parallel paths is the most important and in some cases clearly dominant over other pathways. The relative importance of each path may however change with varying conditions.

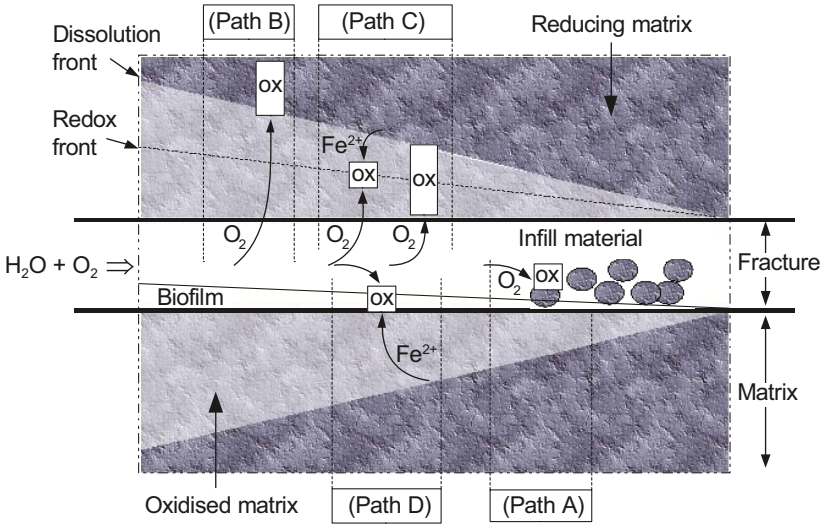

Figure 4-1. *Different pathways for the depletion of oxygen along a flow path in a fracture in the rock. Boxes marked with "ox" denote the oxygen depletion locations. Figure modified from /Sidborn and Neretnieks 2008/.*

Each path in Figure 4-1 may also comprise several serial processes, e.g. transport of oxygen followed by oxidation reaction. The slowest of the serial processes in each path limits the overall rate of that path. This can be illustrated by a scheme of parallel and serial resistances as shown in Figure 4-2.

The resistances in Figure 4-2 are:

R_1 – Microbially mediated surface oxidation of ferrous fracture minerals.

R_2 – Abiotic ferrous mineral surface oxidation.

R_3 – Non-oxidative dissolution of ferrous minerals.

R_4 – Matrix diffusion of dissolved ferrous iron.

R_5 – Matrix diffusion of dissolved oxygen.

R_6 – Homogeneous oxidation of dissolved ferrous iron in the matrix pores.

R_7 – Microbially mediated oxidation of dissolved ferrous iron in the fracture.

It may be noted that the microbially mediated oxidation of ferrous iron is applicable in the larger fractures only. The size of a microbe is of the order of one micrometre /Pedersen 2000, Pedersen and Karlsson 1995/ which prevents them from migrating into the small pores of the rock matrix, which generally are smaller. The influence of microbes on the oxidation rate is therefore expected in parts of the fracture where both oxygen and the reducing ferrous iron are available simultaneously.

Path A represents microbially mediated mineral oxidation, when not limited by diffusive transport resistance. Examples are the oxidation of reducing minerals in small fracture infill particles, fracture coatings or matrix minerals that are exposed to the fracture. The rate of Path A may be fast in regions with large concentration gradients, e.g. at the redox front "tail" in the far right part of the fracture in Figure 4-1, where both oxygen and reducing species are available. However, the rate is negligible in parts of the fracture where the reducing capacity directly available is depleted or parts of the fracture not reached by the intruding oxygen.

Path B represents diffusion of oxygen into the porous rock matrix with abiotic surface oxidation of matrix minerals.

Path C represents non-oxidative dissolution of ferrous matrix minerals, diffusion of the dissolved ferrous iron and oxygen in the pores of the matrix and homogeneous oxidation of the ferrous iron inside the rock matrix.

Path D is the same as Path C with the exception that the dissolved ferrous ions are able to reach the fracture without being depleted and oxidation occurs mediated by microbes in the fracture.

The rate of each of these parallel paths at a given location and at a given time is difficult to estimate. The rates of the microbially mediated reactions depend on many factors, but are assumed to always exceed the corresponding abiotic reactions. Thus, Path D is assumed to be faster than Path C, and Path A faster than Path B. Direct oxidation of ferrous iron in the mineral lattice is also assumed to be faster than the non-oxidative dissolution and consecutive homogeneous oxidation of ferrous ions in the pore water. Thus, Path B is assumed to be faster than Path C.

In order not to underestimate the extent of oxygen intrusion along a flow path, the slowest of the parallel paths, Path C, is therefore chosen to represent the rate of oxygen scavenging. It should be kept in mind however, that the rate of oxygen scavenging is increased considerably under certain circumstances, e.g. in the redox transition zone where both oxygen and ferrous iron are available in the fracture providing a suitable environment for iron-oxidising bacteria. Also, neglecting surface oxidation of ferrous iron in the mineral lattice is probably highly conservative, in particular close to the fracture where the diffusion resistance is low.

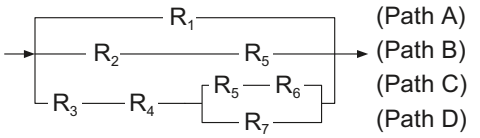

Figure 4-2. *Scheme of parallel paths and serial processes.*

5 Data

5.1 Transport related parameters in the rock matrix

5.1.1 Porosity

The rock matrix adjacent to many fractures in Forsmark was hydrothermally altered at several events prior to 1,000 Ma. This alteration can be seen as a reddening of the rock (Figure 3-6) and is referred to in Sicada as oxidation. The altered rock is characterised by chloritisation of biotite, saussuritisation of plagioclase, hematite dissemination and partial hematitisation of magnetite /Sandström et al. 2010/. The altered zone normally extends a few centimetres perpendicular out from discrete fractures and up to several metres in deformation zones and occurs independently of depth /Sandström et al. 2010, Stephens et al. 2007/. Hydrothermal alteration ("oxidation") is found adjacent to 12% of the open fractures inside deformation zones and 16% of the open fractures outside deformation zones (data delivery SICADA-10-043).

The altered rock generally shows an increase in the connected porosity (measured by the water saturation technique), most likely due to an increase in the frequency of intergranular micro-fractures and the chloritisation of biotite /Sandström et al. 2010/. The median value of the connected porosity of the altered (oxidised), metamorphic granite to granodiorite (rock code 101057_700) is 0.75 vol% (range 0.50 to 0.93%), compared to 0.42 vol% (range 0.28 to 0.66%) of the unaltered rock. However, the porosity measurements in unaltered rock have been carried out within the geology programme and include data from surface samples. Therefore, the porosity of the unaltered rock is probably overestimated in this dataset due to stress release during unloading and exhumation of the bedrock during different episodes /Sandström and Stephens 2009/. For comparison, the measurements of the connected porosity carried out within the bedrock transport programme, which exclusively have been measured on drill core samples, show a median porosity of 0.22 vol% /Crawford 2008/. In the **Data report** for SR-Site a value 0.18 vol% is suggested for use within SR-Site. The porosity measurements on hydrothermally altered ("oxidised") rock were exclusively carried out on drill cores samples and are considered representative for the altered rock /Sandström and Tullborg 2006a/. The intra-granular porosity is also higher in the hydrothermally altered rock and can be seen as non-connected micro-pores within the altered plagioclase /Sandström et al. 2010/.

5.1.2 Effective diffusivity in rock matrix

Flowpath averaged in situ effective diffusivities suggested for use within SR-Site modelling are listed in Section 6.8.12 in the **Data report** for SR-Site. The suggested best estimates and probability density function parameters are presented in Table 5-1.

Thus, for diffusive transport of ferrous ions and oxygen in the rock matrix the mean effective diffusivity can be taken as $D_e = 2.1 \cdot 10^{-14}$ [$m^2\ s^{-1}$].

Table 5-1. Effective diffusivities for use within SR-Site modelling as suggested in the Data report.

Type of solute	Best estimate D_e [$m^2\ s^{-1}$]	μ $\log_{10} D_e$ [$m^2\ s^{-1}$]	σ $\log_{10} D_e$ [$m^2\ s^{-1}$]	Probability density function
Cations and non-charged solutes	$2.1 \cdot 10^{-14}$	–13.7	0.25	Log-normal
Anions	$6.6 \cdot 10^{-15}$	–14.2	0.25	Log-normal

This value is conservative since it is based on formation factors in non-fractured and unaltered matrix rock deep in the matrix. The fractured rock surrounding flow paths generally has a higher capacity for diffusion, as solutes also can diffuse in stagnant fracture water. In Appendix A in the **Data report** for SR-Site the arithmetic mean of the fractured rock formation factors measured on rocks less than five metres but more than 0.5 metres from a PFL anomaly is estimated to be 3.4 times larger than the formation factor of undisturbed rock. This would imply an effective diffusivity of $D_e = 7.2 \cdot 10^{-14}$ [m^2 s^{-1}].

Furthermore, as can be seen from the discussion in Section 5.1.1 the porosity in altered wall rock (0.75%) and unaltered rock (0.18%) differ with a factor 4.2, where altered wall rock is found in 16% of all fractures outside of deformation zones. The altered zone may therefore possess even higher effective diffusivities.

5.1.3 Bulk rock densities

Bulk rock densities for different rock types at the Forsmark site are listed in /Stephens et al. 2007, Table 3-4/. The density of the major rock types in RFM029 and RFM045 are listed in Table 5-2. For volume fractions see Table 5-4.

Table 5-2. Rock densities for the major rock types in Forsmark. From /Stephens et al. 2007, Table 3-4/.

Rock name	SKB Code	Density (kg/m³) Mean/Std
Granite to granodiorite, metamorphic, medium-grained	101057	2,656/12
Pegmatite, pegmatitic granite	101061	2,628/7
Granite, granodiorite and tonalite, metamorphic, fine- to medium-grained	101051	2,688/28
Granite, metamorphic, aplitic	101058	2,639/12
Amphibolite	102017	2,963/75
Granite, fine- to medium-grained	111058	2,634/10
Felsic to intermediate volcanic rock, metamorphic	103076	2,732/75
Diorite, quartz diorite and gabbro, metamorphic	101033	2,934/100

5.2 Hydraulic properties in the repository volume

In this section the hydraulic properties of the ramp and shafts, extending from the repository to the ground surface, are evaluated. Also the corresponding properties of the transport and deposition tunnels in the repository are evaluated. This is done in order to evaluate the possibility of these structures to provide undesirable fast transport paths for intruding oxygen to the canisters in the repository.

In order to prevent water flow in the ramp and shafts, these structures are backfilled with clay up to –200 metres above sea level (m.a.s.l.) according to the reference design, where the top sealing starts. The depth of the top sealing is determined in the **Closure production report** with regard to the presence of water conducting structures and the expected depth of permafrost in Forsmark. Figure 5-2 indicates the reference design for closure of the ramp and shafts.

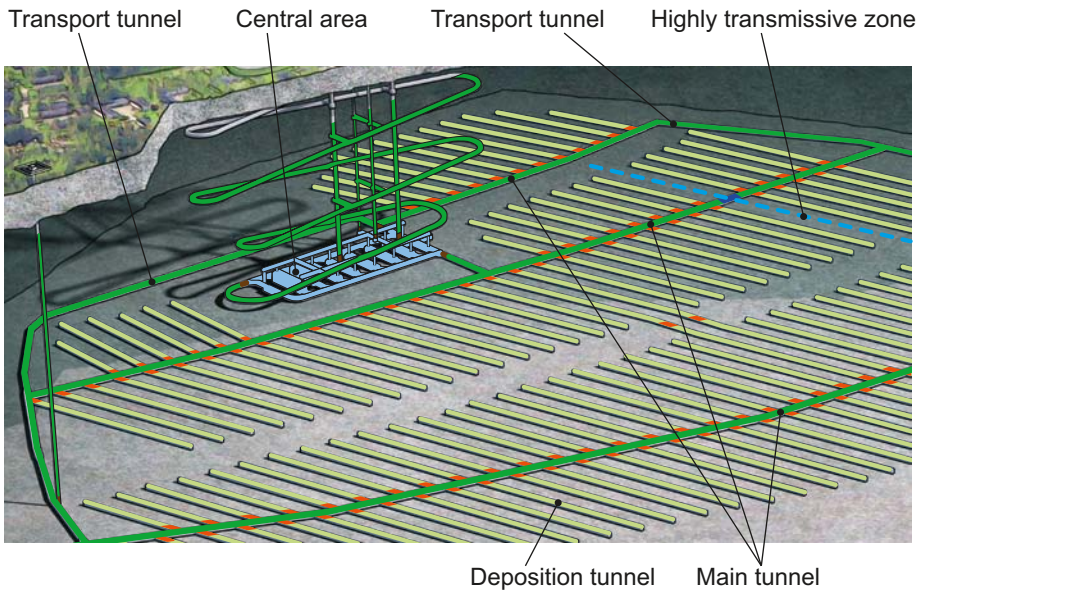

Figure 5-1. *Reference design for closure of main and transport tunnels and the central area. Figure adopted from the* ***Closure production report****.*

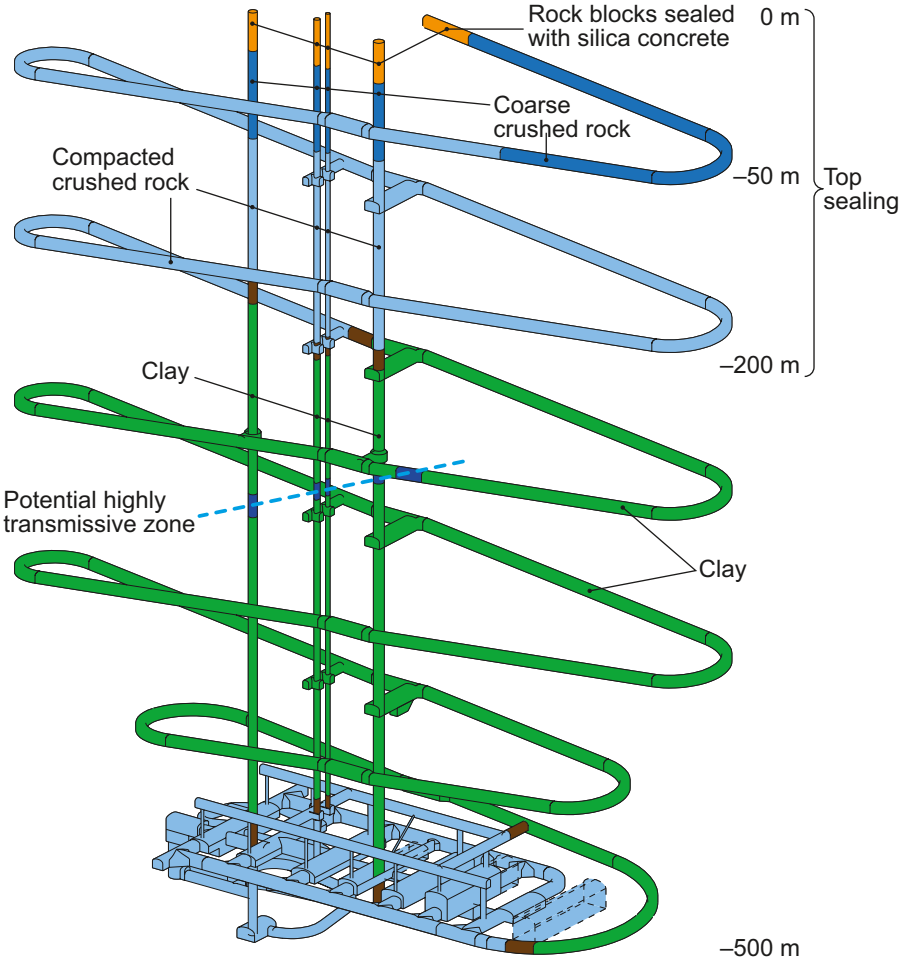

Figure 5-2. *Reference design for closure of ramp and shafts. Figure adopted from the* ***Closure production report****.*

5.2.1 Hydraulic conductivities in designed repository structures

Design premises for backfill (deposition tunnels), buffer (deposition holes), and closure (ramp, shafts, boreholes, and transport tunnels) are available in /SKB 2009/. This report includes requirements on e.g. conductivities used for the reference designs. The reference designs for Backfill, Buffer, and Closure are described in the **Backfill production report** (Backfill, e.g. $K < 10^{-10}$ m/s), **Buffer production report** (Buffer), and **Closure production report** (Closure, e.g. $K < 10^{-8}$ m/s below top sealing including the Excavation Damaged Zone, EDZ).

These values may be compared with hydraulic conductivities for typical fracture (FFM) domains in Forsmark and also with hydraulic conductor domains (HCD). The rock domains outside of FFM domains have been assigned a homogeneous hydraulic conductivity with a depth trend according to Table 5-3 for use in hydrogeological modelling with an equivalent continuous porous media (ECPM) representation of the fractured rock /Follin et al. 2007/. From this it may be argued that these engineered structures do not provide faster transport paths than the ones that are naturally occurring at the site.

Table 5-3. Homogeneous hydrogeological properties used outside the FFM. The table is reproduced from /Follin et al. 2007, Table 3-6/.

Elevation	HRD properties outside FFM	
(m RHB 70)	*K* (m/s)	Kinematic porosity
> –200	$1 \cdot 10^{-7}$	$1 \cdot 10^{-5}$
–200 to –400	$1 \cdot 10^{-8}$	$1 \cdot 10^{-5}$
< –400	$3 \cdot 10^{-9}$	$1 \cdot 10^{-5}$

5.3 Hydraulic properties during glaciation

Under temperate conditions, the global hydraulic head gradient is determined by the topography of the ground surface. When the ice front margin passes over the repository, the global gradient is expected to be considerably larger, resulting in considerably lower flow-wetted surface to flow rate ratios (see Eqns. 2-1 to 2-6), also referred to as the flow related transport resistance or F-factor. The modelling in this report uses F-factors from hydrogeological modelling for different glaciation cases /Joyce et al. 2010, Vidstrand et al. 2010/. The cases are briefly described in Section 8.1, and the hydraulic properties for these cases are described in detail in /Joyce et al. 2010, Vidstrand et al. 2010/.

5.4 Reducing capacity in the rock

5.4.1 Reducing minerals in rock matrix

The geological site descriptive modelling was performed using two different scales of model volumes, the regional and local model volumes. The motivation for the selection of these volumes is presented in /SKB 2006b/. The geological local model volume covers the volume of the repository including accesses and the immediate environment. The geological regional model volume places the local model volume in a larger context and provides e.g. hydrogeological boundary conditions (Figure 5-3). The target volume in Forsmark refers to the rock volume which has been selected for the excavation of the repository at the site (Figure 5-4). It is defined as the parts of rock domains RFM029 (dominant) and RFM045 (subordinate) that are situated beneath the gently dipping zones ZFMA2, ZFMA3 and ZFMF1 and north-west of the steeply dipping zone ZFMNE0065. Eight rock types (Table 5-4) comprise more than 99% of the total volume of these rock domains /Stephens et al. 2007/.

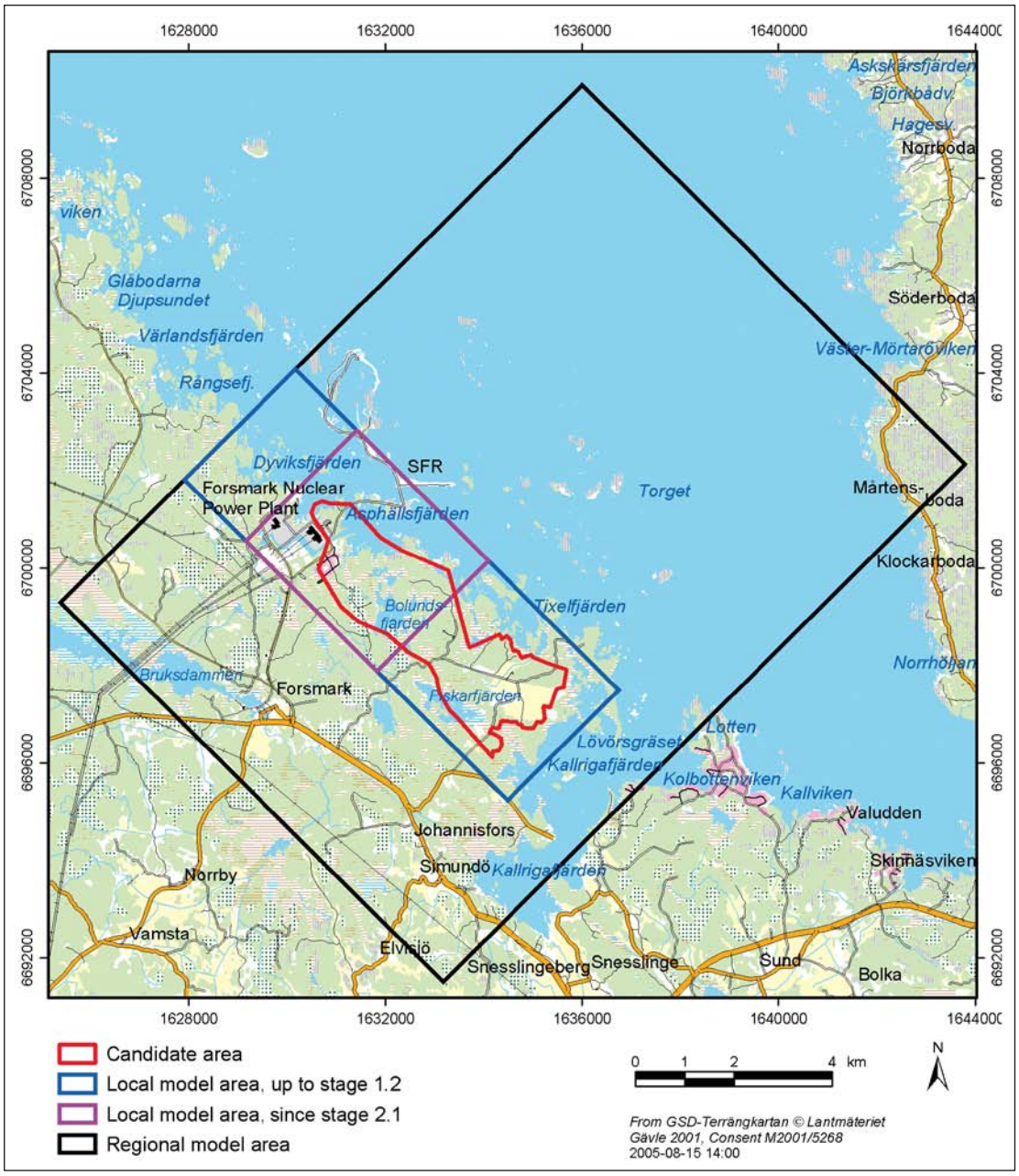

Figure 5-3. *Extent of the geological regional and local model areas at Forsmark. Adopted after /SKB 2008/.*

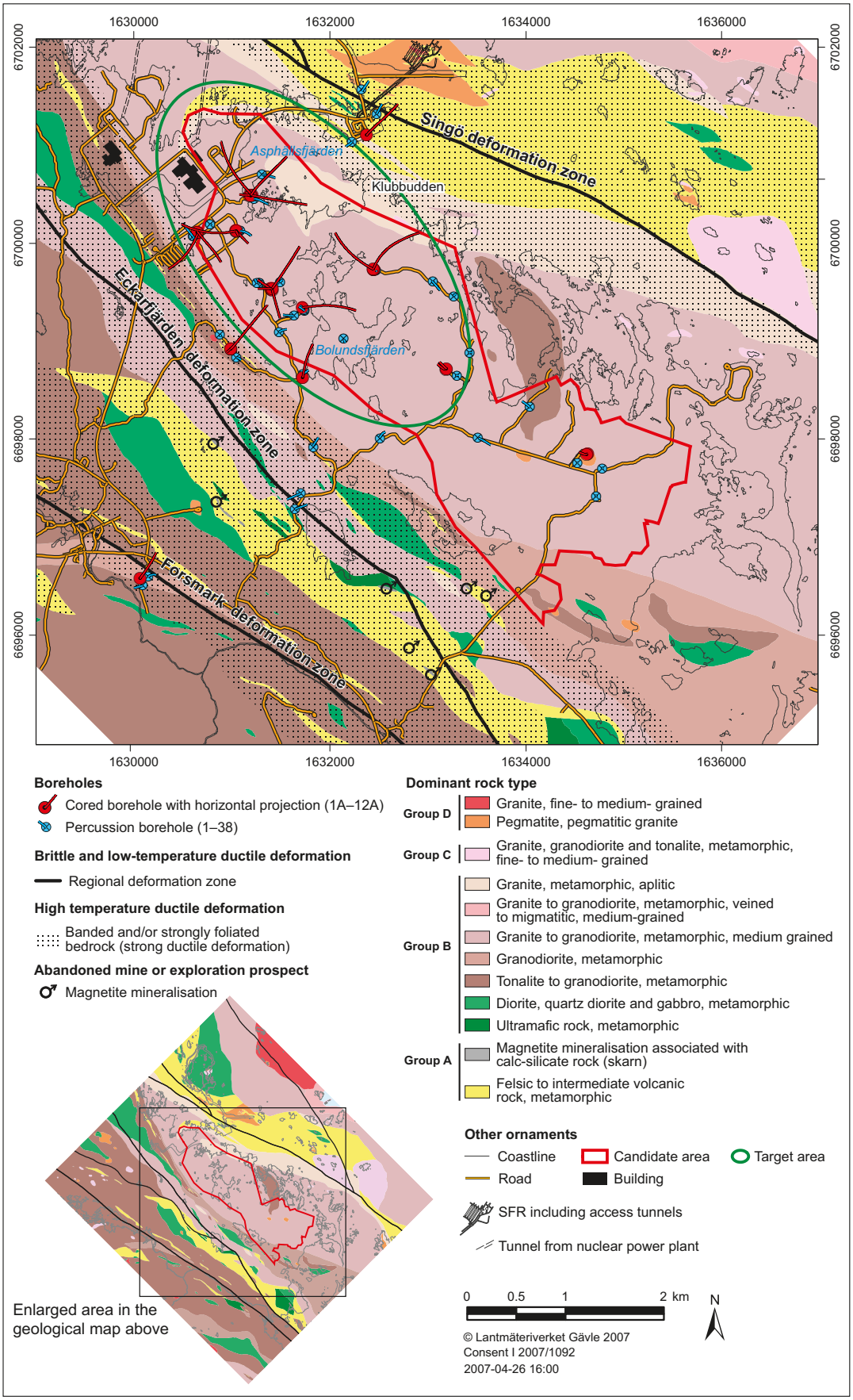

Figure 5-4. *Surface bedrock geological map of the Forsmark site showing the spatial distribution of rock units dominated by a particular rock type. Adopted after /SKB 2008/.*

Table 5-4. Quantitative estimates in volume-percent of the major and most common subordinate rock types found within rock domains RFM029 and RFM045 /Stephens et al. 2007/ and their median content of biotite, amphibole and opaque minerals given as vol% /Sandström and Stephens 2009/.

Rock name	SKB Code	RFM029	RFM045	Biotite	Amphibole	Opaque*
Granite to granodiorite, metamorphic, medium-grained	101057	73.6	18.0	5.4	< 0.2	0.2
Pegmatite, pegmatitic granite	101061	13.3	13.9	0.6	< 0.2	< 0.2
Granite, granodiorite and tonalite, metamorphic, fine- to medium-grained	101051	4.6	9.0	9.4	< 0.2	< 0.2
Granite, metamorphic, aplitic	101058	1.5	49.3	2.0	< 0.2	0.3
Amphibolite	102017	4.4	6.3	< 0.2	42.0	0.6
Granite, fine- to medium-grained	111058	1.5	1.3	3.0	< 0.2	0.4
Felsic to intermediate volcanic rock, metamorphic	103076	0.4	1.2	12.6	< 0.2	< 0.2
Diorite, quartz diorite and gabbro, metamorphic	101033	0.2	0.2	7.6	25.8	0.4

*Magnetite is the most common opaque mineral, only minor grains of pyrite have been found in the major rock types /Petersson et al. 2005/.

Evaluation and selection of representative data of the mineralogy and geochemistry of the different rock types within the geological regional model volume are presented in /Sandström and Stephens 2009/. Data from the regional model area were chosen in order to obtain a sufficiently large statistical basis for all different rock types. The rock types within the target volume are the same as those found outside in the regional model volume and the geochemical and mineralogical data of different rock types compiled from the regional model volume are representative for the rock types within the local model and target volume. Based on the data presented in /Sandström and Stephens 2009/, the following conclusions regarding the reducing capacity in the rock matrix can be made:

- The main minerals identified within rocks of the regional model volume with significant Fe(II)-content are biotite, chlorite, amphibole, magnetite, pyrite, pyroxene and olivine.
- Biotite is, by far, the main Fe(II)-bearing mineral in the rock matrix (Table 5-4).
- In hydrothermally altered, reddened ("oxidised") rock found adjacent to many fractures (rock codes 101051_700 and 101057_700), the biotite has been replaced by chlorite. This alteration normally extends less than a centimetre to a few centimetres into the rock matrix /Sandström and Tullborg 2006a/. In deformation zones several metres of red-stained rock have been found in the drill cores /Stephens et al. 2007/. The difference in degree of oxidation (Fe(III)/Fe(total)) between altered and unaltered rock is smaller than 2σ /Sandström et al. 2010/. Therefore, it is not considered necessary to treat the altered rock differently considering the reducing capacity. However, the hydrothermally altered rocks show a higher porosity than the unaltered rock (section 5.1.1).
- In amphibolite (rock code 102017) and metamorphic diorite, quartz diorite and gabbro (rock code 101033), amphibole (hornblende) is the main Fe(II)-bearing mineral (Table 5-4).
- Significant amounts of pyroxene and olivine are only found in metamorphic ultramafic rock (rock code 101004) which is found as a few small occurrences outside the geological local model area in Forsmark /Stephens et al. 2007/. They are not considered in this report due to their low abundance. The Fe(II)-content in these minerals is typically high /Deer et al. 1992/ and neglecting these minerals in models used for the evaluation of oxygen ingress is therefore considered conservative.
- Trace amounts of pyrite and magnetite occur in most rock types at the Forsmark site, generally at concentrations < 0.2 vol% /Sandström and Stephens 2009/. Both pyrite and magnetite are reducing minerals; especially pyrite (FeS_2) has a high reducing capacity since it contains both ferrous iron and sulphide. The combined reducing capacity of these minerals is, however, small compared to that of biotite in the rock matrix due to their low abundance. Furthermore, neglecting the presence of pyrite and magnetite during the oxygen intrusion modelling is considered conservative.

Based on these conclusions, it is inferred that the simplified model where all Fe(II) in the rock is assumed to be present in biotite is reasonable since biotite as mentioned above, by far, is the most abundant Fe(II)-bearing mineral in the dominating granitic rocks at Forsmark. This assumption is also considered conservative since the presence of e.g. sulphides provides a higher reducing capacity in the rock matrix than that used in the modelling.

The Fe(II)-content in the dominant metamorphic granite to granodiorite (rock code 101057) and the subordinate metamorphic granite, granodiorite and tonalite (rock code 101051) has been determined by whole rock geochemical analyses combined with Mössbauer spectroscopy /Sandström and Stephens 2009, Sandström and Tullborg 2006a/. In rock types where no Mössbauer spectroscopy data are available, the Fe(II)-content has been calculated based on the content of Fe(II)-bearing minerals and the geochemical composition of these minerals. The calculations are described in Appendix B and the results are presented in Table 5-5 and Figure 5-5.

Table 5-5. Fe(II) content (wt%) in rock matrix for different rock types in Forsmark. Parameters μ_e and σ_e are the mean and standard deviation of the natural logarithm of the content obtained from the lognormal distribution. For calculations see Appendix B.

	101057	101051	101058	101061	102017	111058	103076	101033	RFM029[1]	RFM045[1]
μ_e	0.28	0.76	–0.11	–0.35	1.70	–0.03	0.76	1.59	–	–
σ_e	0.20	0.55	0.18	0.16	0.18	0.20	0.65	0.28	–	–
Median	1.33	2.14	0.90	0.71	5.49	0.97	2.13	4.90	1.50	1.42
Mean	1.36	2.49	0.91	0.72	5.58	0.99	2.63	5.10	1.52	1.44
Std	0.28	1.49	0.17	0.12	1.01	0.20	1.91	1.47	0.23	0.18

[1] Values obtained from stochastic simulation.

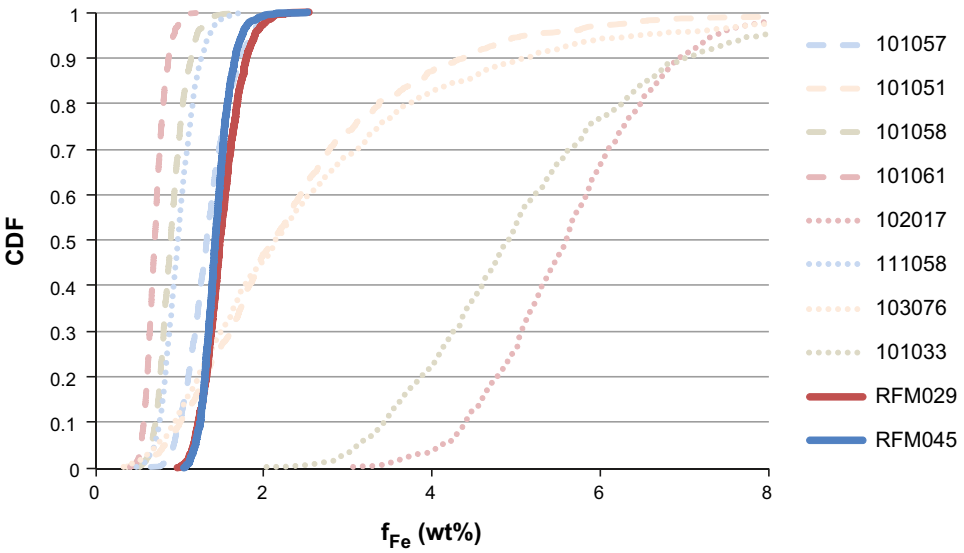

Figure 5-5. *Cumulative density function (CDF) of the ferrous iron content in the rock matrix for individual rock types and for rock domains RFM029 and RFM045.*

Representativity of the data outside of the geological model volume

Recharge of glacial melt-water into the rock /Vidstrand et al. 2010/ may occur outside of the geological regional model volume, indicated in Figure 5-3, from which data have been collected during the site investigation programme. To estimate how representative the data collected during the site investigations /Sandström and Stephens 2009, SKB 2008/ are outside of the geological regional model volume, comparison was made with regional geological data compiled during the feasibility studies carried out in the Tierp municipality /Bergman et al. 1999/ and in a review of the geology of the Bergslagen region /Stephens et al. 2009/. In general, it can be concluded that the bedrock within a potential recharge area (see /Vidstrand et al. 2010/) is dominated by metamorphic granodiorites, tonalites, granites and subordinate metamorphic sedimentary, volcanic and mafic rocks. These are the same rock types as those found within the regional model volume in Forsmark, although the proportions of the different rock types differ between the different model scales. Undeformed granite and metamorphic mafic, volcanic and sedimentary rocks are, for example, more common within the potential recharge domain.

It is considered that extending the data from the regional model volume to the potential recharge domain is conservative with respect to reducing capacity based on the following:

- The metamorphic granite to granodiorite (rock code 101057), which dominates within the regional model volume, contains small amounts of biotite and opaque mineral and has a low Fe-content compared with most of the other analysed granitoids in the Forsmark area. Granitoids with higher content of biotite, opaque minerals and Fe are more common within the potential recharge domain.
- The Fe-content in the metamorphic mafic and volcanic rocks which are more common in the potential recharge domain is higher than in the granitoids which are more common within the regional model volume.
- Metamorphic volcanic rocks, which are more common in the potential recharge domain, are often associated with sulphide and magnetite mineralisations, adding to the reducing capacity.
- Metamorphic sedimentary rocks are more common within the potential recharge domain. These rocks typically have higher biotite content than the metamorphic granite to granodiorite that dominates within the regional model volume.

5.4.2 Reducing minerals in fracture coatings

The geochemistry and redox capacity of fracture minerals in Forsmark have been presented together with qualitative interpretations in /Sandström et al. 2008b/. A quantitative mapping campaign of fracture minerals in drill cores from Forsmark was carried out by /Eklund and Mattsson 2009/ and a statistical analysis of the obtained data was subsequently presented in /Löfgren and Sidborn 2010/. The main part of the quantitative mapping was devoted to open fractures within PFL-sections, i.e. drill core sections surrounding a PFL-anomaly (transmissivity $\geq 10^{-9}$ m^2 s^{-1}) by one metre on each side.

The most frequently found mineral along water conductive fractures is calcite which was quantitatively estimated in 32% of all open fractures, followed by chlorite (24%), clay minerals (11%), pyrite (10%) and hematite (0.4%) /Löfgren and Sidborn 2010/. The most common fracture minerals are unevenly distributed in the fracture system, and no distinct variation with depth can be seen /Stephens et al. 2007/.

Significant Fe(II)-bearing fracture minerals in Forsmark are chlorite, clay minerals and pyrite /Sandström et al. 2008b/. The average thickness of these fracture minerals is listed in Table 5-6. The most common clay mineral in fractures in Forsmark is corrensite, a mixed-layer clay consisting of alternating layers (1:1) of chlorite and smectite/vermiculite (general chemical mineral formulas are given in Table 5-7). Fracture filling chlorite and clay minerals are difficult to differentiate during drill core mapping due to varying degrees of interlayering between chlorite and clay minerals. X-ray diffraction show that most fracture-coating chlorite, especially in water conductive fractures, consists of a mixture of chlorite and corrensite /Sandström et al. 2008b/.

Table 5-6. Averaged fracture mineral thickness d_{mean} (m) for Fe(II)-bearing fracture coatings where these factors could be quantitatively estimated (f_{quant}% of the mapped fractures). Modified from /Löfgren and Sidborn 2010/.

Mineral	$\overline{d}_{mean}$ (m)	μ of ln d_{mean}	σ of ln d_{mean}	f_{quant} (%)
Chlorite	$206 \cdot 10^{-6}$	–9.05	1.06	24
Clay minerals	$135 \cdot 10^{-6}$	–9.42	1.01	11
Pyrite	$6 \cdot 10^{-6}$	–16.14	2.90	10

Table 5-7. General mineral formulas of the main Fe(II)-bearing fracture minerals in Forsmark, from /Deer et al. 1992/. Smectite is a clay mineral and part of the mixed layer clay corrensite.

Chlorite	$(Mg,Fe^{2+},Fe^{3+},Mn,Al)_{12}[(Si,Al)_8O_{20}](OH)_{16}$
Smectite	$(½Ca,Na)_{0.7}(Mg,Fe,Al)_6[(Si,Al)_8O_{20}]\ (OH_4)\cdot nH_2O$
Pyrite	$Fe^{2+}S_2$

The amount of Fe(II) available in fracture filling material has been determined by combining data of Fe(total) in fracture fillings, Mössbauer analyses of bulk fracture filling material /Sandström et al. 2004, 2008a, b, Sandström and Tullborg 2005, 2006b/ (data delivery SICADA_10_021) and quantitative data of the amount of fracture filling material /Löfgren and Sidborn 2010/. Most analysed samples consists of a mixture of fracture minerals /Sandström et al. 2008b/ and an evaluation of the representativity of the samples was carried out before any calculations were carried out, for details see Appendix C.

All Fe(II) in fracture-fillings is assumed to be present in chlorite. Other common Fe-bearing minerals such as hematite, goethite, epidote and prehnite only contain trace amounts of Fe(II) /Deer et al. 1992/ and are therefore not significant for oxygen consumption. The results of the calculations are presented in Table 5-8.

Table 5-8. Fe(II)-content in bulk fracture fillings on fracture surfaces, E(x) = expected value or mean.

$E(Fe(II)_{mean})$	3.7 wt%
μ of $\ln(Fe(II)_{mean})$	0.84
σ of $\ln(Fe(II)_{mean})$	0.97
E(Fe(II))	23 g/m^2
μ of ln(Fe(II)/m^2)	2.10
σ of ln(Fe(II)/m^2)	1.44

5.5 Availability of reducing minerals

In the previous Section 5.4, the reducing capacity in the rock matrix and fracture coatings is estimated. The present section aims to estimate the availability of this reducing capacity for the scavenging of intruding oxygen. The rate of heterogeneous mineral reactions is commonly given per unit reactive surface, e.g. the specific dissolution rate of biotite in Section 2.2. Thus, an estimation of the active specific surface area is needed if the rate is limited by reaction kinetics (see Section 2.4 for the relative importance of transport and reaction kinetics).

5.5.1 Initial specific reactive surface area

In kinetic experiments for determining dissolution rates for various minerals, the results are generally obtained as a rate per weight of the sample. This rate is generally related to the specific surface of the sample, and is commonly presented in units of moles m^{-2} s^{-1} (See e.g. Eqns. 2-16 and 2-25). Although the geometrical surface is used in some experiments, the specific surface area is commonly taken as the BET surface area (m^2 g^{-1}) of the sample. Hence, it is assumed that the entire BET surface is available for reaction. For this assumption to be valid, the material is crushed to small size fractions (75 to 125 μm in Eqn. 2-16). The size of the crushed mineral fraction used needs to be sufficiently small so that intra-particle transport resistance can be neglected. Furthermore, new fresh surfaces created by the crushing process and de-stressing of the samples, are assumed to have the same properties as the old surfaces.

When using this surface reaction rate for in situ mineral grains, we need to consider the following:

- The in situ mineral grains are generally larger than the size fraction used for determining the specific rate.
- The fresh surfaces created in the grinding and sieving process may have somewhat different properties than the surfaces in situ.

Geometrical biotite grain sizes have been estimated from 262 samples from four different boreholes in Forsmark (Appendix A). The grains are assigned a simplified box-shaped geometry according to Figure 5-6. In the rock, biotite occurs as irregularly shaped sheets (Figure 5-7) and the estimated geometrical surface based on the box geometry is conservative. The average size of biotite crystals in the major metamorphic granite to granodiorite in Forsmark is in the order of 400×200×100 μm (Appendix A, Figure 5-6 and Figure 5-7). However, the size of biotite crystals varies both within and between different rock types and crystals less than 100 μm long as well as crystals up to several millimetres long are also present in the rock.

In Section 3.2 it was concluded, based on observations on a mineral scale, that alteration/dissolution of biotite mainly proceeds from the edge (grey areas in Figure 5-6) inward, whereas reactions on the basal surfaces are much slower. Therefore, only the edge surfaces are considered as available for dissolution/reaction. Those surfaces are in reality not smooth as in the simplified box-shaped grain illustration in Figure 5-6.

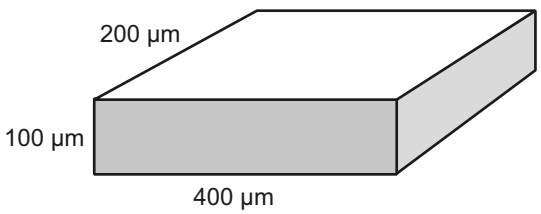

Figure 5-6. *Schematic illustration of an average biotite grain from Forsmark. Gray areas represent external surfaces assumed to be available for dissolution/reaction.*

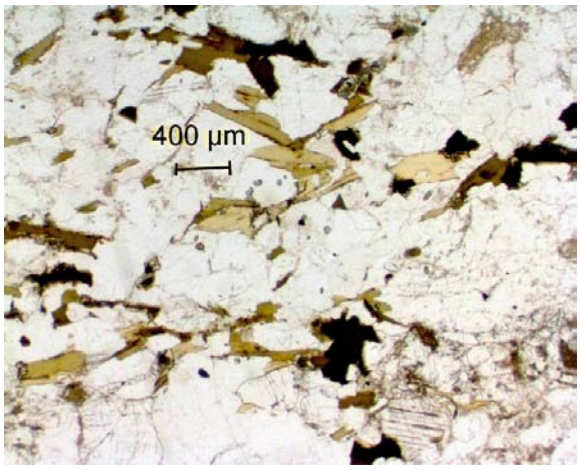

Figure 5-7. *Photomicrograph (transmissive light) of typical biotite crystals in metamorphic granite to granodiorite (rock code 101057). All green and dark minerals in the image are biotite crystals. Adopted from /Drake et al. 2006/.*

Surface roughness factors, λ, defined as the ratio between the real particle surface and idealised smooth surfaces have been estimated in /André et al. 2009/ and are assumed to be independent of particle size. The surface roughness factors estimated from granite samples in Forsmark and Laxemar are in the range 6 to 13. This surface roughness factor should not be confounded with the commonly referred surface roughness defined as the ratio between geometrical and BET surface (e.g. /White and Brantley 2003/). Applying this range to biotite surfaces is probably highly conservative due to the tendency of the layered sheet structure of biotite to split up upon weathering, leading to presumably higher surface roughness.

Nevertheless, with a presumably conservative surface roughness factor $\lambda = 10$, the specific external surface area of a typical biotite grain is thus estimated to be:

$$a_{\mathrm{EXT}} = 2\lambda\left(\frac{1}{a}+\frac{1}{b}\right) = 150{,}000\ \left[\mathrm{m_b^2\ m_b^{-3}}\right] \qquad 5\text{-}1$$

where $a = 0.4\cdot10^{-3}$ metres and $b = 0.2\cdot10^{-3}$ metres according to the estimations in Appendix A.

This approach neglects any additional intra-particle surfaces, and may be accurate for rapid surface dissolution rates compared to the transport rates in the mineral grain. For slow dissolution rates compared to transport rates, we may assume that all of the available surfaces of the crystal are contributing to dissolution, the case of which the BET surface may better describe the available reactive surface. The measured BET surfaces on crushed samples are estimated to:

$$a_{\mathrm{BET}} = \rho_{\mathrm{b}} a'_{\mathrm{BET}} = 3\cdot10^{6}\ \left[\mathrm{m_b^2 m_b^{-3}}\right] \qquad 5\text{-}2$$

with a biotite density $\rho_{\mathrm{b}} = 3\cdot10^{6}$ [g m^{-3}] and an assumed BET surface $a'_{\mathrm{BET}} = 1$ [m^2 g^{-1}], based on measured BET surfaces for crushed samples of fresh biotite used for weathering rate experiments listed in /White and Brantley 2003/.

It should be noted that these BET surfaces are measured on de-stressed samples in the laboratory. The corresponding values from in situ biotite grains are presumably smaller. The effect of de-stressing on BET surface area measurements has been evaluated in /André et al. 2009/ where measurements were carried out on crushed and sieved granite samples of different size fractions as well as on intact drillcores. It was found that the BET surface for the size fraction 71–125 µm was approximately ten times larger than for the intact rock. If these results are valid also for biotite, the value given in Eqn. 5-2 based on crushed biotite should be reduced by a factor of ten in order to represent intact biotite.

The two estimations in Eqns. 5-1 and 5-2 may be considered as end-members of a range of surface area contributions. The actual specific surface contributing to the release of ferrous iron from biotite would be somewhere in between these values. Depending on the relative rates between surface dissolution and intra-particle diffusive transport, a small or large fraction of the particles internal surfaces may contribute to the reactive surface.

Rock matrix

The initial specific reactive surface of biotite in the bulk rock, prior to any oxidation, can now be estimated by:

$$\left(\frac{A_{\text{biotite}}}{V}\right)_0 = \frac{a_i v_{\text{biotite}}}{1{,}000\ \text{ø}_\text{m}}\ [\text{m}^2\ \text{L}_{\text{water}}^{-1}] \qquad 5\text{-}3$$

where a_i refers to either of a_{EXT} or a_{BET}, $v_{biotite}$ is the volume fraction of biotite in the rock and $ø_m$ is the rock matrix porosity.

In the modelling efforts in this report, all ferrous iron is assumed to be present in biotite. This is argued for in Section 5.4.1. The volume fraction of the biotite in the rock is then estimated according to:

$$v_{\text{biotite}} = \frac{f_{\text{Fe,r}}}{f_{\text{Fe,b}}}\frac{\rho_\text{r}}{\rho_\text{b}} = 0.074\ \left[\text{m}_{\text{biotite}}^3\ \text{m}_{\text{rock}}^{-3}\right] \qquad 5\text{-}4$$

where $f_{Fe,r}$ is the mean mass fraction of ferrous iron in the bulk rock, estimated in Section 5.4.1 to be 1.52 wt% in RFM029 and 1.44 wt% in RFM045, which are the two major rock domains in the Forsmark area. The mean mass fraction of ferrous iron in biotite $f_{Fe,b}$ is estimated from geochemical and oxidation factor (Mössbauer) analyses in /Sandström and Tullborg 2006a/ to be 17.3 wt% (See Appendix B.1). Bulk rock density is taken as $\rho_r = 2.656 \cdot 10^6$ [g m^{-3}] (see Section 5.1.3) and biotite density $\rho_b = 3 \cdot 10^6$ [g m^{-3}].

Based on the estimations in this section, and with a rock matrix porosity $ø_m = 0.0018$ (see Section 5.1.1) the initial specific reactive surface of biotite in the bulk rock would be within the range:

$$\left(\frac{A_{\text{biotite}}}{V}\right)_0 [\text{m}^2\ \text{L}_{\text{water}}^{-1}] = \begin{matrix} 122.82 \cdot 10^3 & (\text{based on } a_{\text{BET}}) \\ 6.141 \cdot 10^3 & (\text{based on } a_{\text{EXT}}) \end{matrix} \qquad 5\text{-}5$$

Chlorite adjacent to rock fractures has pseudomorphically replaced biotite and the size of the chlorite crystals is similar to the biotite crystals although the available reactive surface is larger due to the more porous character of chlorite (cf. Figure 3-10). The chlorite crystals also contain lenses of other secondary minerals such as titantite, adularia, prehnite and laumontite /Sandström et al. 2010/.

Fracture coatings

An average thickness of a chlorite coating is estimated in Section 5.4.2. The specific reactive surface of this pure coating is calculated from Eqn. 5-3 with the assumption that the coating possesses the same porosity as the bulk rock ($ø_c = ø_m = 0.0018$) and that the external biotite grain surface, a_{EXT} in Eqn. 5-1, applies also for chlorite.

The volume fraction of mineral in a chlorite coating is then estimated to:

$$v_{\text{chlorite}} = 1 - ø_\text{c} = 0.9982\ \left[\text{m}_{\text{chlorite}}^3 \text{m}_{\text{coating}}^{-3}\right] \qquad 5\text{-}6$$

The specific reactive surface of chlorite in fracture coatings based on the mineral grain external surface is then estimated to:

$$\left(\frac{A_{\text{chlorite}}}{V}\right)_0 [\text{m}^2\text{m}_{\text{water}}^{-3}] = 83.18 \cdot 10^3 \quad (\text{based on } a_{\text{EXT}}) \qquad 5\text{-}7$$

Pyrite is present in the rock matrix as scattered occurrences (< 0.2 vol%), often as euhedral cubic crystals. Normal crystal size of pyrite in the rock matrix is in the order of 100·100·100 µm, however, the variation is large /Drake et al. 2006/.

5.5.2 Temporal changes in the available reactive surface

As a consequence of oxidation, dissolution or other weathering processes, the specific surface of the grains decreases with time. This is frequently implemented in models by means of the shrinking core or unreacted core model, explained in the following.

The volume and available surface area of a mineral grain can be expressed as a function of a characteristic length, B. As an example we define B as the length of one of the sides of the box shaped grain in Figure 5-6. The other sides of the box can then be expressed as a function of B, e.g. B = 200 µm, $A = 2B$ = 400 µm, and $C = 0.5B$ = 100 µm. The volume and specific area (excluding the basal plane) are then $V_{grain} = ABC = 1B^3$ and $A_{grain} = 2AC + 2BC = 3B^2$. Depending on the shape of the grain, the factors 1 and 3 may differ, e.g. for a spherical grain the volume is $V_{grain} = (4/3)\pi B^3$ and the area $A_{grain} = 4\pi B^2$, where the specific length B is taken as the particle radius. The grain volume and area are thus proportional to the cube and square of the characteristic length, independently of the shape of the particle:

$$V_{grain} = \alpha B^3 \qquad 5\text{-}8$$

$$A_{grain} = \beta B^2 \qquad 5\text{-}9$$

Assuming that there are n biotite grains of this size and shape in a volume of rock, and that these grains have a mass fraction of ferrous iron $f_{Fe,b}$ [$g_{Fe}\ g_{biotite}^{-1}$], the initial concentration of ferrous iron in the rock can be expressed:

$$c_{Fe,0}\left[\mathrm{mol_{Fe}m_{rock}^{-3}}\right] = n f_{Fe,b}\frac{\rho_b}{M_{Fe}}\alpha B^3 \qquad 5\text{-}10$$

where ρ_b and M_{Fe} are the biotite density and molecular weight of iron respectively. After some time, the biotite is partially depleted of ferrous iron, which now has a concentration in the rock c_{Fe} [$\mathrm{mol_{Fe}\ m_{rock}^{-3}}$] and the unreacted core in the biotite grains has shrunk to a characteristic length b:

$$c_{Fe}\left[\mathrm{mol_{Fe}m_{rock}^{-3}}\right] = n f_{Fe,b}\frac{\rho_b}{M_{Fe}}\alpha b^3 \qquad 5\text{-}11$$

Solving Eqns. 5-10 and 5-11 for the characteristic lengths B and b:

$$B = \left(\frac{M_{Fe}}{\rho_b}\frac{c_{Fe,0}}{n\alpha f_{Fe,b}}\right)^{1/3} \qquad 5\text{-}12$$

$$b = \left(\frac{M_{Fe}}{\rho_b}\frac{c_{Fe}}{n\alpha f_{Fe,b}}\right)^{1/3} \qquad 5\text{-}13$$

The specific surface of the biotite in the rock can now be expressed as a function of the initial specific surface derived in Eqn. 5-5:

$$\frac{A_{biotite}}{V} = g\left(\frac{A_{biotite}}{V}\right)_0 \qquad 5\text{-}14$$

or (using Eqn. 5-9):

$$\frac{\beta b^2}{V} = g\left(\frac{\beta B^2}{V}\right)_0 \qquad 5\text{-}15$$

The proportionality factor g is thus $g = b^2/B^2$. Eqns. 5-12 to 5-14 then gives:

$$\frac{A_{biotite}}{V} = \left(\frac{A_{biotite}}{V}\right)_0\left(\frac{c_{Fe}}{c_{Fe,0}}\right)^{2/3} \qquad 5\text{-}16$$

5.6 Reducing capacity in the designed repository

5.6.1 Reducing minerals in crushed rock closure (> –200 m.a.s.l.)

The shallow (>–200 m.a.s.l.) parts of ramp and shafts will be backfilled with crushed rock. It is assumed in this report that this crushed rock closure possesses the same reducing capacity as the main rock types in Forsmark. In Section 5.4.1 this capacity is attributed to ferrous iron comprised in minerals in the rock. The ferrous iron content in the crushed rock closure is therefore estimated to approximately 1.5 wt%. See Table 5-5.

5.6.2 Buffer, backfill, and bentonite closure (< –200 m.a.s.l.)

The bentonite clay intended to be used as backfill for the underground openings below –200 m.a.s.l. comprises in addition to the ferrous and sulphide mineral content also approximately 0.25 wt% organic materials. See also Table 2-1 for an estimation of total amounts of organic substances in the repository volume.

The reference backfill raw material comprises 45–90 wt% of montmorillonite. Amounts of the accessory minerals comprised in different backfilling materials are listed, according to the reference design, in Table 3-2 in the **Backfill production report**. Notable is the mica/illite content estimated to 6–8 wt% in the Milos backfill.

In Table 3-6 in the **Backfill production report**, the installed dry density for the reference design backfill is calculated to $1.4 \cdot 10^6$ [g m^{-3}]. This implies approximate mica/illite content per installed backfill volume of 100 [$kg_{mica/illite}$ m^{-3}].

5.7 Oxidising capacity in recharge water

The oxygen in the intruding recharge water is a parameter that has relatively large influence on the extent of intrusion of oxygen in the rock (see e.g. Figure 8-1 for modelling results). The oxygen concentration, here denoted c_{10}, in rain water in equilibrium with the atmosphere can be calculated by Henry's law:

$$c_{10} = k_H^\circ P_{0,O_2} \qquad 5\text{-}17$$

where P_{0,O_2} is the partial pressure of oxygen at the ground surface, which is taken as 0.21 atm. The Henry's law constant for oxygen is $k_H^\circ = 10^{-2.68}$ and $10^{-2.96}$ [mol L^{-1} atm^{-1}] at 0°C and 25°C respectively. The oxygen concentration in rainwater in equilibrium with the atmosphere is then:

$$c_{10}(0°C) = 0.21 \cdot 10^{-2.68} = 0.44 \cdot 10^{-3} \text{ [mol L}^{-1}\text{]} \qquad 5\text{-}18$$

$$c_{10}(25°C) = 0.21 \cdot 10^{-2.96} = 0.23 \cdot 10^{-3} \text{ [mol L}^{-1}\text{]} \qquad 5\text{-}19$$

Based on theoretical estimations, the oxygen concentration may be higher in glacial melt water than in water equilibrated with the atmosphere. This is explained in the following.

As the glacier is forming, snow accumulates in an increasingly thick layer. With time and increasing depth of the snow cover, re-crystallisation occurs forming a coarse-grained porous firn. The pores of the firn are interconnected and thus, the gas phase composition in the pores is in equilibrium with the atmosphere. As the glacier gradually grows, the pressure increases and the pore space decreases. At some depth, the pores of the firn are no longer interconnected (close-off zone) and air is entrapped in the ice as air bubbles.

The amount of gas entrapped in the ice depends on the atmospheric pressure, pore volume per gram of ice, and the temperature at the close-off location:

$$n\left[\mathrm{mol_{gas}\ g_{ice}^{-1}}\right] = 0.10133\frac{P_c v_c}{RT_c} \qquad 5\text{-}20$$

where P_c [atm], v_c [cm^3 g^{-1}], and T_c [K] are the pressure, pore volume per gram of ice, and the temperature at the close-off location. R = 8.314 [Pa m^3 mol^{-1} K^{-1}] is the universal gas constant.

The pore volume at close-off is shown to be correlated with the temperature according to /Raynaud and Lebel 1979/:

$$v_c = 7.4\cdot10^{-4}\ T_c - 0.057 \qquad 5\text{-}21$$

The atmospheric pressure can be estimated as a function of elevation:

$$P_c = P_0 e^{-m_{air} g h_c/(kT_c)} \qquad 5\text{-}22$$

where m_{air} [kg molecule^{-1}] is:

$$m_{air} = \frac{M_{air}}{1{,}000\ N_A} \qquad 5\text{-}23$$

The product of the Avogadro's constant N_A and the Boltzmann constant k is the universal gas constant R so:

$$P_c = P_0 e^{-M_{air} g h_c/(1{,}000RT_c)} \qquad 5\text{-}24$$

From Eqns. 5-20, 5-21 and 5-24, the amount of oxygen entrapped in the ice can be expressed as a function of elevation and temperature at the close-off zone:

$$n\ [\mathrm{mol\ g_{ice}^{-1}}] = \frac{P_{0,O_2}}{R} e^{-M_{air} g h_c/(1{,}000RT_c)}\left(7.5\cdot10^{-5} - \frac{0.0058}{T_c}\right) \qquad 5\text{-}25$$

The maximum entrapped oxygen is obtained when the close-off occurs close to the ground surface, h_c = 0:

$$n\ [\mathrm{mol\ g_{ice}^{-1}}] = \frac{P_{0,O_2}}{R}\left(7.5\cdot10^{-5} - \frac{0.0058}{T_c}\right) \qquad 5\text{-}26$$

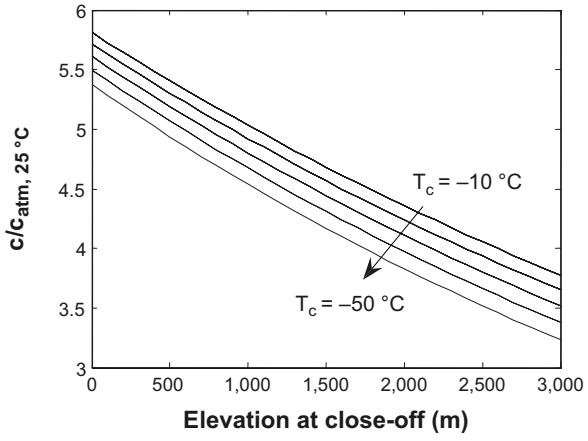

Figure 5-8. *Ratio between oxygen concentration in glacial melt water and water in equilibrium with atmospheric oxygen at 25°C as a function of elevation and temperature at close-off.*

For a partial pressure of oxygen of P_{0,O_2} = 0.21 [atm], and a temperature at close-off T_c = –10°C:

$$n = \frac{0.21}{8.314}\left(7.5 \cdot 10^{-5} - \frac{0.0058}{263}\right) = 1.34 \cdot 10^{-6}\ [\text{mol g}_{\text{ice}}^{-1}] \qquad 5\text{-}27$$

Assuming this amount is dissolved into the melt water under the ice, isolated from the atmosphere, and that one kilogram of ice equals one litre of melt water, a maximum concentration would be:

$$c_{10} = 1.34 \cdot 10^{-3}\ [\text{mol L}_{\text{w}}^{-1}] \qquad 5\text{-}28$$

A maximum recharge dissolved oxygen concentration of $c_{10} = 1.5 \cdot 10^{-3}$ [mol L_w^{-1}] is used in calculations in this report, representing glacial melt water. However, this value must be regarded as highly conservative. In Section 2.3.3 it is concluded that there are considerable photosynthetic and heterotrophic populations on most of the studied glaciers and ice sheets in the world. With these populations thriving on the glacier surface, the entrapped oxygen at the close-off zone is likely to be lower. Observations of anaerobic microbial activity in glacier surface ice blocks suggest low oxygen concentrations in these sample locations.

It may also be noted that the theoretically maximum concentration as calculated above is for ice that was formed close to the ground surface. For ice formed at higher altitude the theoretical concentration is lower. This may suggest that the highest concentrations in the melt water would occur in the beginning of the melting phase, decreasing with time. Furthermore, the melt water at the ice front is likely to be a mixture of melt water from ice formed at different altitudes.

5.8 Glacial melt water pH

Geochemical modelling and sampled data of glacial groundwater at different locations in Sweden suggests that a range of pH from 9.0 to 9.3 can be proposed for infiltrated glacial melt waters in the bedrock /Salas et al. 2010/. It is however not clear from these model results if this high pH will also prevail in the stagnant water in the pores of the rock matrix during glacial melt water ingress at Forsmark. In the calculations in this report a pH range 7.5 to 8.5 is used with a central value pH 8.0 for the base case calculations. Given that mineral dissolution and chemical reactions occurs relatively close to the flow channels this central value is deemed to be conservative.

6 Analytical oxygen ingress calculations

In Section 4, a conceptualisation of the main processes involved in the depletion of oxygen along flow paths in the rock is presented. It is evident from the complexity of the various processes that a model accounting for all relevant pathways would be extensive and complicated. Furthermore, the results from such a model would be difficult to interpret and would not be transparent. In Section 4 it was also argued that Path C would be the slowest of the parallel paths that may have a major influence on the extent of oxygen intrusion. Therefore, based on conservative constraints, Path C, shown in Figure 6-1, is chosen for the modelling efforts in the following.

The rock matrix is highly heterogeneous on a mineral grain scale, with micro-fractures of different sizes, connected inter-granular pore space, and the mineral grains themselves. In the models the averaged properties of the "real" matrix are used to define an equivalent homogeneous porous medium. This artificial matrix comprises the reducing capacity and diffusive properties of the real matrix, but homogeneously averaged over the entire volume. This should be kept in mind in the discussions regarding e.g. the redox front location or depth in the matrix, which in the model is an averaged parameter, not necessarily representative to the real redox front depth at a specific location. This is especially the case when discussing distances on the mineral grain size scale.

In Section 6.2, a simplified analytical solution is developed that is applicable when diffusion of dissolved species in the matrix limits the oxidation rate. It describes the location of the redox front along a flow path in the rock as well as in the rock matrix as a function of time of continuous supply of oxygenated water. In Section 6.3, a simplified analytical solution is developed that may be applied for a pseudo-steady state situation when the oxygen concentration fronts in the matrix and in the fracture are approximately stationary. This stationary situation develops when the diffusive and advective transport of oxygen exactly balances the oxygen depletion and the amount of reducing minerals is large.

We start by defining a set of differential equations describing the processes illustrated in Figure 6-1. These equations form the basis for the development of the analytical solutions in the subsequent sections.

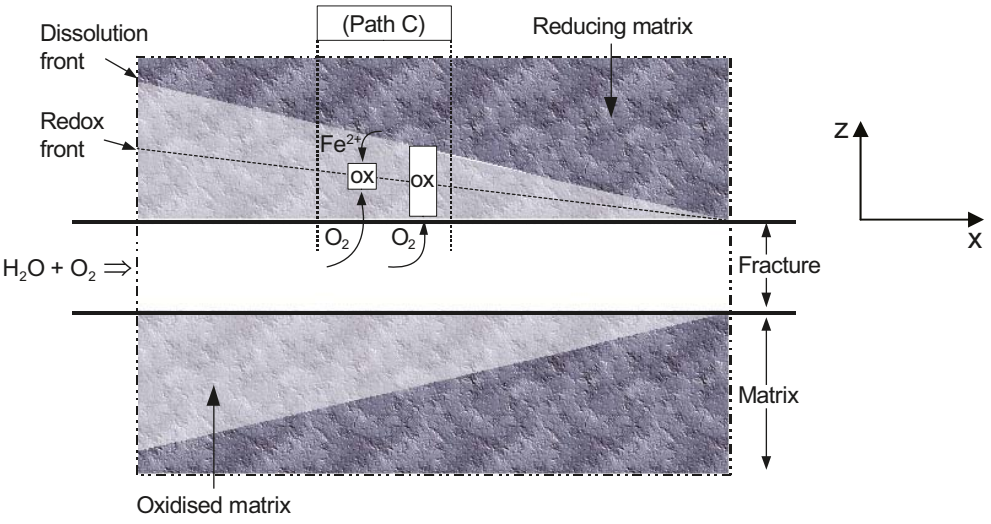

Figure 6-1. *Simplified conceptualisation used in the models.*

6.1 Governing equations

In the rock matrix, ferrous ions in biotite are assumed to dissolve into the pore solution, and react with dissolved oxygen. The matrix biotite is gradually depleted from its ferrous iron content. This process may be described by a coupled system of differential equations, one for each of the species: oxygen dissolved in the pore water c_1, ferrous ions dissolved in the pore water c_2, and ferrous iron comprised in biotite in the rock c_3:

$$\frac{\partial c_1}{\partial t} - D_\mathrm{p}\frac{\partial^2 c_1}{\partial z^2} = -f R_\mathrm{ox} \qquad \text{(Dissolved } O_2 \text{ in matrix)} \qquad 6\text{-}1$$

$$\frac{\partial c_2}{\partial t} - D_\mathrm{p}\frac{\partial^2 c_2}{\partial z^2} = R_\mathrm{diss} - R_\mathrm{ox} \qquad \text{(Dissolved } Fe^{2+} \text{ in matrix)} \qquad 6\text{-}2$$

$$\frac{\partial c_3}{\partial t} = -R_\mathrm{diss} \qquad \text{(Fe(II) in matrix)} \qquad 6\text{-}3$$

where t is the time, z is the direction into the matrix perpendicular to the flow direction in the flow path (see Figure 6-1), D_p is the diffusivity in the pores of the rock matrix, R_ox is the homogeneous reaction rate between dissolved ferrous ions and oxygen, R_diss is the volumetric dissolution rate of ferrous ions from biotite in the rock, and f is the stoichiometric factor between oxygen and ferrous ions according to the reaction formula given in Eqn. 2-29. These parameters have all been defined in Sections 2.1.2 (D_p), 2.2.1 (R_diss), and 2.2.3 (R_ox and f).

The volumetric non-oxidative dissolution rate of ferrous iron from biotite R_diss, depends on the specific reactive surface of biotite $A_\mathrm{react}/V_\mathrm{rock}$ which is estimated in Section 5.5. Thus, R_ox and R_diss can be written:

$$R_\mathrm{ox}[\mathrm{mol_{Fe}\ L_{water}^{-1}\ s^{-1}}] = k_\mathrm{r} c_1 c_2 c_\mathrm{OH}^2 - / k_\mathrm{H}^\circ \qquad 6\text{-}4$$

$$R_\mathrm{diss}[\mathrm{mol_{Fe}\ L_{water}^{-1}\ s^{-1}}] = k_\mathrm{Fe,diss}\left(\frac{A_\mathrm{biotite}}{V}\right)_0\left(\frac{c_3}{c_{30}}\right)^{2/3}\left(1-\frac{c_2}{c_{20}}\right) \qquad 6\text{-}5$$

where $(A_\mathrm{biotite}/V)_0$ is the initial specific reactive surface of biotite in the rock, c_{20} is the ferrous ion solubility in the pore water, and c_{30} is the initial concentration of ferrous iron in minerals in the rock matrix per volume of pore water.

In the fracture, dissolved ferrous ions are assumed to react with oxygen but any ferrous minerals present as fracture infill are neglected. Furthermore, dissolved oxygen and ferrous ions may diffuse into and out from the adjacent rock matrix. This process may be described by the reactive transport equations:

$$\frac{\partial c_1}{\partial t} - D_\mathrm{a}\frac{\partial^2 c_1}{\partial x^2} + v\frac{\partial c_1}{\partial x} = D_\mathrm{e}\frac{2}{\delta}\frac{\partial c_1}{\partial z}\bigg|_{z=0} - f R_\mathrm{ox} \qquad \text{(Dissolved } O_2 \text{ in fracture)} \qquad 6\text{-}6$$

$$\frac{\partial c_2}{\partial t} - D_\mathrm{a}\frac{\partial^2 c_2}{\partial x^2} + v\frac{\partial c_2}{\partial x} = D_\mathrm{e}\frac{2}{\delta}\frac{\partial c_2}{\partial z}\bigg|_{z=0} - R_\mathrm{ox} \qquad \text{(Dissolved } Fe^{2+} \text{ in fracture)} \qquad 6\text{-}7$$

where D_a, v, and δ are the diffusivity in the fracture, advective water velocity, and fracture aperture width respectively. D_e is the effective diffusivity in the rock matrix (= $\varnothing_\mathrm{m} D_\mathrm{p}$, see Section 2.1.2). Eqns. 6-8 and 6-9 are coupled with the equation system for the matrix (Eqns. 6-1 to 6-3) by the flux term of oxygen and ferrous ions at the fracture/matrix boundary $(\partial c/\partial z)_{z=0}$.

6.2 Oxidation limited by diffusion resistance

6.2.1 Simplifications

In the rock matrix

The reactive process in the rock matrix as described by Eqns. 6-1 to 6-3 is comprised by two main processes, transport and reaction. These two processes act in series, so that the slowest of them determines the overall rate of the reactive process. If the diffusion of dissolved species in the pores of the matrix is slow compared to the dissolution/reaction rates, the reactive process is thus governed by the transport resistance. This implies a sharp reaction front that propagates further into the matrix with time.

With this simplification, the system of differential equations in Eqns. 6-1 to 6-3 is reduced to one equation for reactive transport of oxygen in the matrix:

$$\frac{\partial c_1}{\partial t} - D_\mathrm{p}\frac{\partial^2 c_1}{\partial z^2} = -R(c_1) \qquad 6\text{-}8$$

where $R(c_1)$ is assumed infinite (fast reaction kinetics compared to diffusion resistance).

In the fully transient system described by Eqns. 6-1 to 6-3, the dissolution/reaction front propagates into the rock matrix with time coupled with a change in concentration profiles. If the diffusion of dissolved species in the pores of the matrix is fast compared to the front displacement, the concentration profiles are always at steady-state for a certain front location. In this report this is referred to as the pseudo-steady-state assumption. This is also discussed in Section 2.1.2. This simplification is permitted for high concentrations of ferrous minerals in the matrix when the capacity of the solid is much larger than that of the liquid in the pores /Neretnieks 1986/.

The mass rate of oxygen diffusing into the rock matrix through a fracture/matrix interfacial area A can be expressed:

$$\frac{\mathrm{d}N_{\mathrm{O}_2}}{\mathrm{d}t}\left[\mathrm{mol}_{\mathrm{O}_2}\mathrm{s}^{-1}\right] = -1{,}000 D_\mathrm{p}\text{ø}_\mathrm{m}\frac{\mathrm{d}c_1}{\mathrm{d}z}A \qquad 6\text{-}9$$

where ø_m is the porosity of the rock matrix. The oxygen transported into the matrix reacts with ferrous iron, for which a corresponding mass rate can be expressed:

$$\frac{\mathrm{d}N_{\mathrm{Fe}}}{\mathrm{d}t}[\mathrm{mol}_{\mathrm{Fe}}\mathrm{s}^{-1}] = 1{,}000\, A\frac{\mathrm{d}d}{\mathrm{d}t}c_{30}\text{ø}_\mathrm{m} \qquad 6\text{-}10$$

where dd/dt is the rate at which the front propagates into the matrix.

Correcting for the stoichiometry of the reaction between oxygen and ferrous iron, these two mass rates are equal:

$$-D_\mathrm{p}\frac{\mathrm{d}c_1}{\mathrm{d}z} = \frac{\mathrm{d}d}{\mathrm{d}t}f c_{30} \qquad 6\text{-}11$$

where f is the stoichiometric factor for the reaction between ferrous ions and oxygen.

The pseudo-steady state approximation and the approximation of a fast reaction rate at the redox front imply that the oxygen concentration gradient in the matrix can be expressed:

$$-\frac{\mathrm{d}c_1}{\mathrm{d}z} = \frac{c_{10}-0}{d} \qquad 6\text{-}12$$

By combining Eqns. 6-11 and 6-12, an expression describing the front progression rate into the matrix:

$$\frac{\mathrm{d}d}{\mathrm{d}t} = \frac{D_\mathrm{p}c_{10}}{df c_{30}} \qquad 6\text{-}13$$

The resulting expression in Eqn. 6-13 may be integrated to obtain the location of the redox front in the matrix as a function of time:

$$d = \sqrt{\frac{2D_\mathrm{p}c_{10}t}{f c_{30}}} = \sqrt{\frac{2D_\mathrm{e}c_{10}t}{f\text{ø}_\mathrm{m}c_{30}}} \qquad 6\text{-}14$$

In the fracture

Similarly as for the matrix, the reactive process in the fracture described by Eqns. 6-6 and 6-7 is comprised by two main processes, transport and reaction, the slowest of which controls the rate of the overall process. Assuming fast reaction kinetics between dissolved oxygen and ferrous iron, the reactive process described by Eqns. 6-6 and 6-7 is reduced to one equation for oxygen. Applying the approximation in Eqn. 6-12 and neglecting diffusive transport of dissolved species in the main flow direction of the fracture ($\partial^2 c_1/\partial x^2 = 0$) this equation becomes:

$$\frac{\partial c_1}{\partial t} + v\frac{\partial c_1}{\partial x} = D_e \frac{2}{\delta}\frac{\partial c_1}{\partial z}\bigg|_{z=0} = D_e \frac{2}{\delta}\frac{c_1|_{z=0}}{d} \qquad 6\text{-}15$$

Transport along the flow direction is thus assumed to be dominated by advective flow in the fracture and the reaction rate is assumed infinite.

6.2.2 Resulting analytical solution

The coupled simplified expressions in Eqns. 6-8 and 6-15 are solved by the method proposed by /Cooper and Liberman 1970/ for the case where the distance to the redox front at $x = 0$ (inlet of the fracture) is described by Eqn. 6-14 and with the following initial and boundary conditions:

$$c_1\,(x, z, t = 0) = 0$$

$$c_3\,(x, z, t = 0) = c_{30}$$

$$c_1\,(x = 0, z = 0, t) = c_{10}$$

The resulting solution describes the distance d, to the reaction front in the matrix as a function of time and distance x, downstream along the fracture:

$$d(x,t) = \sqrt{\frac{2D_e c_{10} t}{f \phi_m c_{30}}} - \frac{2D_e x}{v\delta} = \sqrt{\frac{2D_e c_{10} t}{f \phi_m c_{30}}} - \frac{2D_e x}{Ti} \qquad 6\text{-}16$$

where the relation $v\delta = Ti$ is described in Section 2.1.1.

The expression derived in Eqn. 6-16 is valid for $d > 0$, otherwise d is zero. Recalling the definition of the flow related transport resistance or the F-factor (flow wetted surface to flow rate ratio) in Section 2.1.1 (Eqn. 2-3):

$$F = \frac{A_Q}{Q_{flow}} = \frac{2L}{Ti}$$

where L is the distance along the flow path and T and i are the flow path hydraulic transmissivity and head gradient respectively. We may rewrite Eqn. 6-16 in terms of the F-factor:

$$d(x,t) = \sqrt{\frac{2D_e c_{10} t}{f \phi_m c_{30}}} - D_e F \qquad 6\text{-}17$$

It may be noted from Eqns. 6-16 and 6-17 that the F-factor determines the interaction between the flowing water and the rock matrix in this case. It should also be noted that the F-factor may be expressed as a function of the product of flow velocity and fracture aperture. However, these parameters, independently, do not influence the interaction in this case. Furthermore, the F-factor is frequently evaluated from borehole experiments whereas flow velocities and fracture apertures are difficult to estimate from experiments.

Eqn. 6-17 describes the distance d, to the reaction front in the matrix as a function of time and F-factor for the flow path. The distance d, is large for low F-factors and decreases towards zero as the F-factor increases along the flow path. We may thus calculate the F-factor for the flow path when $d = 0$:

$$F = \frac{1}{D_e}\sqrt{\frac{2D_e c_{10} t}{f \phi_m c_{30}}} = \sqrt{\frac{2c_{10} t}{f D_e \phi_m c_{30}}} \qquad 6\text{-}18$$

Figure 6-2 shows the resulting F-factor as a function of time for a ferrous iron solid concentration of $c_{30} = f_{Fe,r}\rho_r/(1{,}000\ \phi_m M_{Fe}) = 380.5$ [$mol_{Fe}\ L_{water}^{-1}$], $\phi_m = 0.0018$, $D_e = 2.1 \cdot 10^{-14}$ [$m^2\ s^{-1}$] and $f = 0.25$ [$mol_{O_2} mol_{Fe}^{-1}$] and for three different incoming oxygen concentrations.

This figure may be interpreted as follows. Assume a recharge oxygen concentration of $1.5 \cdot 10^{-3}$ mol/L_{water} at the inlet of the fracture. After 1,000 years of continuous recharge, the oxygen front has penetrated a distance in the fracture that corresponds to an F-factor of $F = 5{,}144$ yr/m or $F = 1.622 \cdot 10^{11}$ s/m. For a fracture with hydraulic transmissivity $T = 10^{-8}$ m^2/s and a hydraulic head gradient $i = 0.01$, this implies that oxygen has penetrated $L = TiF/2 = 8.11$ m after 1,000 years of continuous recharge.

The results in this section are valid for diffusion limited reactive transport. For cases when diffusion is rapid compared to dissolution and chemical reaction, the results in this section do not apply. The extent of oxygen ingress in such situations is evaluated in the following section.

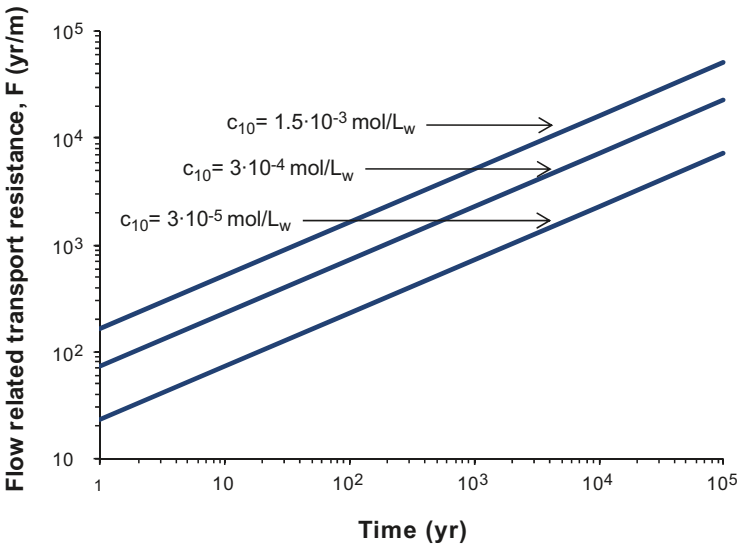

Figure 6-2. *Diffusion limited reactive transport. F-factor as a function of time for the analytical evaluation of oxygen intrusion. c_{10} denotes the incoming oxygen concentration.*

6.3 Oxidation limited by reaction kinetics

6.3.1 Simplifications

In the rock matrix

When the oxidation reaction occurs close to the fracture, the diffusion resistance of intruding oxygen into the matrix is low. Here, the depletion of oxygen is governed by reaction kinetics rather than the diffusion resistance. The oxidation of ferrous iron was conceptualised as occurring in two consecutive steps, dissolution of ferrous iron from minerals and homogeneous oxidation of dissolved ferrous iron by oxygen. The rates of these reactions are described in Eqns. 6-4 and 6-5. The overall rate is thus determined by the slower of these two processes. In the following we make the assumption that ferrous iron is depleted from the matrix domain only by reaction with oxygen. Hence, out-diffusion of dissolved ferrous iron to the fracture is neglected, which implies that the number of moles of ferrous ions dissolved equals the number of moles reacting with oxygen. We may then set the dissolution rate R_{diss} and reaction rate R_{ox} in Eqns. 6-4 and 6-5 equal and solve for the ferrous ion concentration, c_2:

$$c_2 = \frac{c_{20} k_2}{(k_2 + c_1 k_1)} \qquad 6\text{-}19$$

where $k_1 = \frac{k_r}{k_H^\circ} c_{20} c_{OH^-}^2$ and $k_2 = k_{\text{Fe,diss}} \left(\frac{A_{\text{biotite}}}{V}\right)_0 \left(\frac{c_3}{c_{30}}\right)^{2/3}$.

Next we apply the assumption that the concentration profile of oxygen reaches a steady-state for a given ferrous mineral concentration. This is permitted when the change in mineral concentration is slow. This implies that $\partial c_1/\partial t = 0$ in Eqn. 6-1. Substituting Eqn. 6-19 into the rate expression R_{ox} in Eqn. 6-4, the reactive-transport equation for oxygen in Eqn. 6-1 then reduces to:

$$D_p \frac{d^2 c_1}{dz^2} = f \frac{c_1 k_1}{1 + c_1 k_1/k_2} \qquad 6\text{-}20$$

The right-hand side of this expression describes a reaction rate that gradually changes from zero-order to first-order with decreasing oxygen concentration:

When $\frac{k_1}{k_2} c_1 \gg 1$: $\frac{c_1 k_1}{1 + c_1 k_1/k_2} \approx k_2$ (zero-order kinetics)

When $\frac{k_1}{k_2} c_1 = 1$: $\frac{c_1 k_1}{1 + c_1 k_1/k_2} \approx 0.5 k_2$ (zero-order kinetics)

When $\frac{k_1}{k_2} c_1 \ll 1$: $\frac{c_1 k_1}{1 + c_1 k_1/k_2} \approx k_1 c_1$ (first-order kinetics)

We start by studying the case when the oxygen concentration in the fracture c_{1f} (at $x = 0$) is low and the depletion of oxygen throughout the matrix domain follows first-order kinetics. The general solution to Eqn. 6-20 then becomes:

$$c_1 = a_1 e^{z\sqrt{f k_1/D_p}} + a_2 e^{-z\sqrt{f k_1/D_p}} \qquad 6\text{-}21$$

Far from the fracture ($z \to \infty$) the oxygen concentration approaches zero so the integration constant $a_1 = 0$. In the fracture ($z = 0$) the concentration is $c_1(z = 0) = c_{1f}$, so the integration constant $a_2 = c_{1f}$.

The particular solution for the concentration and concentration gradient then becomes:

$$c_1 = c_{1f} e^{-z\sqrt{f k_1/D_p}} \qquad 6\text{-}22$$

$$\frac{dc_1}{dz} = -c_{1f} \sqrt{\frac{f k_1}{D_p}} e^{-z\sqrt{\frac{f k_1}{D_p}}} \qquad 6\text{-}23$$

A general sketch of the oxygen concentration and concentration gradient profile for this case is shown in Figure 6-3.

Next we study the case when the oxygen concentration in the fracture c_{1f} (at $x = 0$) is high so that the oxygen consuming reaction changes from zero-order at high concentrations to first-order at low concentrations. The zero-order depletion is valid down to an oxygen concentration of $c_{1c} = k_2/k_1$. This concentration is reached at a distance z_c in the matrix. A sketch of the two domains is shown in Figure 6-4.

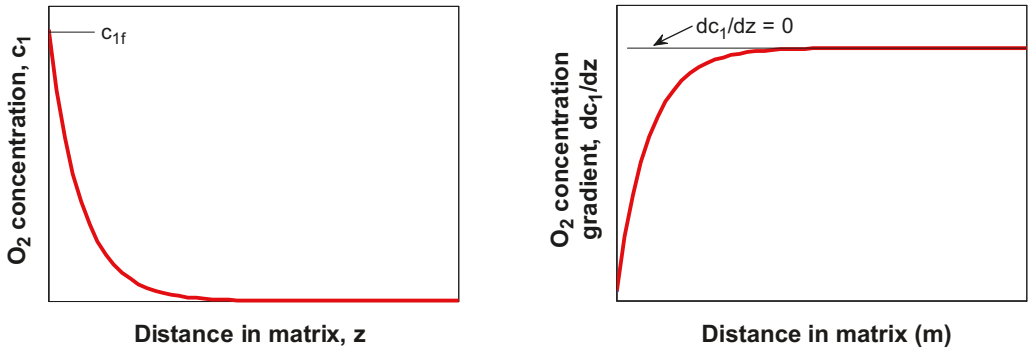

Figure 6-3. *General sketch of the O_2 concentration profile and concentration gradient profile in the matrix for the case of 1'st order reaction kinetics.*

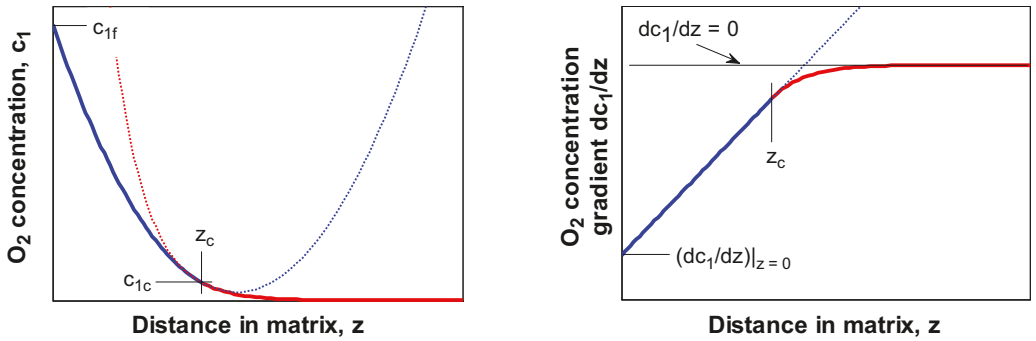

Figure 6-4. *Two spatial domains in the rock matrix where the rate of oxygen depletion is described by 0'th order kinetics (blue solid curve) and 1'st order kinetics (red solid curve).*

The general solution to Eqn. 6-20 for the zero-order case is:

$$c_1 = \frac{f}{2}\frac{k_2}{D_p} z^2 + a_3 z + a_4 \qquad 6\text{-}24$$

In the fracture ($z = 0$) the concentration is c_1 ($z = 0$) = c_{1f}, so $a_4 = c_{1f}$. The oxygen concentration and concentration gradient profiles for $z < z_c$ can then be written:

$$c_1 = \frac{f}{2}\frac{k_2}{D_p} z^2 + a_3 z + c_{1f} \qquad 6\text{-}25$$

$$\frac{dc_1}{dz} = \frac{f\ k_2 z}{D_p} + a_3 \qquad 6\text{-}26$$

For lower concentrations $c_1 < c_{1c}$ at $z > z_c$ the first-order depletion is valid.

Therefore the solution for the first-order depletion in Eqns. 6-22 and 6-23 is transposed to this case:

$$c_1 = c_{1c}\, e^{-(z-z_c)\sqrt{f k_1/D_p}} \qquad 6\text{-}27$$

$$\frac{dc_1}{dz} = -c_{1c}\sqrt{\frac{f\ k_1}{D_p}}\, e^{-(z-z_c)\sqrt{\frac{f\ k_1}{D_p}}} \qquad 6\text{-}28$$

At $z = z_c$ both the concentration and the concentration gradient profiles are continuous. Thus Eqns. 6-25 and 6-27 are equal at $z = z_c$ and so are Eqns. 6-26 and 6-28:

$$\frac{f}{2}\frac{k_2}{D_p}z_c^2 + a_3 z_c + c_{1f} = c_{1c}$$

$$\frac{f\ k_2 z_c}{D_p} + a_3 = -c_{1c}\sqrt{\frac{f\ k_1}{D_p}}$$

This algebraic system and the relation $c_{1c} = k_2/k_1$ may be solved to obtain a_3 and z_c:

$$z_c = \frac{\sqrt{D_p k_1 k_2}\sqrt{2c_{1f}k_1 - k_2} - k_2\sqrt{D_p k_1}}{\sqrt{f}k_1 k_2} \qquad 6\text{-}29$$

$$a_3 = \left.\frac{dc_1}{dz}\right|_{z=0} = -\sqrt{\frac{2fc_{1f}k_2}{D_p} - \frac{fk_2^2}{D_p k_1}} \qquad 6\text{-}30$$

In the fracture

Similarly as for the matrix we assume that the concentration profile of oxygen in the fracture reaches a steady-state for a given ferrous mineral concentration. This is permitted when the change in mineral concentration is slow. This implies that $\partial c_1/\partial t = 0$ in Eqn. 6-8. As for the matrix calculations, out-diffusion of ferrous ions in the matrix to the fracture is neglected. This implies that oxidation of dissolved ferrous iron is neglected in the fracture and occur only in the matrix. Furthermore we assume that transport of dissolved oxygen along the fracture is dominated by advection, and that diffusion of dissolved oxygen in the flow direction can be neglected. This implies that $D_a\partial^2 c_1/\partial x^2 = 0$ in Eqn. 6-8, which then reduces to:

$$v\frac{\partial c_1}{\partial x} = D_e\frac{2}{\delta}\left.\frac{\partial c_1}{\partial z}\right|_{z=0} \qquad 6\text{-}31$$

Using the relation $v\delta = Ti$ (see Section 2.1.1), this equation can be written:

$$\frac{\partial c_1}{\partial x} = \frac{2D_e}{Ti}\left.\frac{\partial c_1}{\partial z}\right|_{z=0} \qquad 6\text{-}32$$

In the previous section the concentration gradient in the matrix was derived for two cases (Eqns. 6-23 and 6-26). These expressions at $z = 0$ are applied here:

$c_1 \le c_{1c} = \frac{k_2}{k_1}$: $$\left.\frac{dc_1}{dz}\right|_{z=0} = -c_1\sqrt{\frac{f\ k_1}{D_p}} \qquad 6\text{-}33$$

$c_1 \ge c_{1c} = \frac{k_2}{k_1}$: $$\left.\frac{dc_1}{dz}\right|_{z=0} = -\sqrt{\frac{2fc_1k_2}{D_p} - \frac{fk_2^2}{D_p k_1}} \qquad 6\text{-}34$$

Eqn. 6-31 may then be solved for these two cases. We start with the solution for a low incoming oxygen concentration $c_{10} \le k_2/k_1$ at $x = 0$. For this case oxygen depletion follows first-order kinetics throughout the rock matrix and Eqn. 6-33 applies along the entire fracture. With the boundary condition $c_1(x = 0) = c_{10}$ the solution to Eqn. 6-31 then becomes:

$$c_1 = c_{10}e^{-\frac{2D_e x}{Ti}\sqrt{\frac{fk_1}{D_p}}} \qquad 6\text{-}35$$

A sketch of the concentration profile is shown in Figure 6-5a.

For the case with a high incoming oxygen concentration $c_{10} > k_2/k_1$, both Eqns. 6-33 and 6-34 apply at different distances downstream in the fracture. Eqn. 6-34 applies upstream in the fracture at $x \le x_c$ where the oxygen concentration $c_1 \ge k_2/k_1$. Eqn. 6-33 applies at $x \ge x_c$ where the oxygen concentration $c_1 \le k_2/k_1$. A sketch of the concentration profile is shown in Figure 6-5b.

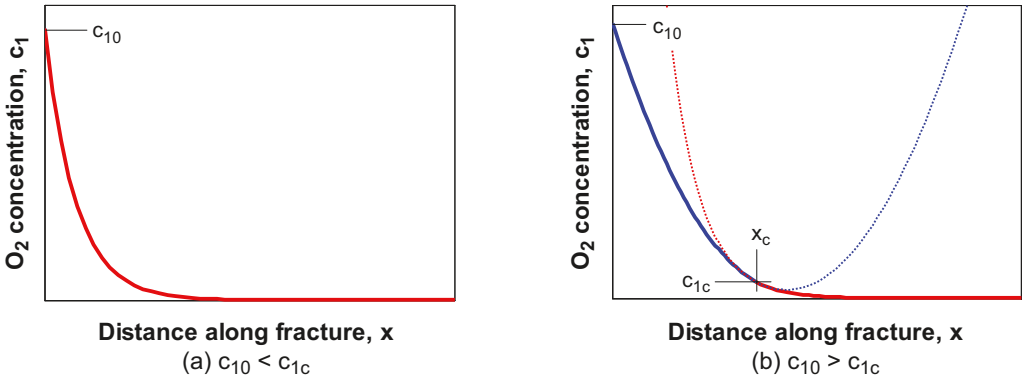

Figure 6-5. *Sketch of oxygen concentration profiles for $c_{10} < c_{1c}$ (a) and $c_{10} > c_{1c}$ (b).*

With the boundary condition $c_1(x = 0) = c_{10}$ the solution for this case at $x \leq x_c$ becomes:

$$c_1 = c_{10} - \frac{2D_e}{Ti} x \sqrt{\frac{2c_{10} f k_2}{D_p} - \frac{f k_2^2}{D_p k_1} + \frac{2D_e^2 f k_2}{D_p (Ti)^2} x^2} \qquad 6\text{-}36$$

The solution in Eqn. 6-35 is transposed to be valid for $x \geq x_c$ and with the boundary condition $c_1(x = x_c) = c_{1c}$:

$$c_1 = c_{1c} e^{-\frac{2D_e(x - x_c)}{Ti} \sqrt{\frac{f k_1}{D_p}}} \qquad 6\text{-}37$$

The distance x_c may be calculated from Eqn. 6-36 to:

$$x_c = \frac{TiD_p}{2D_e f k_2} \left(\sqrt{\frac{2c_{10} f k_1 k_2 - f k_2^2}{D_p k_1}} - \sqrt{\frac{2c_{1c} f k_1 k_2 - f k_2^2}{D_p k_1}} \right) \qquad 6\text{-}38$$

The analytical solution in Eqns. 6-35, 6-36 and 6-37 shows the relation between the concentration of oxygen in the fracture and the distance x in the flow direction. It is also apparent in these equations that the concentration is related to the flow related transport resistance or F-factor (= $2x/(Ti)$) in the fracture. With the relations $D_e = D_p \phi_m$ and $F = 2x/(Ti)$ we may rewrite the solution equations. Eqn. 6-35 valid for first-order reaction kinetics throughout the rock matrix then becomes:

$$c_1 = c_{10} e^{-F \phi_m \sqrt{D_p f k_1}} \qquad 6\text{-}39$$

For the case when both zero-order and first-order reaction kinetics control the depletion of oxygen at different locations along the fracture, a critical F-factor indicating the transition between the two domains is written based on Eqn. 6-38:

$$F_c = \frac{2x_c}{Ti} = \frac{1}{\phi_m} \left(\sqrt{\frac{2c_{10}}{f D_p k_2} - \frac{1}{f D_p k_1}} - \sqrt{\frac{2c_{1c}}{f D_p k_2} - \frac{1}{f D_p k_1}} \right) \qquad 6\text{-}40$$

The oxygen concentration upstream of this critical F-factor becomes based on Eqn. 6-36:

$$c_1 = c_{10} - F \phi_m \sqrt{2c_{10} D_p f k_2 - \frac{D_p f k_2^2}{k_1} + (F \phi_m)^2 \frac{D_p f k_2}{2}} \qquad 6\text{-}41$$

The oxygen concentration downstream of the critical F-factor becomes based on Eqn. 6-37:

$$c_1 = c_{1c} e^{-(F - F_c) \phi_m \sqrt{D_p f k_1}} \qquad 6\text{-}42$$

Eqns. 6-39 to 6-42 may thus be applied to flow paths for which the flow related transport resistance is known and they are interchangeable with Eqns. 6-35 to 6-38 when the fracture transmissivity T and gradient i (or Darcy flow velocity and fracture aperture, $Ti = v\delta$) are known.

6.4 Results for the analytical evaluation

The rate of scavenging of oxygen along a flow-path in the rock is initially limited by chemical reaction kinetics between oxygen and reducing minerals in the matrix. The extent of ingress in this situation may be estimated using the analytical solution derived in Section 6.3. For longer times when the reducing capacity in the matrix minerals adjacent to the fracture is depleted the extent of ingress may be estimated using the analytical solution derived in Section 6.2. The time to deplete the ferrous iron from the matrix minerals adjacent to the fracture is however expected to be thousands of years with a continuous supply of oxygen (see Section 2.4.1).

The base case parameters used in the following are shown in Table 6-1. When not elsewhere stated these are the parameters used also for the sensitivity analyses.

From the parameters given in Table 6-1 we may calculate other input parameters used for the base case calculations. Eqn. 2-16 gives the ferrous ion dissolution rate constant at pH 8:

$$k_{\mathrm{Fe,diss}} = 10^{-8.66} c_{\mathrm{H^+}}^{0.51} + 10^{-18.92} c_{\mathrm{H^+}}^{-0.81} = 5.5 \cdot 10^{-13} \left[\mathrm{mol_{Fe(II)}\ m_b^{-2}\ s^{-1}}\right]$$

For the pseudo-steady state calculations we assume that the ferrous iron in the matrix has not become depleted. Therefore the specific reactive surface of biotite per volume of pore water is taken as the initial specific surface. This is estimated using Eqn. 5-3:

$$\frac{A}{V} = \left(\frac{A_{\mathrm{biotite}}}{V}\right)_0 = \frac{a_{\mathrm{EXT}}\, \nu_{\mathrm{biotite}}}{1{,}000\ \text{ø}_{\mathrm{m}}} = 6{,}141 \left[\mathrm{m_b^2\ L_w^{-1}}\right]$$

The parameters k_1 and k_2 used in the analytical solution can now be calculated for the base case at pH 8:

$$k_1 = \frac{k_{\mathrm{r}}}{k_{\mathrm{H}}^{\circ}} c_{20} c_{\mathrm{OH^-}}^2 = 0.0018 \left[\mathrm{mol_{Fe(II)} mol_{O_2}^{-1}\ s^{-1}}\right]$$

$$k_2 = k_{\mathrm{Fe,diss}} \frac{A}{V} = 3.38 \cdot 10^{-9} \left[\mathrm{mol_{Fe(II)} L_w^{-1}\ s^{-1}}\right]$$

The critical oxygen concentration when the transition from zero-order kinetics to first-order kinetics is estimated for this case:

$$c_{1\mathrm{c}} = \frac{k_2}{k_1} = 1.8 \cdot 10^{-6} \left[\mathrm{mol_{O_2} L_w^{-1}}\right]$$

Table 6-1. Base case parameters for the analytical evaluation.

Parameter	Value	Unit	Description
a_{EXT}	$1.5 \cdot 10^{5}$	$\mathrm{m_b^2\ m_b^{-3}}$	External reactive surface of biotite grains (see Section 5.5.1)
c_{10}	$1.5 \cdot 10^{-3}$	$\mathrm{mol_{O_2}\ L_w^{-1}}$	Recharge oxygen concentration in glacial melt water (see Section 5.7)
c_{20}	$1.8 \cdot 10^{-6}$	$\mathrm{mol_{Fe^{2+}}\ L_w^{-1}}$	Ferrous ion solubility
D_{e}	$2.1 \cdot 10^{-14}$	$\mathrm{m^2\ s^{-1}}$	Effective diffusivity in rock matrix (see Section 5.1.2)
D_{p}	$1.17 \cdot 10^{-11}$	$\mathrm{m^2\ s^{-1}}$	Pore diffusivity in rock matrix (=$D_{\mathrm{e}}/\text{ø}_{\mathrm{m}}$)
$f_{\mathrm{Fe,r}}$	0.0144	$\mathrm{g_{Fe(II)}\ g_r^{-1}}$	Mass fraction of ferrous iron in rock (see Section 5.4.1)
k_{H}°	$1.3 \cdot 10^{-3}$	$\mathrm{mol_{O_2} L_w^{-1} atm_{O_2}^{-1}}$	Henry's law constant for oxygen (see Section 2.2.3)
k_{r}	$1.33 \cdot 10^{12}$	$\mathrm{M_{OH}^{-2} atm_{O_2}^{-1}\ s^{-1}}$	Oxidation rate constant (see Section 2.2.3)
M_{Fe}	55.845	$\mathrm{g\ mol^{-1}}$	Molecular weight for iron
pH	8.0	–	Fixed solution pH (see Section 5.8)
ø_{m}	0.0018	$\mathrm{m_w^3 m_r^{-3}}$	Rock matrix transport porosity (see Section 5.1.1)
ρ_{r}	$2.656 \cdot 10^{6}$	$\mathrm{g_r\ m_r^{-3}}$	Bulk rock density (see Section 5.1.3)
ν_{biotite}	0.074	$\mathrm{m_b^3 m_r^{-3}}$	Volume fraction of biotite in rock (vol biotite/vol rock) (=$f_{\mathrm{Fe}}\rho_{\mathrm{r}}/(f_{\mathrm{Fe,b}}\rho_{\mathrm{b}})$) (see Section 5.5.1)

The oxygen concentration and concentration gradient profiles in the rock matrix at the inlet of the fracture ($x = 0$) is shown for the base case in Figure 6-6a and b. It is seen that the oxygen penetrates to approximately six millimetres into the matrix and that zero-order reaction kinetics (blue solid curve) dominates for this case. Thus we may conclude that dissolution of ferrous minerals controls the depletion of oxygen in this case.

Downstream in the fracture, the concentration gradually decreases and we may expect a different behaviour in the rock matrix. In Figure 6-6c to h, concentration and concentration gradient profiles are shown for different fracture oxygen concentrations as expected at different locations downstream in the fracture. It is seen that when the fracture concentration has decreased to 0.3 mM the ingress is approximately three millimetres. The dissolution of ferrous iron still dominates the rate of oxygen depletion and the concentration gradient at the fracture/matrix interface (at $x = 0$) has dropped to approximately half of the gradient in Figure 6-6b. When the fracture concentration decreases further downstream in the fracture it is seen that the depletion of oxygen is increasingly controlled by first-order reaction kinetics (solid red curve). This indicates that the dissolution of ferrous ions occurs rapidly enough so that the homogeneous oxidation rate controls the depletion of oxygen.

Next we apply the analytical solution for the fracture using the solutions in Eqns. 6-39, 6-41 and 6-42. The parameters used are the same as for the matrix calculations. In Figure 6-7a the pseudo-steady state oxygen concentration profile is shown as a function of the flow related transport resistance or F-factor in the fracture using the base case parameters. In this case oxygen is estimated to penetrate a distance corresponding to an F-factor of ~9,000 yr/m along the flow-path. Incoming oxygen concentration is 1.5 mM at $F = 0$. At this location the oxygen concentration profile in the matrix corresponds to Figure 6-6a where the extent of ingress is approximately six millimetres. At an F-factor of ~5,500 yr/m the oxygen concentration has decreased to 0.3 mM as indicated in the figure. The concentration profile in the rock matrix at this location corresponds to Figure 6-6c extending approximately three millimetres into the rock matrix. Indicated in the figure is also the concentration 0.03 mM which is reached at an F-factor of ~8,500 yr/m. Here, the concentration profile in the matrix corresponds to Figure 6-6e, extending approximately one millimetre into the rock. For the base case calculation in Figure 6-7a, we may conclude that scavenging of oxygen is, in the major part of the fracture, limited by ferrous iron dissolution kinetics in the rock matrix. This is also the case for a lower recharge concentration of oxygen as shown in Figure 6-7b. The incoming oxygen concentration at $F = 0$ is in this case 0.3 mM, which approximately corresponds to water in equilibrium with the atmosphere. Oxygen may in this case be estimated to penetrate a distance corresponding to an F-factor of ~4,000 yr/m along the flow-path. With an incoming oxygen concentration of 0.03 mM, which is 10% of the concentration in equilibrium with the atmosphere, the scavenging of oxygen along the flow-path is to a larger extent limited by oxidation reaction kinetics as can be seen in Figure 6-7c. Also in this case however, scavenging of oxygen in the major part of the fracture is limited by ferrous iron dissolution kinetics in the rock matrix.

Next the sensitivity of various input parameters is studied. The proposed rate expressions for dissolution R_{diss} (see Eqn. 6-4 and Eqn. 2-16) and oxidation R_{ox} (see Eqn. 6-5) are both pH dependent. The pH in infiltrating glacial melt water is proposed to be 9.0 to 9.3 (see Section 5.8) but to what extent this is valid also in the stagnant water inside the pores of the rock matrix is not entirely clear. A pH of 8.0 is chosen for the base case. Oxygen concentration profiles in the rock matrix expected at different locations downstream in the fracture at different pH are shown in Figure 6-8. It is seen that for lower pH, oxidation kinetics become increasingly important. However, for relatively high oxygen concentrations in the fracture as in Figure 6-8a and b, ferrous iron dissolution controls the rate of oxygen scavenging in the major part of the matrix. Therefore, the effect of pH on the extent of oxygen ingress can be attributed to the pH dependence of k_{diss} in the rate expression R_{diss} (see Eqn. 6-5). For lower oxygen concentrations in the fracture as in Figure 6-8c and d, pH changes have a larger influence on the extent of oxygen ingress. This can be attributed to the quadratic pH dependence of the oxidation reaction R_{ox} (see Eqn. 6-4) which becomes increasingly important with decreasing oxygen concentrations.

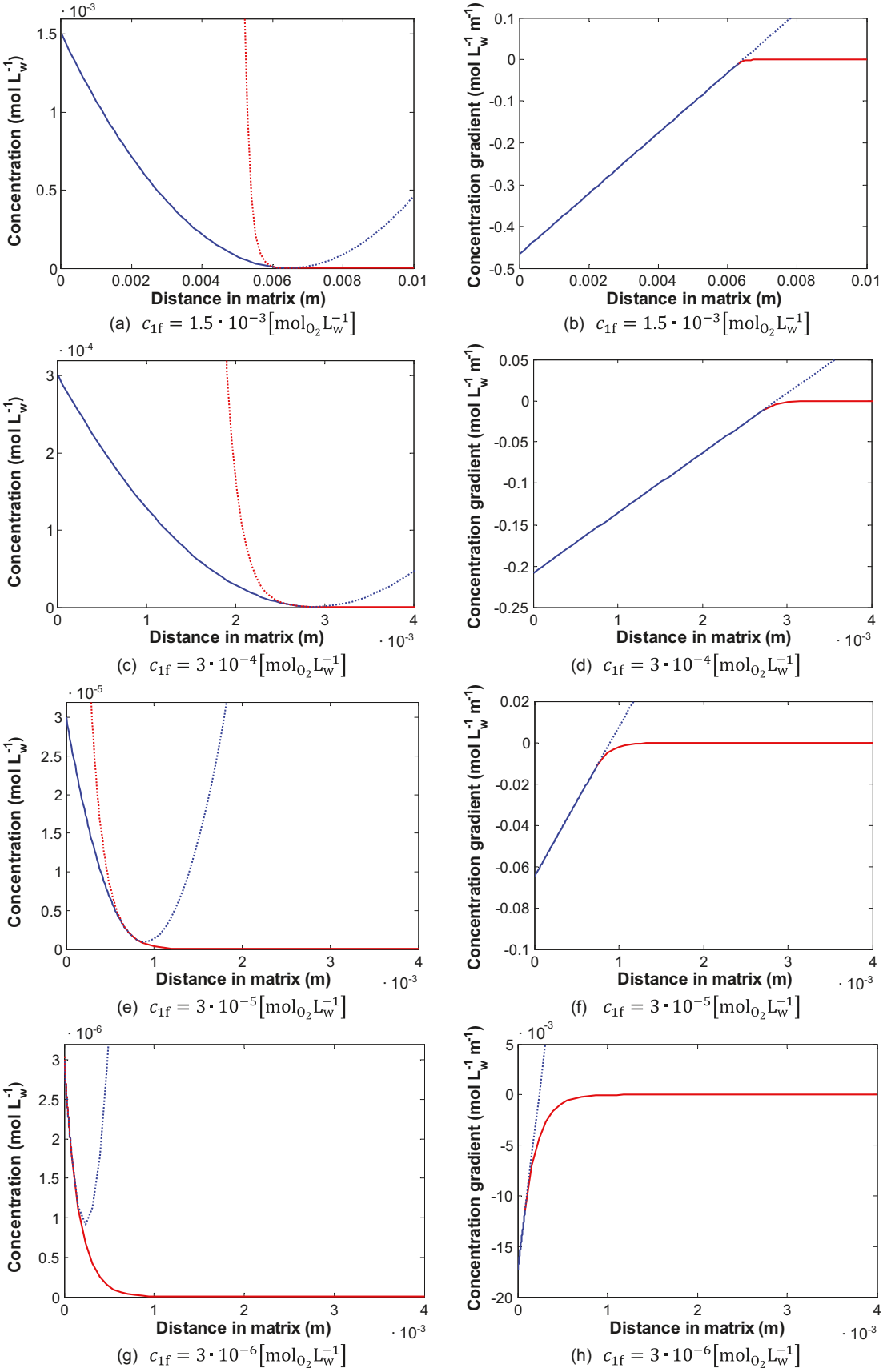

Figure 6-6. *Pseudo-steady state oxygen concentration and concentration gradient profiles expected in the rock matrix at different fracture concentrations c_{1f} at pH 8. The solution is represented by the solid curves.*

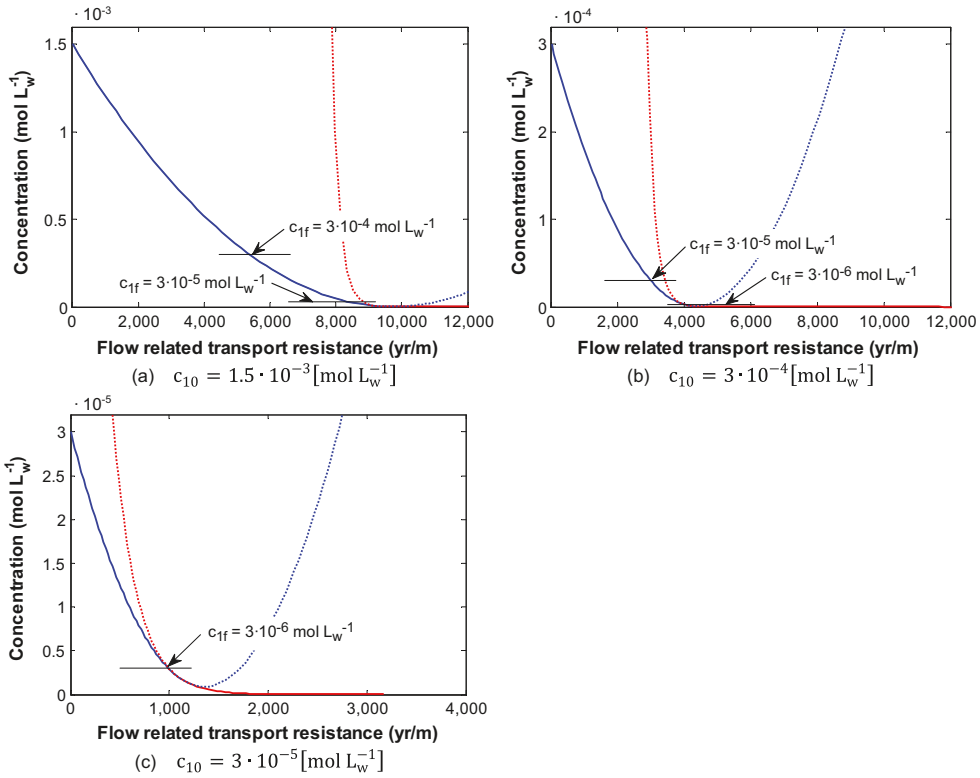

Figure 6-7. *Pseudo-steady state oxygen concentrations expected at different cumulative F-factors along a flow-path in the rock. Three different recharge oxygen concentrations, (a) 1.5mM (base case), (b) 0.3mM and (c) 0.03mM.*

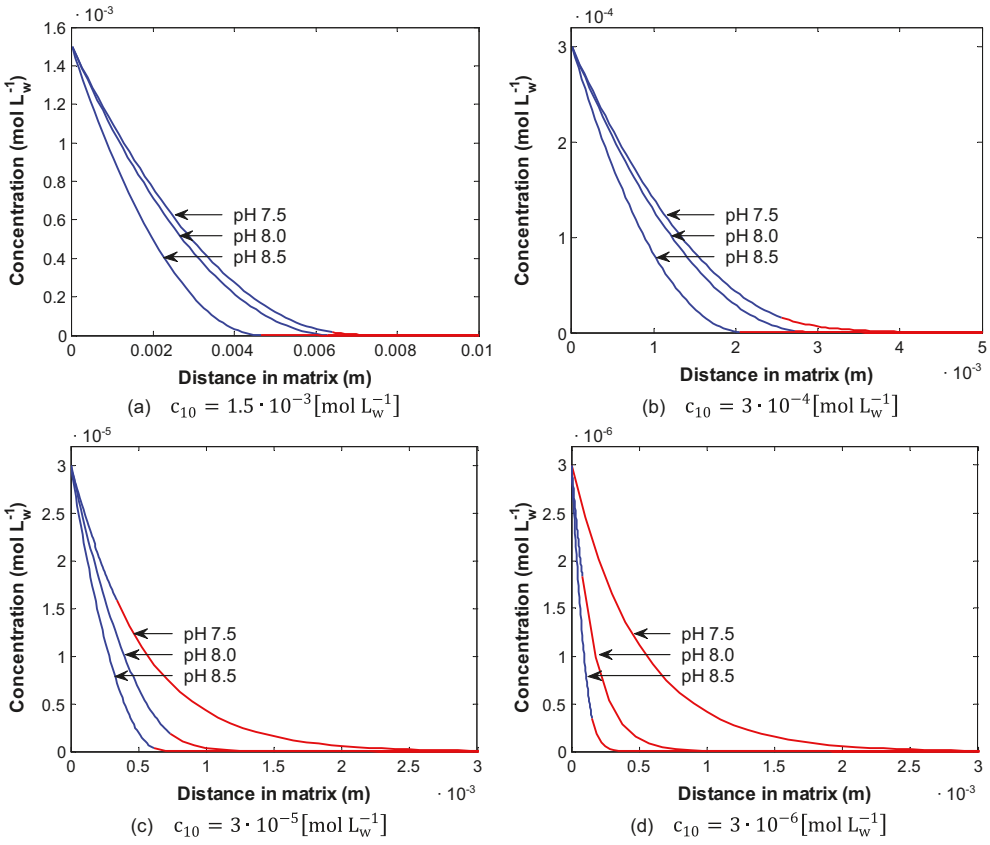

Figure 6-8. *Pseudo-steady state oxygen concentration profiles expected in the rock matrix at different fracture concentrations c_{1f} and at different pH.*

The effect of pH on the ingress of oxygen along flow paths in fractures in the rock is evaluated next. In Figure 6-9a, the recharge oxygen concentration is 1.5 mM and it is seen that dissolution kinetics in the matrix controls the scavenging of oxygen along the flow path over the entire pH range. This is also the case with a lower recharge concentration of 0.3 mM as shown in Figure 6-9b. A decreased pH from 8.0 in the base case to 7.5 has a minor effect on the extent of oxygen ingress along the flow path for these relatively high recharge concentrations. This is explained by the relatively small change in k_{diss} in the pH range 7.5 to 8.0 (see Figure 2-4). For a low recharge concentration as in Figure 6-9c, a decreased pH has a relatively large impact, due to the quadratic pH dependence of R_{ox} which for lower oxygen concentrations become increasingly important.

With the base case parameterisation, it is concluded that dissolution kinetics has a large influence on the scavenging of oxygen. Therefore, the available specific reactive surface of biotite in the rock matrix would be expected to have a large influence on the extent of oxygen ingress. Oxygen concentration profiles are shown in Figure 6-10 for different recharge oxygen concentrations and for a range of assumed available specific surface areas of biotite. As expected, the reactive surface area has a relatively large influence on the ingress of oxygen along the flow path for high recharge oxygen concentrations as in Figure 6-10a and b. Increasing the specific reactive surface by a factor of four results in a halved oxygen ingress along the flow path. For lower recharge oxygen concentrations the influence of reactive surface area decreases as oxidation reaction kinetics become increasingly important in the scavenging of the oxygen. If the oxidation reaction alone limits the scavenging of oxygen, a change in the reactive surface would have no effect on the extent of intrusion. This would be the case for very low oxygen concentrations (e.g. in the situation in Figure 6-8d at pH 7.5).

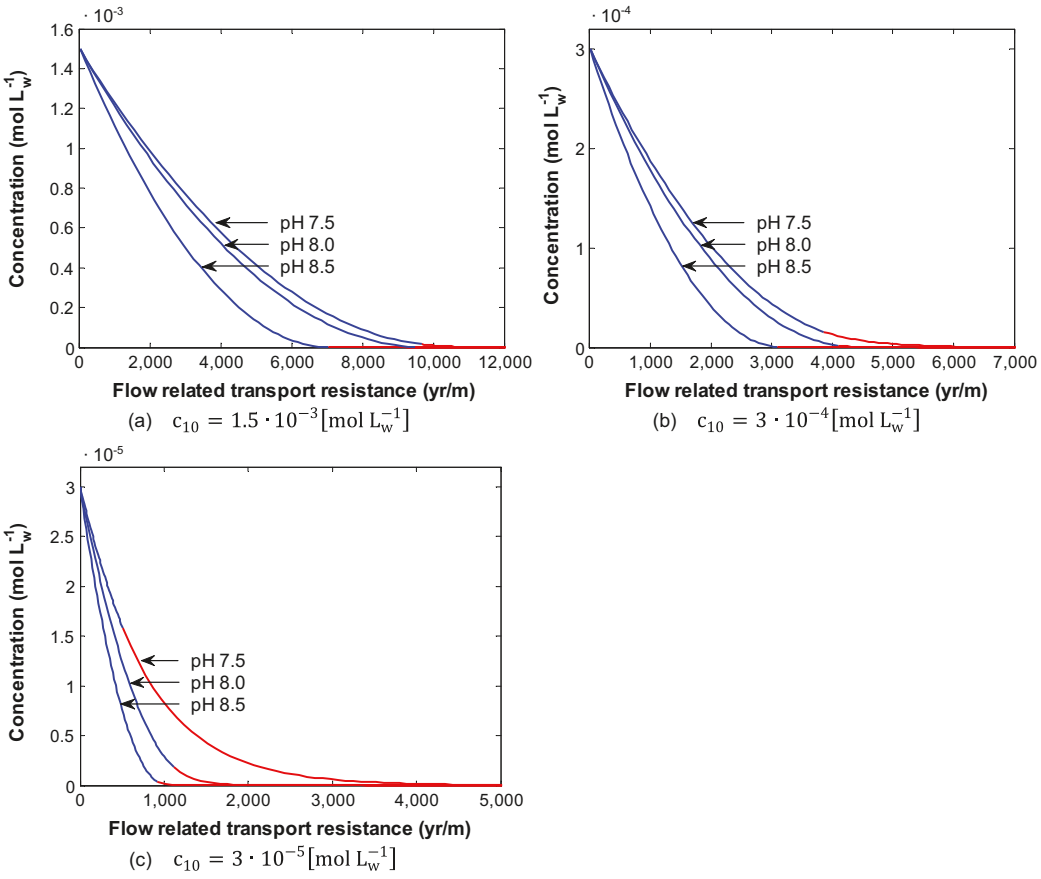

Figure 6-9. *Pseudo-steady state oxygen concentration profiles expected at different cumulative F-factors along a flow path in the rock for different recharge oxygen concentrations and at different pH.*

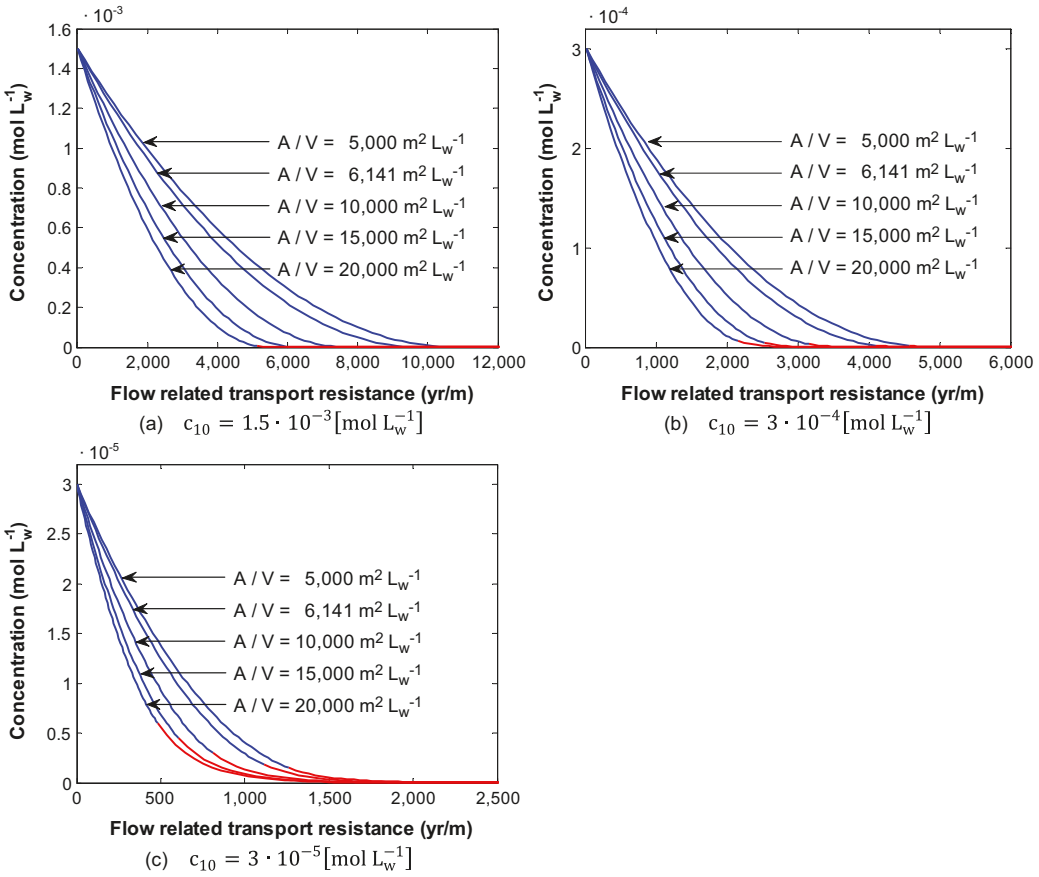

Figure 6-10. *Pseudo-steady state oxygen concentration profiles expected at different cumulative F-factors along a flow path in the rock for different recharge oxygen concentrations and at different available specific surface areas.*

In the base-case calculations the rock matrix porosity and effective diffusivity used are valid for unaltered and unfractured rock. In Sections 5.1.1 and 5.1.2 it is suggested that the porosity and the effective diffusivity in the altered zone adjacent to fractures is higher compared with the base-case situation. With an effective matrix diffusivity of $D_e = 7.2 \cdot 10^{-14}$ m^2 s^{-1} and a porosity of 0.0075 $\mathrm{m_w^3 m_r^{-3}}$, the pore diffusivity in the matrix is $D_p = 9.6 \cdot 10^{-12}$ m^2 s^{-1} and the available specific reactive surface becomes $A/V = 1{,}474\ \mathrm{m_b^2 L_w^{-1}}$. The oxygen concentration profiles in the matrix at the inlet of the flow-path (at $F = 0$) is shown for this case in Figure 6-11 together with results for the base-case for different boundary oxygen concentrations in the fracture at pH 8.0. The oxygen concentration profile along the flow-path is shown for different recharge oxygen concentrations in Figure 6-12.

As a result of the decreased pore diffusivity and specific reactive surface, oxygen penetrates further into the matrix compared with the base-case. This is seen in Figure 6-11. Despite the lower concentration gradient at the fracture/matrix interface, it is seen in Figure 6-12 that the oxygen ingress along the flow-path is lower compared to the base-case. This is because the flux term (the effective diffusivity times the concentration gradient) over the fracture/matrix boundary is larger than in the base-case. The ingress is approximately half of that in the base-case for a recharge concentration of 1.5 mM.

The simplifications underlying the analytical solution are tested against results obtained from numerical simulations using PHREEQC (1D results for matrix concentrations profiles) and PHAST (2D results for the flow path and matrix concentration profiles). The PHREEQC 1D calculations for the matrix and the PHAST 2D calculations for the fracture and matrix are explained in detail in Section 7. As a validation of the analytical solution comparative results are presented in Appendix E.

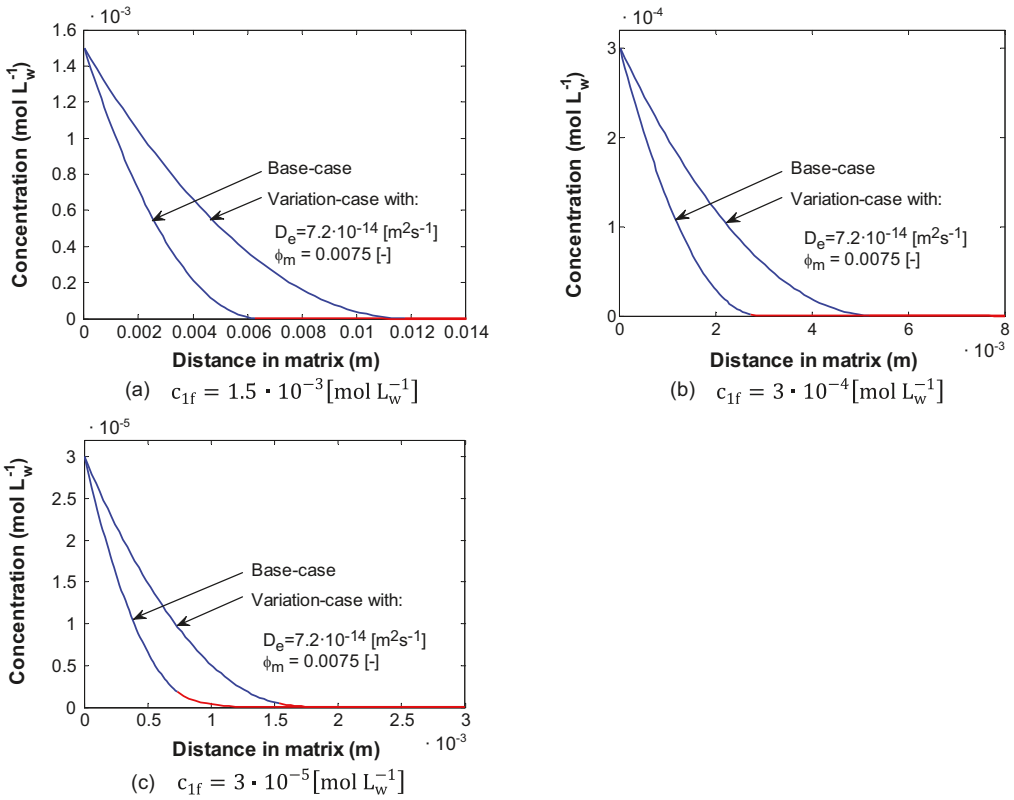

Figure 6-11. *Pseudo-steady state oxygen concentration profiles expected in the rock matrix at different fracture concentrations c_{1f} for the base-case and a variation-case with higher porosity and effective diffusivity.*

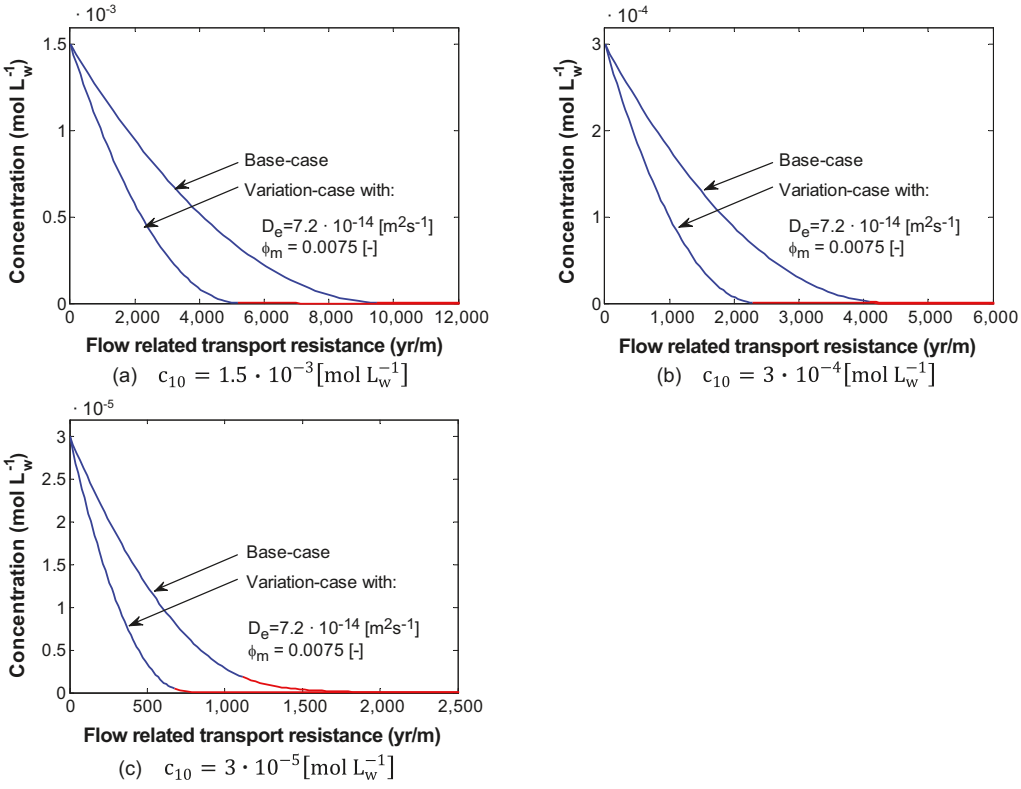

Figure 6-12. *Pseudo-steady state oxygen concentration profiles expected at different cumulative F-factors along a flow path in the rock for different recharge oxygen concentrations for the base-case parameters and a variation-case with higher porosity and effective diffusivity.*

7 Numerical oxygen ingress calculations

Numerical models with the ability to handle more complex chemistry are developed in this section. The numerical model is used to test different hypotheses, such as the effect of increased reaction kinetics (e.g. due to microbial activity or pH drift), and decreased reaction kinetics (e.g. due to limited available reactive surfaces and pore clogging of secondary minerals).

7.1 Background and state of the art

The oxygen penetration in fractured crystalline rocks has been explored by means of reactive transport models that incorporated a variety of processes /Glynn and Voss 1999, Guimerà et al. 1999, 2006, MacQuarrie et al. 2010, Sidborn and Neretnieks 2008, Spiessl et al. 2008/. The conceptual models may differ with regard to the flow system or which reaction and transport processes are considered.

Characterising low permeability fractured media is a complex task because hydraulic conductivity can vary over several orders of magnitude within short distances. Variability is caused by fractures or fractured zones that are interconnected and strongly condition the groundwater flow, as most of the flow is carried through a limited number of major fractures. Because of these difficulties, a number of approaches have been developed /Bodin et al. 2003, Knudby and Carrera 2005, Selroos et al. 2002/. They can be classified into three groups: continuum porous models that do not describe fracture geometry, discrete fracture network models that reproduce all fractures while usually ignoring the matrix, and an intermediate approach that consists of an explicitly modelled hydraulically dominant fracture that is embedded in a 3-D continuum model representing minor fractures. This concept combines the simplicity of simulating a continuum domain and while taking into account the main fractures or fractured zones which carry most of the water.

This last approach is the most commonly used for reactive transport modelling of fractured crystalline rock. Depending on the considered dynamic mechanisms (advection and/or diffusion) and the geochemical reactions considered either in the fracture, and/or the fracture coating and/or the matrix, conceptual approaches may differ widely /MacQuarrie et al. 2010/ (Table 7-1). Also, the dimensions of the system (fracture and matrix size) may be very different, from centimetre scale to hundreds of metres.

The primary objectives of these models are to provide a greater understanding of the basic processes controlling the transport of O_2 and to identify the important parameters controlling oxygen ingress and the uncertainty associated with these parameters. The results of the uncertainty analyses indicate the most important parameters controlling oxygen ingress. The results depend also on the physical and geochemical conceptual model implemented. Numerical models may involve complex systems, but some simplifications are often needed to minimize CPU times. This is the reason analytical solutions are sometimes preferred to assess the problem /Sidborn and Neretnieks 2008/, even though the geochemical system is simplified.

The objective of the numerical evaluation in this section is twofold:

- To validate the analytical solution developed in this report to assess the ingress of oxygen in fractured crystalline rock.
- To perform a sensitivity analysis on key parameters and determine their influence on the extent of oxygen penetration along a recharge flow path.

Table 7-1. Summary of reactive transport models for oxygen depletion in fractured crystalline rocks (OF, FF, FZ stand for open fracture, filled fracture or fracture zone respectively).

		Advective-dispersive zone				Diffusive zone			
		OF, FF, FZ	**length**	**O_2 reacts with**	**Complexity of the geochemical model**	**Matrix and coating**	**width**	**O_2 reacts with**	**Complexity of the geochemical model**
/Guimerà et al. 1999/	1D	FF	500 m	chlorite	equilibrium or first-order kinetic dissolution of mineral, secondary minerals, pH buffering.	–	–	–	–
	1D	–	–	–	–	matrix	infinite	biotite and/ or pyrite	equilibrium or first-order kinetic dissolution of mineral, secondary minerals, pH buffering.
	2D	FF	500 m	chlorite	first-order kinetic dissolution of mineral, secondary minerals, pH buffering.	matrix	350 m	biotite and/ or pyrite	first-order kinetic dissolution of mineral, secondary minerals, pH buffering.
/Glynn and Voss 1999/	2D	OF	500 m	–	–	matrix	–	biotite	dissolution rate.
/Guimerà et al. 2006/	1D	FF	400 m	annite	first-order dissolution rate of mineral depending on pH, secondary mineral precipitation, pH buffering.	–	–	–	–
	1D	–	–	–	–	matrix	infinite	annite	first-order dissolution rate of mineral depending on pH, secondary mineral precipitation, pH buffering.
/Sidborn and Neretnieks 2008/	analytical solutions	OF	infinite	–	–	coating	fixed coating + infinite matrix	biotite and chlorite	first-order dissolution rate of mineral at fixed pH.
	analytical solutions	OF	infinite	–	–	matrix	infinite	biotite	first-order dissolution rate of mineral at fixed pH.
/Spiessl et al. 2008/	2D	OF	500 m	chlorite	irreversible monod type dissolution rate; secondary mineral precipitation.	coating +matrix	3 m	biotite and pyrite	irreversible monod type dissolution rate; secondary mineral precipitation.
	2D	FZ	500 m	chlorite	irreversible monod type dissolution rate; secondary mineral precipitation.	matrix	3 m	biotite and pyrite	irreversible monod type dissolution rate; secondary mineral precipitation.
/MacQuarrie et al. 2010/	2D	FF	500 m	chlorite	zero-order dissolution rate of mineral with monod-type inhibition term for low O_2-concentration.	matrix	50 m	biotite	zero-order dissolution rate of mineral with monod-type inhibition term for low O_2-concentration.
	2D	FZ	500 m	chlorite	zero-order dissolution rate of mineral with monod-type inhibition term for low O_2-concentration.	matrix	50 m	biotite	zero-order dissolution rate of mineral with monod-type inhibition term for low O_2-concentration.

7.2 Conceptual model for the numerical evaluation

A general conceptualisation of the processes that are deemed to influence the extent of oxygen ingress along a fracture with oxygen-containing recharge groundwater is presented in Section 4. Based on this conceptualisation, the number of processes considered in the modelling efforts in this report was conservatively reduced in Section 6, so that only the slowest oxygen scavenging pathways are accounted for. It should be emphasised that other oxygen scavenging processes than those included in the modelling evaluation, may act in parallel and further reduce the extent of oxygen ingress.

A sketch of the modelled processes as well as the boundaries of the modelled domains is shown in Figure 7-1. The numerical evaluation strictly follows the conceptualisation used in Section 6, without the simplifications underlying the analytical evaluation. The numerical models can be described by the coupled equation system in Eqns. 6-1 to 6-7. This implies that the dissolution/reaction front indicated in Figure 7-1 is no longer sharp, as in the diffusion limited case in Section 6.2, but diffuse. The width of the diffuse front is determined by the relative rates between transport and reaction in the matrix.

These equations are implemented into two different numerical models. The main difference between the models is the dimensions of the modelled domains. The solutions are compared to the results of the analytical solution developed previously in Section 6.

The characteristics of the two different numerical models are summarised below:

- **Model 1:** 1D model that represents the rock matrix adjacent to the fracture at the location of recharge (domain indicated in blue in Figure 7-1). The processes considered are: diffusion of dissolved species, kinetic dissolution of iron-bearing minerals and kinetic oxidation of aqueous ferrous iron.
- **Model 2:** 2D dual-porosity transport model (domain indicated in red in Figure 7-1). The processes considered are: advection, diffusion of dissolved species and kinetic oxidation of aqueous ferrous iron in the fracture; diffusion of dissolved species, kinetic dissolution of iron-bearing minerals and kinetic oxidation of aqueous ferrous iron in the matrix.

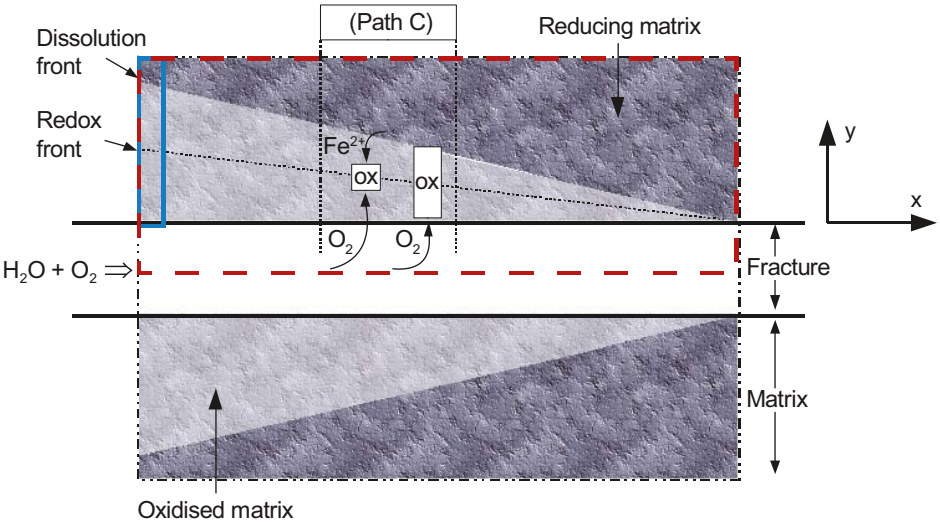

Figure 7-1. Conceptual sketch of oxygen intrusion along a fracture with adjacent reducing rock matrix. The blue rectangular domain delimits the system for Model 1 and the red dashed rectangular domain delimits the system for Model 2.

7.3 Numerical codes and approaches available

7.3.1 PHREEQC

PHREEQC /Parkhurst and Appelo 1999/ is a geochemical computer code for simulating chemical reactions and transport processes in natural or polluted groundwaters. It is based on equilibrium chemistry of aqueous solutions interacting with minerals, gases, solid solutions, ion exchangers and sorption surfaces. It also includes the capability of modelling kinetic reactions with rate equations specified by the users. Moreover, it includes an explicit finite difference algorithm for calculations of 1-D advective-dispersive transport and optionally, diffusion in stagnant zones. PHREEQC can simulate solute transport in fractured bedrock aquifers that can be conceptualised as dual-porosity flow systems subject to one-dimensional advective-dispersive transport in the bedrock fractures and diffusive transport in the bedrock matrix. These can be performed in two ways:

- Dual-porosity transport model that uses a finite-difference approach to simulate the transfer between one-dimensional advective-dispersive transport in the bedrock fractures and diffusive transport in the bedrock matrix. The accuracy of the methods has been discussed by /Lipson et al. 2007/.
- Dual-porosity transport model that uses single rate mass transfer between the advective-dispersive and the diffusive zones.

PHREEQC is used for Model 1, the 1D matrix diffusion model.

7.3.2 PHAST

PHAST /Parkhurst et al. 2004/ is a 3D multicomponent reaction-transport code, which can be used to simulate transient groundwater flow with or without geochemical reactions. This reactive transport model code solves problems with the finite differences method. The reaction-transport equations are solved by using a sequential approach in which transport and reaction are divided into separate calculations for each time step. First the components are transported and then geochemical reactions are calculated. The solute-transport simulator HST3D is used for the transport calculations and the program PHREEQC is used for the geochemical calculations. The advantage of this code is the ability to simulate more complex hydrodynamic situations with respect to the possibilities of PHREEQC.

This code is used for Model 2, the 2D dual-porosity transport model.

7.4 Implementation of the model

7.4.1 Model 1: 1D matrix diffusion model

Model 1 represents the reducing rock matrix adjacent to the fracture (See Figure 7-1). The fracture is not included in this 1D model and therefore no advective transport is considered. Solute transport occurs exclusively by diffusion in the pores of the rock matrix.The rock matrix is implemented as a homogeneous porous medium with averaged properties such as the porosity, initial reducing capacity, and the initially available specific reactive surface areas. The calculations assume that the recharge water concentrations (transversally flowing along a theoretical fracture zone on the model boundary) remain constant during the simulation time. Therefore, prescribed boundary conditions have been applied in the first cell of the model. On the other hand, the initial porewater solution has been considered to be in equilibrium with the reducing minerals comprised in the rock matrix and, consequently, no oxygen is present.

Figure 7-2 represents a schematic view of the discretisation of the numerical system, with examples of initial (IC) and boundary (BC) conditions for Case 1 (without coating as a reactive material zone in the first block of the system), and Case 2 (with coating included).

The size of the cells has to be small enough so that the concentration gradients can be properly described. A grid of 80 cells has been considered (with a constant dx of 0.125 millimetres) and test runs were carried out to ensure that a sufficiently fine grid is used. These tests are explained in Section 7.5 and Appendix D. A discussion regarding the time discretisation is also included in Appendix D.

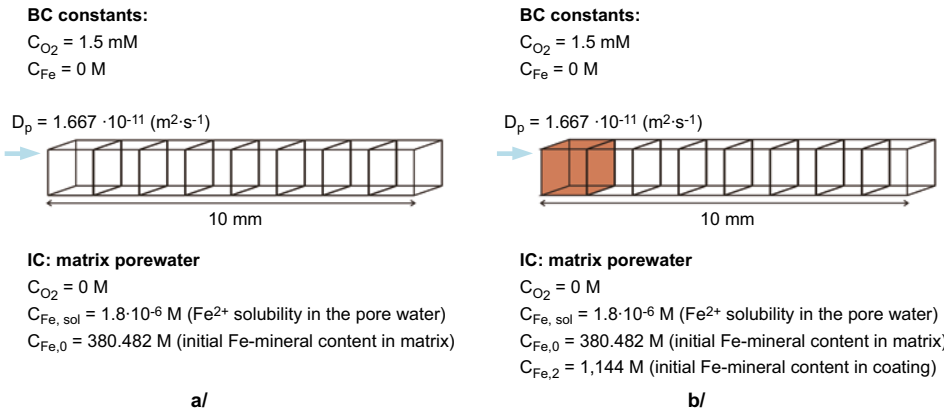

Figure 7-2. *Conceptual sketch of the numerical 1D model (Model 1), representing the porous rock matrix adjacent to the fracture zone; a/ Case 1 (without coating) and b/ Case 2 (including a coating layer).*

In Case 1 (Figure 7-2a), the flowing water in the fracture interacts directly with the homogeneous rock matrix. In Case 2 (Figure 7-2b), an additional material zone (coating) associated to alteration zones around fractures has been added between the "non altered rock matrix" and the fracture zone. The coating layer is mineralogically characterised by a higher ratio of iron-bearing mineral than the remaining porous matrix. On the other hand, the reactive surface area of this mineral is also higher in the coating layer (Table 7-2 and Table 7-3). The transport and the geochemical parameters used in both cases (Table 7-2 and Table 7-3) are the same as those used for the analytical solution described in Section 6.

Table 7-2. Parameters used in the so-called "Base Case" for Case 1 of Models 1 and 2.

	Parameter	Value	Unit	Description
Model 1 dimensions	L_y	0.01	m	Length of the domain
	dy	0.125	mm	Space discretisation ($dy = L_y/N_{cell}$)
	N_{cell}	80	–	Number of cells
Model 2 dimensions	L_x	20	m	Length of the domain in x-direction
	dx	0.1–0.5	m	Non-uniform space discretisation in x-direction
	N_{cell}	46	–	Number of cells in x-direction
	L_y	0.01	m	Length of the domain in y-direction
	dy	0.05–0.5	mm	Non-uniform space discretisation in y-direction
	N_{cell}	25	–	Number of cells in y-direction
Transport parameters	$ø_m$	0.0018	–	Porosity in matrix (Section 5.1.1)
	D_e	$2.1\cdot10^{-14}$	m^2s^{-1}	Effective diffusivity (Section 5.1.2)
	D_p	$1.17\cdot10^{-11}$	m^2s^{-1}	Pore diffusivity ($D_p = D_e/ø_m$)
Chemical parameters	$f_{Fe,m}$	0.0144	g g^{-1}	Mass fraction of ferrous iron in rock matrix (Section 5.4.1)
	ρ_r	$2.66\cdot10^{6}$	g m^{-3}	Bulk rock density (Section 5.1.3, Rock Code 101057)
	M_{Fe}	55.845	g mol^{-1}	Molecular weight of iron
	$c_{Fe,0}$	380.482	mol L_{water}^{-1}	Initial Fe(II) solid concentration in matrix ($=f_{Fe,m}\rho_r/(1{,}000\ M_{Fe}ø_m)$)
	$c_{Fe,sol}$	$1.8\cdot10^{-6}$	mol L_{water}^{-1}	Initial concentration of Fe^{2+} in the matrix porewater
	$(A/V)_0$	6,141	$m^2L_{water}^{-1}$	Initial specific surface area in matrix (see Section 5.5.1)
	$c_{Fe,sol,m}$	$1.8\cdot10^{-6}$	mol L_{water}^{-1}	Ferrous ion solubility in the matrix pore water
	k_{diss}	$5.45\cdot10^{-13}$	$mol_{Fe}m^{-2}s^{-1}$	Non-oxidative Fe(II) dissolution rate constant (Eqn. 6-5)
	k_r	$1.33\cdot10^{12}$	$M^{-2}atm^{-1}s^{-1}$	Homogeneous oxidation rate constant (see Eqn. 6-4)
	k°_H	$1.3\cdot10^{-3}$	mol $L^{-1}atm^{-1}$	Henry's law constant for oxygen (see Eqn. 6-4)
	c_{OH}	$1\cdot10^{-6}$	mol L_{water}^{-1}	OH^- concentration (see Eqn. 6-4)
	pH	8.0	–	Fixed pH
	c_{O_2}	$1.5\cdot10^{-3}$	mol L_{water}^{-1}	Boundary O_2 concentration (see Section 5.7)

Table 7-3. Parameters used in the so-called "Base Case" for Case 2 of Models 1 and 2.

	Parameter	Value	Unit	Description
Model dimension	L_x	20	m	Length of the fracture in x-direction
	L_y	0.01	m	Length of the domain in y-direction
	$L_{y,coating}$	0.0002	m	Pure chlorite coating thickness
	dy	0.0001	m	Space discretisation ($dy = L_y/N_{cell}$)
	N_{cell}	100	–	Number of cells in y-direction
Transport parameters	$ø_m$	0.0018	–	Porosity in matrix (Section 5.1.1)
	D_e	$2.1 \cdot 10^{-14}$	$m^2 s^{-1}$	Effective diffusivity (Section 5.1.2)
	D_p	$1.17 \cdot 10^{-11}$	$m^2 s^{-1}$	Pore diffusivity ($D_p = D_e/ø_m$)
Chemical parameters	$f_{Fe,m}$	0.0144	$g\ g^{-1}$	Mass fraction of Fe(II) in rock matrix (see Section 5.4.1)
	$f_{Fe,coating}$	23	$g\ m^{-2}$	Mass of Fe(II) per chlorite coated fracture surface area
	ρ_r	$2.66 \cdot 10^6$	$g\ m^{-3}$	Bulk rock density (Section 5.1.3, Rock Code 101057)
	M_{Fe}	55.845	$g\ mol^{-1}$	Molecular weight of iron
	$c_{Fe,1}$	380.482	$mol\ L_{water}^{-1}$	Initial Fe(II) solid concentration in matrix ($= f_{Fe,m}\rho_r/(1{,}000\ M_{Fe}ø_m)$)
	$c_{Fe,2}$	1,144.0	$mol\ L_{water}^{-1}$	Initial Fe(II) solid concentration in coating ($= m_{Fe}/(1{,}000\ M_{Fe}ø_m d_{coating})$)
	$c_{Fe,sol}$	$1.8 \cdot 10^{-6}$	$mol\ L_{water}^{-1}$	Initial concentration of Fe^{2+} in the matrix porewater
	$(A/V)_0$	6,141	$m^2 L_{water}^{-1}$	Initial specific surface area in matrix (see Section 5.5.1)
	$(A/V)_{coating}$	83,333	$m^2 L_{water}^{-1}$	Initial specific surface area in coating
	$c_{Fe,sol,m}$	$1.8 \cdot 10^{-6}$	$mol\ L_{water}^{-1}$	Ferrous ion solubility in the matrix pore water
	k_{diss}	$5.45 \cdot 10^{-13}$	$mol_{Fe} m^{-2} s^{-1}$	Non-oxidative Fe(II) dissolution rate constant (Eqn. 6-5)
	k_r	$1.33 \cdot 10^{12}$	$M^{-2} atm^{-1} s^{-1}$	Homogeneous oxidation rate constant (see Eqn. 6-4)
	k°_H	$1.3 \cdot 10^{-3}$	$mol\ L^{-1} atm^{-1}$	Henry's law constant for oxygen (see Eqn. 6-4)
	c_{OH}	$1 \cdot 10^{-6}$	$mol\ L_{water}^{-1}$	OH^- concentration (see Eqn. 6-4)
	pH	8.0	–	Fixed pH
	c_{O_2}	$1.5 \cdot 10^{-3}$	$mol\ L_{water}^{-1}$	Boundary O_2 concentration (see Section 5.7)

7.4.2 Model 2: 2D dual-porosity transport model

The double porosity system has been implemented to be solved with the PHAST code /Parkhurst et al. 2004/. The modelled domain (see Figure 7-3a and b) is composed by (1) a fracture represented by a linear group of grid blocks, and (2) the adjacent matrix, represented by a sheet of grid blocks. Along the fracture zone, the transport of solutes takes place by advection and molecular diffusion. However, the transport of solutes to the porous matrix takes place only by diffusion, according to the Fick's second law. The hydraulic conductivity in the matrix cells is set to be low to mimic the conductivity of a non-fractured host rock, in order to consider negligible advective transport of solutes. Conceptually, the transport mechanisms and the geochemical reactions in the matrix cells are implemented the same way as in Model 1 (Table 7-2 and Table 7-3).

In the present study, 180 days have been implemented as the simulation time. The fracture length included in the model is 20 m, and a non-uniform grid has been used (Figure 7-3). As commented for Model 1, the domain discretisation has been refined enough so that the concentration front was represented by decreasing values in several adjacent grid blocks. In this way, the domain has been divided in 1,150 cells, with incremental values for *dx* (from 0.1 to 0.5 metres) and *dy* (from 0.05 to 0.5 millimetres). Test runs were carried out to ensure that a sufficiently fine grid was used. These tests are explained in Section 7.5 and in Appendix D.

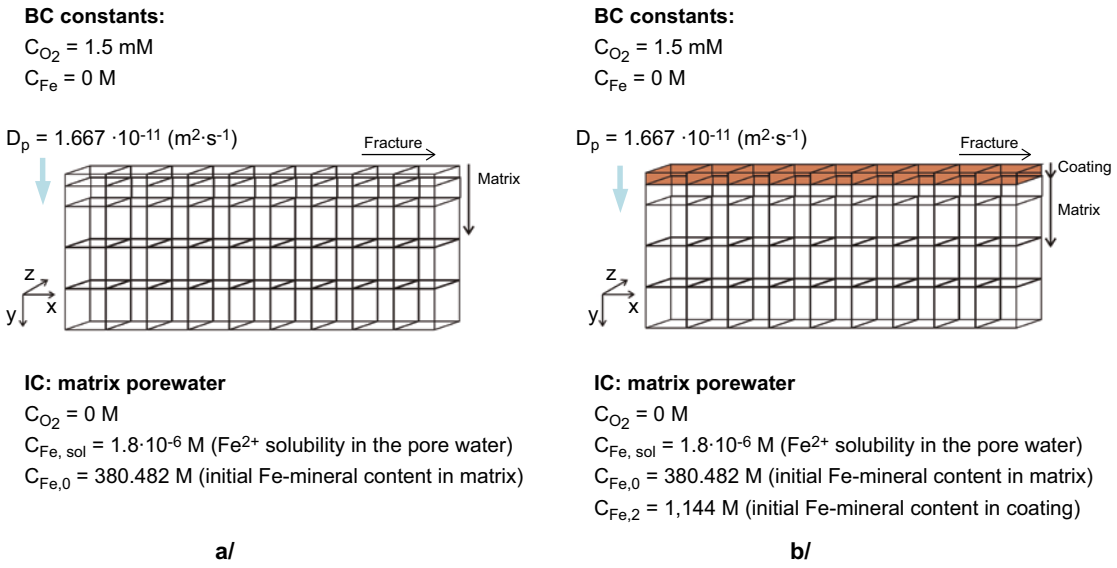

Figure 7-3. *Conceptual sketch of the numerical 2D model (Model 2) representing the porous rock matrix adjacent to the fracture; a/ Case 1 (without coating) and b/ Case 2 (with a fracture coating included).*

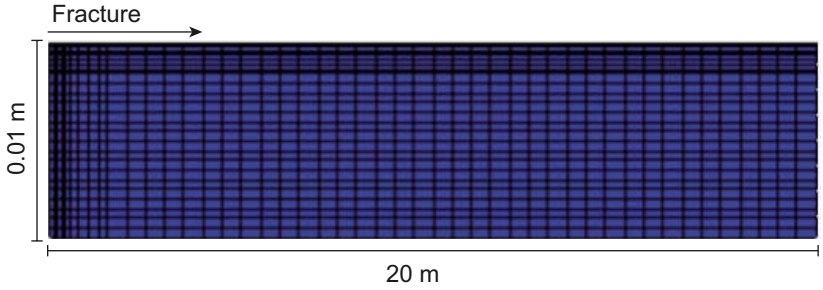

Figure 7-4. *Sketch of the grid used in the numerical 2D model, representing the length of the fracture and of the porous rock matrix adjacent to the fracture.*

7.5 Transport validation

7.5.1 Transport validation

In order to confirm that the hydrodynamic mechanisms of each model are accurately implemented, an exercise of transport validation has been performed. In these exercises, the concentration of a conservative tracer is imposed at the entrance of the system (with the same initial concentration as oxygen: 1.5 mM).

Model 1: 1D PHREEQC model

The conservative tracer is transported along the column by diffusion alone.

Considering the diffusion coefficient and the length of the column (0.01 m), the characteristic diffusion time ($t_c = L_y^2 \phi_m / D_e = L_y^2 / D_p$) in the system is approximately 100 days. Comparing with the simulation results, the conservative tracer concentration tends to be constant along the column after approximately 100 days (Figure 7-5).

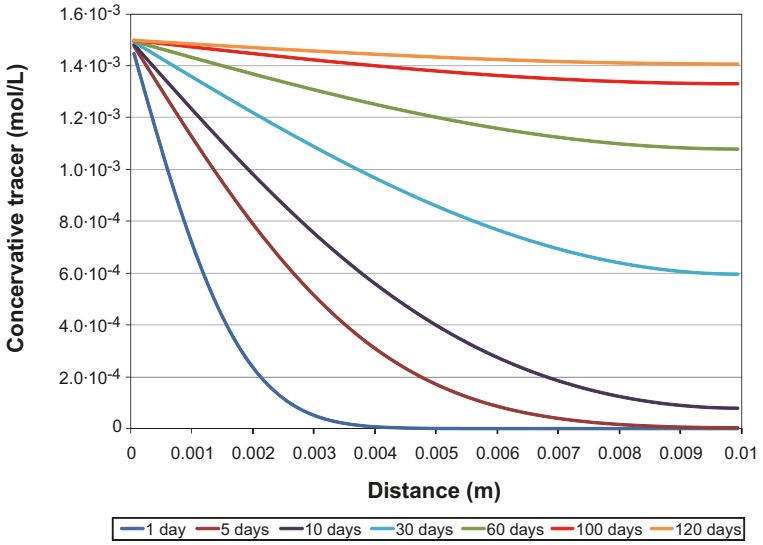

Figure 7-5. *Evolution of a conservative component used for the validation of the transport mechanisms (1D diffusion model. Model 1, Case 1).*

Model 2: 2D PHAST model

Oxygen is transported along the fracture zone, diffusing into the matrix. For the validation of the transport model, oxygen was considered as a conservative tracer. A diffusion coefficient of $5 \cdot 10^{-12}$ m^2/s was applied.

The conservative transport of oxygen in Model 2 is compared to a semi-analytical solution developed by /Haggerty 1995/ (Figure 7-6). This analytical solution simulates one-dimensional advective-dispersive transport of a conservative species in a saturated, isothermal, dual-porosity (mobile/immobile) system. The mass transfer between material zones is rate-limited. A steady-state regime for fluid flow and a homogeneous distribution of the material properties have been assumed.

The most common approximation of the rate-limited mass transfer between mobile and immobile domains is a single first-order mass transfer rate. Values of the first-order rate coefficient happen to be the harmonic mean of the multirate series /Haggerty and Gorelick 1995/. /Haggerty et al. 2000/ formulated multirate mass transfer in terms of convolution integral. This solution is compared to the results obtained by the 2D dual porosity model, using PHAST. A very good fit has been obtained (Figure 7-6), confirming a good implementation of the hydrodynamics into the different models.

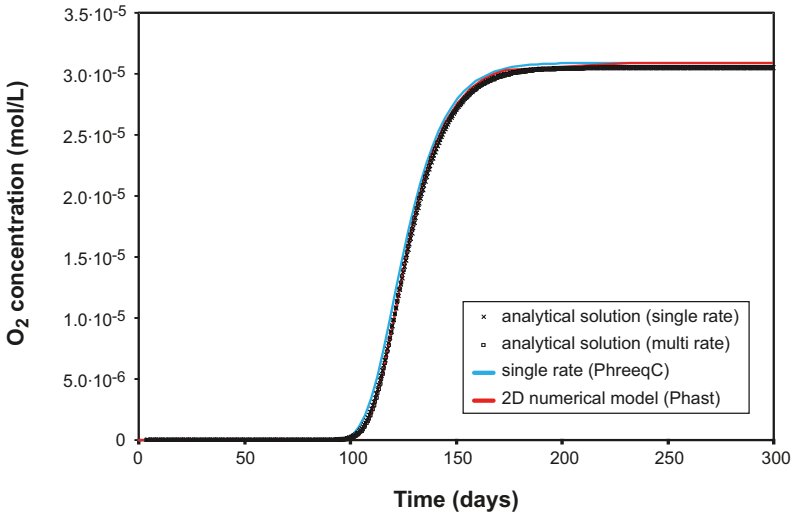

Figure 7-6. *Conservative profile of the evolution of the oxygen concentrations implemented as a conservative component for the transport validation of Model 2.*

7.6 Results for the Base Case

7.6.1 Model 1: 1D diffusion model

The advance of the oxygen front into the matrix has been calculated during one year of simulation time. The so-called "Base Case" considers a constant pH of 8.0 and a constant oxygen concentration in the boundary waters of 1.5 mM. The results for Case 1 (without coating) and for Case 2 (with coating included) are described in the next sections.

Case 1 (without coating)

During the early stages (0–1 day), the gradient of oxygen concentrations between the boundary of the model (groundwater solution flowing along the fracture zone) and the rock matrix (reactive pore-water) is significant, promoting the oxygen transport by diffusion into the matrix. As a result, the matrix thickness affected by the oxygen diffusion is around 0.004–0.005 metres (Figure 7-7). After 15 days, the gradient of oxygen concentration has been significantly reduced, and the advance of the oxygen front reaches a pseudo-steady state, becoming stable between 0.007 and 0.008 metres (Figure 7-7). This process is controlled by the oxygen diffusion from the boundary and the rate of oxygen consumption as a consequence of its reactivity with the iron-bearing minerals and the aqueous species (redox reactions). As shown in Figure 7-7, the oxygen front remains relatively stable after 15 days. The oxygen concentrations range between 10^{-4} mol/L at a distance from the boundary of 0.005 metres to values of approximately 10^{-9} mol/L from 0.0078 metres.

The total amount of the dissolved iron-mineral during this process is shown in Figure 7-8. After 30 days of oxygen diffusion into the matrix, a significant decrease of the amount of the dissolved iron-mineral occurs at 0.007 metres from the model boundary, coinciding with the front of the relatively high oxygen concentrations (Figure 7-7). Despite that the amount of dissolved mineral continuously increases with time, mineral dissolution mainly occurs within 0.006–0.007 metres from the boundary supplying oxygen. For larger distances, the dissolution of iron-mineral ceases to be effective (Figure 7-8), as a consequence of the very low oxygen concentrations at these distances in the matrix.

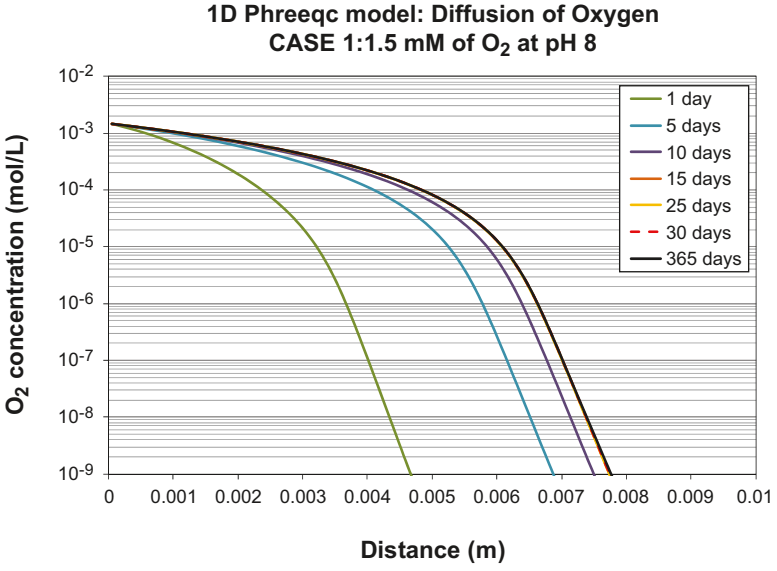

Figure 7-7. *Evolution of the concentration in the rock matrix under the assumptions of the so-called "Base Case" for Case 1 of Model 1 (PHREEQC 1D model without coating, with a pH value of 8.0 and 1.5 mM of oxygen concentration in the boundary aqueous solution).*

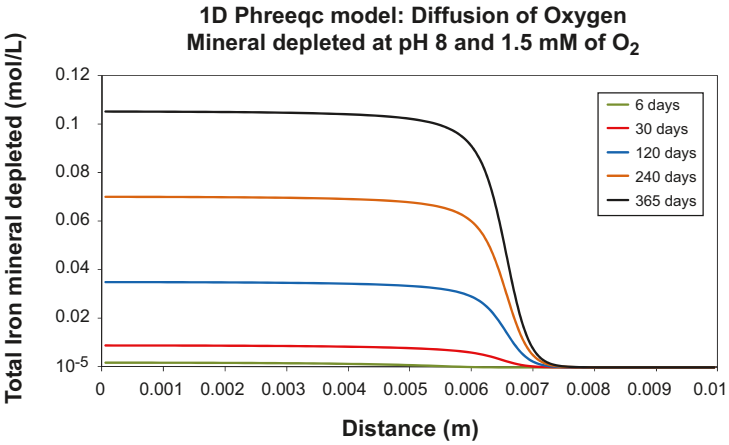

Figure 7-8. *Evolution of the total amount of iron-mineral dissolved under the assumptions implemented for Case 1 of Model 1 (PHREEQC 1D model without coating).*

The trend of the Fe(II) concentration evolves according to the evolution of the oxygen front (Figure 7-9). With respect to the initial Fe(II) concentration in the pore-water (in equilibrium with respect to the iron-mineral considered in the calculations), the Fe(II) concentration decreases as a consequence of redox reactions in the presence of relatively high oxygen concentrations. The aqueous species of Fe(III) generated in this process would precipitate in equilibrium as amorphous Fe(III) oxyhydroxides, if it had been included in our calculations. After 0.007 metres, a significant increase in Fe(II) concentration has been simulated (to $1.8 \cdot 10^{-6}$ mol/L), indicating that the oxidation of the Fe(II) aqueous species is negligible at this distance in the matrix.

It is important to emphasise that the amount of dissolved iron-mineral during the first year is lower than 0.04% of the total amount of mineral assigned to the rock matrix. Therefore, approximately 3,500 years would be necessary to completely deplete the mineral source of Fe(II), under the assumptions considered in this case. However, this time is very sensitive with respect to the rate of the mineral dissolution and the precipitation of the amorphous Fe(III) oxyhydroxides (not implemented in these calculations). Some tests have been performed in order to assess the sensitivity of the results in reference to the advance of the front of oxygen concentrations when considering precipitation of amorphous Fe(III) oxyhydroxides. Numerically, it has been verified that the precipitation of amorphous Fe(III) oxyhydroxides is not a relevant process controlling oxygen and Fe(II) concentrations in the matrix pore-water.

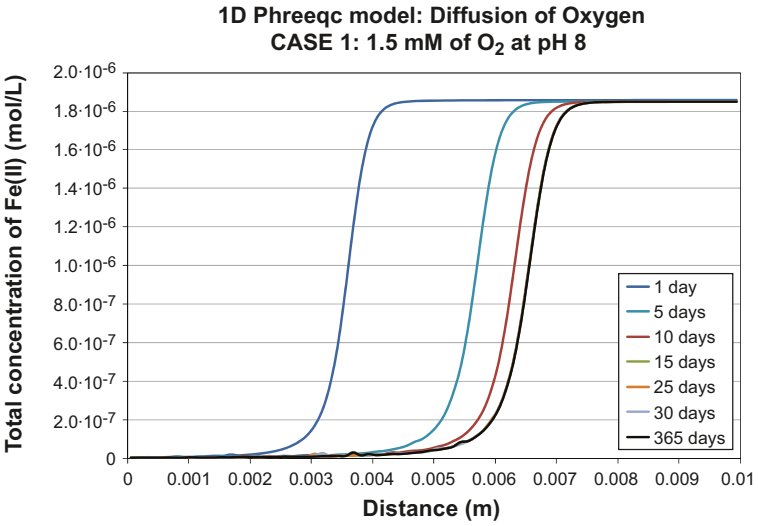

Figure 7-9. *Evolution of the total Fe(II) concentration for Case 1 (without coating) of Model 1. The assumptions implemented in this model are those described for the so-called "Base Case" (1.5 mM of oxygen and pH 8.0 in the boundary waters).*

Case 2 (with coating included)

The results obtained for Case 2 (considering to the presence of a coating layer) show that the front of the relatively high oxygen concentration is located at approximately the same position as for Case 1 (Figure 7-10). Despite the higher oxygen consumption in the coating layer, the continuous supply of oxygen from the boundary is sufficient to maintain the concentration gradient within the matrix. Consequently, we can affirm that a key factor for the advance of the oxygen into the matrix is the oxygen concentration in the boundary water. A similar trend has been calculated for the distribution of the Fe(II) concentration (Figure 7-10). In this way, it is predictable that a key factor controlling Fe(II) concentration is the distribution of oxygen concentration in the matrix.

In reference to the iron-bearing mineral dissolved after 1 year of oxygen diffusion (Figure 7-11), the results show that the total amount of mineral dissolved is around 0.1 mol/L in most of the rock matrix. In the coating layer, the amount of mineral dissolved is more than one order of magnitude higher (around 1.4 mol/L). In both cases, at around 0.007 m from the boundary, the dissolution of iron-bearing mineral is practically negligible.

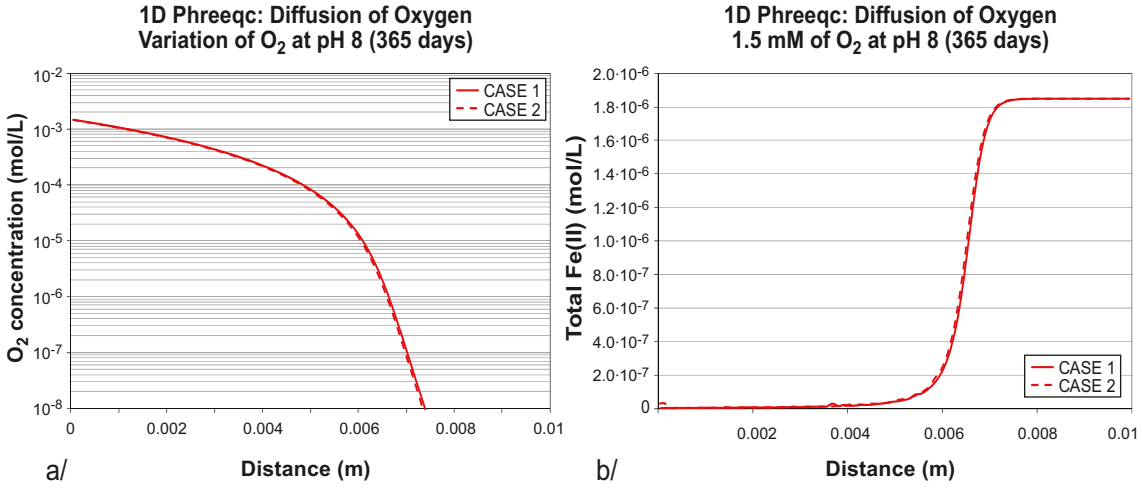

Figure 7-10. *Profiles of the computed a/ oxygen and b/ Fe(II) concentrations in the rock matrix after 1 year for Cases 1 and 2 of Model 1 (PHREEQC 1D model with and without coating).*

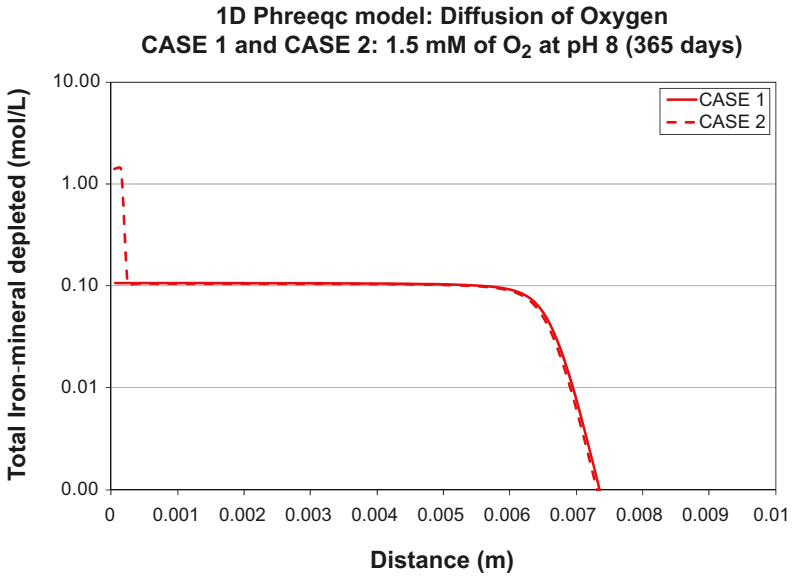

Figure 7-11. *Comparison of the total amount of iron-mineral depleted in the rock matrix for Cases 1 and 2 of Model 1 (PHREEQC 1D model with and without coating).*

7.6.2 Model 2: 2D dual porosity model

In Model 2, advective and diffusive transport of oxygen along the fracture and in the rock matrix has been calculated for a simulation time of 180 days. As commented for Model 1, the so-called "Base Case" considers a constant pH of 8.0 and a constant oxygen concentration in the boundary water of 1.5 mM. The results from Case 1 and 2 of the 2D model (with and without coating respectively), are described below.

Case 1 (without coating)

As described for Model 1, the oxygen transport into the matrix is carried out by diffusion from the fracture zone. The oxygen transport along the fracture zone occurs mainly by advection, with decreasing concentration along the flow path as a consequence of the oxygen consumption by (1) mineral oxidation and (2) diffusion into the adjacent matrix. Therefore, the oxygen concentration along the fracture zone is progressively increasing over time and decreasing over the fracture length. Consequently, the oxygen gradient and the rate of diffusive transport into the matrix decrease for incremental values of X (Figure 7-12a).

After 180 days of simulation, the oxygen concentration in the fracture is practically negligible after approximately 16 metres (Figure 7-12b). The oxygen front does not significantly advance after 150 days from the beginning of the oxygen input. However, the steady state for the advance of the oxygen front in the matrix is reached already after 20–30 days (Figure 7-12c; similarly as modelled by the 1D PHREEQC model). In the fracture zone, no iron-bearing mineral has been considered in the fracture filling. Therefore, the evolution of the iron concentration is a consequence of the conservative transport by advection of these aqueous species, and affected by the diffusion from the matrix porewater. The plot of the Fe(II) concentrations in the matrix shows, however, the same trend as that commented for Model 1 (Figure 7-9 and Figure 7-13). Also the calculated amount of iron mineral dissolved shows the same trend as calculated with Model 1 (Figure 7-14).

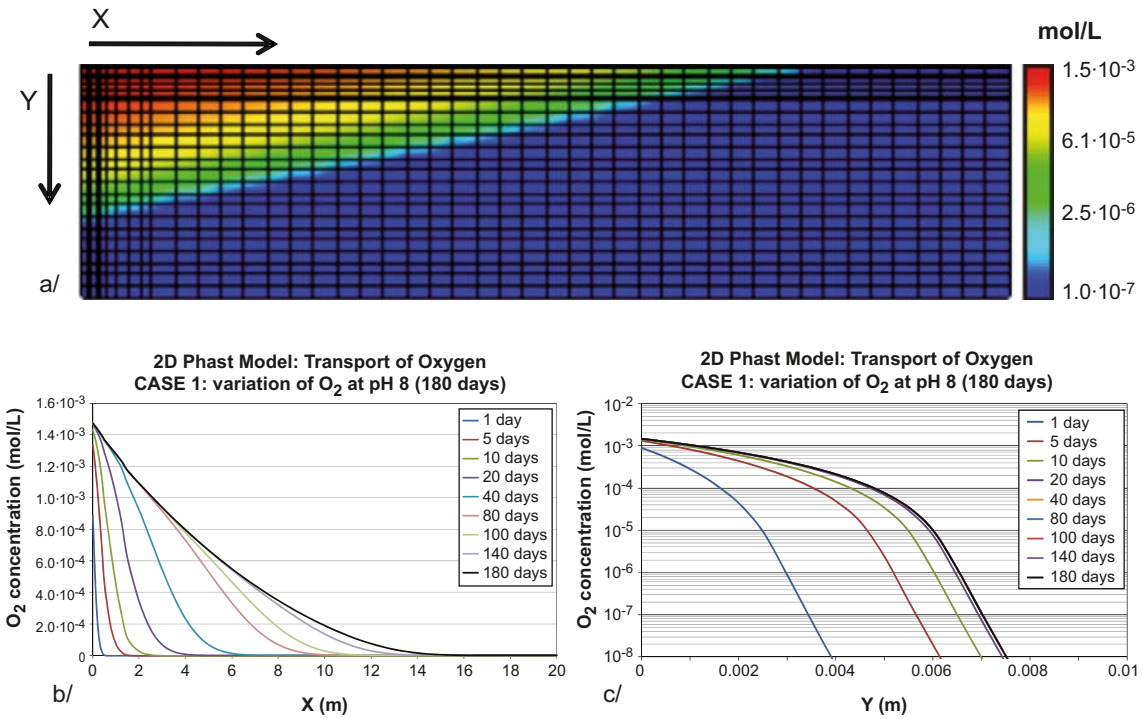

Figure 7-12. *a/ Distribution of the oxygen concentration calculated after 180 days of simulation time under the assumptions implemented in Case 1 of Model 2 for the so-called "Base-Case". b/ Evolution of the trends of oxygen concentrations along the fracture zone and, c/ in a section in the matrix rock.*

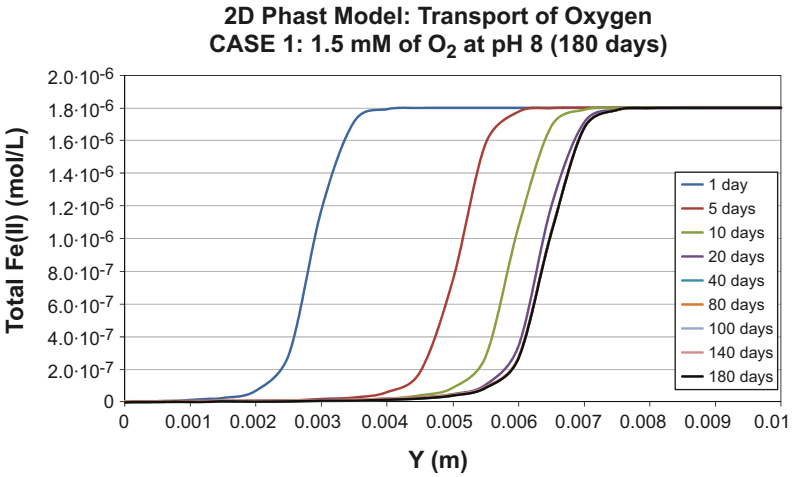

Figure 7-13. *Evolution of the total Fe(II) concentration in the rock matrix for Case 1 of Model 2 (PHAST 2D model without coating).*

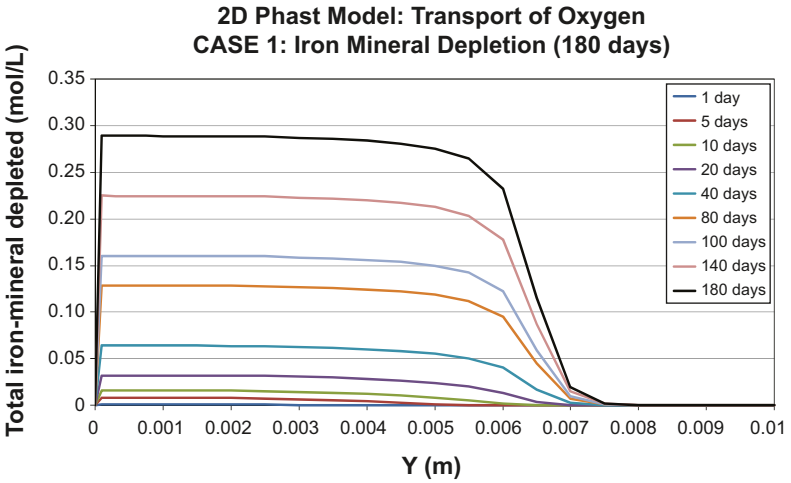

Figure 7-14. *Evolution of the amount of iron-mineral dissolved in the rock matrix for Case 1 of Model 2 (PHAST 2D model without coating).*

Case 2 (with coating included)

As simulated for Model 1, the advance of the oxygen front into the matrix is not very sensitive with respect to the existence of the coating, when the maximum oxygen concentration has been considered on the model boundary (Figure 7-15c). However, the presence of the coating is a key factor controlling the advance of the oxygen along the fracture zone, from which oxygen diffuses into the adjacent matrix pore-water (Figure 7-15a and b). After a simulation time of 180 days, the oxygen front extends approximately 11–12 metres along the fracture when a coating, associated to the fracture walls, is implemented in the model. In contrast, it reaches 15–16 metres along the fracture when a coating is not considered.

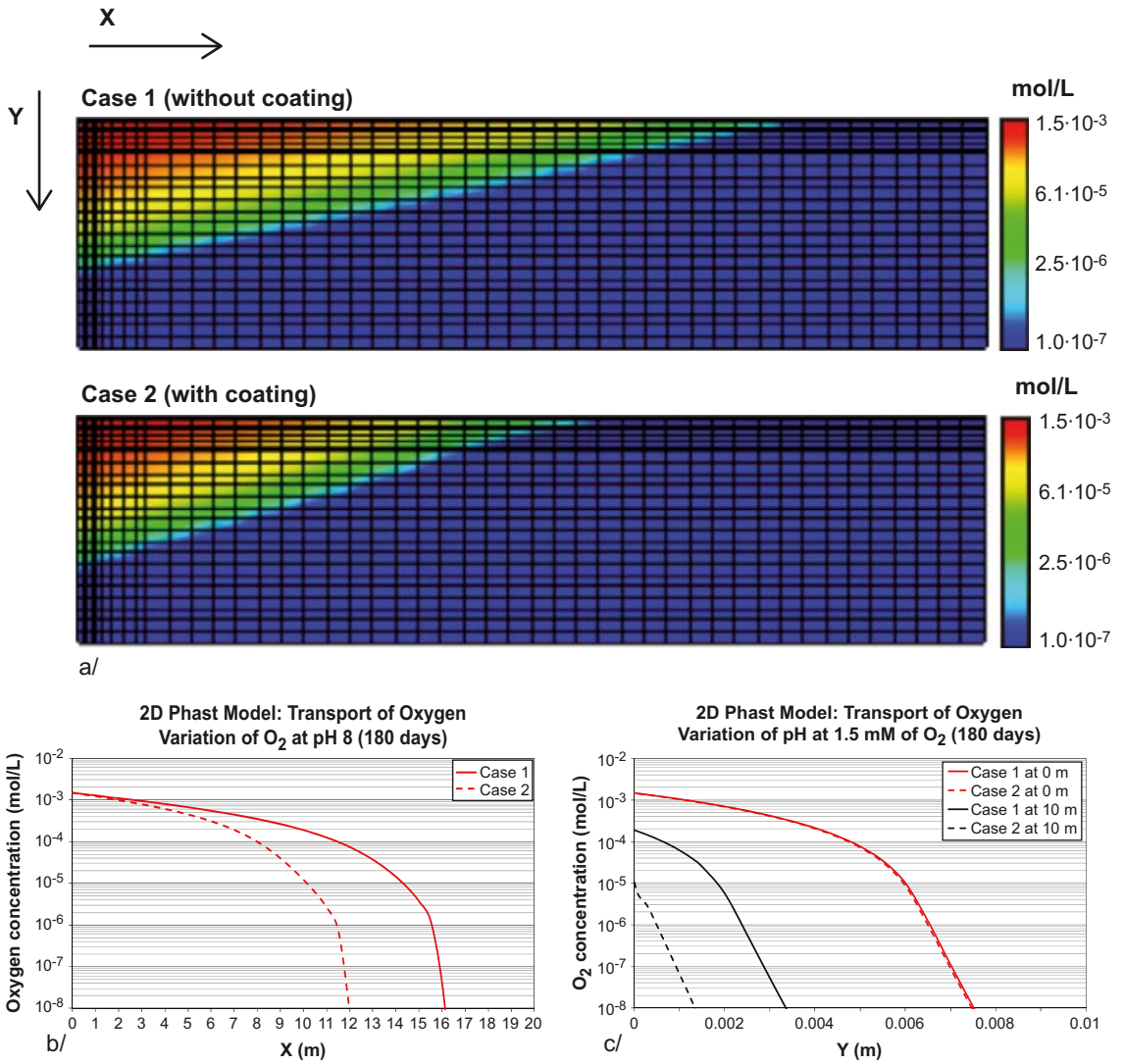

Figure 7-15. *Distribution and comparison of the oxygen concentrations calculated for a simulation time of 180 days under the assumptions implemented for Cases 1 and 2 of Model 2 (PHAST 2D simulations with and without coating). Evolution of the oxygen concentration b/ along the fracture zone, and c/ in a section in the rock matrix.*

As expected, the total iron concentration evolves accordingly to the iron-mineral dissolution. In the domain where relatively high oxygen concentrations have been computed, Fe(II) aqueous species are oxidised to Fe(III) aqueous species, whose concentrations would be, in turn, controlled by the precipitation of amorphous Fe(III) oxyhydroxides. Therefore, despite the total iron concentration supplied by the iron-mineral dissolution is higher in Case 2 of Models 1 and 2, the trend of the Fe(II) concentration is practically identical to that calculated for Case 1 (Figure 7-16). The rate of iron-mineral dissolution is basically controlled by the oxygen concentration present in the matrix pore-water, which is in turn controlled by its transport by diffusion. Consequently, despite that the plots of the amount of iron-mineral dissolved are practically identical on the boundary where maximum oxygen concentrations are calculated (X = 0.0 m), the presence of the coating is responsible for the decrease of the amount of the iron-mineral dissolution into the matrix when no coating have been implemented (Figure 7-17).

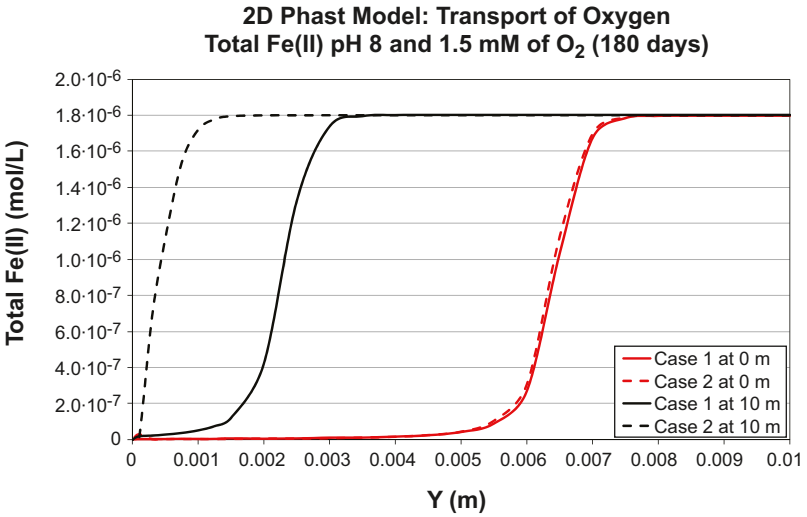

Figure 7-16. *Results of total Fe(II) concentrations in the matrix for a simulation time of 180 days in two sections at X = 0.0 m and X = 10.0 m along the fracture zone under the assumptions implemented for Cases 1 and 2 of Model 2 (PHAST 2D simulations with and without coating).*

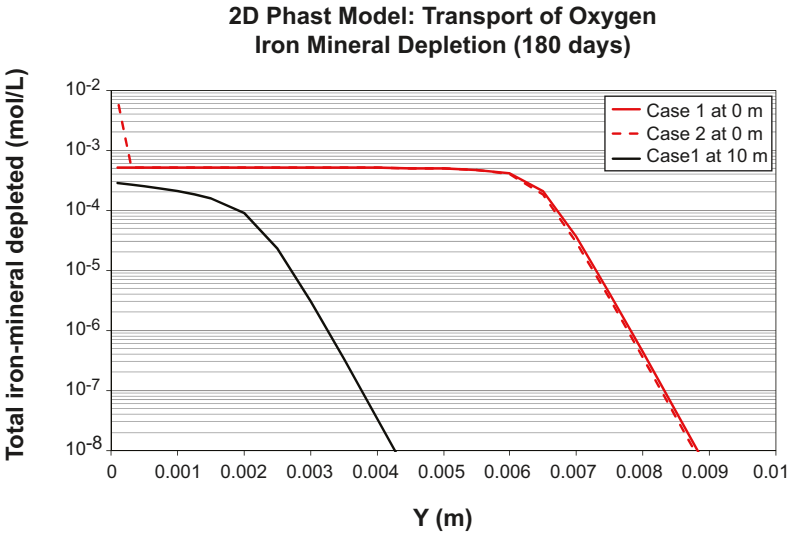

Figure 7-17. *Results of the amount of iron-mineral dissolved in the matrix after 180 days of simulation time in two sections at X = 0.0 m and X = 10.0 m along the fracture zone under the assumptions implemented for Cases 1 and 2 of Model 2 (PHAST 2D simulations with and without coating).*

7.7 Sensitivity analysis and uncertainty evaluation

A sensitivity analysis has been performed in order to assess the influence of different parameters on the advance of the front of the relatively high oxygen concentrations. The parameters studied are the reactive surface area of the iron-mineral, the porosity of the matrix, the pH in the pore water, and the oxygen concentration in the boundary water.

7.7.1 Iron-mineral reactive surface area

The assessment of the influence of the reactive surface area of the iron-mineral on its kinetic dissolution has been performed using calculations with the 1D PHREEQC Model. Two alternative reactive surface areas have been implemented: 5,000 and 20,000 m^2L^{-1} (6,141 m^2L^{-1} was considered in the so-called "Base Case").

As expected, when higher reactive iron-mineral surface areas are implemented, the advance of the oxygen front into the matrix is less than that calculated for the Base Case (Figure 7-18). As a result, higher gradients of oxygen concentrations are simulated. The amount of iron-mineral dissolved is also very sensitive with respect to this parameter (Figure 7-19). After one year of simulation time, the amount of mineral dissolved is 3.5 times higher when the reactive surface area is increased from 5,000 to 20,000 m^2L^{-1} . Consequently, the time estimated for the complete depletion of the iron-minerals in the matrix adjacent to the fracture zone is around 1,000 years when considering a reactive surface area of around 20,000 m^2L^{-1} (3,500 years were estimated with the assumptions implemented for the Base Case).

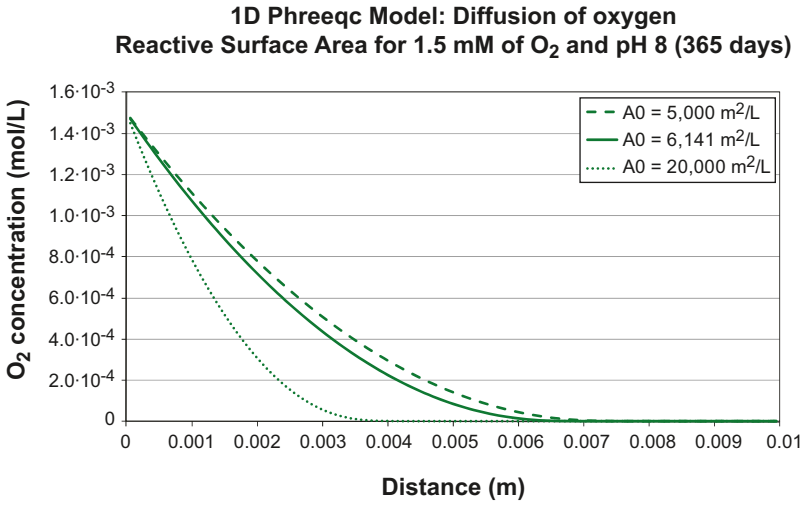

Figure 7-18. *Variability of the evolution of the oxygen concentration for different reactive surface areas in the rock matrix (sensitivity case performed for Case 1 of Model 1; PHREEQC 1D models without coating).*

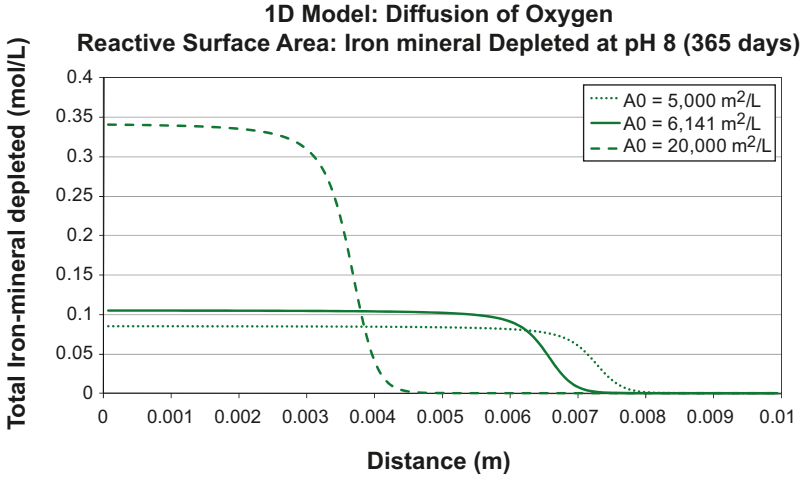

Figure 7-19. *Variability of the amount of dissolved iron-mineral for different reactive surface areas in the rock matrix (sensitivity case for Case 1 of Model 1; PHREEQC 1D models without coating).*

7.7.2 Porosity and diffusion coefficient

The rock matrix porosity implemented also influences the kinetic dissolution of the iron-mineral, because the diffusion coefficient is correlated with the porosity in the numerical system using the PHREEQC code (when higher porosity values are considered, lower numerical diffusion coefficients result). Some tests have been performed for Case 1 of Model 1, described in previous sections.

A porosity of 0.004 (instead of 0.0018) has been tested. In this way, a new diffusion coefficient of $5.24 \cdot 10^{-12}$ $m^2 s^{-1}$ has been implemented for this sensitivity case. This value is slightly lower to that the one used in the Base Case ($1.17 \cdot 10^{-11}$ $m^2 s^{-1}$) and, consequently, the advance of the oxygen front is also slightly limited (Figure 7-20). However, the trend of the amount of the iron-mineral dissolved is significantly different (Figure 7-21). Under these assumptions, the amount of dissolved mineral is significantly decreased (from 0.105 mol/L to 0.048 mol/L), and the iron-mineral would be completely depleted from the matrix adjacent to the fracture walls in around 8,000 years.

In conclusion, if higher porosities are numerically implemented (decreasing accordingly the diffusion coefficient), the total amount of the dissolved iron-mineral decreases. In this way, the oxygen front reaches higher lengths into the matrix rock from the fracture wall. The amount of mineral dissolved is sensitive with respect to slight variations of the diffusion coefficient.

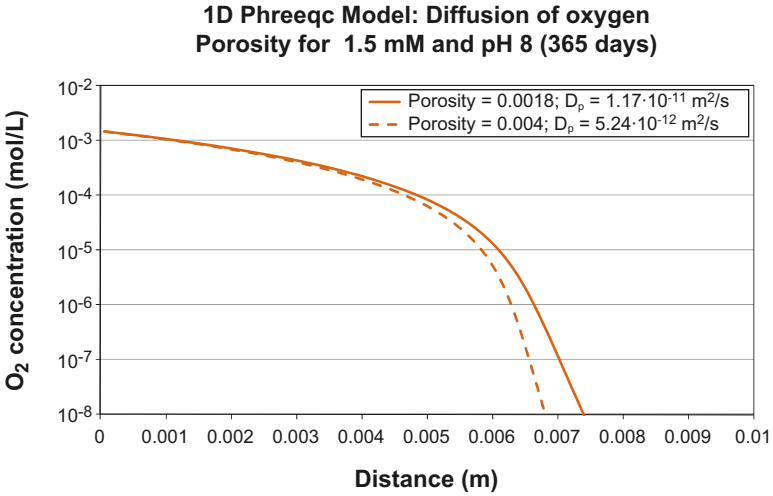

Figure 7-20. *Variability of the evolution of the oxygen concentration for different porosities of the rock matrix (sensitivity case of Case 1 of Model 1; PHREEQC 1D models without coating).*

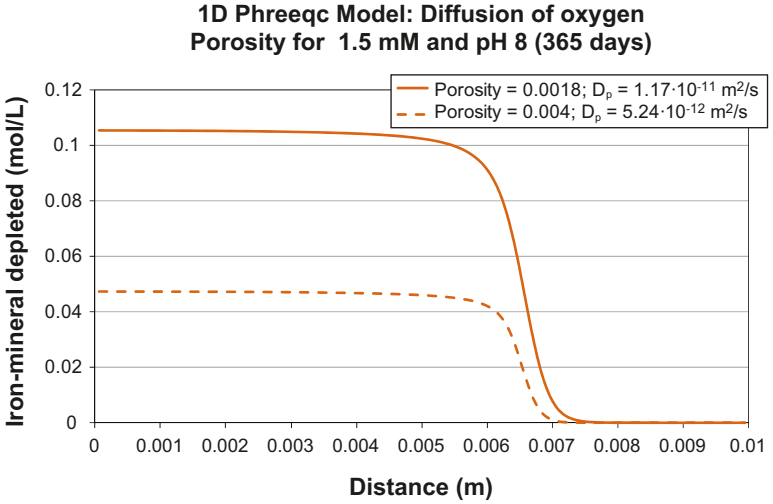

Figure 7-21. *Variability of the amount of dissolved iron-mineral for different porosities of the rock matrix (sensitivity case of Case 1 of Model 1; PHREEQC 1D models without coating).*

7.7.3 Influence of pH on kinetic dissolution of iron-bearing minerals

Dissolution rates of minerals such as silicates and aluminosilicates, R (mol $m^{-2}yr^{-1}$), are usually written as a function of proton concentration by means of empirical rate laws:

$$R = k_H [H^+]^m + k_0 + k_{OH} [H^+]^n$$

which describe parallel acid- and base-promoted dissolution reactions. The k_H, k_0 and k_{OH} are the acid, neutral and alkaline constants respectively. The reaction orders, n and m, /Lasaga 1995, Malmström and Banwart 1997/ are usually fractional due to the existence of a variety of surface sites with different adsorption and reaction energies. In the Base Case, the dissolution constant is proposed for a fixed pH of 8. As shown in Figure 7-22, the dissolution rate of these minerals is dependent on the pH of the aqueous solutions. Therefore, a sensitivity analysis of the effect of different solution pH has been performed.

Two sensitivity cases have been analyzed: (1) a pH of 7.5, with an associated dissolution rate of the iron-mineral estimated to $4.70 \cdot 10^{-13}$ $mol_{Fe} m^{-2} s^{-1}$, and (2) a pH of 8.5, with a rate of $1.02 \cdot 10^{-12}$ $mol_{Fe} m^{-2} s^{-1}$, which differs from the previous case by one and a half order of magnitude. Although the sensitivity analysis has been performed for Cases 1 and 2 of Models 1 and 2, for simplicity, only the results obtained for Case 1 of Model 1 (PHREEQC 1D model without coating) have been used to illustrate the effect of the pH variability on the concentration profiles in the matrix. The influence of this variability on the advance of the oxygen front along the fracture zone has been illustrated by Case 1 of Model 2 (PHAST 2D model without coating).

The results of the 1D model using PHREEQC show the influence of the variation of pH on the advance of the oxygen front (Figure 7-23). For pH values of 7.5 or higher, the advance of the oxygen front decreases with increasing pH. This is a consequence of the increase of the dissolution rate of the iron-mineral and, therefore, of the amount of the dissolved iron-mineral (Figure 7-24). As expected, an increase of the pH values (and the dissolution rate) has a similar effect to that reproduced increasing the reactive surface area of the iron-mineral (Figure 7-19). The amount of the iron-mineral dissolved into the matrix is practically doubled for pH values of the boundary solution of around 8.5.

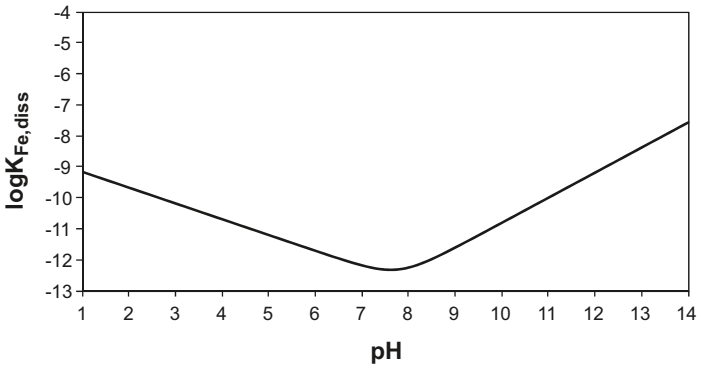

Figure 7-22. *Evolution of the rate of the Fe(II) release from biotite dissolution /Malmström and Banwart 1997/ as a function of the groundwater pH.*

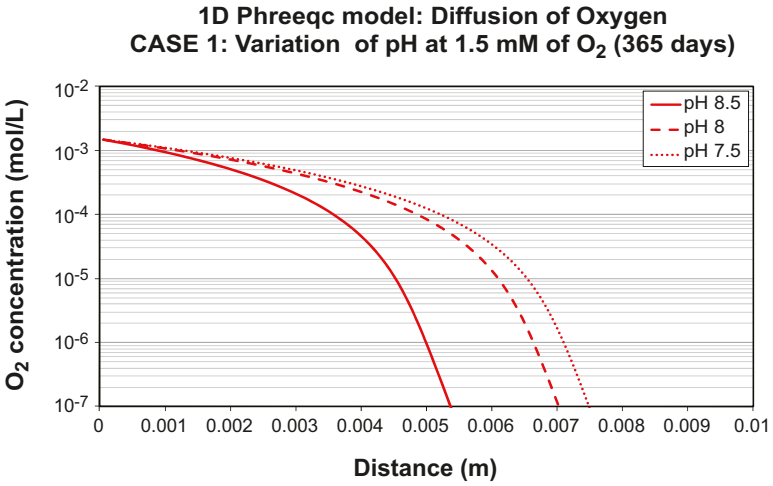

Figure 7-23. *Variability of the evolution of the oxygen concentration for different groundwater pH (sensitivity case performed for Case 1 of Model 1; PHREEQC 1D models without coating).*

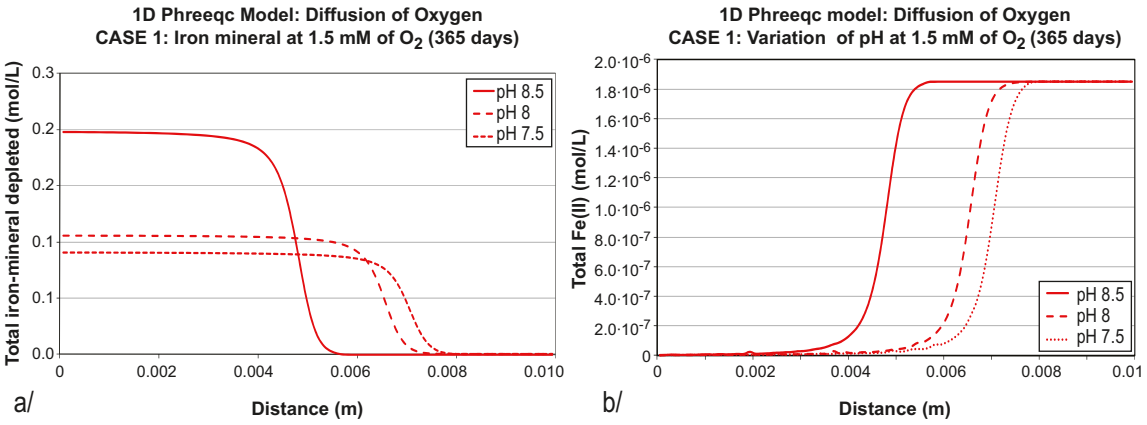

Figure 7-24. *Variability of the evolution of a/ the amount of iron-mineral dissolved, and b/ the total Fe(II) concentration for different groundwater pH (sensitivity case performed for Case 1 of Model 1; PHREEQC 1D models without coating).*

Similarly, the results obtained by Model 2 show that the advance of the oxygen front is not very sensitive to pH values in the range between 7.5 and 8.0 (around 14–16 m, Figure 7-25). However, for pH values around 8.5, the advance of the oxygen front is significantly less, reaching 11–12 m after 180 days of simulation time.

The influence of pH can be seen in both Cases 1 and 2 (with and without coating) of the 1D Model. Independently on the presence or absence of a coating, it is verifiable that for higher pH values the oxygen front reaches shorter distances in the matrix and the amount of iron-bearing mineral depletion is higher.

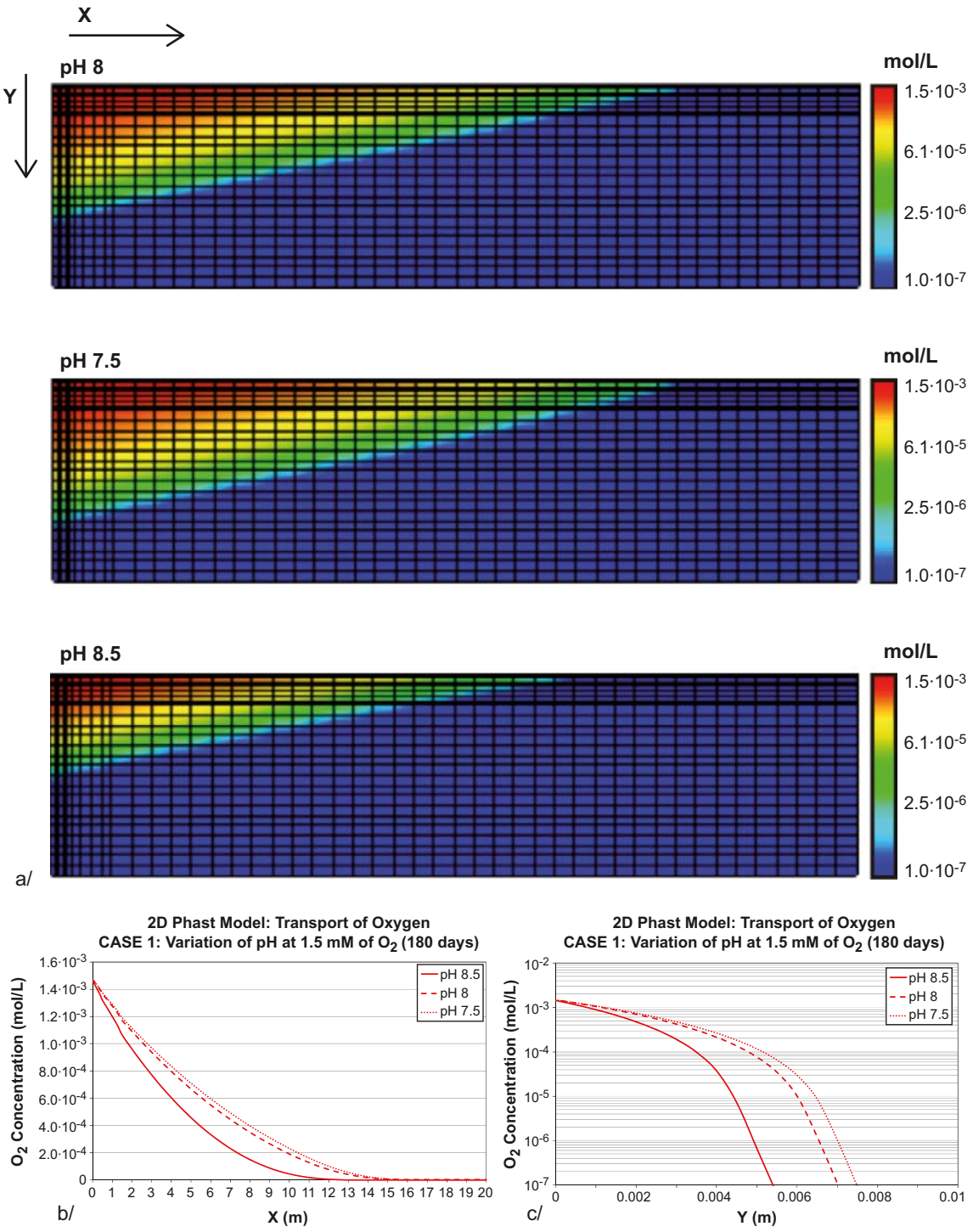

Figure 7-25. *Distribution and comparison of the oxygen concentration calculated for a simulation time of 180 days under the assumptions implemented for Case 1 of Model 2 (PHAST 2D simulations without coating) for different groundwater pH values. b/ Evolution of the oxygen concentration along the fracture zone (at Y = 0.0 m) and, c/ in a section in the matrix rock (at X = 0.0 m).*

7.7.4 Boundary O_2 concentration influence on the progression of the oxygen front

The oxygen concentration in the boundary water is a key factor controlling the development and the advance of the oxygen front by diffusion into the matrix, and the dissolution of the iron-mineral. Therefore, a sensitivity analysis of this parameter has been performed.

The so-called "Base Case" has been considered as a pessimistic environmental condition for the redox buffer capacity of the system, because a high oxygen concentration in the ice melt water has been implemented in the calculations ($1.5 \cdot 10^{-3}$ mol O_2 per litre of groundwater solution). The sensitivity analysis of the oxygen concentration in the boundary water has been performed for $3 \cdot 10^{-4}$ mol/L (oxygen concentration in equilibrium with the atmospheric oxygen) and $3 \cdot 10^{-5}$ mol/L (one order of magnitude less).

As for the sensitivity case with a varying pH in the boundary water (described in the previous section), the sensitivity analysis of the oxygen concentration in the boundary water has been performed for Cases 1 and 2 of Models 1 and 2. However, for simplicity, only the results obtained for Case 1 of Model 1 (PHREEQC 1D model without coating) have been used in order to illustrate the effect of the oxygen variability in the rock matrix. The influence of this variability on the advance of the oxygen front along the fracture zone and the influence of the existence of a coating on the fracture walls have been illustrated by Cases 1 and 2 of Model 2 (PHAST 2D model without and with coating).

After a simulation time of one year, the oxygen concentration front reaches ~7 mm from the fracture boundary when an oxygen concentration of 1.5 mM has been imposed in the boundary water. As expected, this front does not reach 4 and 2 mm when the oxygen concentrations in the boundary water are 0.3 and 0.03 mM respectively (Figure 7-26). In any case, the oxygen front has reached the steady state condition. The dissolution front is located in the same position (Figure 7-27), with a maximum amount of mineral dissolved of slightly more than 0.1 moles of iron-mineral per litre of porewater. Under these assumptions, the iron-mineral in the matrix adjacent to the fracture will be completely depleted in around 3,500 years.

Along the fracture zone, the oxygen front reaches between 16.0 and 17.0 m for the Base Case, and between 3.0 and 9.0 m when the oxygen concentrations in the boundary water range between $3 \cdot 10^{-4}$ and $3 \cdot 10^{-5}$ mol/L (Figure 7-28).

If coating is considered on the fracture walls, the oxygen advance is significantly less, as shown in Figure 7-29. The influence of the coating is more significant when the high oxygen concentrations are implemented in the boundary waters. Regarding the oxygen diffusion into the matrix, the effect of the coating is that described in Section 7.6.

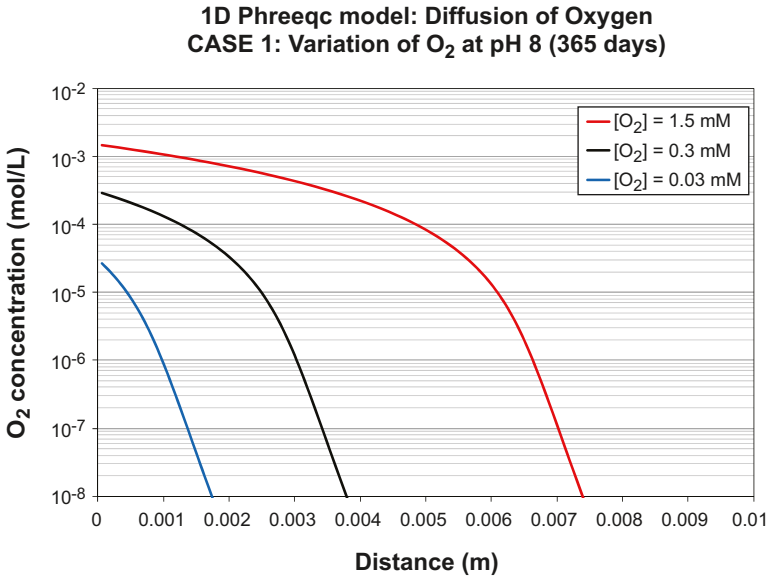

Figure 7-26. *Variability of the evolution of the oxygen concentration in the matrix rock for different oxygen concentrations in the boundary water (sensitivity case performed for Case 1 of Model 1; PHREEQC 1D models without coating).*

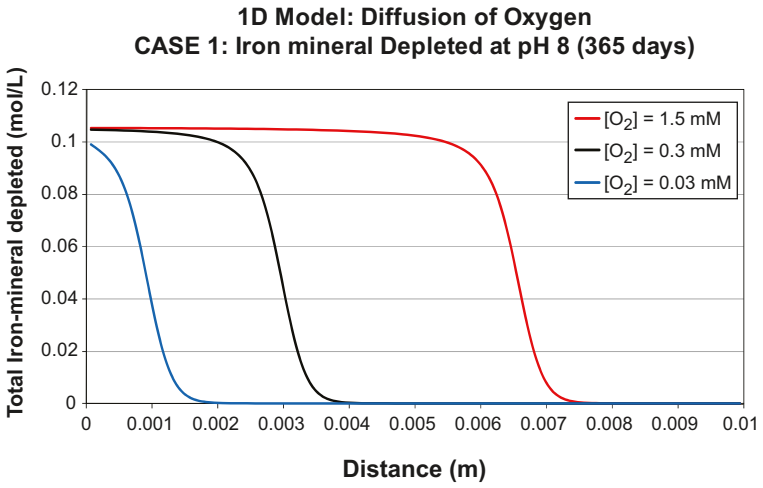

Figure 7-27. *Variability of the evolution of the amount of iron-mineral dissolved in the matrix rock for different oxygen concentrations in the boundary water (sensitivity case performed for Case 1 of Model 1; PHREEQC 1D models without coating).*

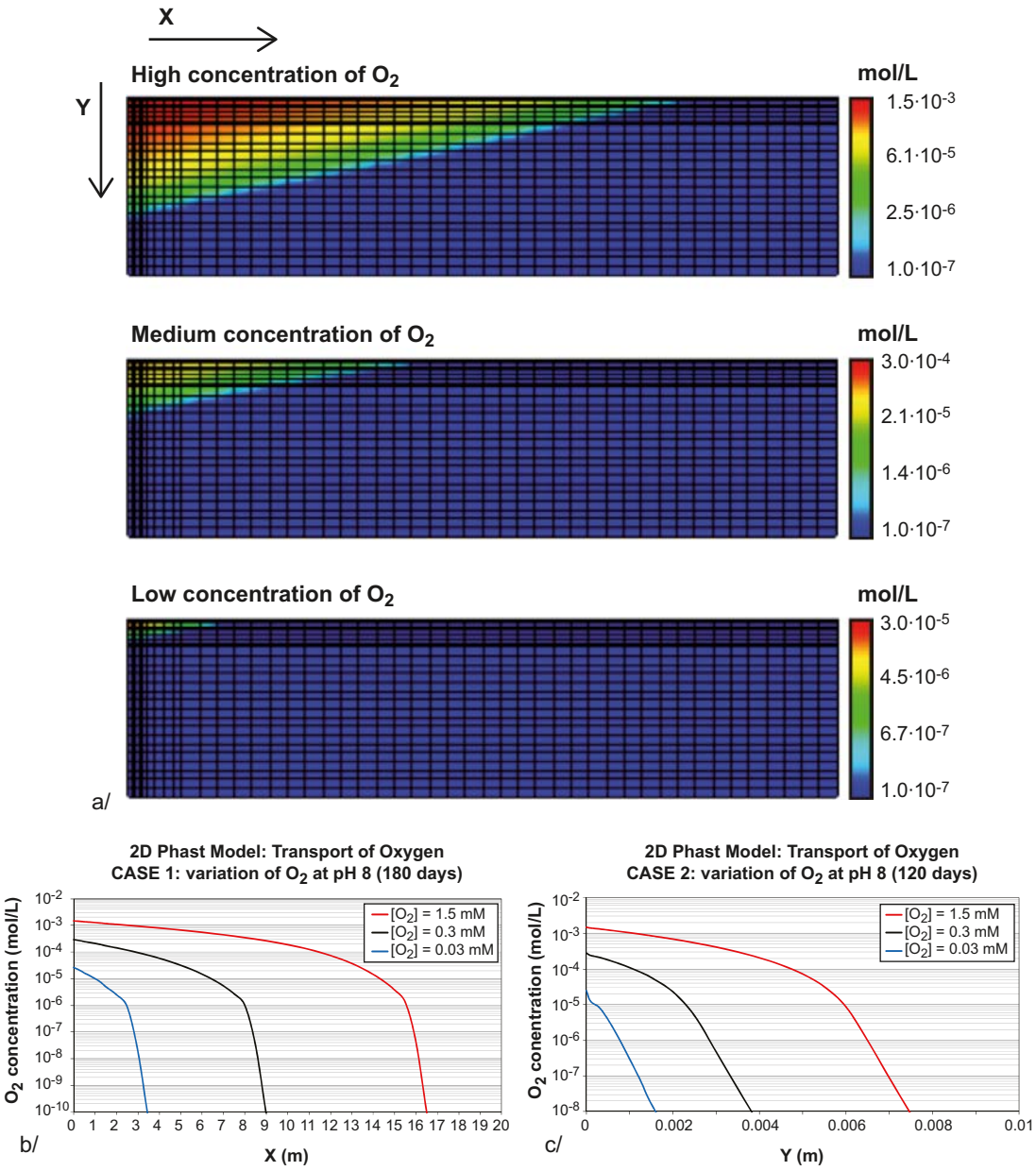

Figure 7-28. *Distribution and comparison of the oxygen concentration calculated after a simulation time of 180 days under the assumptions implemented for Case 1 of Model 2 (PHAST 2D simulations without coating) for different oxygen concentrations in the boundary waters. b/ Evolution of the oxygen concentration along the fracture zone (at Y = 0.0 m) and, c/ in a section in the matrix rock (at X = 0.0 m).*

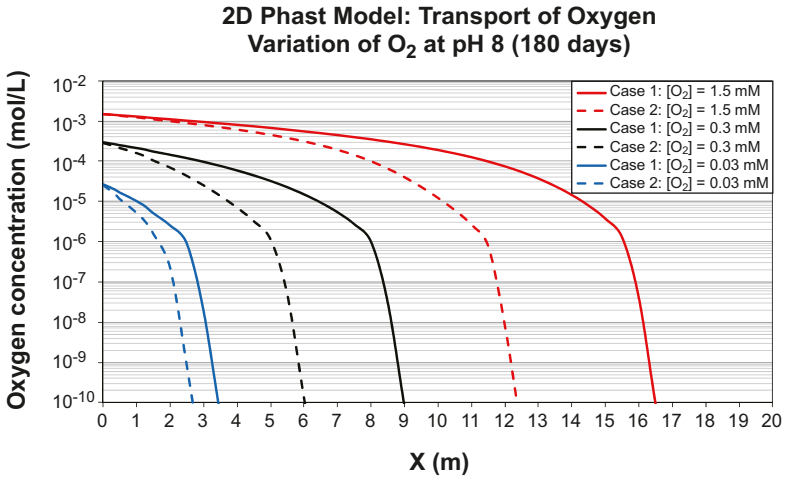

Figure 7-29. *Variability of the evolution of the oxygen concentration along the fracture zone (at Y = 0.0 m) for different oxygen concentrations in the boundary water (sensitivity case performed for Cases 1 and 2 of Model 2; PHAST 2D models with and without coating).*

7.7.5 Conclusions

The models presented in this section reproduce the oxygen transport in an initially anoxic hydrogeological environment, which is in equilibrium with respect to a Fe(II)-mineral phase. The objective is to estimate the redox buffer capacity of fractured lithologies when an input of oxygenated waters occurs. The input of the oxic waters is performed through a fracture zone where the groundwater composition has been considered (1) constant, in the PHREEQC 1D models, and (2) evolving according to the transport mechanisms (by advection and diffusion) under hydraulic conditions of prescribed flow rates, in the PHAST 2D models.

A so-called “Base Case” has been defined, in which the boundary waters are characterised by a fixed pH of 8.0 and an oxygen concentration of 1.5 mM, which is the assumed concentration of glacial melting waters during a theoretical glacial stage. With these assumptions, the advance of the oxygen diffusion and the front of dissolution of the iron-mineral has been reproduced in the matrix and along the fracture zone. A steady state profile in the matrix is reached after a simulation time of 15 days (when the oxygen front becomes relatively stable reaching 7–8 millimetres from the boundary). A steady state profile along the fracture zone is reached after a simulation time of 180 days (when the oxygen front becomes stable reaching 16 metres from the oxygen injection point). In this context, the iron-mineral would be fully depleted from the matrix adjacent to the fracture zone after a time no longer than 3,500 years.

A series of key parameters has been identified in controlling the iron-mineral dissolution and, consequently, the oxygen transport into the matrix and along the fracture zone. Some of these parameters affect the rate of the dissolution kinetics of the iron-mineral, such as its reactive surface area and the groundwater pH. Other parameters affect the transport mechanisms of oxygen, such as the oxygen concentration in the boundary water and the porosity of the matrix. Sensitivity analyses have been performed in order to assess the influence of the variability of these parameters on the buffer redox capacity of the system.

In general, the maximum variability has been obtained when the oxygen concentration of the boundary waters changes. As expected, the maximum advance of the dissolution front is obtained for the highest oxygen concentrations. The variability of the pH only affects the obtained results between a certain range of values. Between pH 7.5 and 8.0 no significant differences have been simulated. However, between pH 8.0 and 8.5, the results are very sensitive with respect to slight variations of pH.

The advance of the oxygen front is also controlled by the dissolution rate of the iron-mineral and, consequently, by the implementation of the reactive surface area. Additionally, the effect of the presence of coating (associated to the fracture walls) on the buffer redox capacity has also been analysed. The presence of the coating does not significantly influence the location of the dissolution front in the matrix when the maximum oxygen concentrations are considered on the boundary of the model (X = 0.0 m). However, it effectively determines the transport of oxygen along the fracture zone and, consequently, into the adjacent matrix porewater by diffusion.

Other parameters and processes, such as the implementation of the precipitation of amorphous Fe(III) oxyhydroxides in the calculations, have not shown a significant influence in controlling the advance of the oxygen front.

8 Summary of the model results in relation to hydrogeological glaciation modelling

In Section 6.2 an analytical solution was derived for the case when oxygen depletion along a flow path is limited by diffusion resistance in the rock matrix. The validity of the solution has been evaluated in /Sidborn and Neretnieks 2007, 2008/, where the analytical results were also compared with numerical results. In Section 6.3 an analytical solution was derived for the case when the scavenging of oxygen is limited by dissolution or reaction kinetics. The simplifications underlying this analytical solution were tested against a numerical analysis that is presented in Section 7. Comparative results from these tests are included in Appendix E. In the numerical evaluation the fully coupled equation system is solved numerically in PHREEQC (1D) and PHAST (2D) for different cases with different parameterisations. It can be concluded that the results from the analytical and numerical solutions agree well for the cases studied.

It is apparent from the results from these sections that the simplifications underlying the analytical solution in Section 6.2 are not valid for short times, when reducing minerals are directly exposed to the flowing water in the fracture. It is seen from the numerical results in Section 7 and from similar results in /Sidborn and Neretnieks 2008/ that in this situation, the concentration profiles of the dissolved species, i.e. oxygen and ferrous ions, are basically stationary. This quasi-stationary phase is well described by the analytical solution in Section 6.3 and the numerical solution in Section 7. For longer times however, diffusion resistance increases as the minerals closest to the fracture are depleted from their ferrous iron content and the concentration profiles begin progressing further into the matrix and downstream along the flow path. With the high incoming oxygen concentration in the base case it was concluded from the analytical evaluation in Section 6.3 that the depletion of oxygen is limited by the dissolution of ferrous minerals. The depletion of ferrous iron from biotite is evaluated for this case in Section 2.4.1, where it is seen that over a time period of 1,000 years only a minor change in ferrous iron content would be expected (from 380 to ~300 $mol_{Fe}L_w^{-1}$ in Figure 2-7). In Figure 8-1, the pseudo-steady state solution from Section 6.3 extrapolated in time for different recharge oxygen concentrations is combined with the analytical solution for the diffusion limited case from Section 6.2. The horizontal curves represent the domain where chemical kinetics limits the scavenging of oxygen and the sloped curves represent the domain where the depletion is limited by matrix diffusion. The transition between these two domains is governed by the transient depletion of ferrous iron in the rock matrix minerals, which is not included in the pseudo-steady state analytical solution in Section 6.3. Therefore, there is an unrealistically sharp transition between the domains in Figure 8-1, Figure 8-2, and Figure 8-3.

It should be emphasized that the analytical solutions exclude the oxidation of fracture fillings, such as coatings comprising a larger reducing capacity (approximately 3.7 wt% Fe(II) in Table 5-8) than the rock matrix (approximately 1.5 wt% in Table 5-5) and having a larger specific reactive surface per volume of coating (Section 5.5). The models also neglect any microbial activity, which would be expected wherever reducing minerals are exposed to oxygenated flowing water.

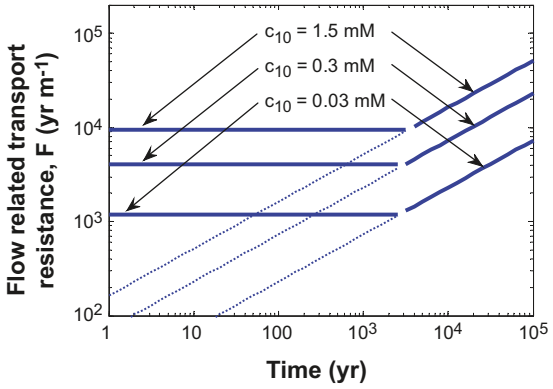

Figure 8-1. *The extent of oxygen ingress in terms of the flow-path F-factor as a function of time for different recharge oxygen concentrations at pH 8. Horizontal lines represent an extrapolation of the pseudo-steady state analytical solution (Section 6.4) for an oxygen concentration level of 3 µM. The solid and dotted sloped lines represent the analytical solution for the diffusion limited case (Section 6.2.2).*

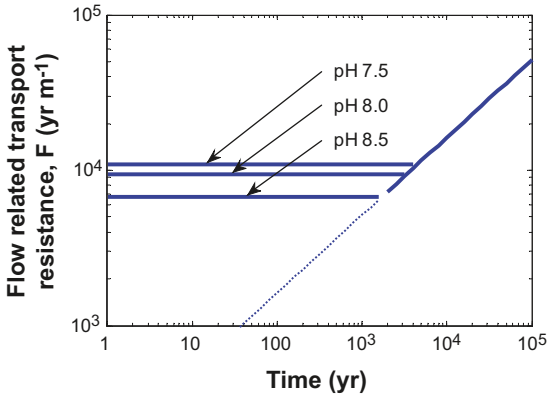

Figure 8-2. *The extent of oxygen ingress in terms of the flow-path F-factor as a function of time for the base-case recharge oxygen concentration 1.5 mM at different solution pH. Horizontal lines represent an extrapolation of the pseudo-steady state analytical solution (Section 6.4) for an oxygen concentration level of 3 µM. The solid and dotted sloped lines represent the analytical solution for the diffusion limited case (Section 6.2.2).*

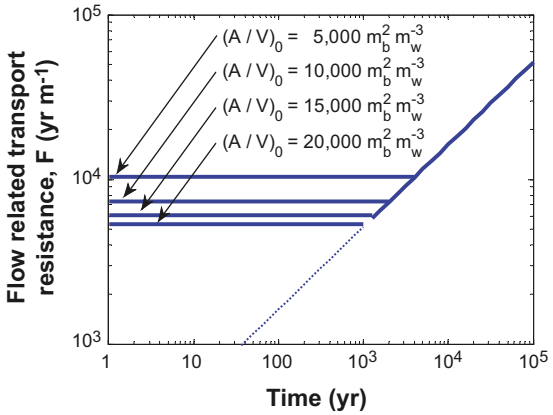

Figure 8-3. *The extent of oxygen ingress in terms of the flow-path F-factor as a function of time for the base-case recharge oxygen concentration 1.5 mM at different available specific surface of biotite. Horizontal lines represent an extrapolation of the pseudo-steady state analytical solution (Section 6.4) for an oxygen concentration level of 3 µM. The solid and dotted sloped lines represent the analytical solution for the diffusion limited case (Section 6.2.2).*

8.1 Hydrogeological glaciation model results

This section includes a brief description of different hydraulic situations that may be expected during a glacial cycle and how data are obtained from hydrogeological modelling for the most unfavourable situations. The temperate phase refers to present day conditions and the different glacial situations are illustrated in Figure 8-4.

When a glacier advances, generally the ice above the ground surface is associated with an underground frozen zone in front of and below the front margin, referred to as permafrost (Figure 8-4b). During the melting phase of a glaciation cycle there is normally no permafrost at the ice margin. Instead, an elevated sea level of melt water is expected in front of the ice margin (Figure 8-4c) and a less steep ice profile than when the ice advances. The glaciation case illustrated in Figure 8-4a, represents an advancing ice profile but without permafrost.

During the major part of a complete glaciation cycle, the Forsmark area is assumed to be covered by a warm-based ice sheet with underlying unfrozen rock. The hydraulic gradient over the repository volume under these conditions is very low.

In the hydrogeological modelling of recharge flow paths at Forsmark, two different approaches have been applied. These approaches are briefly described in the following. For a comprehensive description of the models and additional results for glaciation scenarios that are not included in this report, see /Joyce et al. 2010, Vidstrand et al. 2010/.

The two approaches differ mainly in the representation of the fracture network and the size of the modelled domain. In the first approach /Vidstrand et al. 2010/ a very large model domain is used and the fracture network is represented by an equivalent continuous porous medium (ECPM). In the second approach /Joyce et al. 2010/, the flow paths in the rock are represented by a discrete fracture network (DFN) in a less extensive model domain. For safety assessment purposes, the relatively short and fast flowing channels from the ground surface to canister positions in the repository are the most critical. Therefore, the size of the domain is less important as long as the properties of the most rapid flow paths are accurately described. For the highly heterogeneous rock in Forsmark the DFN model is deemed to be better suited. It can also be concluded by comparing the results from these two approaches that the DFN model produces somewhat lower travel times for the most rapid flow paths. In the choice between these two approaches the use of the DFN model results for the oxygen ingress calculations is therefore conservative in a safety assessment perspective.

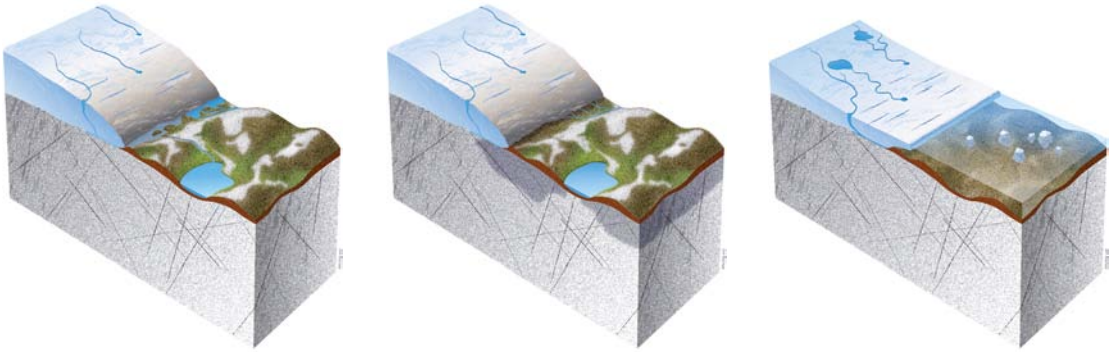

Figure 8-4. *Glacial situations expected during different periods in a glaciation cycle. a) steep ice front profile without permafrost, b) steep ice front profile including permafrost as expected during glacier advancement, c) flat ice front profile with an elevated sea level and no permafrost as expected during ice front retreat.*

In the post-processing of the results from the DFN model, particles are released in each canister position and their routes through the discrete fractures are back-tracked along the calculated flow-field to the ground surface. For each particle, several parameters are recorded along the flow-path, such as the residence time, path length, coordinates and flow related transport resistance or F-factor. Thus, the particle back-tracking algorithm gives cumulative data for these parameters for the entire flow path extending from the ground-surface under the ice to the canister positions in the repository. It should be emphasized that transient effects due to ice front movement such as temporal changes in hydraulic gradients and flow direction in individual flowing structures are not reflected in the results. The obtained properties should thus be interpreted as snapshots for a given ice front location. As an example, a recharge flow path for one ice front location may become a discharge flow path for another location. These two situations may be studied separately, but the transition between them is not captured in the particle tracking.

For the oxygen ingress calculations the most important performance measure is the flow path F-factor, which is explained in Section 2.1.1. F-factors obtained from the oxygen ingress model calculations in previous sections may be related to these flow path F-factors to assess the extent of oxygen ingress to the canister positions in the repository.

From the hydrogeological model results it can be concluded that the glacial situation illustrated in Figure 8-4a, and assuming a stationary ice front margin just above the repository volume, yields flow paths to the repository with the lowest F-factors of all the glacial situations studied. It may be noted that this situation with a steep ice profile, in the absence of permafrost is generally not expected at Forsmark during a glaciation cycle. However, although this situation is unlikely, it can not be ruled out as impossible in a safety assessment. The two ice front margin locations that yield the lowest recharge flow path F-factors are illustrated in Figure 8-5.

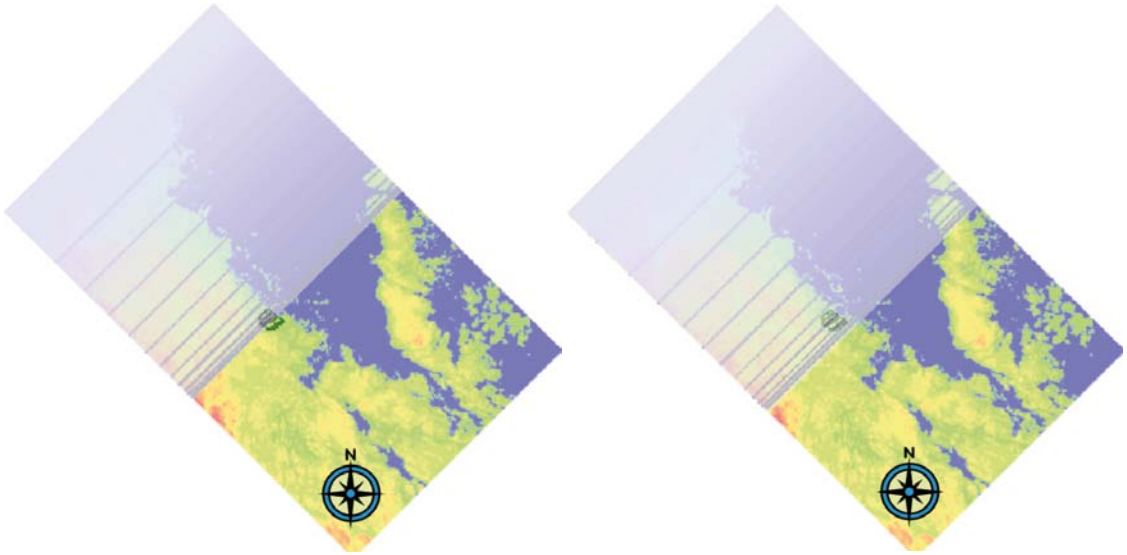

(a) Ice location II (b) Ice location III

Figure 8-5. *Ice front locations used for oxygen intrusion modelling. a) Ice location II where the ice front margin is centred over the repository volume. b) Ice location III where the entire repository volume is below the ice front.*

The F-factors for the recharge flow paths reaching each canister position are illustrated in Figure 8-6a and c, and the corresponding cumulative distributions for all flow paths are shown in Figure 8-6b and d. It may be noted that canister positions marked in grey have no associated flow path. Also in the cumulative distribution it can be seen that only approximately 15% (1,051 out of 6,916) and 17% (1,184 out of 6,916) of the particle-tracking flow paths are included in the distribution for ice location II and III respectively. This is because some of the flow-paths are so slow that the released particles have not reached the ground-surface during the simulated time and are therefore excluded. Canister positions that do not fulfil defined criteria of e.g. safety distance to deformation zones, are also excluded.

From these results it can be concluded that the hydraulic situation for ice location III yields particle track flow-paths with lower F-factors and thereby more rapid transport paths for oxygen than ice location II. Furthermore, it is seen that the most sensitive part of the repository volume is different for ice location II and III. It is important to note that this shift is the effect of a rather small displacement of the ice front margin. This can also be seen from Table 8-1 and Table 8-2 where the 30 most rapid oxygen ingress flow-paths (lowest F-factors) for each ice front position are listed. The 30 canister positions are all unique for the two ice front locations.

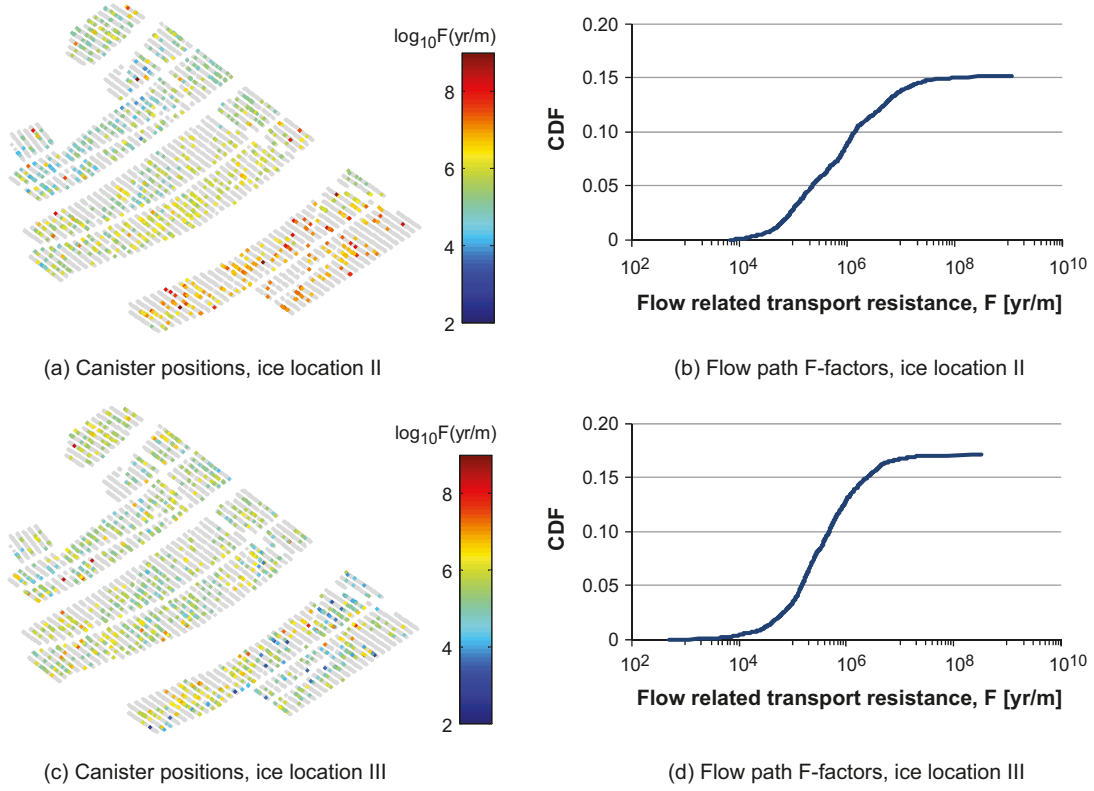

Figure 8-6. *Flow related transport resistance for complete flow paths from the ground surface to canister positions in the repository. Flow paths associated with grey canister positions are excluded (see text). The number of flowpaths included is 1,051 for ice location II and 1,184 for ice location III. The total number of particles released is 6,916.*

Table 8-1. The 30 most rapid flow paths (lowest F-factors) for ice location II.

#POINT	F_{tot}	Canister position			Recharge location		
	(yr/m)	x	y	z	x	y	z
1494	6747	1631444	6700249	–466.40	1628936	6702218	2.06
1594	7939	1631414	6700472	–467.06	1628929	6702295	0.83
1532	8080	1631321	6700439	–468.21	1630938	6701209	–3.98
985	8700	1631466	6700682	–464.59	1630425	6701141	–0.32
984	9030	1631472	6700678	–466.29	1628912	6702279	1.83
1621	9315	1631447	6700495	–467.91	1629751	6702793	–6.77
511	10180	1630740	6699925	–468.08	1629265	6701698	–0.48
980	10971	1631493	6700660	–467.65	1629478	6702594	–1.69
1608	11957	1631500	6700406	–466.33	1629220	6702531	–0.81
2031	12600	1630822	6699469	–464.68	1629280	6701722	–0.53
411	12840	1630678	6700162	–474.38	1629109	6701902	0.34
801	13290	1630871	6700078	–467.78	1629095	6701898	0.40
766	13382	1631372	6700552	–471.29	1629410	6702611	–0.95
804	14220	1630885	6700067	–473.54	1629283	6701725	–0.51
996	14500	1631408	6700725	–464.43	1628620	6702070	4.20
626	14850	1630752	6700016	–472.17	1629097	6701904	0.27
3023	15400	1631430	6699903	–468.18	1629511	6701010	2.66
1600	15600	1631458	6700439	–467.06	1630425	6701141	–0.32
639	15610	1630850	6699945	–466.30	1629026	6702009	–0.03
629	15950	1630766	6700005	–469.61	1629097	6701904	0.27
410	16390	1630682	6700157	–468.49	1629026	6702009	–0.03
728	17940	1630779	6700097	–468.83	1629026	6702009	–0.03
1029	18870	1631159	6700063	–463.82	1629273	6701682	–0.57
1544	19010	1631402	6700379	–470.28	1630064	6701729	–0.92
424	19230	1630710	6700186	–466.74	1628966	6702205	1.02
693	20090	1630903	6699955	–465.85	1628680	6702153	1.28
648	20110	1630892	6699911	–469.26	1629019	6701967	0.34
633	20560	1630787	6699991	–471.42	1629098	6701878	0.62
1589	20900	1631556	6700315	–466.2	1630075	6701731	–0.73
808	21590	1630904	6700052	–465.93	1629019	6701967	0.34

Table 8-2. The 30 most rapid flow paths (lowest F-factors) for ice location III.

#POINT	F_{tot}	Canister position			Recharge location		
	(yr/m)	x	y	z	x	y	z
4772	508	1631508	6699085	–465.72	1630385	6699454	8.47
5250	848	1632036	6699306	–468.77	1630384	6699464	8.39
6397	1190	1632905	6699537	–472.36	1632283	6700322	–3.51
5516	1710	1632223	6699470	–465.59	1632390	6700628	–1.79
5786	1780	1632277	6699626	–463.77	1632416	6700736	–1.64
5842	1800	1632362	6699617	–464.87	1631971	6701804	–4.08
6505	2480	1632636	6699867	–468.11	1632372	6700581	–1.93
5938	3540	1632596	6699457	–465.21	1632298	6700365	–5.55
6313	3770	1632836	6699537	–466.09	1632069	6701377	–0.28
6492	3940	1632700	6699821	–468.72	1632266	6700270	–0.21
4892	3952	1631633	6699147	–466.37	1630430	6699464	7.11
5804	4232	1632480	6699441	–464.52	1630430	6699464	7.11
5743	4570	1632508	6699372	–463.70	1632318	6700433	–5.07
5373	4762	1632228	6699274	–467.76	1630415	6699463	7.47
6350	5500	1632564	6699818	–467.49	1632273	6700292	–0.95
6340	6150	1632614	6699784	–468.06	1632389	6700623	–1.64
5590	6700	1632199	6699534	–464.51	1632085	6701418	0.36
4406	6810	1632213	6700111	–466.70	1631481	6701998	–7.43
6331	6890	1632659	6699754	–468.55	1632110	6701418	–0.01
6351	7400	1632559	6699821	–467.52	1632318	6700433	–5.07
6393	7870	1632886	6699552	–466.15	1632185	6700517	–2.53
5788	7930	1632268	6699634	–463.89	1632109	6701429	–0.17
5020	7972	1631771	6699196	–467.98	1630275	6699480	4.96
6012	8270	1632662	6699461	–468.6	1631371	6700776	–3.14
6886	9231	1632737	6700039	–465.41	1631523	6702230	–2.47
6348	9500	1632574	6699811	–467.44	1631744	6701860	–10.25
5104	9840	1631868	6699228	–469.45	1630537	6699469	5.39
5635	9862	1632334	6699492	–468.91	1630415	6699463	7.47
6868	9880	1632837	6699971	–470.2	1632397	6700650	–2.52
6383	9950	1632836	6699584	–466.76	1631751	6701863	–10.08

8.2 Applied results for oxygen ingress

In this section the analytical solution for the oxygen ingress along a flow-path derived in Section 6 are combined with information on flow related transport resistance (F-factors) obtained from hydrogeological modelling in Section 8.1 for the most pessimistic stationary ice front locations. The base-case situation with an oxygen recharge concentration of 1.5 mM and pH 8.0 is shown in Figure 8-7 for stationary ice locations II and III. It is seen that there is a small overlap between the curves indicating that some of the canister positions are exposed to oxygen under these conditions. With lower oxygen recharge concentration of 0.3 mM shown in Figure 8-8 some canister positions are exposed at ice location III but to a much lower oxygen concentration. None of the canister positions are exposed to oxygen concentrations exceeding 0.1 μM for ice location II in this case.

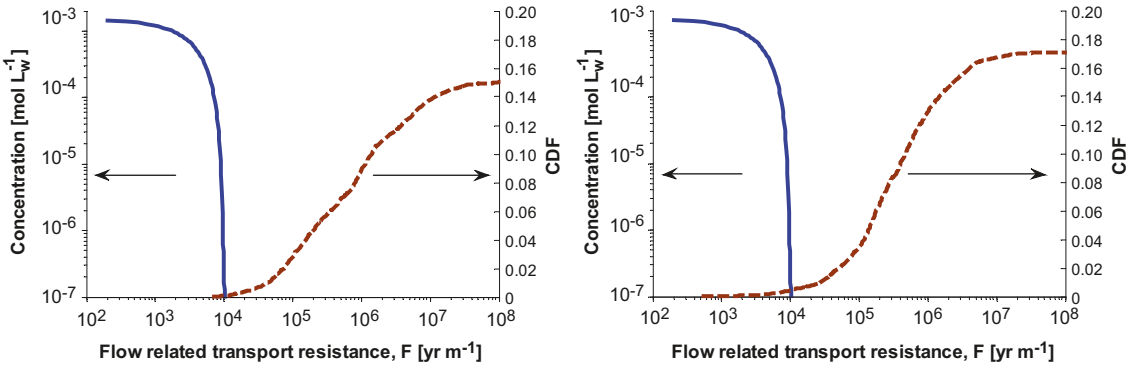

(a) Ice location II (b) Ice location III

Figure 8-7. *Superpositioned plots of the oxygen concentration profile (blue curve) along flow-paths for the base-case with a 1.5 mM recharge concentration and CDF (dashed red curves) of flow-paths obtained from hydrogeological modelling for (a) ice location II and (b) ice location III.*

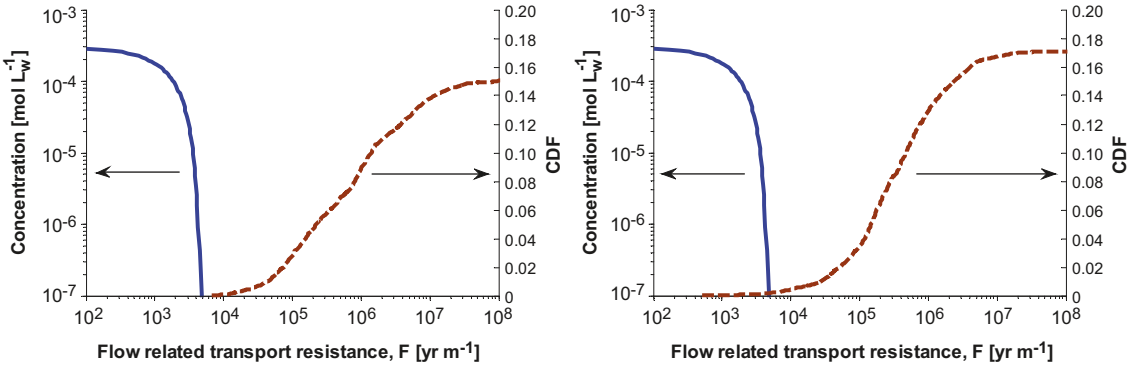

(c) Ice location II (d) Ice location III

Figure 8-8. *Superpositioned plots of the oxygen concentration profile (blue curve) along flow-paths for a 0.3 mM recharge concentration and CDF (dashed red curves) of flow-paths obtained from hydrogeological modelling for (a) ice location II and (b) ice location III.*

9 Discussion and conclusions

The objective of this report is to evaluate the potential for dissolved oxygen to reach canister positions in a repository for spent nuclear fuel at Forsmark. Therefore, the aim of the calculations and model efforts is to calculate the ingress of oxygen under conservatively chosen conditions, for use in a safety assessment. Additional oxygen scavenging processes that are neglected in the models include e.g. biological pathways, which may have a major influence on the extent of oxygen ingress under certain conditions.

Assumptions and uncertainties

Present day observations show that microbially mediated degradation of organic material close to the ground surface dominates oxygen consumption under temperate conditions. The result is that reducing conditions generally persist below just a few metres below the ground surface. In Section 2.3 it is also shown that microbially mediated reduction of dissolved oxygen is likely to occur also during different phases of a glaciation cycle. Although this activity is qualitatively described and observed at existing glaciers, it is difficult to quantify. Therefore, microbially mediated degradation of organic matter is conservatively neglected in the calculations in this report.

In the absence of organic matter of ground surface origin, ferrous minerals contained in the rock matrix are the largest source for reducing capacity in the rock. Other natural reductants such as sulphide, hydrogen and methane, are also present in the rock. The amounts of dissolved hydrogen and methane in the pore water in the matrix are however low compared to the ferrous iron comprised in the matrix minerals. Estimating the rate at which these dissolved gases are supplied over large distances to fractures carrying oxygen is difficult, and would introduce additional uncertainties.

Therefore, ferrous iron comprised in the rock is, conservatively, the only source of reducing capacity that is considered in the model calculations.

In Section 4 it was concluded that the consumption of oxygen by reaction with ferrous iron is influenced by several parallel reaction paths. The fastest of these paths at given conditions would control the extent of oxygen ingress. In the calculations in this report, only the slowest of these reaction paths is considered in the calculations. In this reaction path, the oxidation of ferrous iron is assumed to occur in two consecutive steps, non-oxidative dissolution of ferrous ions and homogeneous oxidation reaction with oxygen. Thus, the possibility of direct oxidation of ferrous iron in the mineral lattice is neglected and the ferrous ions need to be dissolved into the pore water prior to their reaction with oxygen. For the time-scales of interest in this report (stationary ice front over a thousand years) and the pH and oxygen concentration ranges studied, scavenging of oxygen is to a large extent limited by the non-oxidative dissolution. Therefore, this is likely a conservative assumption. Also, observations at the mineral grain scale indicate that oxidation of ferrous iron may occur in the mineral lattice. This can be seen in Figure 3-8 where pyrite has been replaced by the oxidised goethite and in Figure 3-10 where precipitation of ferric oxihydroxide appear to occur in between the sheets in the layered mineral grain structure of chlorite. It may be argued that precipitation of secondary minerals would clog the pores of the rock matrix and thereby hinder the diffusion of dissolved species. This is neglected in the calculations in this report based on observations that porosities in the altered zone adjacent to fractures are rather larger than smaller compared with the unaltered rock, despite the presence of secondary precipitates.

The reactive surface of reducing minerals in the rock matrix is assumed to equal the total external mineral grain surface per volume of pore water corrected for an estimated surface roughness. An average external surface for mineral grains is estimated based on a simplified box shaped symmetry and visual size estimations of 260 individual biotite grains from different boreholes and depths at Forsmark. The external area was increased by a factor of ten to account for surface roughness. This factor is derived for crushed granite samples at Forsmark. Due to the layered structure of mineral grains of biotite and chlorite this factor is presumably larger than for the granite samples. Furthermore, the layered structure of biotite and chlorite may split open upon weathering which would further increase the availability of internal surfaces. The biotite external surface area corrected

for roughness is therefore deemed to be a conservative estimation of the reactive surfaces of biotite in the rock. The assumed initial specific surface area of biotite is $a_{EXT}/\rho_b = 0.05\ m_b^2\ g_b^{-1}$ which is a few percent of typical measured internal BET surfaces (~1 $m_b^2\ g_b^{-1}$) of non-weathered biotite grains found in the literature (e.g. /White and Brantley 2003/).

Recharging glacial melt water is expected to possess pH in the range 9.0 to 9.3 (see Section 5.8). Given that the dissolution and oxidation reactions occur in the matrix relatively close to the flowing water in the fractures (within one centimetre for the base-case) the pH should not differ largely from that in the fracture. At pH 9 the rate of oxygen scavenging would be enhanced compared to the base-case calculations with an assumed pH 8. This conclusion is based on the rate expressions for both non-oxidative dissolution R_{diss} (see Eqn. 2-20) and homogeneous oxidation R_{ox} (in Eqn. 2-27). The assumed pH 8 is therefore deemed to be conservative.

The oxygen concentration in glacial melt-water is assumed to be up to 1.5 mM in the calculations. This high concentration is approximately five times the concentration in rain water, and is obtained from theoretical estimates and not by samples of subglacial melt waters. It may be emphasised that this is the maximum theoretical concentration calculated for ice formed at ground surface level and at a temperature of –10°C. Ice formed at higher elevation and at lower temperature would have a lower theoretical concentration. Furthermore, it is concluded in Section 2.3.3 that photosynthetic and heterotrophic microbial populations thrive on the surface of most studied glaciers and ice sheets, and that the activity in some cases is so high that the ice surface blocks become anaerobic. It is also concluded that below many glaciers there are anaerobic processes ongoing. These observations suggest that the high oxygen concentration used in the modelling is highly conservative.

During an ice front passage, the hydraulic situation in the rock changes drastically. Not only would flow rates be expected to increase but also the flow pattern will change upon the transient changes in hydraulic head gradients. Recharge flow paths may become discharge flow paths and previously inactive parts of fractures with practically stagnant water may become important flow channels. With a typical ice melt rate of 200 m/yr the ice front passes over the repository volume in approximately ten years. During this time the hydraulic conditions at the site are continuously changed. For the oxygen intrusion calculations such transient effects are impossible to model accurately. Instead hydraulic properties for snapshots of stationary ice front locations are used. This is probably conservative for a normal ice front passage, since it would take some time to reach a steady-state flow situation for each new front location. However, there is a small probability that the ice halts temporarily during the ice advance or retreat and the possibility of this to occur in an unfavourable location close to the repository location can not be ruled out in the safety assessment. Therefore, the most unfavourable ice front location, resulting in high hydraulic gradients, is assumed to persist over a period of 1,000 years in the calculations in this report. Although this situation can not be ruled out, it is considered to be unlikely. The probability of a halting ice in an unfavourable location during a period of 200 years is somewhat higher. The ice front profile assumed in the hydraulic modelling is based on a theoretical profile /Paterson 1994/, which may be representative for a growing ice (see Figure 8-4a). A growing ice is however likely to be accompanied by a frozen tongue of permafrost extending a couple of kilometres under the ice (see Figure 8-4b). This frozen zone has been shown to act as a barrier for the flowing groundwater /Vidstrand et al. 2010/. During the melting phase this permafrost barrier is absent but the ice front profile is then likely not as steep as the theoretical profile (see Figure 8-4c), resulting in a lower hydraulic gradient. Furthermore, the melting ice is assumed to be accompanied by an elevated sea level in front of the ice, which would further decrease the hydraulic gradient.

The influence of eskers, melt water tunnels under the ice, on the hydraulic properties has not been studied explicitly in the hydrogeological models. Such hydraulically active tunnels under the ice could possibly have some impact on the flow pattern under the ice, e.g. with a hydraulic gradient acting perpendicular to the gradient caused by the ice front. Simulations with a different ice front direction have been performed /Vidstrand et al. 2010/, showing no significant difference in flow-path F-factors. The direction of the hydraulic gradient is therefore deemed to be of minor influence. An esker extending some distance in under the ice could, however, potentially give rise to such gradients for longer times than the ice front passing over the repository in just ten years. Assuming an ice melt rate of 200 m/yr and using the results for the most unfavourable stationary ice front location during 1,000 years could perhaps represent an esker of length 1,000 yr · 200 m/yr = 200 km. The active part of an esker is expected to be less, and the pressure in the esker to be higher than atmospheric pressure.

Model results

The pseudo-steady state results from the analytical and numerical evaluation for the concentration profile of oxygen in the rock matrix agree well for most cases studied and especially in situations with high oxygen concentrations that are the most critical for safety assessment purposes (see Appendix E).

From the analytical evaluation it can therefore be concluded that the pseudo-steady state oxygen ingress is controlled by dissolution of ferrous minerals in the matrix for the base-case with a recharge oxygen concentration of 1.5 mM and pH 8. Under these conditions a relatively small fraction of the ferrous iron in matrix minerals, exposed to the recharge concentration, will be depleted over a period of one thousand years (~20% in Figure 2-7). The pseudo-steady state results are therefore deemed to be a good approximation for this case over a thousand years. For longer times diffusion resistance would become increasingly important and eventually limit the rate of oxygen depletion and control the extent of oxygen ingress (see Figure 8-1).

At a flow-path distance corresponding to an F-factor of ~5,400 yr/m the concentration has decreased to 0.3 mM under these conditions. Applying the hydrogeological model results for the worst-case ice location III, 14 canister positions in the repository would be exposed to this concentration or higher. For ice location II none of the canister positions would be exposed to this concentration. At a flow-path distance corresponding to an F-factor of ~9,400 yr/m the concentration has decreased to 3 μM. This concentration or higher would affect 25 canister positions for ice location III. For ice location II only six canister positions would be exposed to this concentration or higher.

With a recharge oxygen concentration in the glacial melt water of 0.3 mM, a flow-path distance corresponding to an F-factor of ~3,000 yr/m would be reached by oxygen at a concentration of 0.03 mM. Applying the hydrogeological model results for the worst-case ice location III, this concentration or higher would affect approximately seven canister positions. An F-factor of ~4,000 yr/m is reached by oxygen at a concentration of 3 μM which would affect 11 canister positions for ice location III. For ice location II none of the canister positions would be exposed to oxygen at a concentration of 3 μM or higher.

It should be emphasised that these results refer to concentrations reaching deposition holes in the repository. With an intact bentonite buffer in the deposition holes, the concentration reaching the canister surface is less.

The effect of the presence of a reducing fracture coating is evaluated using the numerical 2D model in PHAST. It is concluded that the extent of oxygen ingress into the matrix is not significantly affected by the presence of the coating (See Section 7.6). However, the concentration gradient at the fracture/matrix interface is steeper than for the case without coating. Since the pore diffusivity is assumed to be the same for the two cases, this implies that the flux of oxygen into the matrix is larger for the case with coating included. This effect is more prominent for high oxygen concentrations in the fracture. This is expected as the depletion of oxygen is limited by dissolution kinetics for high oxygen concentrations. With lower oxygen concentrations in the fracture, the scavenging of oxygen is increasingly limited by the homogeneous oxidation kinetics. Therefore, the higher specific surface of minerals in the coating as compared to the matrix has less influence when the oxygen concentration is low.

As expected from the reasoning above, the ingress of oxygen downstream along the flow-path is not much affected by the presence of a fracture coating when the recharge oxygen concentration is low (0.03 mM in Figure 7-29). For higher recharge concentrations the ingress along the fracture is less than for the case without coating. With an oxygen recharge concentration of 0.3 mM the ingress of oxygen is approximately 65% of that without the coating. With an oxygen recharge concentration of 1.5 mM the ingress of oxygen is approximately 75% of that without the coating.

It should be emphasised that the calculations involving reducing fracture coatings can not be regarded to be conservative. These calculations are based on the assumption that the entire fracture surface is coated by chlorite with a mean reducing capacity based on a sampled lognormally distributed chlorite thickness.

Comparison with observations

Observations from sampled boreholes and soil pipes during the site investigation give a clear indication that oxygen is consumed within the top soil or the upper few metres of the rock during temperate conditions. In contrast to the site investigations in Laxemar, no redox transition zone has been detected in the bedrock in Forsmark, probably because most boreholes have casing in their upper 100 metres.

The observation of preserved well-developed cubic crystals of Palaeozoic pyrite and asphaltite in fractures and fracture zones in the upper 150 metres of the bedrock further indicates that reducing conditions have prevailed in most parts of the fracture system over the past 250 Ma. This could probably be attributed to the characteristic sub-horizontal to gently dipping, highly transmissive fracture zones in the upper hundred metres at Forsmark, which creates a strong horizontal component in the groundwater flow.

However, the observation of pyrite and the oxidised goethite coexisting in water conductive zones (mainly in the near-surface extensions of the deformation zones ZFMA1, ZFMA8, and ZFMENE1208B), may suggest that oxygen ingress has occurred along channelled flow paths in these zones. Since the age of this goethite is not known, it is not possible to determine when the intrusion may have occurred.

It can be concluded that the modelled rapid ingress paths for oxygen to repository depth can not be seen in the observations made at the site. In a highly heterogeneous fracture system with channelled flow in a few transmissive flow paths it may be argued that such flow paths have remained unnoticed. The observations made should instead be compared with modelled results for an average flow path. Since no indications of oxygen ingress has been observed, except for some goethite in highly transmissive zones, this may suggest that the assumptions underlying the calculations are highly conservative.

10 References

SKB's (Svensk Kärnbränslehantering AB) publications can be found at www.skb.se/publications.

References with abbreviated names

Backfill production report, 2010. Design, production and initial state of the backfill and plug in deposition tunnels. SKB TR-10-16, Svensk Kärnbränslehantering AB.

Buffer production report, 2010. Design, production and initial state of the buffer. SKB TR-10-15, Svensk Kärnbränslehantering AB.

Closure production report, 2010. Design, production and initial state of the closure. SKB TR-10-17, Svensk Kärnbränslehantering AB.

Data report, 2010. Data report for the safety assessment SR-Site. SKB TR-10-52, Svensk Kärnbränslehantering AB.

Radionuclide transport report, 2010. Radionuclide transport calculations for the safety assessment SR-Site. SKB TR-10-50, Svensk Kärnbränslehantering AB.

Other public references

Aitchison J, Brown J A C, 1957. The lognormal distribution. Cambridge: Cambridge University Press.

Akagawa F, Yoshida H, Yogo S, Yamomoto K, 2006. Redox front formation in fractured crystalline rock: an analogue of matrix diffusion in an oxidizing front along water-conducting fractures. Geochemistry: Exploration, Environment, Analysis, 6, pp 49–56.

Anderson C R, James R E, Fru E C, Kennedy C B, Pedersen K, 2006. In situ ecological development of a bacteriogenic iron oxide-producing microbial community from a subsurface granitic rock environment. Geobiology, 4, pp 29–42.

André M, Malmström M E, Neretnieks I, 2009. Specific surface area determinations on intact drillcores and evaluation of extrapolation methods for rock matrix surfaces. Journal of Contaminant Hydrology, 110, pp 1–8.

Annersten H, 1974. Mössbauer studies of natural biotites. American Mineralogist 59, pp 143–151.

Apps J A, van De Kamp P C, 1993. Energy gases of abiogenic origin in the Earth's crust. In: Howell D G (ed). The future of energy gases. Professional Paper 1570, U.S. Geological Survey, Denver, Colorado, pp 81–132.

Arcos D, Pérez del Villar L, Bruno J, Domènech C, 2008. Geochemical modelling of the weathering zone of the "Mina Fe" U deposit (Spain): A natural analogue for nuclear spent fuel alteration and stability processes in radwaste disposal. Applied Geochemistry, 23, pp 807–821.

Auqué L, Gimeno M J, Gómez J, Nilsson A-C, 2008. Potentiometrically measured Eh in groundwaters from the Scandinavian Shield. Applied Geochemistry, 23, pp 1820–1833.

Banwart S, Gustafsson E, Laaksoharju M, Nilsson A-C, Tullborg E-L, Wallin B, 1994. Large-scale intrusion of shallow water into a vertical fracture zone in crystalline bedrock: Initial hydrochemical perturbation during tunnel construction at the Äspö Hard Rock Laboratory, southeastern Sweden. Water Resources Research, 30, pp 1747–1763.

Bergman T, Hedenström A, 2006. Forsmark site investigation. Petrographic analysis of gravel and boulders in the Forsmark candidate area. SKB P-06-87, Svensk Kärnbränslehantering AB.

Bergman T, Johansson R, Lindén A H, Rudmark L, Stephens M, Isaksson H, Lindroos H, 1999. Förstudie Tierp. Jordarter, bergarter och deformationszoner. SKB R-99-53, Svensk Kärnbränslehantering AB.

Bodin J, Delay F, de Marsily G, 2003. Solute transport in a single fracture with negligible matrix permeability: 1. fundamental mechanisms. Hydrogeology Journal, 11, pp 418–433.

Byegård J, Selnert E, Tullborg E-L, 2008. Bedrock transport properties. Data evaluation and retardation model. Site descriptive modelling, SDM-Site Forsmark. SKB R-08-98, Svensk Kärnbränslehantering AB.

Cera E, Bruno J, Grivé M, Rollin C, Ahonen L, Kaija J, Blomqvist R, El Aamrani F Z, Casas I, de Pablo J, 1999. Redox processes in the Palmottu uranium deposit. The Palmottu Natural Analogue Project. Archive Report Y50/99/19, Geological Survey of Finland.

Chapman N A, McKinley I G, Shea M E, Smellie J A T, 1991. The Poços de Caldas project: Summary and implications for radioactive waste management. SKB TR 90-24, Svensk Kärnbränslehantering AB.

Chi Fru E, 2008. Constraints in the colonization of natural and engineered subterranean igneous rock aquifers by aerobic methane-oxidizing bacteria inferred by culture analysis. Geobiology, 6, pp 365–375.

Cooper R S, Liberman D A, 1970. Fixed-bed adsorption kinetics with pore diffusion control. Industrial & Engineering Chemistry Fundamentals, 9, pp 620–623.

Cramer J, Smellie J (eds), 1994. Final report of the AECL/SKB Cigar Lake Analog Study. SKB TR 94-04, Svensk Kärnbränslehantering AB.

Crawford J, 2008. Bedrock transport properties Forsmark. Site descriptive modelling, SDM-Site Forsmark. SKB R-08-48, Svensk Kärnbränslehantering AB.

Crespo M T, Pérez del Villar L, Quejido A J, Sánchez M, Cózar J S, Fernández-Díaz M, 2003. U-series in Fe-U-rich fracture fillings from the oxidised cap of the "Mina Fe" uranium deposit (Spain): implications for processes in a radwaste repository. Applied Geochemistry, 18, pp 1251–1266.

Cross J E, Haworth A, Lichtner P C, MacKenzie A B, Moreno L, Neretnieks I, Nordstrom D K, Read D, Romero L, Scott R D, Sharland S M, Tweed C J, 1991. Testing models of redox front migration and geochemistry at the Osamu Utsumi mine and Morro do Ferro analogue studie sites, Poços de Caldas, Brazil. SKB TR 90-21, Svensk Kärnbränslehantering AB.

Crow E L, Shimizu K (eds), 1988. Lognormal distributions: theory and applications. New York: Marcel Dekker.

Deer W A, Howie R A, Zussman J, 1992. An introduction to the rock-forming minerals. 2nd ed. Harlow: Longman.

Dideriksen K, Christiansen B C, Baker J A, Frandsen C, Balic-Zunic T, Tullborg E-L, Mørup S, Stipp S L S, 2007. Fe-oxide fracture fillings as a palæo-redox indicator: Structure, crystal form and Fe isotope composition. Chemical Geology, 244, pp 330–343.

Dideriksen K, Christiansen B C, Frandsen C, Balic-Zunic T, Mørup S, Stipp S L S, 2010. Paleo-redox boundaries in fractured granite. Geochimica et Cosmochimica Acta, 74, pp 2866–2880.

Dittmar T, Lara R J, 2001. Molecular evidence for lignin degradation in sulfate-reducing mangrove sediments (Amazônia, Brazil). Geochimica et Cosmochimica Acta, 65, pp 1417–1428.

Drake H, Tullborg E-L, 2006. Oskarshamn site investigation. Mineralogical, chemical and redox features of red-staining adjacent to fractures – Results from drill core KLX04. SKB P-06-02, Svensk Kärnbränslehantering AB.

Drake H, Tullborg E-L, 2009. Fracture mineralogy Laxemar. Site descriptive modelling, SDM-Site Laxemar. SKB R-08-99, Svensk Kärnbränslehantering AB.

Drake H, Sandström B, Tullborg E-L, 2006. Mineralogy and geochemistry of rocks and fracture fillings from Forsmark and Oskarshamn: Compilation of data for SR-Can. SKB R-06-109, Svensk Kärnbränslehantering AB.

Drake H, Tullborg E-L, Annersten H, 2008. Red-staining of the wall rock and its influence on the reducing capacity around water conducting fractures. Applied Geochemistry, 23, pp 1898–1920.

Drake H, Tullborg E-L, MacKenzie A B, 2009. Detecting the near-surface redox front in crystalline bedrock using fracture mineral distribution, geochemistry and U-series disequilibrium. Applied Geochemistry, 24, pp 1023–1039.

Ehrlich H L, 1996. Geomicrobiology of manganese. In: Geomicrobiology. 3rd ed. New York: Marcel Dekker, pp 389–489.

Eklund S, Mattsson K-J, 2009. Forsmark site investigation. Quantitative mapping of fracture minerals in Forsmark. SKB P-08-47, Svensk Kärnbränslehantering AB.

Eliasson T, 1993. Mineralogy, geochemistry and petrophysics of red coloured granite adjacent to fractures. SKB TR 93-06, Svensk Kärnbränslehantering AB.

Eliasson T, Tullborg E-L, Landström O, 1989. Fracture filling mineralogy and geochemistry at the Swedish HDR research site. In: Baria R (ed). Hot dry rock geothermal energy: Camborne School of Mines International Conference. London: Robertson Scientific Publications, pp 425–435.

Follin S, 2008. Bedrock hydrogeology Forsmark. Site descriptive modelling, SDM-Site Forsmark. SKB R-08-95, Svensk Kärnbränslehantering AB.

Follin S, Johansson P-O, Hartley L, Jackson P, Roberts D, Marsic N, 2007. Hydrogeological conceptual model development and numerical modelling using CONNECTFLOW, Forsmark modelling stage 2.2. SKB R-07-49, Svensk Kärnbränslehantering AB.

Gascoyne M, 1997. Evolution of redox conditions and groundwater composition in recharge-discharge environments on the Canadian Shield. Hydrogeology Journal, 5, pp 4–18.

Gascoyne M, 1999. Long-term maintenanceof reducing conditions in a spent nuclear fuel repository. A re-examination of critical factors. SKB R-99-41, Svensk Kärnbränslehantering AB.

Gascoyne M, Cramer J J, 1987. History of actinide and minor element mobility in an Archean granitic batholith in Manitoba, Canada. Applied Geochemistry, 2, pp 37–53.

Gauthier-Lafaye F, Ledoux E, Smellie J, Louvat D, Michaud V, Pérez del Villar L, Oversby V, Bruno J, 2000. OKLO-natural analogue phase II: behaviour of nuclear reaction products in a natural environment. Final Report EUR 19139 EN, Contract No F14W-CT96-0020, European Commission.

Gentzschein B, 1986. Hydrological investigations at the Klipperås study site. SKB TR 86-08, Svensk Kärnbränslehantering AB.

Glynn P D, Voss C I, 1999. Geochemical characterization of Simpevarp ground waters near the Äspö Hard Rock Laboratory. SKI Report 96:29, Statens kärnkraftinspektion (Swedish Nuclear Power Inspectorate).

Guimerà J, Duro L, Jordana S, Bruno J, 1999. Effects of ice melting and redox front migration in fractured rocks of low permeability. SKB TR-99-19, Svensk Kärnbränslehantering AB.

Guimerà J, Duro L, Delos A, 2006. Changes in groundwater composition as a consequence of deglaciation. Implications for performance assessment. SKB R-06-105, Svensk Kärnbränslehantering AB.

Gutiérrez M G, Guimerà J, de Llano A Y, Benitez A H, Humm J, Saltink M, 1997. Tracer test at El Berrocal site. Journal of Contaminant Hydrology, 26, pp 179–188.

Gylling B, Birgersson L, Moreno L, Neretnieks I, 1998. Analysis of a long-term pumping and tracer test using the channel network model. Journal of Contaminant Hydrology, 32, pp 203–222.

Haggerty R, 1995. Aquifer Remediation in the Presence of Rate-Limited Mass Transfer. Ph.D. thesis. Stanford University, Stanford, California.

Haggerty R, Gorelick S M, 1995. Multiple-rate mass transfer for modeling diffusion and surface reactions i media with pore-scale heterogeneity. Water Resources Research, 31, pp 2383–2400.

Haggerty R, McKenna S A, Meigs L C, 2000. On the late-time behavior of tracer test breakthrough curves. Water Resources Research, 36, pp 3467–3479.

Hallbeck L, 2008. Evaluating hydrochemical data from shallow groundwater in Forsmark from a microbiological perspective. SKB R-08-75, Svensk Kärnbränslehantering AB.

Hallbeck L, 2009. Microbial processes in glaciers and permafrost. A literature study on microbiology affecting groundwater at ice sheet melting. SKB R-09-37, Svensk Kärnbränslehantering AB.

Hallbeck L, 2010. Principal organic materials in a repository for spent nuclear fuel. SKB TR-10-19, Svensk Kärnbränslehantering AB.

Hallbeck L, Pedersen K, 2008a. Characterization of microbial processes in deep aquifers of the Fennoscandian Shield. Applied Geochemistry, 23, pp 1796–1819.

Hallbeck L, Pedersen K, 2008b. Explorative analyses of microbes, colloids and gases together with microbial modelling. Site description model. SDM-Site Laxemar. SKB R-08-109, Svensk Kärnbränslehantering AB.

Hallbeck L, Pedersen K, 2008c. Explorative analysis of microbes, colloids and gases. SDM-Site Forsmark. SKB R-08-85, Svensk Kärnbränslehantering AB.

Hofmann B A, 1999. Geochemistry of natural redox fronts – a review. Nagra Technical Report 99-05, National Cooperative for the Disposal of Radioactive Waste, Switzerland.

Holmes D C, Pitty A E, Noy D J, 1990. Geomorphological and hydrogeological features of the Poços de Caldas caldera and the Osamu Utsumi mine and Morro do Ferro analogue study sites, Brazil. SKB TR 90-14, Svensk Kärnbränslehantering AB.

Holmes D C, Pitty A E, Noy D J, 1992. Geomorphological and hydrogeological features of the Poços de Caldas caldera analogue study sites. Journal of Geochemical Exploration, 45, pp 215–247.

Ivanovich M, Harmon R S (eds), 1992. Uranium-series disequilibrium: application to earth, marine, and environmental sciences. 2nd ed. Oxford: Calredon Press.

Jeong G Y, Kim H B, 2003. Mineralogy, chemistry, and formation of oxidized biotite in the weathering profile of granitic rocks. American Mineralogist, 88, pp 352–364.

Joyce S, Simpson T, Hartley L, Applegate D, Hoek J, Jackson P, Swan D, Marsic N, Follin S, 2010. Groundwater flow modelling of periods with temperate climate conditions – Forsmark. SKB R-09-20, Svensk Kärnbränslehantering AB.

Kalinowski B E, Schweda P, 1996. Kinetics of muscovite, phlogopite, and biotite dissolution and alteration at pH 1–4, room temperature. Geochimica et Cosmochimica Acta, 60, pp 367–385.

Knoblauch C, Zimmermann U, Blumenberg M, Michaelis W, Pfeiffer E M, 2008. Methane turnover and temperature response of methane-oxidizing bacteria in permafrost-affected soils of northeast Siberia. Soil Biology and Biochemistry, 40, pp 3004–3013.

Knudby C, Carrera J, 2005. On the relationship between indicators of geostatistical, flow and transport connectivity. Advances in Water Resources, 28, pp 405–421.

Laaksoharju M, Smellie J, Tullborg E-L, Gimeno M, Hallbeck L, Molinero J, Waber N, 2008. Bedrock hydrogeochemistry Forsmark. Site descriptive modelling, SDM-Site Forsmark. SKB R-08-47, Svensk Kärnbränslehantering AB.

Landström O, Smellie J, Tullborg E-L, 1989. Mineralogical and geochemical studies of fracture-infillings in drillcore KLJ 01. In: Bäckblom G, Stanfors R (eds). Interdisciplinary study of post-glacial faulting in the Lansjärv area Northern Sweden 1986–1988. SKB TR 89-31, Svensk Kärnbränslehantering AB.

Landström O, Tullborg E-L, Eriksson G, Sandell Y, 2001. Effects of glacial/post-glacial weathering compared with hydrothermal alteration – implications for matrix diffusion. Results from drillcore studies in porphyritic quartz monzodiorite from Äspö SE Sweden. SKB R-01-37, Svensk Kärnbränslehantering AB.

Larsson N-Å, 1989. Hydrogeological conditions. In: Bäckblom G, Stanfors R (eds). Interdisciplinary study of post-glacial faulting in the Lansjärv area Northern Sweden 1986–1988. SKB TR 89-31, Svensk Kärnbränslehantering AB.

Lasaga A C, 1995. Fundamental approaches in describing mineral dissolution and precipitation rates. Reviews in Mineralogy and Geochemistry, 31, pp 23–86.

Lide D R, Frederikse H P R, 1995. CRC Handbook of chemistry and physics: a ready-reference book of chemical and physical data. 76th ed. Boca Raton, FL: CRC Press.

Liebner S, Rublack K, Stuehrmann T, Wagner D, 2009. Diversity of aerobic methanotrophic bacteria in a permafrost active layer soil of the Lena Delta, Siberia. Microbial ecology, 57, pp 25–35.

Lin L-H, Slater G F, Sherwood Lollar B, Lacrampe-Couloume G, Onstott T C, 2005. The yield and isotopic composition of radiolytic H_2, a potential energy source for the deep subsurface biosphere. Geochimica et Cosmochimica Acta, 69, pp 893–903.

Lindberg R D, Runnells D D, 1984. Ground water redox reactions: An analysis of equilibrium state applied to Eh measurements and geochemical modeling. Science, 225, pp 925–927.

Lipson D S, McCray J E, Thyne G D, 2007. Using PHREEQC to simulate solute transport in fractured bedrock. Ground Water, 45, pp 468–472.

Lowson R T, 1982. Aqueous oxidation of pyrite by molecular oxygen. Chemical Reviews, 82, pp 461–497.

Löfgren M, Sidborn M, 2010. Statistical analysis of results from the quantitative mapping of fracture minerals in Forsmark. Site descriptive modelling – complementary studies. SKB R-09-30, Svensk Kärnbränslehantering AB.

MacQuarrie K T B, Mayer K U, 2005. Reactive transport modeling in fractured rock: A state-of-the-science review. Earth-Science Reviews, 72, pp 189–227.

MacQuarrie K T B, Mayer K U, Jin B, Spiessl S M, 2010. The importance of conceptual models in the reactive transport simulation of oxygen ingress in sparsely fractured crystalline rock. Journal of Contaminant Hydrology, 112, pp 64–76.

Madigan M T, Martinko J M, Parker J, 2003. Microbial growth. In: Brock biology of microorganisms. 10th ed. Upper Saddle River, NY: Prentice Hall, pp 137–166.

Madigan M T, Martinko J M, Dunlap P V, Clark D P, 2009. Brock biology of microorganisms. 12th ed. San Francisco, CA: Pearson Benjamin Cummings.

Malmström M, Banwart S, 1997. Biotite dissolution at 25°C: The pH dependence of dissolution rate and stoichiometry. Geochimica et Cosmochimica Acta, 61, pp 2779–2799.

Malmström M, Banwart S, Lewenhagen J, Duro L, Bruno J, 1996. The dissolution of biotite and chlorite at 25°C in the near-neutral pH region. Journal of Contaminant Hydrology, 21, pp 201–213.

Murakami T, Utsunomiya S, Yokoyama T, Kasama T, 2003. Biotite dissolution processes and mechanisms in the laboratory and in nature: Early stage weathering environment and vermiculitization. American Mineralogist, 88, pp 377–386.

Neretnieks I, 1986. Some uses for natural analogues in assessing the function of a HLW repository. Chemical Geology, 55, pp 175–188.

Nishimoto S, Yoshida H, 2010. Hydrothermal alteration of deep fractured granite: Effects of dissolution and precipitation. Lithos, 115, pp 153–162.

Parkhurst D L, Appelo C A J, 1999. User's guide to PHREEQC (version 2): a computer program for speciation, batch-reaction, one-dimensional transport, and inverse geochemical calculations. Water-Resources Investigations Report 99-4259, U.S. Geological Survey, Denver, Colorado.

Parkhurst D L, Kipp K L, Engesgaard P, Charlton S R, 2004. PHAST: a program for simulating ground-water flor, solute transport, and multicomponent geochemical reactions. Techniques and Methods 6-A8, U.S. Geological Survey Denver, Colorado.

Paterson W S B, 1994. The physics of glaciers. 3rd ed. Oxford: Pergamon.

Pedersen K, 2000. Microbial processes in radioactive waste disposal. SKB TR-00-04, Svensk Kärnbränslehantering AB.

Pedersen K, Karlsson F, 1995. Investigations of subterranean microorganisms. Their importance for performance assessment of radioactive waste disposal. SKB TR 95-10, Svensk Kärnbränslehantering AB.

Pedersen K, Arlinger J, Eriksson S, Hallbeck A, Hallbeck L, Johansson J, 2008. Numbers, biomass and cultivable diversity of microbial populations relate to depth and borehole-specific conditions in groundwater from depths of 4–450 m in Olkiluoto, Finland. The ISME journal, 2, pp 760–775.

Petersson J, Berglund J, Danielsson P, Skogsmo G, 2005. Forsmark site investigation. Petrographic and geochemical characteristics of bedrock samples from boreholes KFM04A–06A, and a whitened alteration rock. SKB P-05-156, Svensk Kärnbränslehantering AB.

Puigdomenech I, Ambrosi J-P, Eisenlohr L, Lartigue J-E, Banwart S A, Bateman K, Milodowski A E, West J M, Griffault L, Gustafsson E, Hama K, Yoshida H, Kotelnikova S, Pedersen K, Michaud V, Trotignon L, Rivas Perez J, Tullborg E-L, 2001. O_2 depletion in granitic media. The REX project. SKB TR-01-05, Svensk Kärnbränslehantering AB.

Putnis A, 2002. Mineral replacement reactions: from macroscopic observations to microscopic mechanisms. Mineralogical Magazine, 66, pp 689–708.

Pérez del Villar L, Pelayo M, Cózar J S, La Cruz B de, Pardillo J, Reyes E, Cabarello E, Delgado A, Nuñez R, Ivanovich M, Hasler S E, 1997. Mineralogical and geochemical evidence of the migration/retention processes of U and Th in fracture fillings from the El Berrocal granitic site (Spain). Journal of Contaminant Hydrology, 26, pp 45–60.

Pérez del Villar L, Bruno J, Campos R, Gómez P, Cózar J S, Garralón A, Buil B, Arcos D, Carretero G, Ruiz Sánchez-Porro J, Hernán P, 2002. The uranium ore from Mina Fe (Salamanca, Spain) as a natural analogue of processes in a spent fuel repository. Chemical Geology, 190, pp 395–415.

Pérez del Villar L, Reyes E, Delgado A, Núñez R, Pelayo M, Cózar J S, 2003. Argillization processes at the El Berrocal analogue granitic system (Spain): mineralogy, isotopic study and implications for the performance assessment of radwaste geological disposal. Chemical Geology, 193, pp 273–293.

Raynaud D, Lebel B, 1979. Total gas content and surface elevation of polar ice sheets. Nature, 281, pp 289–291.

Romero L, Neretnieks I, Moreno L, 1992. Movement of the redox front at the Osamu Utsumi uranium mine, Poços de Caldas, Brazil. Journal of Geochemical Exploration, 45, pp 471–502.

Rouhiainen P, Heikkinen P, 1998. Difference flow measurements at the Palmottu site in boreholes R387 and R388. Archive report, Y50/98/03, Geological Survey of Finland, Nuclear Waste Disposal Research.

Salas J, Gimeno M J, Auqué L, Molinero J, Gómez J, Juárez I, 2010. SR-Site – hydrogeochemical evolution of the Forsmark site. SKB TR-10-58, Svensk Kärnbränslehantering AB.

Sandström B, Stephens M, 2009. Mineralogy, geochemistry, porosity and redox properties of rocks from Forsmark. Compilation of data from the regional model volume for SR-Site. SKB R-09-51, Svensk Kärnbränslehantering AB.

Sandström B, Tullborg E-L, 2005. Forsmark site investigation. Fracture mineralogy. Results from fracture minerals and wall rock alteration in boreholes KFM01B, KFM04A, KFM05A and KFM06A. SKB P-05-197, Svensk Kärnbränslehantering AB.

Sandström B, Tullborg E-L, 2006a. Forsmark site invetigation. Mineralogy, geochemistry, protosity and redox capacity of altered rock adjacent to fractures. SKB P-06-209, Svensk Kärnbränslehantering.

Sandström B, Tullborg E-L, 2006b. Forsmark site investigation. Fracture mineralogy. Results from KFM06B, KFM06C, KFM07A, KFM08A, KFM08B. SKB P-06-226, Svensk Kärnbränslehantering AB.

Sandström B, Tullborg E-L, 2009. Episodic fluid migration in the Fennoscandian Shield recorded by stable isotopes, rare earth elements and fluid inclusions in fracture minerals at Forsmark, Sweden. Chemical Geology, 266, pp 135–151.

Sandström B, Savolainen M, Tullborg E-L, 2004. Forsmark site investigation. Fracture mineralogy. Results from fracture minerals and wall rock alteration in boreholes KFM01A, KFM02A, KFM03A and KFM03B. SKB P-04-149, Svensk Kärnbränslehantering AB.

Sandström B, Tullborg E-L, De Torres T, Ortiz J E, 2006. The occurrence and potential origin of asphaltite in bedrock fractures, Forsmark, central Sweden. GFF, 128, pp 233–242.

Sandström B, Tullborg E-L, Page L, 2008a. Forsmark site investigation. Fracture mineralogy and $^{40}Ar/^{39}Ar$ ages of adularia in fracture filling and K-feldspar in breccia. Data from drill cores KFM01C, KFM01D, KFM02B, KFM04A, KFM06A, KFM06B, KFM07A, KFM08A, KFM08B, KFM08C, KFM08D, KFM09A, KFM09B, KFM10A and KFM11A. SKB P-08-14, Svensk Kärnbränslehantering AB.

Sandström B, Tullborg E-L, Smellie J, MacKenzie A B, Suksi J, 2008b. Fracture mineralogy of the Forsmark site. SDM-Site Forsmark. SKB R-08-102, Svensk Kärnbränslehantering AB.

Sandström B, Tullborg E-L, Larson S Å, Page L, 2009. Brittle tectonothermal evolution in the Forsmark area, central Fennoscandian Shield, recorded by paragenesis, orientation and $^{40}Ar/^{39}Ar$ geochronology of fracture minerals. Tectonophysics, 478, pp 158–174.

Sandström B, Annersten H, Tullborg E-L, 2010. Fracture-related hydrothermal alteration of metagranitic rock and associated changes in mineralogy, geochemistry and degree of oxidation: a case study at Forsmark, central Sweden. International Journal of Earth Sciences, 99, pp 1–25.

Savage D, Cave M R, Milodowski A E, George I, 1987. Hydrothermal alteration of granite by meteoric fluid: an example from the Carnmenellis Granite, United Kingdom. Contributions to Mineralogy and Petrology, 96, pp 391–405.

Savage D, Arthur R C, Saito S, 1999. Geochemical factors in the selection and assessment of sites for the deep disposal of radioactive wastes. Geological Society, London, Special Publications, 157, pp 27–45.

Selroos J O, Walker D D, Ström A, Gylling B, Follin S, 2002. Comparison of alternative modelling approaches for groundwater flow in fractured rock. Journal of Hydrology, 257, pp 174–188.

Sidborn M, Neretnieks I, 2007. Long term redox evolution in granitic rocks: modelling the redox front propagation in the rock matrix. Applied Geochemistry, 22, pp 2381–2396.

Sidborn M, Neretnieks I, 2008. Long-term oxygen depletion from infiltrating groundwaters: model development and application to intra-glaciation and glaciation conditions. Journal of Contaminant Hydrology, 100, pp 72–89.

SKB, 2004. RETROCK Project. Treatment of geosphere retention phenomena in safety assessments. Scientific basis of retention processes and their implementation in safety assessment models (WP2). Work package 2 report of the RETROCK concerted action. SKB R-04-48, Svensk Kärbränslehantering AB.

SKB, 2006a. Hydrogeochemical evaluation. Preliminary site description Laxemar subarea – version 2.1. SKB R-06-70, Svensk Kärnbränslehantering AB.

SKB, 2006b. Site descriptive modelling Forsmark stage 2.1. Feedback for completion of the site investigation including input from safety assessment and repository engineering. SKB R-06-38, Svensk Kärnbränslehantering AB.

SKB, 2008. Site description of Forsmark at completion of the site investigation phase. SDM-Site Forsmark. SKB TR-08-05, Svensk Kärnbränslehantering AB.

SKB, 2009. Design premises for a KBS-3V repository based on results from the safety assessment SR-Can and some subsequent analyses. SKB TR-09-22, Svensk Kärnbränslehantering AB.

Smellie J A T, 1985. Uranium-series disequilibrium studies of drillcore Km3 from the Kamlunge test-sites northern Sweden. Mineralogical Magazine, 49, pp 271–279.

Smellie J, Karlsson F, 1996. A reappraisal of some Cigar Lake issues of importance to performance assessment. SKB TR 96-08, Svensk Kärnbränslehantering AB.

Smellie J A T, Karlsson F, 1999. The use of natural analogues to assess radionuclide transport. Engineering Geology, 52, pp 193–220.

Spiessl S M, MacQuarrie K T B, Mayer K U, 2008. Identification of key parameters controlling dissolved oxygen migration and attenuation in fractured crystalline rocks. Journal of Contaminant Hydrology, 95, pp 141–153.

Stephens M B, Fox A, La Pointe P R, Simeonov A, Isaksson H, Hermanson J, Öhman J, 2007. Geology Forsmark. Site descriptive modelling Forsmark stage 2.2. SKB R-07-45, Svensk Kärnbränslehantering AB.

Stephens M B, Ripa M, Lundström I, Persson L, Bergman T, Ahl M, Wahlgren C-H, Persson P-O, Wickström L, 2009. Synthesis of the bedrock geology in the Bergslagen region, Fennoscandian Shield, south-central Sweden. Uppsala: Geological Survey of Sweden. (Serie Ba 58)

Stumm W, Lee G F, 1961. Oxygenation of ferrous iron. Industrial and Engineering Chemistry, 53, pp 143–146.

Sugimori H, Yokoyama T, Murakami T, 2009. Kinetics of biotite dissolution and Fe behavior under low O_2 conditions and their implications for Precambrian weathering. Geochimica et Cosmochimica Acta, 73, pp 3767–3781.

Suksi J, Rasilainen K, Casanova J, Ruskeeniemi T, Blomqvist R, Smellie J A T, 2001. U-series disequilibria in a groundwater flow route as an indicator of uranium migration processes. Journal of Contaminant Hydrology, 47, pp 187–196.

Tullborg E-L, 1989. The influence of recharge water on fissure-filling minerals – A study from Klipperås, southern Sweden. Chemical Geology, 76, pp 309–320.

Tullborg E-L, Drake H, Sandström B, 2008. Palaeohydrogeology: a methodology based on fracture mineral studies. Applied Geochemistry, 23, pp 1881–1897.

Vidstrand P, Follin S, Zugec N, 2010. Groundwater flow modelling of periods with periglacial and glacial climate conditions – Forsmark. SKB R-09-21, Svensk Kärnbränslehantering AB.

Wersin P, Spahiu K, Bruno J, 1994. Time evolution of dissolved oxygen and redox conditions in a HLW repository. SKB TR 94-02, Svensk Kärnbränslehantering AB.

White A F, Brantley S L, 2003. The effect of time on the weathering of silicate minerals: why do weathering rates differ in the laboratory and field? Chemical Geology, 202, pp 479–506.

Williamson M A, Rimstidt J A, 1994. The kinetics and electrochemical rate-determining step of aqueous pyrite oxidation. Geochimica et Cosmochimica Acta, 58, pp 5443–5454.

Appendix A

Biotite crystal grain size estimation

The size of an average biotite grain was determined by measurements in thin sections using a scale grid under a transmissive light microscope. Measurements were carried out on all biotite crystals along a transverse across each thin section. Thin sections representing different orientations relative to the main orientation of the biotite crystals were selected in order to obtain data of the length of all three orientations of the mineral grains. A simplified box shape was applied for describing the biotite grains (Figure A-1). The obtained data are approximate since the exact orientation of each biotite crystal could not be determined. A mean value was calculated from all measurements in each thin section and then a mean value of each length axis was calculated. The results are presented in Table A-1 and the underlying measurements of individual crystals are listed in Table A-2.

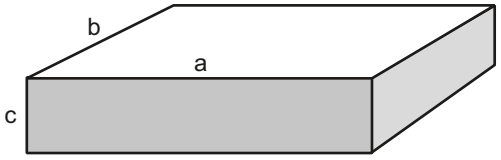

Figure A-1. *Schematic box shaped model of a biotite grain.*

Table A-1. Average lengths of biotite crystals.

Orientation	Length (µm)
a	400
b	200
c	100

Table A-2. Measured lengths of individual biotite crystals.

KFM05A 702.42 m		KFM05A 689.33 m		KFM01A 110.9 m		KFM02A 416.498 m		KFM10A 334.49 m	
a (µm)	c (µm)	a (µm)	c (µm)	a (µm)	b (µm)	a (µm)	c (µm)	a (µm)	b (µm)
500	300	500	200	200	50	1,000	200	300	100
300	100	200	200	100	100	400	200	500	200
600	100	500	200	300	100	700	200	300	50
300	200	100	100	200	50	600	300	200	100
100	100	300	100	200	200	200	200	200	100
300	100	300	100	200	100	400	200	300	200
400	100	200	50	300	100	600	200	200	100
400	200	400	300	400	100	400	200	400	100
400	100	500	300	600	300	600	200	200	30
300	300	400	300	500	100	800	600	200	100
500	300	800	200	200	100	400	200	100	100
500	300	100	100	200	100	600	400	50	50
300	200	600	300	800	200	800	400	300	100
200	200	300	300	300	200	800	400	400	300
300	100	100	100	200	100	600	600	800	100
500	300	500	100	300	100	1,000	400	200	100
200	100	300	100	200	100	100	100	200	100
300	200	300	100	600	100	200	100	300	100
200	100	400	100	200	200	400	200	500	100
300	100	400	100	400	100	400	200	500	200
300	200	400	100	200	100	200	200	400	100
300	300	300	200	200	200	200	200	300	100

Continued on next page

Continued from previous page

KFM05A 702.42 m		KFM05A 689.33 m		KFM01A 110.9 m		KFM02A 416.498 m		KFM10A 334.49 m	
a (µm)	**c (µm)**	**a (µm)**	**c (µm)**	**a (µm)**	**b (µm)**	**a (µm)**	**c (µm)**	**a (µm)**	**b (µm)**
400	200	100	100	200	100	200	100	300	200
300	100	200	100	300	100	1,000	200	100	100
400	200	300	100	300	100	400	200	700	100
500	100	200	100	300	200	400	400	700	400
300	200	200	50	600	100	200	200	400	200
500	100	300	100	100	100	600	100	600	100
400	300	300	200	500	200	600	400	400	200
500	100	300	100	500	200	400	200		
600	500	300	100			600	200		
700	200	500	200			200	200		
200	100	200	50			400	100		
200	100	200	100			200	100		
400	300	400	100			1,000	400		
400	100	300	200			600	400		
300	200	200	100			600	200		
200	200	300	200			400	200		
600	300	100	100			100	100		
300	50	200	20			100	50		
300	100	200	100			400	200		
700	100	300	200			1,000	400		
400	100	300	100			800	400		
500	200	500	300			600	200		
300	100	400	300			400	200		
300	200	600	100			200	200		
600	200	200	50			300	100		
300	50	200	200			1,000	200		
100	100	200	100			600	400		
200	50	300	100			600	400		
200	50	200	100			1,000	600		
100	100	300	50			400	200		
200	100	200	100			1,000	600		
300	300	400	100			100	100		
200	200	100	100			200	100		
200	100	400	200			100	100		
400	200	300	300						
400	100	200	100						
600	200	400	200						
400	100	1,000	300						
100	100	100	100						
100	50	400	200						
500	100	200	100						
300	200	200	200						
1,000	200	200	200						
600	600	300	100						
400	200								
300	200								
500	300								
100	100								
600	300								
100	100								
500	100								
200	100								
100	100								
300	100								
300	50								
400	200								
500	100								
358	**167**	**312**	**147**	**320**	**130**	**502**	**251**	**347**	**132**

Appendix B

Calculations of the Fe(II) content in the rock matrix

Mössbauer data are available from the dominating metamorphic granite to granodiorite (rock code 101057) and the subordinate metamorphic granite, granodiorite and tonalite (rock code 101051). The Fe(II)-content of these rock types was calculated using the total oxidation factor (Fe(III)/Fe(total)) obtained by Mössbauer analysis and the Fe(total) content of these rock types obtained by ICP-AES analysis. Data from representative samples of each rock type have been used in the calculations /Sandström and Stephens 2009/ using data deliveries SICADA_08_172 and SICADA_08_201.

For the other subordinate rocks comprising more than 2 vol% of rock domains RFM029 and RFM045 (rock codes 101058, 101061, and 102017), no Mössbauer data were available and the Fe(II)-content in these rock types was calculated according to the procedure in Section B.1.

The oxidation factors calculated in Section B.1 are then included in the dataset of oxidation factors already measured for rock codes 101057 and 101051, and subsequent estimations of the ferrous iron content in the bulk rock at Forsmark is carried out in Section B.2.

B.1 Calculations of oxidation factors for subordinate rocks lacking Mössbauer analyses

The Fe(II)-content was calculated in rock types comprising more than 2 vol% of rock domains RFM029 and RFM045 lacking Mössbauer analyses. The rock types considered are:

- Metamorphic aplitic granite (rock code 101058).
- Pegmatite (rock code 101061).
- Amphibolite (rock code 102017).

Significant Fe(II)-bearing minerals in these rock types are biotite, chlorite, amphibole and magnetite /Sandström and Stephens 2009/.

1. First, the Fe(II)-content in the significant Fe(II)-bearing minerals was calculated:

   Biotite

   The Fe(II)-content in biotite was calculated by combing in situ SEM-EDS analyses of the Fe(total)-content in biotite /Sandström and Tullborg 2006a/ (data delivery SICADA_10_009_2) and Mössbauer analyses of representative whole rock samples /Sandström and Stephens 2009/ (data delivery SICADA_08_201).

   An oxidation factor for biotite of 0.11 was assigned using the silicate oxidation factor from one whole rock sample where biotite was the only significant Fe-bearing silicate mineral (KFM08A 183.13O in Table 5-5 in /Sandström and Tullborg 2006a/). Data from samples containing significant amounts (i.e. detectable in the Mössbauer spectra) of other Fe-bearing silicates such as epidote were omitted. However, epidote which only incorporates Fe(III) /Deer et al. 1992/, is present as trace amounts in all rock samples and the assigned oxidation factor of 0.11 is most likely somewhat higher than the true value of biotite and is therefore considered conservative. Although it is difficult to distinguish biotite from chlorite due to the overlap in the Mössbauer Spectra /Annersten 1974/, microscopy shows that biotite is the dominating Fe-bearing silicate in sample KFM08A 183.13O /Sandström and Tullborg 2006a/.

   The Fe(II)-content of biotite was given by:
   $Fe(II)_{biotite} = Fe(total)_{biotite}(1 - \text{silicate oxidation factor})$

   The numerical values used and the calculated result are given below

Mean biotite Fe(total)-content:	19.4 wt %
Biotite oxidation factor, Fe(III)/Fe(total):	0.11
Calculated biotite Fe(II)-content:	**17.3 wt %**

Chlorite

The Fe(II)-content in chlorite was calculated by combing *in situ* SEM-EDS analyses of the Fe(total)-content in chlorite /Sandström and Tullborg 2006a/ (data delivery SICADA_10_009_2) and an estimated oxidation factor of 0.2. One Mössbauer analysis of a rock sample with chlorite as the only Fe-bearing silicate is available in SICADA and indicates a low oxidation factor (0.08) for chlorite in the rock matrix /Sandström and Tullborg 2006a/. However, since chlorite in the rock matrix e.g. formed during hydrothermal alteration of biotite under oxidising conditions at > 1,000 Ma /Sandström et al. 2010/, it could be argued that the chlorite in general would be expected to be more oxidised than the primary biotite (although the degree of oxidation of the rock was very limited during this event /Sandström et al. 2010/). Therefore, an oxidation factor of 0.2 has been used in the calculation, which is considered conservative. Given these calculations and assumptions, the following values were obtained:

Mean chlorite Fe(total)-content:	27.9 wt %
Chlorite oxidation factor, Fe(III)/Fe(total):	0.2
Calculated chlorite Fe(II)-content:	**22.3 wt %**

Amphibole

No geochemical analyses of amphibole (hornblende) are available from the Forsmark site investigation. Therefore, the Fe(II)-content of amphibole (hornblende) from the Laxemar site (9.5 wt%) /Drake and Tullborg 2006/ has been used in the calculations. Since the geochemistry of Forsmark amphiboles is not known, it has not been possible to evaluate how accurate this value is for the Forsmark amphiboles. However, it is only in the amphibolite (rock code 102017) that amphibole has a significant impact on the overall Fe(II)-content in the rocks and these data have low impact on the overall reducing capacity of the rock matrix at Forsmark.

Opaque minerals

Opaque minerals are usually not differentiated during the quantitative mineralogical analyses. Since magnetite is the dominating opaque mineral in Forsmark /Petersson et al. 2005/, all opaques have here been assumed to be magnetite for simplicity. After magnetite, pyrite is the most common opaque mineral and due to the large reducing capacity of pyrite, the generalisation that all opaque minerals are magnetite is conservative.

Magnetite contains 24 wt% Fe(II) given its mineral formula ($Fe^{2+}Fe_2^{3+}O_4$) /Deer et al. 1992/. Compared to biotite, chlorite and amphibole, the magnetite content is small in all rock types in Forsmark (generally < 0.2 vol%).

2. The Fe(II)-content in the different rock types was calculated based on the sum of the major Fe(II)-bearing minerals in each rock type as follows:

$$\mathrm{Fe(II)}_{\mathrm{rock}} = \frac{\sum V_{\mathrm{mineral}} \rho_{\mathrm{mineral}} \mathrm{Fe(II)}_{\mathrm{mineral}}}{\rho_{\mathrm{rock}}}$$

where

$\mathrm{Fe(II)}_{\mathrm{rock}}$ Fe(II) in rock matrix (wt%)

$\mathrm{Fe(II)}_{\mathrm{mineral}}$ Fe(II)-content in the major Fe(II)-bearing minerals, obtained by the calculations described above.
- *biotite: 17.2 wt%*
- *chlorite: 22.3 wt%*
- *amphibole: 9.5 wt%*
- *magnetite: 23.8 wt%*

V_{mineral} Volume of major Fe(II)-bearing minerals (m^3), calculated based on the modal mineral-content (vol%) determined by point counting data from representative samples /Sandström and Stephens 2009/ (data delivery SICADA_08_172). ($V_{\mathrm{mineral}} = \mathrm{vol\%}_{\mathrm{mineral}}/100$)

$\rho_{mineral}$ Density of major Fe(II)-bearing minerals, mean values from literature /Deer et al. 1992/.
– *biotite: 3,000 kg m^{-3}*
– *chlorite: 3,000 kg m^{-3}*
– *amphibole: 3,300 kg m^{-3}*
– *magnetite: 5,200 kg m^{-3}*

ρ_{rock} Rock density, mean values from /Stephens et al. 2007/, data delivery SICADA_07_008.
– *rock code 101058: 2,639 kg m^{-3}*
– *rock code 101061: 2,628 kg m^{-3}*
– *rock code 102017: 2,963 kg m^{-3}*

3. An oxidation factor for each rock type was then calculated based on the obtained Fe(II)-content and the measured Fe(total)-content of each rock type. The Fe(total)-content has been determined by ICP-AES analysis. Data from representative samples of the rock types have been used in the calculations /Sandström and Stephens 2009/ using data delivery SICADA_08_172. The oxidation factor was calculated according to:

   Oxidation factor = 1 – Fe(II)/Fe(total)

The obtained results from the calculations are presented in Table B-1, Table B-2, and Table B-3.

Table B-1. Results of the calculations of Fe(II) in rock type 101058.

Sample	Fe(tot) wt%	Calculated Fe(II) wt%	Calculated oxidation factor
KFM06A 636.34	1.82	1.53	0.16
KFM09A 443.32	1.77	1.50	0.15
PFM000278	0.71	0.45	0.37
PFM001106	1.60	0.77	0.52
PFM001160	0.68	0.26	0.62
PFM005205	1.29	0.67	0.48

Table B-2. Results of the calculations of Fe(II) in rock type 101061.

Sample	Fe(tot) wt%	Calculated Fe(II) wt%	Calculated oxidation factor
KFM03B 62.33	0.81	0.57	0.29
PFM000198	0.55	0.36	0.34
PFM000656	0.51	0.21	0.60
PFM001163	0.57	0.29	0.49
PFM001243	1.43	1.12	0.22

Table B-3. Results of the calculations of Fe(II) in rock type 102017.

Sample	Fe(tot) wt%	Calculated Fe(II) wt%	Calculated oxidation factor
KFM04A 737.41	7.11	5.25	0.26
KFM05A 355.87	6.46	4.68	0.28
PFM001010	8.50	6.67	0.22
PFM001183	8.65	6.07	0.30

B.2 Calculations of ferrous iron content in major rock types at Forsmark

The Mössbauer analyses carried out for rock codes 101057 and 101051 were combined with the oxidation factors calculated in Section B.1. The resulting cumulative distribution of Fe(II)/Fe(tot) for the major rock types in Forsmark is shown along with a fitted lognormal distribution in Figure B-1.

The distribution parameters are $\mu_e = -0.34$ and $\sigma_e = 0.15$.

This lognormal distribution of the Fe(II)/Fe(tot) content is assumed to apply to the major rock types at Forsmark. These rock types and their quantitatively estimated volume fractions in rock domains RFM029 and RFM045 /Stephens et al. 2007/ are shown in Table B-4.

The total iron content in these rock types has previously been published in /Sandström and Stephens 2009/. The cumulative distribution of total iron (Fe_2O_3) in these rock types are shown in Figure B-2.

The distribution parameters for these rock types are summarised in Table B-5. The Fe(II) content in these rock types were calculated assuming a Fe(II)/Fe(tot) content described by the distribution in Figure B-1, by the formula:

$$\mathrm{Fe(II)} = \mathrm{oxfactor} \cdot \frac{2M_{\mathrm{Fe}}}{M_{\mathrm{Fe_2O_3}}}\mathrm{Fe_2O_3}$$

The product of two lognormally distributed variates is also lognormally distributed /Aitchison and Brown 1957, Crow and Shimizu 1988/, so the distribution parameters for the Fe(II) content are calculated according to:

$$\mu_{e,\mathrm{Fe(II)}} = \ln\left(\frac{2M_{\mathrm{Fe}}}{M_{\mathrm{Fe_2O_3}}}\right) + \mu_{e,\mathrm{oxfactor}} + \mu_{e,\mathrm{Fe_2O_3}}$$

$$\sigma_{e,\mathrm{Fe(II)}} = \sqrt{\sigma^2_{e,\mathrm{oxfactor}} + \sigma^2_{e,\mathrm{Fe_2O_3}}}$$

Table B-4. Volume fractions (vol%) of main rock types in rock domains RFM029 and RFM045.

Rock name	SKB Code	RFM029	RFM045
Granite to granodiorite, metamorphic, medium-grained	101057	73.6	18.0
Pegmatite, pegmatitic granite	101061	13.3	13.9
Granite, granodiorite and tonalite, metamorphic, fine- to medium-grained	101051	4.6	9.0
Granite, metamorphic, aplitic	101058	1.5	49.3
Amphibolite	102017	4.4	6.3
Granite, fine- to medium-grained	111058	1.5	1.3
Felsic to intermediate volcanic rock, metamorphic	103076	0.4	1.2
Diorite, quartz diorite and gabbro, metamorphic	101033	0.2	0.2

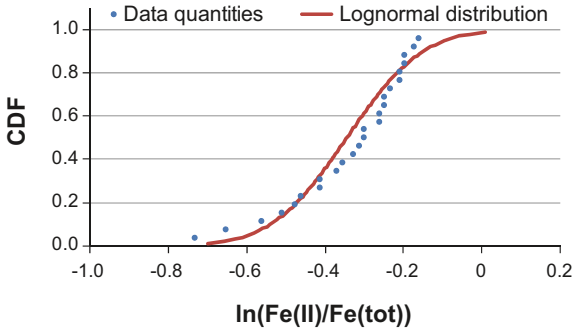

Figure B-1. *Cumulative distribution of Fe(II)/Fe(tot) content in the major rock types at Forsmark.*

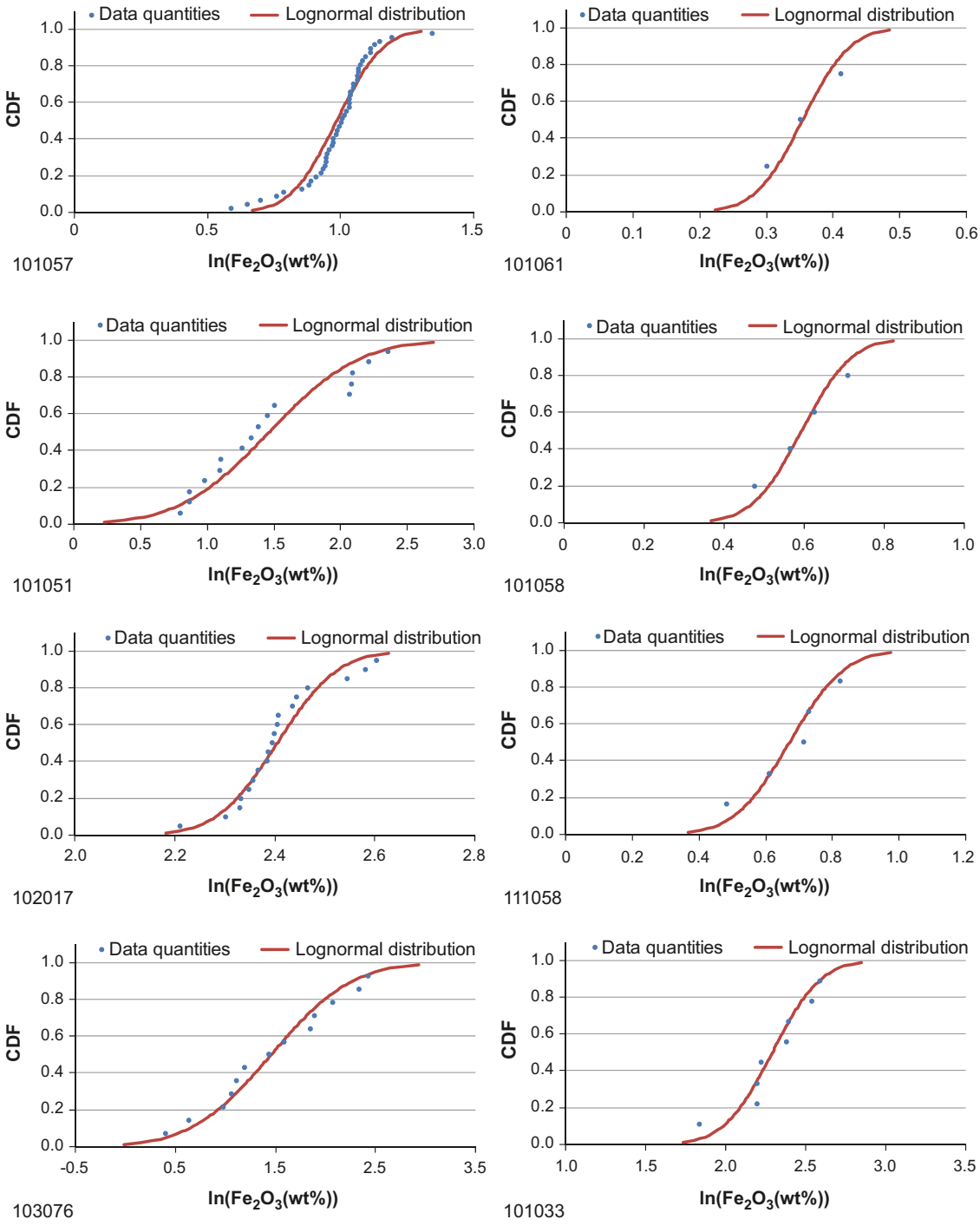

Figure B-2. *Cumulative distribution of total iron (Fe_2O_3) in the main rock types at Forsmark.*

Table B-5. Distribution parameters for total iron (Fe_2O_3) and ferrous iron in the main rock types at Forsmark.

Rock type	Fe_2O_3 (wt%)		Fe(II) (wt%)	
	μ_e	σ_e	μ_e	σ_e
101057	0.9855	0.1360	0.2834	0.2039
101061	0.3543	0.0561	–0.3478	0.1620
101051	1.4633	0.5302	0.7611	0.5516
101058	0.5939	0.0978	–0.1082	0.1808
102017	2.4047	0.0954	1.7026	0.1795
111058	0.6714	0.1301	–0.0308	0.2001
103076	1.4571	0.6339	0.7550	0.6519
101033	2.2912	0.2387	1.5890	0.2830

Finally the ferrous iron content in RFM029 and RFM045 was calculated stochastically from the ferrous iron distributions for each rock type weighted by the volume fractions given in Table B-4. The resulting Fe(II) content (wt%) in RFM029 and RFM045 from the stochastic simulation is given in Table B-6.

The ferrous iron content (wt%) in the different rock types as well as the weighted content in rock domains RFM029 and RFM045 is illustrated in Figure B-3.

Table B-6. Distribution parameters for ferrous iron in rock domains RFM029 and RFM045.

Fe(II) (wt%)	RFM029	RFM045
Median	1.50	1.42
Mean	1.52	1.44
STD	0.23	0.18

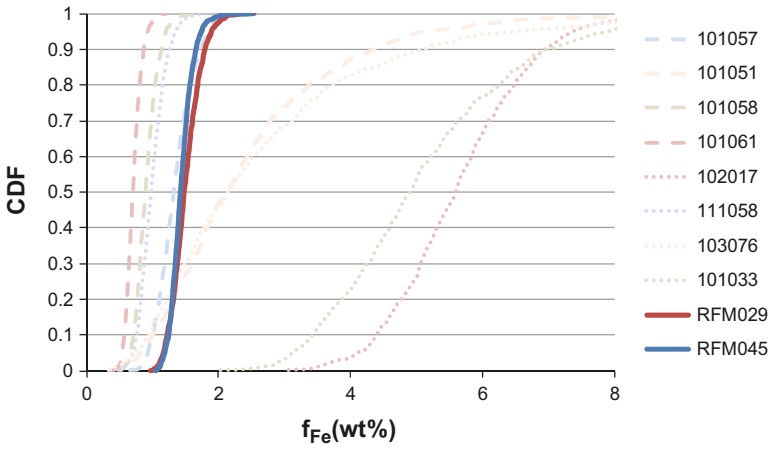

Figure B-3. *Cumulative distribution of ferrous iron content (wt%) in the major rock types in Forsmark and in rock domains RFM029 and RFM045.*

Appendix C

Calculations of the Fe(II) content in fracture fillings

The Fe(II)-content in fracture filling minerals was calculated using ICP-AES data of the Fe(total)-content of bulk fracture fillings and the total oxidation factor obtained by Mössbauer analysis of the same samples /Sandström and Tullborg 2005, 2006b, Sandström et al. 2004, 2008a, 2008b/ (data delivery SICADA_10_021). Data of fracture fillings consisting of single mineral phases (e.g. analcime and asphaltite) were omitted before calculation. The geochemical analyses used for Fe(total) estimations are summarised in Table C-1. A lognormal distribution function was fitted to the data as shown in Figure C-1, and the distribution parameters were $\mu_e = 1.65$ and $\sigma_e = 0.90$.

Sampled oxidation factors of bulk fracture minerals are listed in Table C-2. A lognormal distribution function was fitted to the data as shown in Figure C-2. The distribution function is perhaps not well fitted to the data but is deemed to cover the range of oxidation factors measured. Furthermore it may be noted that some of the lower values in Table C-2 are sampled in deformation zones and may have become partially oxidised. The distribution parameters are $\mu_e = -0.46$ and $\sigma_e = 0.38$.

Table C-1. Geochemical ICP-AES analyses of total iron (Fe_2O_3) content in bulk fracture fillings.

Sample	Borehole	Secup (m)	Seclow (m)	Fe_2O_3 (wt%)
KFM06C:451.64–451.82	KFM06C	451.64	451.82	0.50
KFM02B:500.72–500.84	KFM02B	500.72	500.84	0.54
KFM02B:499.84–499.95	KFM02B	499.84	499.95	0.74
KFM01A:188.10–188.20	KFM01A	188.10	188.20	1.02
KFM02B:500.36–500.47	KFM02B	500.36	500.47	1.04
KFM08C:523.47–523.73	KFM08C	523.47	523.73	1.15
KFM11A:376.43–376.60	KFM11A	376.43	376.60	1.18
KFM02A:893.45–893.45	KFM02A	893.45	893.45	1.43
KFM01B:49.39–49.45	KFM01B	49.39	49.45	1.44
KFM09B:49.73–50.10	KFM09B	49.73	50.10	1.81
KFM02A:118.25–118.25	KFM02A	118.25	118.25	2.03
KFM09B:11.35–11.42	KFM09B	11.35	11.42	2.17
KFM01B:28.65–28.65	KFM01B	28.65	28.65	2.42
KFM09B:391.28–391.37	KFM09B	391.28	391.37	2.81
KFM09B:19.37–19.57	KFM09B	19.37	19.57	2.86
KFM11A:450.28–450.64	KFM11A	450.28	450.64	3.06
KFM01C:34.47–34.67	KFM01C	34.47	34.67	3.07
KFM05A:111.56–111.60	KFM05A	111.56	111.60	3.28
KFM01C:12.43–12.51	KFM01C	12.43	12.51	3.67
KFM01C:41.15–41.25	KFM01C	41.15	41.25	3.69
KFM11A:540.19–540.27	KFM11A	540.19	540.27	3.73
KFM01C:17.22–17.40	KFM01C	17.22	17.40	3.94
KFM07A:896.68–896.77	KFM07A	896.68	896.77	4.03
KFM08A:975.50–975.66	KFM08A	975.50	975.66	4.19
KFM09B:168.87–169.06	KFM09B	168.87	169.06	4.53
KFM06A:770.32–770.32	KFM06A	770.32	770.32	4.59
KFM03B:65.20–65.25	KFM03B	65.20	65.25	4.68
KFM11A:685.56–685.94	KFM11A	685.56	685.94	4.91
KFM09B:570.92–571.05	KFM09B	570.92	571.05	4.92
KFM06C:132.35–132.43	KFM06C	132.35	132.43	5.21
KFM09B:310.61–310.83	KFM09B	310.61	310.83	5.41
KFM08A:686.59–686.84	KFM08A	686.59	686.84	5.66
KFM09B:571.13–572.19	KFM09B	571.13	572.19	5.70
KFM02A:423.65–423.65	KFM02A	423.65	423.65	5.91
KFM11A:178.78–178.81	KFM11A	178.78	178.81	6.06
KFM10A:105.79–106.08	KFM10A	105.79	106.08	6.21

Continued on next page

Continued from previous page

Sample	Borehole	Secup (m)	Seclow (m)	Fe_2O_3 (wt%)
KFM11A:426.07–426.21	KFM11A	426.07	426.21	6.49
KFM01A:148.40–148.40	KFM01A	148.40	148.40	6.73
KFM08A:495.07–495.37	KFM08A	495.07	495.37	6.76
KFM01C:39.75–40.02	KFM01C	39.75	40.02	6.79
KFM06C:398.20–398.61	KFM06C	398.20	398.61	6.95
KFM09B:19.81–20.18	KFM09B	19.81	20.18	7.31
KFM08A:197.65–197.88	KFM08A	197.65	197.88	7.60
KFM01C:43.00–43.20	KFM01C	43.00	43.20	7.73
KFM02B:471.49–471.69	KFM02B	471.49	471.69	8.16
KFM02A:516.09–516.09	KFM02A	516.09	516.09	9.06
KFM06B:55.52–55.60	KFM06B	55.52	55.60	9.13
KFM11A:624.45–624.71	KFM11A	624.45	624.71	9.18
KFM06C:482.94–483.32	KFM06C	482.94	483.32	9.76
KFM08A:918.53–918.85	KFM08A	918.53	918.85	9.76
KFM01A:269.90–269.90	KFM01A	269.90	269.90	10.20
KFM08C:829.94–830.02	KFM08C	829.94	830.02	10.40
KFM01A:185.35–185.35	KFM01A	185.35	185.35	10.50
KFM01A:127.40–127.40	KFM01A	127.40	127.40	10.70
KFM01A:149.18–149.18	KFM01A	149.18	149.18	10.80
KFM01A:179.35–179.40	KFM01A	179.35	179.40	11.60
KFM06C:149.54–149.80	KFM06C	149.54	149.80	11.60
KFM05A:629.21–629.21	KFM05A	629.21	629.21	13.90
KFM02A:476.75–476.75	KFM02A	476.75	476.75	14.20
KFM06A:145.62–145.62	KFM06A	145.62	145.62	14.70
KFM01B:47.90–48.00	KFM01B	47.90	48.00	15.00
KFM01B:418.29–418.43	KFM01B	418.29	418.43	15.30
KFM03A:803.85–803.85	KFM03A	803.85	803.85	15.60
KFM09B:121.56–121.98	KFM09B	121.56	121.98	15.80
KFM08C:683.57–683.66	KFM08C	683.57	683.66	16.70
KFM03A:643.80–643.80	KFM03A	643.80	643.80	17.80
KFM08C:904.06–904.13	KFM08C	904.06	904.13	18.20
KFM03A:644.17–644.17	KFM03A	644.17	644.17	22.70

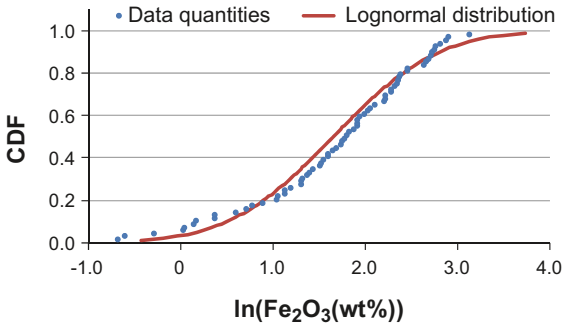

Figure C-1. *Cumulative distribution of Fe_2O_3 data in bulk fracture minerals.*

Table C-2. Oxidation factors (Mössbauer) for bulk fracture minerals. From /Sandström et al. 2008b/.

Sample	Borehole	Secup (m)	Seclow (m)	Fe(II)/Fe(tot)
KFM01C:41.15–41.25	KFM01C	41.15	41.25	0.28
KFM04A:192.00–192.10	KFM04A	192.00	192.10	0.33
KFM01C:39.75–40.02	KFM01C	39.75	40.02	0.43
KFM01C:12.43–12.51	KFM01C	12.43	12.51	0.63
KFM02A:118.25–118.25	KFM02A	118.25	118.25	0.65
KFM03A:451.85–451.90	KFM03A	451.85	451.90	0.70
KFM10A:105.79–106.08	KFM10A	105.79	106.08	0.71
KFM02A:903.65–903.70	KFM02A	903.65	903.70	0.72
KFM08C:829.94–830.02	KFM08C	829.94	830.02	0.73
KFM08C:683.57–683.66	KFM08C	683.57	683.66	0.85
KFM03A:803.85–803.85	KFM03A	803.85	803.85	0.88
KFM09B:121.56–121.98	KFM09B	121.56	121.98	0.88
KFM08C:904.06–904.13	KFM08C	904.06	904.13	0.93

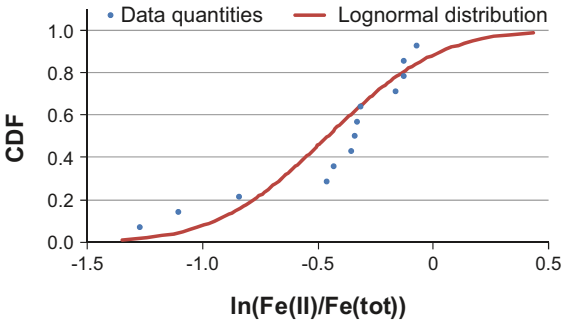

Figure C-2. *Cumulative distribution of Fe(II)/Fe(tot) data in bulk fracture minerals.*

The Fe(II) content in bulk fracture minerals is calculated according to:

Fe(II) = oxfactor · Fe(tot)

The product of two lognormally distributed variates is also lognormally distributed /Aitchison and Brown 1957, Crow and Shimizu 1988/, so the distribution parameters for the Fe(II) content is estimated to

$$\mu_e = \ln\left(\frac{2M_{Fe}}{M_{Fe_2O_3}}\right) - 0.46 + 1.65 = 0.84$$

$$\sigma_e = \sqrt{0.90^2 + 0.38^2} = 0.97$$

The mean Fe(II) content is then calculated to:

$$\mathrm{E}\big(\mathrm{Fe(II)}\big) = e^{0.84+\frac{0.97^2}{2}} = 3.7 \text{ wt\%}$$

The distribution parameters for fracture coating minerals (modified from /Löfgren and Sidborn 2010/) are:

Mineral	μ of ln d_{mean} (m)	σ of ln d_{mean} (m)	f_{quant} (%)
Chlorite	–9.05	1.06	24
Clay minerals	–9.42	1.01	11
Pyrite	–16.14	2.90	10

The amount of ferrous minerals per fracture surface is then calculated to:

$\mathrm{Fe(II)/m^2} = \mathrm{oxfactor} \cdot \mathrm{Fe(tot)} \cdot \rho_{\mathrm{chlorite}} d_{\mathrm{mean}}$

The resulting distribution parameters for ferrous iron in chlorite are:

$$\mu_{\mathrm{e}} = \ln\left(\frac{2M_{\mathrm{Fe}}}{100M_{\mathrm{Fe_2O_3}}}\right) - 0.46 + 1.65 - 9.05\ln(\rho_{\mathrm{chlorite}}) = 2.10$$

$$\sigma_{\mathrm{e}} = \sqrt{0.90^2 + 0.38^2 + 1.06^2} = 1.44$$

The mean ferrous iron per $\mathrm{m^2}$ chlorite coated surface is then:

$$\mathrm{E}\big(\mathrm{Fe(II)}\big) = e^{2.10+\frac{1.44^2}{2}} = 23\ \mathrm{g\ m^{-2}}$$

Appendix D

Sensitivity analysis of space and time discretisation and consequences on CPU times

In order to test the influence of the discretisation of the numerical model, sensitivity analyses have been performed as a first step preceding the implementation of the numerical model described in Section 7. Although these initial test calculations are not numerically identical to the final model, the results shown in the present section can help us to develop the conceptual discussion.

D.1 1D diffusion model

Seven runs have been performed (Table D-1) in order to perform a sensitivity analysis about space and time discretisation. The final objective has been to check the influence on the results of the numerical discretisation, and to optimise the computational time (CPU time).

The results are shown in Figure D-1 and in Figure D-2. With a fixed space discretisation, the variability of the size of the time steps has no effect on the results. Similar results are obtained for the sensitivity analysis of the space discretisation at fixed time steps. The differences in the O_2 and Fe(II) concentrations, and in the amount of iron-mineral dissolved, are due to the fact that less points define the profile when the number of cells decreases (Figure D-2a, b and c).

Although the results do not change with the tested cell dimensions and time steps, computational time is varying (Table D-1). CPU times decrease with the number of cells and with the time discretisation. This is of importance when very large times have to be simulated (several hundreds or thousands of years).

Large CPU times may be also due to the complexity of the geochemical system. Although the geochemical system is quite simplified in this work, two kinetic laws are considered (for the heterogeneous dissolution of the mineral and for the homogeneous oxidation of ferrous iron). Therefore, run 6 has been re-calculated considering the assumption of equilibrium for the Fe(II) oxidation. As observed in Figure D-3, no differences have been computed between the models simulated under kintics and equilibrium assumptions, verifying that kinetic oxidation of dissolved ferrous iron is not a limiting mechanism in the matrix. Furthermore, the CPU time only decreases by 1 minute using the equilibrium approach for the Fe(II) oxidation. With the time and space discretisation tested, the implemented geochemical system is not a limiting factor for computational purposes of the 1D pure diffusion model.

Table D-1. Sensitivity analysis on space and time discretisation. Influence on CPU times.

	N_{cell}	dt (s)	CPU time
run 1	20	500	3h03min
run 2	20	5,000	1h49min
run 3	40	500	3h50min
run 4	40	5,000	13h7min
run 5	10	5,000	21min
run 6	10	50,000	16min
run 7	10	500,000	15min

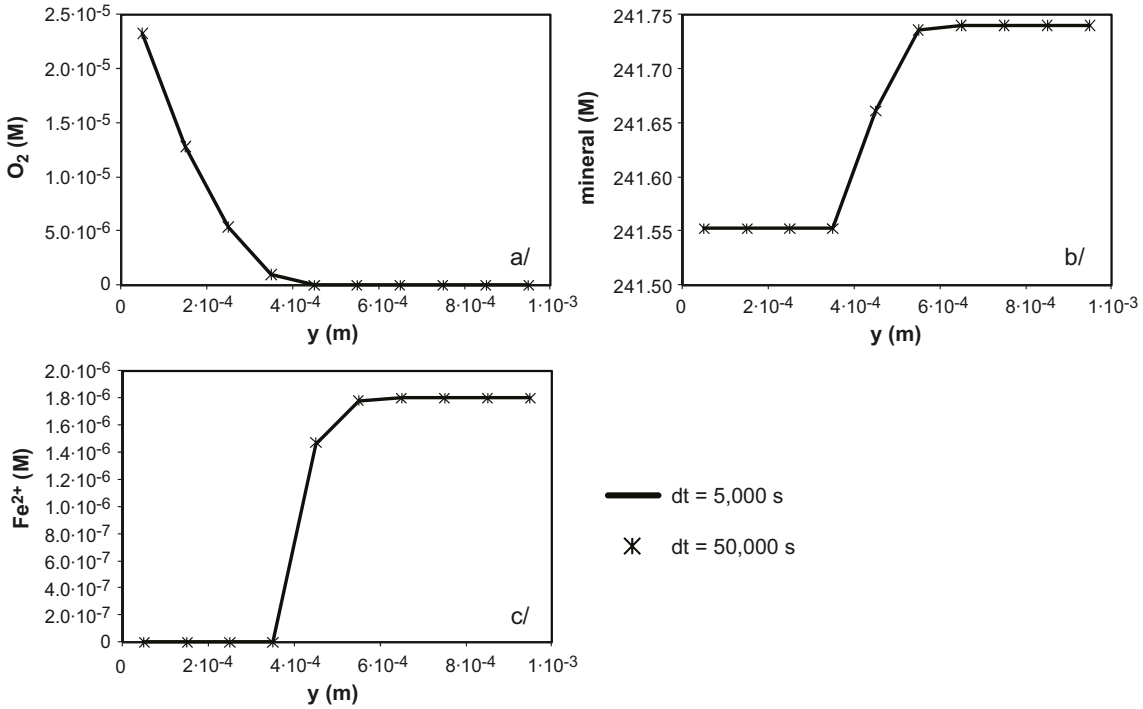

Figure D-1. *Results of the sensitivity analysis about the time discretisation for the Model 1 assumptions with 10 cells and a simulation time of 1 year. a/ Oxygen front in the matrix, b/ total amount of iron-mineral and c/ Fe(II) concentration.*

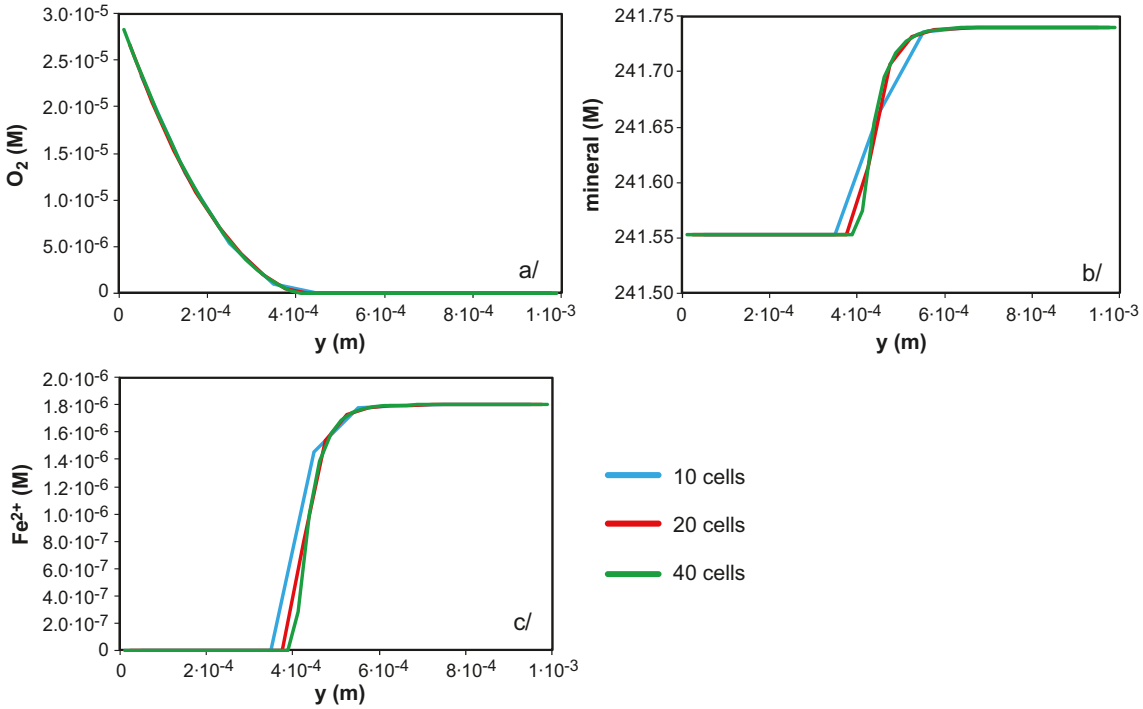

Figure D-2. *Results of the sensitivity analysis about the space discretisation for the Model 1 assumptions and 1 year of simulation time (dt = 5,000 seconds). a/ Oxygen front in the matrix, b/ total amount of iron-mineral and c/ Fe(II) concentration.*

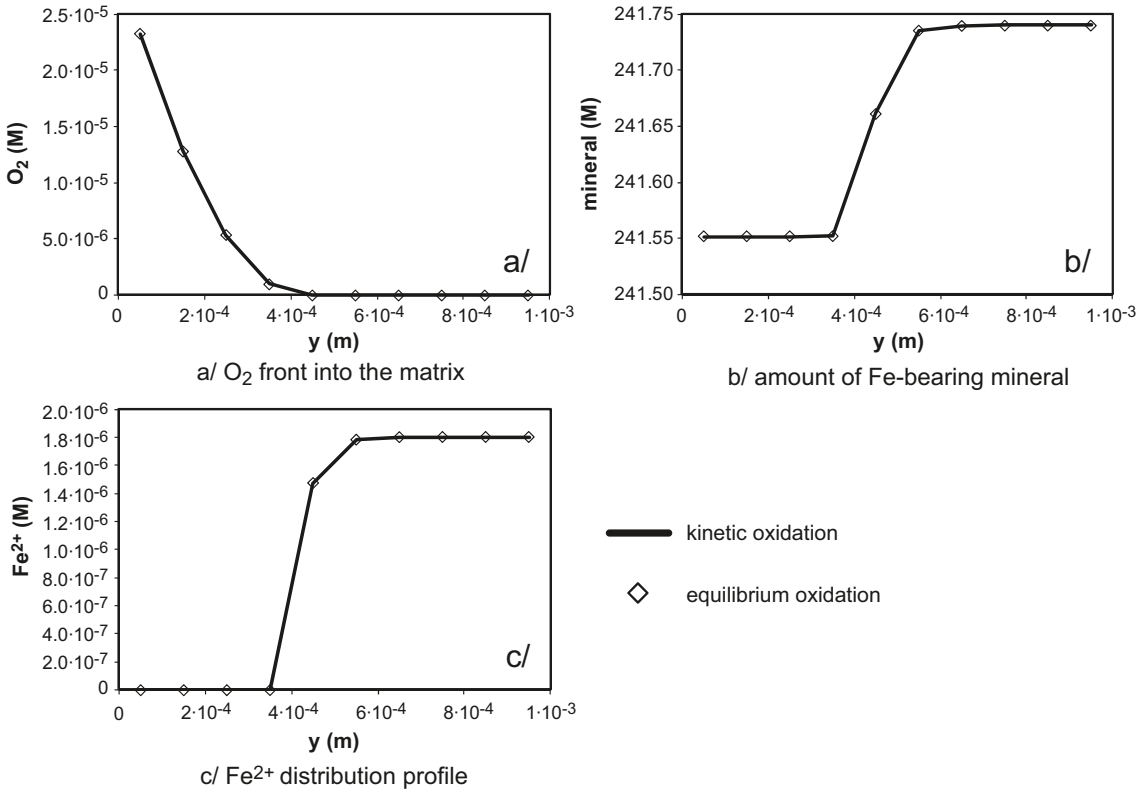

Figure D-3. *Comparison between the results obtained implementing the assumptions of kinetics or equilibrium for the oxidation of the Fe(II) aqueous species, after 1 year of simulation time (dt = 5,000 seconds and 10 cells). a/ Oxygen front in the matrix, b/ total amount of iron-mineral and c/ Fe(II) concentration.*

D.2 2D dual porosity model

A sensitivity analysis about the time discretisation has been performed. No differences in the results are noted for a range of *dt* of 0.01 and 0.02 days (Figure D-4). However, the CPU time for each case is different. Therefore, *dt* of 0.01 days has been chosen in order to obtain the shorter CPU time and more accurate results.

The definition of the grid takes account the variation of grid along the fracture (*X*) and along the matrix (*Y*). To obtain a better resolution of the O_2 diffusion within the domain where maximum oxygen gradients are computed, a non-uniform grid was implemented (near to the entrance zone of O_2 the grid is tighter). Although no significant differences have been obtained using a more refined grid, the O_2 front advances more using a less refined grid (Figure D-5).

It is remarkable as using a more refined grid in Y (Figure D-5a and b), the location of the oxygen front is practically identical to that one simulated with a less refined grid. However, the advance of the oxygen front is significantly modified when increasing cells are numerically implemented along the fracture zone (Figure D-5a and c).

The minimum simulation time decided for this study has been 180 days, in order to attain steady state conditions of the advance of the oxygen and iron-mineral dissolution fronts for the most unfavourable conditions (despite it is attained in the matrix after 20 days of simulation time; Figure D-6). On the other hand, the dimensions of the numerical system are (Figure 7-4): 20 m as the total length of the fracture zone (X), and 10 mm as the maximum thickness of the rock matrix affected by the oxygen diffusion (Y).

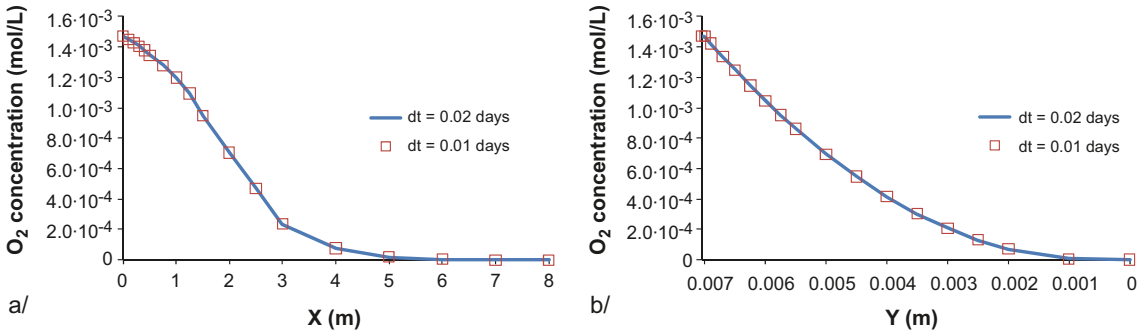

Figure D-4. *Evolution of the oxygen concentration a/ along the fracture zone and b/ in the matrix (Model 2 for 1 year of simulation time), considering dt of 0.01 and 0.02 days.*

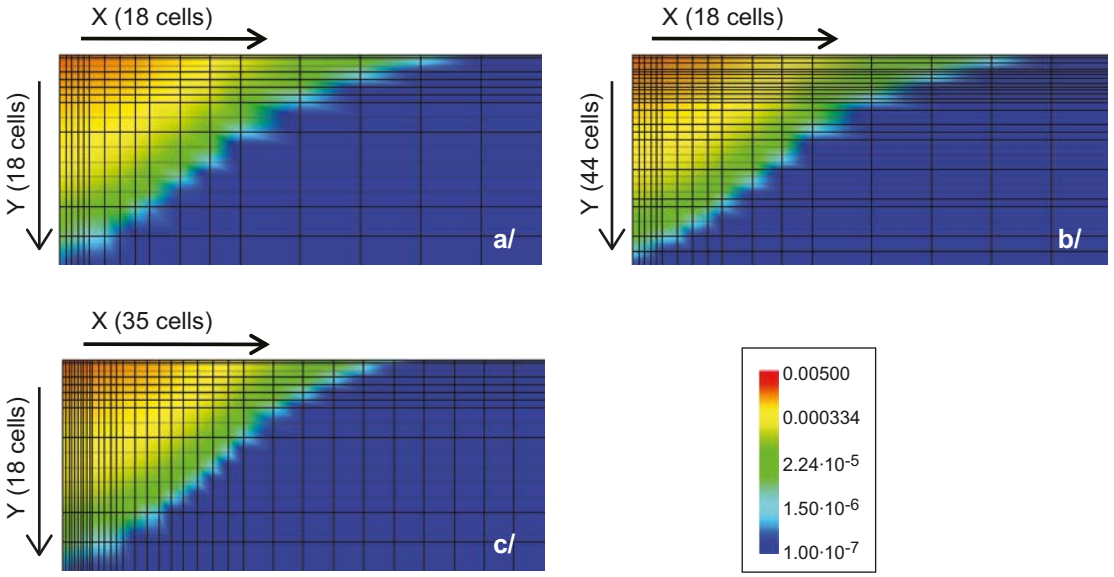

Figure D-5. *Oxygen concentrations (mol/L) after 30 days of simulation time for a numerical grid with a/ 18 nodes in X and Y, b/ with 44 nodes in Y, and with 35 nodes in X. It is remarkable as increasing cells in Y (a/ and b/) the solutions is practically identical. However, the advance of the oxygen front is significantly modified when increasing cells are numerically implemented along the fracture zone (a/ and c/).*

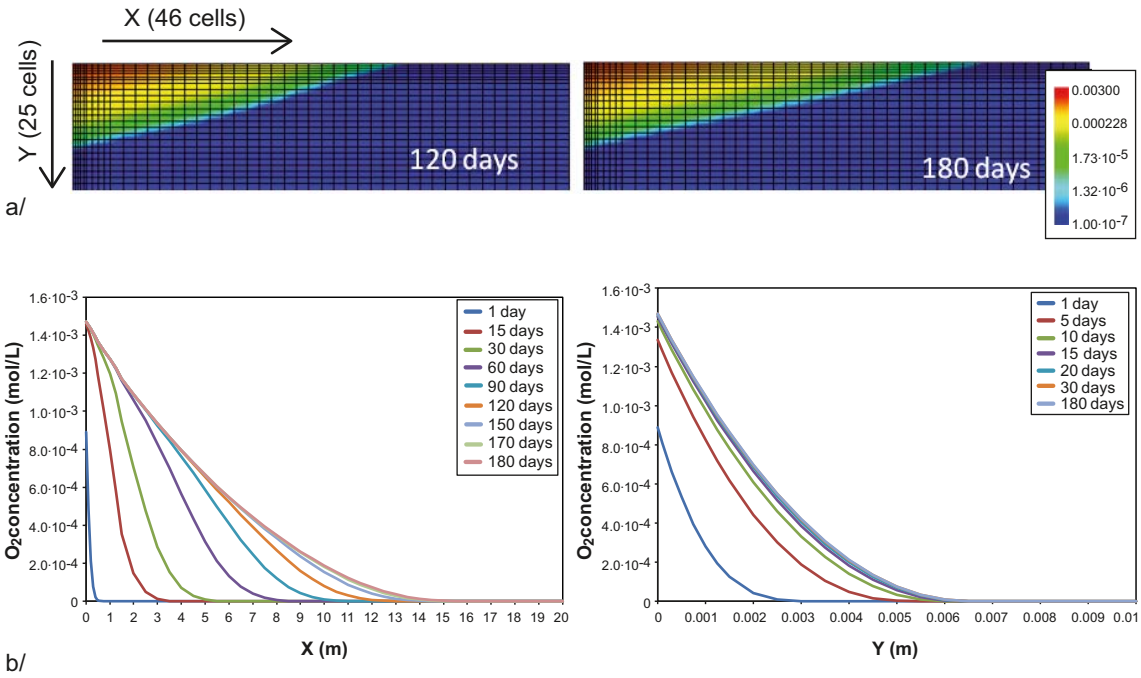

Figure D-6. *a/ Oxygen concentrations (mol/L) after 120 and 180 days of simulation time. b/ Evolution of the oxygen concentration along the fracture zone (X) and in the matrix (Y). It is remarkable as the steady state in reference to the advance of the oxygen front is attained in the matrix after 20 days. However, it is not attained along the fracture zone after 60 days of simulation time.*

Appendix E

Comparison between analytical and numerical solutions at pseudo-steady state conditions

In this appendix, the analytical pseudo-steady state solution for oxygen concentration profiles in the rock matrix and along the flow path is compared with corresponding numerical solutions. Results for the analytical solution in Section 6.4 are compared with solutions from 1D PHREEQC simulations for the rock matrix and 2D PHAST simulations for the rock matrix and along flow-paths presented in Section 7.

In Figure E-1, the analytical result for the oxygen concentration profile in the matrix is compared with PHREEQC simulation results for three different boundary oxygen concentrations in the fracture at pH 8. The concentration profiles agree well for high fracture concentrations as in Figure E-1a and b. There is a slight deviation between the profiles for lower fracture concentrations as in Figure E-1c. This trend is also seen for pH 8.5 in Figure E-2 where the deviation at low boundary concentrations is slightly larger. Also at pH 7.5 as in Figure E-3 the profiles agree well for high concentrations. At low concentrations we see a deviation, where the analytical solution predicts a slightly deeper ingress in the matrix than the numerical solution. This is opposite from the high pH case.

A comparison of the analytical solution with numerical results obtained from PHAST 2D simulations is shown in the following. It may be noted that the 2D simulations in PHAST are extremely computationally demanding. It is concluded that PHAST is not well suited for this kind of stiff problem that involves sharp concentration fronts in both the matrix and flow-path domains. Nevertheless, results for the base case scenario with a recharge concentration of 1.5 mM at pH 8 are shown in Figure E-4. It is seen that the PHAST simulation results approaches the analytical solution for the pseudo-steady state situation both along the flow path and in the matrix at the inlet of the fracture (at $F = 0$). Pseudo-steady state in the matrix is approximately reached already after 20 days. The simulation was stopped after 120 days due to the large CPU time for the simulation and it can be seen that pseudo-steady state along the flow path is not yet reached.

Similar results for lower recharge oxygen concentrations (0.3 and 0.03 mM) at pH 8 are shown in Figure E-5, where it is seen that the deviation increases for lower concentrations.

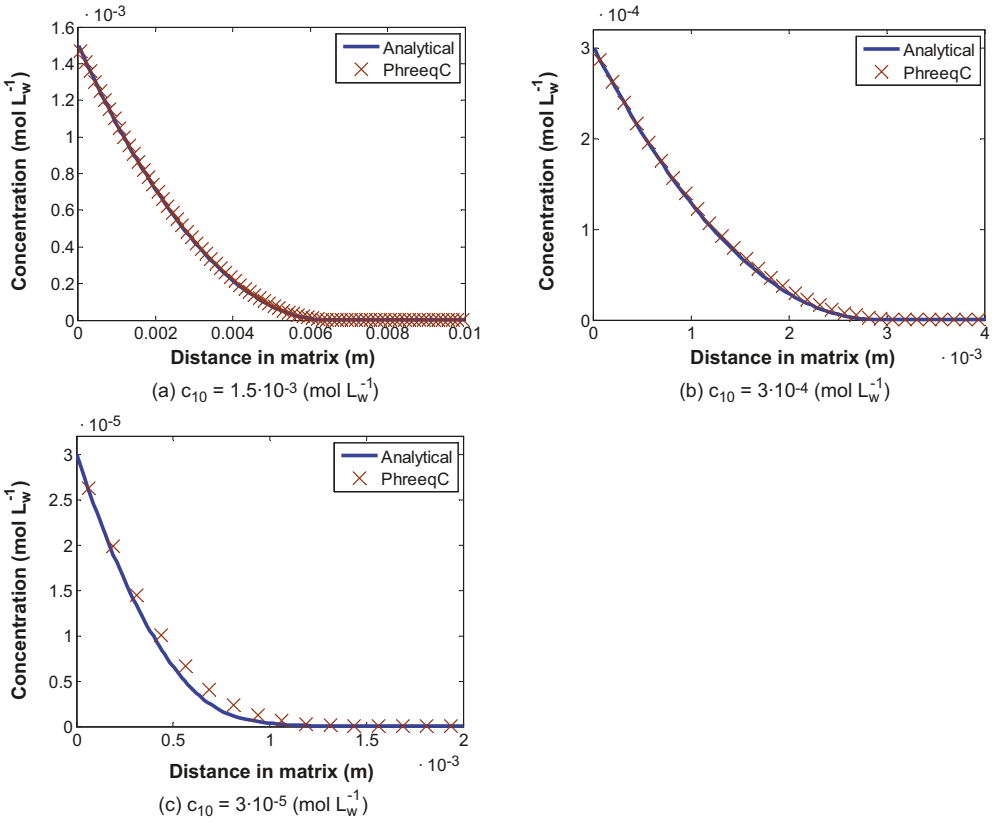

Figure E-1. *Pseudo-steady state oxygen concentration profiles expected in the rock matrix for the base-case at pH 8.0 at different fracture concentrations c_{1f} as calculated analytically and numerically in PHREEQC.*

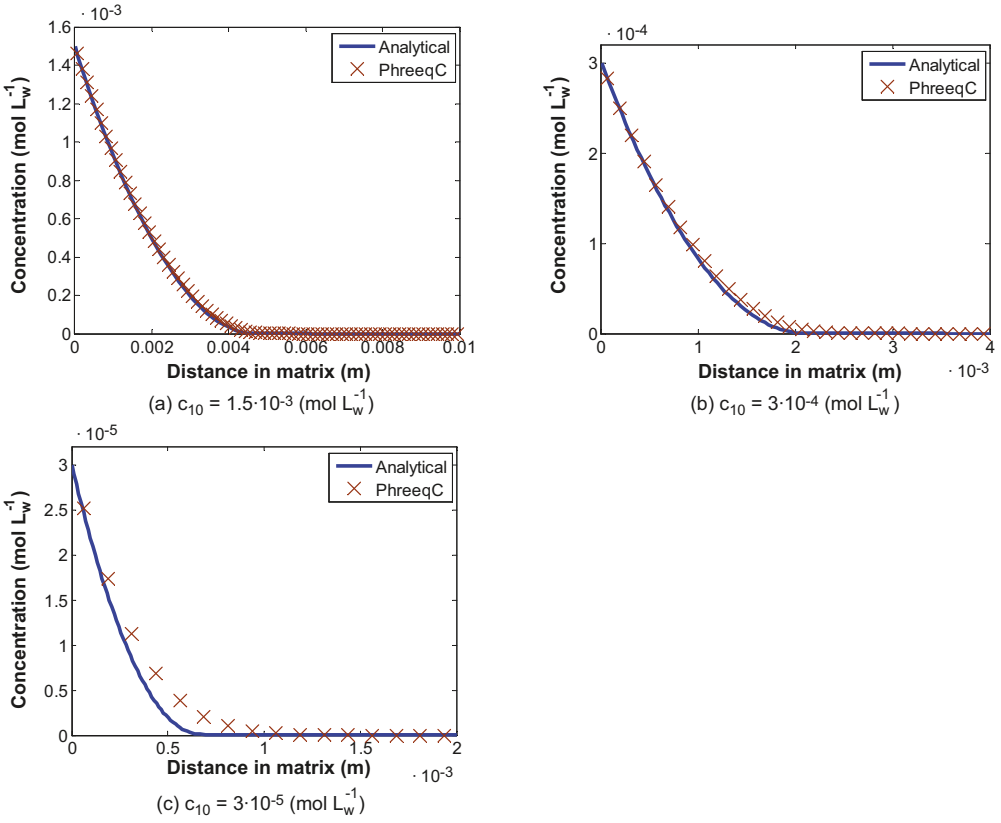

Figure E-2. *Pseudo-steady state oxygen concentration profiles expected in the rock matrix at pH 8.5 at different fracture concentrations c_{1f} as calculated analytically and numerically in PHREEQC (see Section 7).*

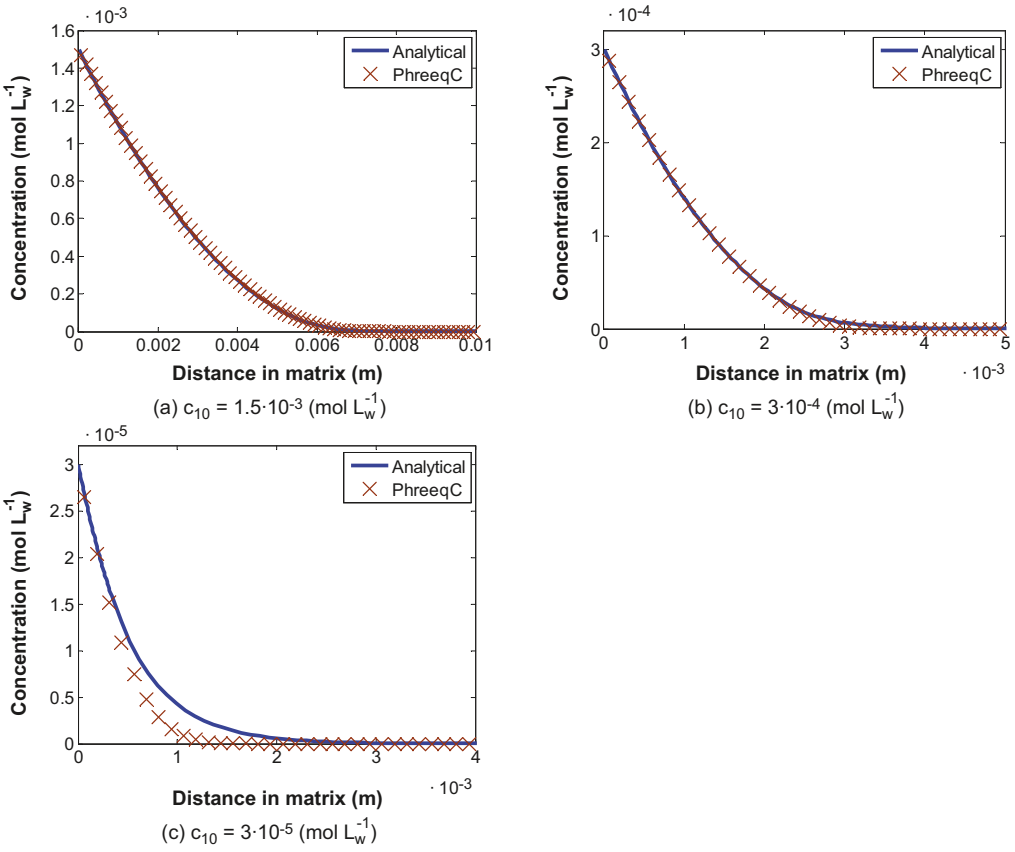

Figure E-3. *Pseudo-steady state oxygen concentration profiles expected in the rock matrix at pH 7.5 at different fracture concentrations c_{1f} as calculated analytically and numerically in PHREEQC.*

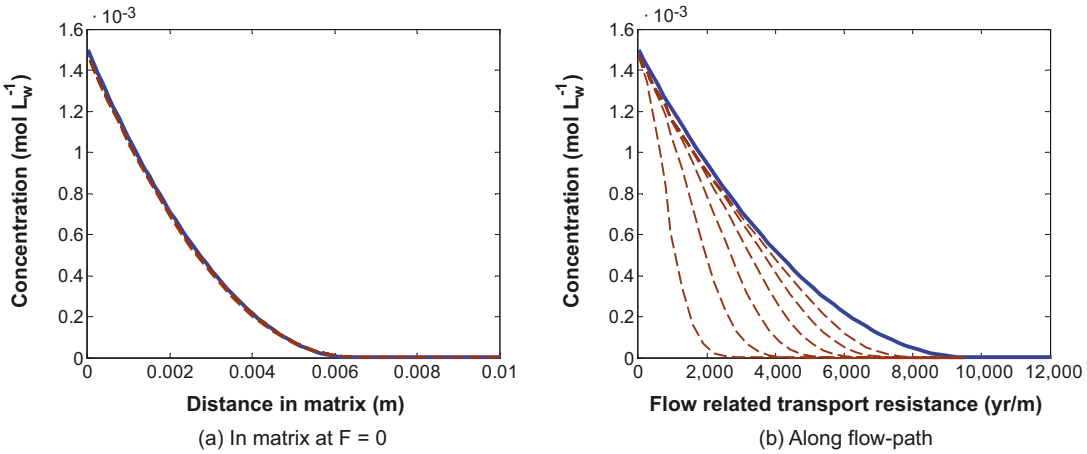

Figure E-4. *Pseudo-steady state oxygen concentration profile calculated analytically (blue curves) compared with the transient numerical solution using PHAST (dashed curves) for times 20, 40, 60, 80, 100 and 120 days at a recharge oxygen concentration of 1.5 mM; (a) in the rock matrix at the inlet of the fracture (at F = 0); (b) downstream along the flow path as a function of the corresponding F-factor.*

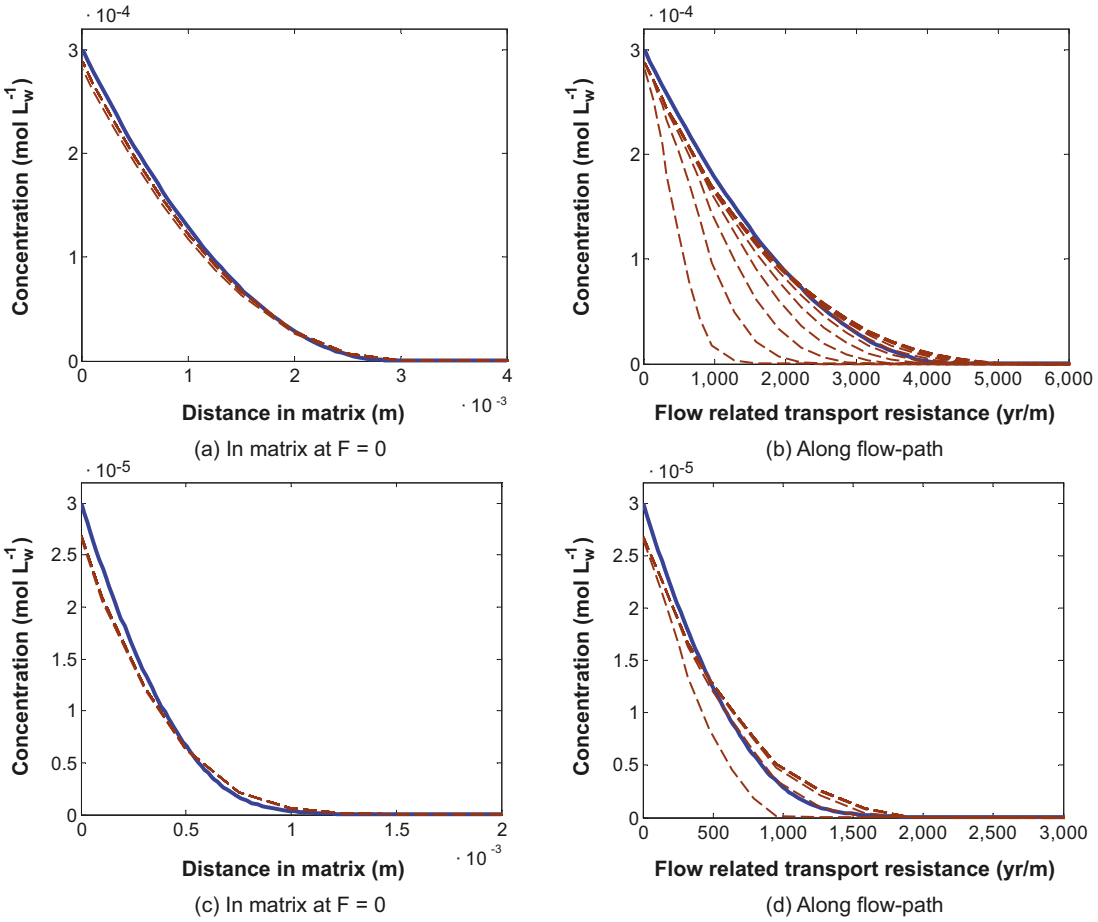

Figure E-5. *Pseudo-steady state oxygen concentration profile calculated analytically (blue and red solid curves) compared with the transient numerical solution using PHAST (dashed curves) for times 10, 20, 30, 40, 50, 60, 70, 80, 90, 100, 110 and 120 days at a recharge oxygen concentration of 0.3 mM and 0.03 mM; (a) and (d) in the rock matrix at the inlet of the fracture (at F = 0); (b) and (d) downstream along the flow path as a function of the corresponding F-factor.*